UNIVERSIDAD COMPLUTENSE DE MADRID
FACULTAD DE CIENCIAS FÍSICAS

TESIS DOCTORAL

Imagen cuantitativa en microscopia 3D con iluminación parcialmente coherente

Quantitative imaging in 3D microscopy with partially coherent illumination

MEMORIA PARA OPTAR AL GRADO DE DOCTOR

PRESENTADA POR

Juan Manuel Soto Rueda

DIRECTORES

José Augusto Rodrigo Martín-Romo
Tatiana Alieva Krasheninnikova

Madrid

UNIVERSIDAD COMPLUTENSE DE MADRID

FACULTAD DE CIENCIAS FÍSICAS

TESIS DOCTORAL

Imagen cuantitativa en microscopia 3D con iluminación parcialmente coherente

Quantitative imaging in 3D microscopy with partially coherent illumination

MEMORIA PARA OPTAR AL GRADO DE DOCTOR

PRESENTADA POR

Juan Manuel Soto Rueda

DIRECTORES

José Augusto Rodrigo Martín-Romo
Tatiana Alieva Krasheninnikova

Departamento de Óptica

Madrid, 2020

Acknowledgements

First of all I would like to express my gratitude to my academic advisors, José Rodrigo and Tatiana Alieva, for guiding me throughout these 4 years of research in the Department of Optics. Thanks to them, I've felt welcomed into the Interdisciplinary Group for Optical Computing since the very first day. In particular, I thank them for their patience, constructive suggestions, encouragement and devotion towards high-quality research as well as for teaching me following these standards. Everything mentioned above has played an imperative role in the successful development of this Phd dissertation and, which is of foremost relevance, the start of my research career. I also acknowledge Óscar Martínez for his help, advices and fruitful scientific discussions.

Secondly, I am very grateful to institutions and collaborators that have received me as a guest researcher during the course of this project. In particular, I thank Pierre Bon and Laurent Cognet from the Laboratoire Photonique, Numérique et Nanosciences (Institut of Optics, University of Bourdeaux) for giving me the chance to collaborate with their group during a 3-month stay. Furthermore, I acknowledge Spanish Ministry of Economy and Competitiveness (MINECO) for funding the project TEC2014-57394-P.

Thirdly, I thank all my colleages from the department, in particular Mercedes, Laura, Óscar and José Luis, for their friendship and support during these years and specially the last months.

Finally, last but not least I have to express my deepest gratitude to my family, particularly to my parents and my sister, for their comprehension and backing. They have taught me the value of effort and perseverance, and these values have guided me to carry out this Phd dissertation.

Once again, thanks to all of you.

Acronyms

AOTF Absorption Optical Transfer Function

ATP Adenosine Triphosphate

BFI Bright-field Illumination

BFP Back Focal Plane

BS Beam Splitter

C-ODT Coherent Optical Diffraction Tomography

cAMP Cyclic Adenosine Monophosphate

CFA Complex Field Amplitude

CL Condenser Lens

CMOS Complementary Metal-oxide-semiconductor

CT Computerized Tomography

CTF Complex Transfer Function

DAPI 4',6-Diamidino-2-phenylindole

DF Diclofenac

DH Digital Holography

DHM Digital Holographic Microscopy

DIC Differential Interference Contrast

DLP Digital Light Processing

DMC Dry Mass Concentration

DMD Digital Micro Device

DMEM Dulbecco's Modified Eagle Medium

DNA Deoxyribonucleic acid

DPC Differential Phase Contrast

EPAC Exchange of protein directly activated by cAMP

ETL Electrically Tunable Lens

FBS Fetal Bovine Serum

FFT Fast Fourier Transform

FSIM Feature Similarity

FT Fourier Transform

FWHM Full Width - Half Maximum

GI Gaussian Illumination

IFFT Inverse Fast Fourier Transform

IGI Inverse Gaussian Illumination

LC-SLM Liquid-Crystal Spatial Light Modulator

LED Light Emitting Diode

LSF Line Spread Function

LV Low-Value

MC Missing Cone

ME Metformin

MnSOD Manganese Superoxide Dismutase

MO Microscope Objective

MTF Modulation Transfer Function

OCR Oxygen consumption rate

ODT Optical Diffraction Tomography

OL Objective Lens

ORM Optical Refocusing Module

PBS Phosphate-Buffered Saline

PC-ODT Partially Coherent Optical Diffraction Tomography

PCI Partially Coherent Illumination

PCM Phase Contrast Microscopy

PFA Paraformaldehyde

POTF Phase Optical Transfer Function

PSF Point Spread Function

QLSI Quadriwave Lateral Shearing Interferometry

QPI Quantitative Phase Imaging

RBC Red Blood Cell

RI Refractive Index

RL Relay Lens

RMSE Root Mean Squared Error

RT Room Temperature

sCMOS Scientific Complementary Metal–Oxide–Semiconductor

SLIM Spatial Light Interference Microscopy

SNR Signal-to-noise ratio

TIE Transport of Intensity Equation

TL Tube Lens

WBC White Blood Cell

List of symbols

Symbol	Description
λ	Illumination wavelength
n	Refractive index
Re[...]	Real part of the argument
Im[...]	Imaginary part of the argument
n_{Re}	Real part of the refractive index
n_{Im}	Imaginary part of the refractive index
$\mathbf{r} = (x, y, z)$	3D position vector
ϕ	Phase
Δn	Refractive index contrast
u	Complex amplitude of the electric field
I	Optical intensity
$[...]^*$	Complex conjugate of the argument
$\mathbf{k}$	Wavevector
$\hat{O}$	Object spectrum
$\hat{I}$	Intensity spectrum
H	Optical Transfer Function
$\mathbf{p} = (p_x, p_y, p_z)$	Frequency vector
SC	Spatial coherence ratio
f	Focal length of the lens
$\mathrm{NA_c}$	Condenser Numerical Aperture
$\mathrm{NA_o}$	Objective Numerical Aperture
V	Scattering potential
P	Real part of the scattering potential
A	Imaginary part of the scattering potential
μ_r	Relative magnetic permeability
ε_r	Relative dielectric permittivity
G	Green's function
$\widehat{[...]}$	Fourier operation of the argument
$\mathbf{s}$	Incident illumination direction
$a^2(\lvert\mathbf{s})$	Incoherent intensity distribution over condenser aperture
h	Point spread function
S	Condenser diaphragm illumination distribution

Symbol	Description
O	Pupil function
B	Intensity of llumination background
δ	Dirac delta function
ε	Absorption parameter linking real and imaginary contributions of the RI
$\Delta x, \Delta y, \Delta z$	Nyquist distances (spatial resolution limit) in x, y and z directions
d	Distance between the ETL and the camera
M	Magnification of the microscope
$z_{defocus}$	Shift along optical axis direction (z) in object space
z_{scan}	Maximum scanned interval along optical axis direction (z)
$\mathrm{p}_\perp$	Radial transverse frequency modulus
$\mathrm{p_S}$	Maximum normalized frequency allowed by the condenser lens
$\mathrm{p_P}$	Maximum normalized frequency allowed by the objective lens
F	Auxiliary function for OTF definition
ψ	Piecewise parameter for OTF definition
Ω	Sample rotation angle around y-axis
κ	Rate of event arrivals in Poisson noise
ν_{ETL}	Frequency of the ETL
t_{exp}	Exposure time of the camera
N	Number of scanning spots in microscope condenser
N_z	Number of slices of intensity z-stack
β	Regularization parameter in Tikhonov and Wiener deconvolution
κ_m	Normalized wavevector magnitude in medium
σ	Standard deviation of gaussian illumination distribution
$\mathbf{r}_c$	Dimensionless coordinate vector
γ	Inverse gaussian amplitude modulation parameter
α	Specific refractive index increment
∇n	Refractive index gradient
τ	Threshold for RI gradient segmentation
R	Ratio of α at two different wavelengths
ν_{cam}	Working frequency of the camera
I_{ETL}	Current applied to the ETL
T	ABCD transfer matrix
D	Free space propagation matrix
L	Lens matrix
θ	Acceptance angle of a lens
PS	Power spectrum estimation

List of Figures

Contents

Abstract

The main research objective of this work is to develop and implement a fast and high resolution technique for reconstructing the 3D refractive index (RI) of weakly absorbing samples. This technique is based on the generalization of optical diffraction tomography (ODT), developed for coherent sample illumination (C-ODT), to the partially coherent case (PC-ODT). In contrast to C-ODT, which involves a specially designed holographic microscope, the proposed PC-ODT technique is implemented in conventional wide-field microscope. The incorporation of the required refocusing module is easy and can be done by a final user unfamiliar with optics (i.e. clinicians and biologists). The low coherent illumination provided by high numerical aperture condenser results in high resolution and reduced speckle noise typical for laser sources used in C-ODT.

This thesis has been divided into eight Chapters, as follows.

In **Chapter 1**, we introduce the field of quantitative label-free 3D microscopy based on tomographic reconstruction of the sample's RI, which has gained increased attention thanks to its capability of revealing cell information (shape, dry mass, density and composition) without using exogenous agents (chemical or fluorescent dyes). The computational reconstruction of 3D RI based on ODT has turned into a widespread alternative to staining techniques as it avoids some of fluorescent imaging's drawbacks like phototoxicity or complex sample preparation.

In **Chapter 2**, we review C-ODT, which is present in most of commercially available ODT implementations. Instead of physically rotating the sample, in the C-ODT microscope the angle of the illumination beam is changed by using, for example, a galvo-mounted mirror. This is often referred to as beam rotation illumination and requires a temporal multiplexing approach to fill the maximum allowed 3D microscope aperture in order to reconstruct the 3D optical scattering potential, which is related to the sample's RI. Thus, this technique involves the acquisition and the computational processing of significant volume of data, as well as it typically requires an expensive off-axis interferometric setup.

An alternative is treated in **Chapter 3**, which describes the fundamentals of PC-ODT, comprising of the proposed algorithm for its implementation and numerical simulations of its performance. In PC-ODT, the sample is simultaneously illuminated from different directions allowed by wide-field microscopes. Then, the 3D RI reconstruction is performed from a stack of through-focus intensity images, $I(\mathbf{r})$, by applying a deconvolution with the effective optical transfer function (OTF) of the system (comprising both absorption and phase contributions). For low spatial coherence illumination, the wide-field microscope transmits the same object spatial-frequency content that C-ODT is able to achieve from multiple illuminations. PC-ODT can significantly reduce the data acquisition time because

it only measures a single stack of images $I(\mathbf{r})$ and simplifies the reconstruction process. The benefits of partially coherent illumination, like the removal of speckle noise or lower phototoxicity risk, are in return accompanied by a lower image contrast for a region of object frequencies which are severely attenuated: the low-value (LV) region.

The experimental setups suitable for PC-ODT are discussed in **Chapter 4**. Our PC-ODT setup involves a wide-field microscope equipped with a LED source, under bright-field illumination (BFI) and attached to an optical refocusing module (ORM), which provides the required through-focus intensity images recorded by a digital camera. The ORM can be easily incorporated in conventional wide-field microscopes and synchronized with a digital camera. Different implementations of ORM setups are discussed. PC-ODT technique is experimentally verified on well-known test samples (i.e., blood cells, diatoms, etc.).

Chapter 5 is devoted to OTF optimization in order to enhance the quality of RI reconstruction with PC-ODT when only a single stack of through-focus intensity images $I(\mathbf{r})$ is available. The OTF strongly depends upon the intensity distribution in the input aperture plane of the microscope condenser lens. An illumination design alleviating the LV region problem has been found, after having explored several illumination patterns (BFI, gaussian, annular and combinations thereof). Particularly, by replacing conventional bright-field with a properly designed gaussian illumination in the condenser aperture, a better balance between the transmitted low and high frequencies (more uniform OTF) is provided. The improvement in RI recovery by using gaussian illumination is demonstrated with both numerical simulations and experimental measurements. Finally, it has been verified that the use of more realistic OTFs, which is calculated by considering the real experimental illumination conditions, significantly increases the accuracy in 3D RI reconstructions.

PC-ODT provides a 3D data acquisition with a spatial resolution similar to C-ODT but with higher tomography frame rate (e.g. 10 fps in 3D) compared to the current state of the art for C-ODT (2.5 fps and 0.5 fps according to Tomocube and Nanolive companies, respectively). In this way, PC-ODT can be extended to video-rate 3D imaging (time-resolved tomography) which is suitable for the study of living cells and dynamic micro-objects, as described in **Chapter 6**. Video-rate 3D RI reconstructions are tested with freely swimming and optically manipulated living yeast bacteria along with living COS-7 cells.

Relevant PC-ODT applications in biomedicine are outlined in **Chapter 7**, more particularly, the 3D RI reconstruction of cells for disease diagnosis (Leishmania, necrosis) as well as cell dry mass and volume estimation. PC-ODT is also tested in a drug screening experiment over primary rat hepatocytes, wherein RI variations of mitochondria are correlated with the damage induced by certain chemicals.

The main achievements derived from this work and the perspectives of future development and applications of PC-ODT are summarized in **Chapter 8**.

Resumen

El principal objetivo de esta tesis es desarrollar e implementar una técnica rápida y de alta resolución para la reconstrucción del índice de refracción (IR) 3D de muestras de absorción débil, basada en la generalización de la tomografía de difracción óptica (TDO), desarrollada para iluminación coherente (TDO-C), al caso parcialmente coherente (TDO-PC), lo que evita el ruido coherente y otros artefactos de la iluminación coherente (láser). Al contrario que la TDO-C, que requiere microscopios holográficos (típicamente en configuraciones interferométricas fuera de eje), la técnica TDO-PC propuesta se implementa en un microscopio de campo amplio. La incorporación del módulo de reenfoque óptico es sencillo y puede ser realizado por un usuario no familiarizado con la óptica (como médicos y biólogos). La iluminación poco coherente proporcionada por un condensador de alta apertura numérica logra una alta resolución y reducción del ruido coherente (*speckle*) típico de las fuentes láser utilizadas en TDO-C.

El contenido de la tesis se ha dividido en ocho capítulos, como sigue.

En el **Capítulo 1** se ha introducido el campo de la microscopía cuantitativa 3D sin marcadores químicos, basada en la reconstrucción tomográfica del IR y que permite obtener información de las muestras celulares (forma, masa seca, densidad, composición, etc.) sin recurrir a agentes exógenos como marcadores químicos o de fluorescencia. La reconstrucción computacional del IR basada en TDO se ha extendido como alternativa a las técnicas de tinción, con el fin de evitar algunos inconvenientes de fluorescencia, como la fototoxicidad o los complejos protocolos de preparación de la muestra.

En el **Capítulo 2** se introduce la TDO-C, presente en la mayoría de las implementaciones comerciales actuales. En vez de rotar la muestra, en el microscopio adaptado para la TDO-C se cambia el ángulo del haz de iluminación utilizando, por ejemplo, un espejo rotante montado sobre un galvanómetro. Este enfoque requiere de un multiplexado temporal para rellenar la apertura del microscopio y reconstruir el potencial de esparcimiento 3D ligado al IR de la muestra. Así, esta técnica involucra la adquisición y el procesamiento computacional de un volumen significativo de datos.

Alternativamente, el **Capítulo 3** describe los fundamentos de la técnica TDO-PC, incluyendo el algoritmo propuesto para su implementación y simulaciones numéricas de su desempeño. En TDO-PC la muestra es iluminada simultáneamente desde diferentes direcciones permitidas por el microscopio de campo claro. La reconstrucción del IR 3D es realizada a partir de un conjunto de imágenes de intensidad $I(\mathbf{r})$, adquiridas reenfocando

la muestra a lo largo de un eje, y aplicando una deconvolución utilizando la función de transferencia óptica (FTO) efectiva del sistema, incluyendo la contribución de fase y de absorción. Para iluminación con baja coherencia espacial el microscopio de campo amplio transmite el mismo contenido frecuencial que su contraparte de TDO-C es capaz de obtener de múltiples iluminaciones. La TDO-PC puede reducir significativamente el tiempo de adquisición de los datos ya que requiere medir un único conjunto de imágenes $I(\mathbf{r})$. Los beneficios de la iluminación parcialmente coherente van acompañados por un menor contraste en la imágenes de intensidad adquiridas y por una región de frecuencias espaciales del objeto severamente atenuadas: la región de valores bajos.

En el **Capítulo 4** se analizan varios montajes experimentales para la implementación de TDO-PC. La TDO-PC es compatible con los microscopios de campo amplio convencionales equipados con fuentes de diodo emisor de luz o halógenas. De esta manera, nuestro montaje experimental de TDO-PC comprende un microscopio de campo amplio con iluminación de campo claro (ICC), unido a un módulo de reenfoque óptico (MRO) que proporciona las imágenes $I(\mathbf{r})$, que son registradas por una cámara digital. Además, diferentes montajes experimentales basados en dicho MRO son estudiados y la TDO-PC ha sido testada en células sanguíneas y diatomeas.

El **Capítulo 5** trata de la optimización de la FTO mediante el diseño de la iluminación en TDO-PC, cuando se dispone de un único conjunto de imágenes $I(\mathbf{r})$. La FTO depende de la forma y la distribución de intensidad en el plano de la apertura de entrada del condensador del microscopio. Hemos encontrado un diseño óptimo capaz de minimizar la región de valores bajos, tras explorar diversos patrones de iluminación (ICC, gaussiana, anular, etc.). Reemplazando la convencional ICC por una iluminación gaussiana diseñada adecuadamente, se consigue un mejor balance entre las frecuencias altas y bajas transmitidas (una FTO más uniforme), lo que ha sido demostrado mediante simulaciones numéricas y mediciones experimentales. También se ha comprobado que el uso de FTO más realistas, calculadas según la iluminación experimental, contribuye a mejorar la calidad del IR 3D.

La TDO-PC proporciona una adquisición de datos 3D con una resolución espacial similar a la de TDO-C pero con una mayor velocidad (10 fps en 3D) en comparación con el estado de la técnica actual para TDO-C (2.5 fps y 0.5 fps según las empresas Tomocube y Nanolive). Así la TDO-PC puede extenderse a la reconstrucción de la muestra como vídeo 3D (tomografía con resolución temporal), que es adecuada para estudiar células vivas y objetos microscópicos dinámicos, como se describe en el **Capítulo 6**. La validación experimental de TDO-PC para reconstruir el IR de muestras vivas se lleva a cabo con bacterias de levadura, tanto nadando libremente como manipuladas ópticamente con pinzas ópticas, y células COS-7 derivadas de tejido de riñón de mono.

Otras aplicaciones relevantes de la TDO-PC se muestran en el **Capítulo 7**, en particular, la reconstrucción del IR 3D de células para diagnóstico de patologías (Leishmania, necrosis), el cálculo de la masa seca y volumen celular; así como la verificación de los efectos de distintos fármacos sobre hepatocitos primarios de ratón. Las variaciones de IR de las mitocondrias de dichos hepatocitos se han relacionado exitosamente con el daño producido por ciertos medicamentos.

Finalmente, los logros principales de este trabajo, así como las previsibles líneas de desarrollo futuro y potenciales aplicaciones de TDO-PC se detallan en el **Capítulo 8**.

Chapter 1

INTRODUCTION

1.1 Quantitative label-free microscopy

Historically, microscopy has been a qualitative technique based on spatial features (e.g. distances, areas, shapes, contours, etc.) with merely imaging purposes. However, the transition to digital microscopy along with the new imaging methods, either based on labeling (i.e. by chemical agents, autofluorescence, etc.) or label-free (like phase imaging and optical tomography), pave the way to a more quantitative microscopy intended to extract meaningful quantitative data, for example the refractive index, density or chemical composition, from the images. In this way, quantitative microscopy enables not only imaging but also quantitatively study the sample. Computational imaging techniques are crucial in this turning point. The evolution of microscopy into a more quantitative technique will provide important scientific benefits such as an improved performance, a better reproducibility of the experiments and the possibility of better comparing the results obtained with different techniques and equipment [1]. From now on, we exclusively focus on the applications of quantitative microscopy in the field of biomedicine, since the possibility of straightforwardly observing and quantitatively characterize tissues and cells (including their organelles) opens a wide range of possibilities to better understand their inner machinery.

One possibility for obtaining quantitative images is fluorescence microscopy, in which one acquires digital images where the intensity value of each pixel encodes information about the local concentrations of fluorophores present at a certain region of interest of the sample [2]. Note that fluorescence imaging enables functional imaging of a cell sample as the fluorophores selectively bind to specific biomolecules or organelles. The labeling of the target region can be achieved in different ways, by using either extrinsic contrast agents (for instance fluorophores like Nile red, green fluorescent protein or methylene blue) or intrinsic properties from the sample (autofluorescence) [3]. The advantage of autofluorescence over extrinsic contrast agents consists of avoiding the sample staining. However, both of these techniques require to modify the cells and its natural environment (for instance, via fixation or by genetic modification) which may lead to misleading results. Moreover, they suffer undesired effects such as photobleaching (consisting of a light-induced destruction of the fluorophore suitable for limited time-lapse studies) and phototoxicity (damage in the sample or modification of its natural behaviour). It is worth remarking that most advances

in cell biology studies reached during the last decade have been obtained thanks to fluorescence microscopy. Moreover, the combination of fluorescence and confocal microscopes has allowed rendering 3D images of the sample [4]. This fact has been recognized by the Nobel Prize in Chemistry in 2014 awarded jointly to Eric Betzig, Stefan W. Hell and William E. Moerner for their development of super-resolved fluorescence microscopy [5].

An alternative to fluorescence, widely applied in biological studies, consists of phase imaging techniques such as Zernike phase contrast microscopy (PCM) [6] or Nomarski Differential Interference Contrast (DIC) [7] which do not involve chemical tagging of the sample and therefore overcoming phototoxicity problems mentioned above. Both techniques turn phase shifts into light intensity (amplitude) variations clearly observable by human eye or recorded by a camera. Although useful, these techniques do not provide quantitative maps of phase variations. Indeed, in both PCM and DIC, the output image is a combination from both phase and amplitude gradient contrasts so the complex-field information cannot be retrieved uniquely [8].

Further, different techniques have been proposed in order to obtain a phase map of the sample, such as digital holographic microscopy (DHM) and phase-shifting interferometric microscopy, which are able to record the complex field of the wave scattered by the sample [9]. In this context, the field of the so-called quantitative phase imaging (QPI) [10, 11] emerged as a possible alternative to fluorescence microscopy to provide quantitative cell analysis without using labeling agents and inspired by the pioneering works of Zernike [6], Nomarski [7] and Gabor holography [12]. Most QPI techniques involve computational retrieving of a 2D phase image that reveals the cell topography from an interferometric measurement of the light scattered by the object, recorded as a hologram by a digital camera. However, they do not provide the 3D structure of the object.

Numerous variants of such a DHM technique have been developed in the last decades demonstrating nearly real-time 2D phase imaging of different transparent objects including living cells, see for example [13–16], with nanoscale sensitivity to dynamic changes in the sample and suitable for studies at different spatial or temporal scales [11, 17]. 2D QPI methods are reasonably simple in sample preparation, yet effective for a wide range of applications involving nearly transparent samples. For instance, in Ref. [17] the assessment of a single red blood cell (RBC) is proposed by monitoring its flickering and in Ref. [18] their membrane deformability is quantified in the presence of different amounts of adenosine triphosphate (ATP). Likewise, in [19] the relationship between the cell cycle stage and the dry mass (derived from a phase measurement) is explored for E. coli cells, while in [20] dynamic 2D phase maps have been exploited to study cardiomyocyte differentiation that is a conventional approach to research heart disease. Furthermore, QPI have also been applied beyond optical microscopy in fields such as material science to study multilayer structures including dielectric-dielectric interfaces [21], X-ray soft tissue research [22–24] and commercial optical fiber profiling [25, 26].

Most of the aforementioned QPI techniques are interferometric and require highly coherent sources (e.g. laser), thus introducing speckle noise and artifacts (ringing, halos, etc.) in the reconstructed object phase. To mitigate these problems there have been also several efforts of developing QPI based on partially coherent illumination, for instance, in a Mach-Zehnder configuration [27–29] or by using a wavefront sensor [30]. Another problem linked to holographic methods is the necessity of a highly stable reference arm, thus

being sensitive to non common-path fluctuations affecting the reference and object beams. This problem is addressed by the quadriwave lateral shearing technique [30], which takes advantage of the wavefront sensor technology thanks to its capability to sample the phase in a given plane without the use of a reference arm.

As an alternative to interferometric methods, QPI can be performed applying the transport of intensity equation (TIE), first developed by Teague [31] and then adapted to optical microscopy [32–35]. TIE is a defocus-based method in which the phase can be retrieved from a calculation of the intensity derivative along the optical axis. Two through-focus intensity images can be used to approximate the axial intensity derivative by using finite differences, however, such estimation is inaccurate. To overcome this shortcoming a higher order TIE method (see Ref. [36]) has been proposed to better estimate the intensity derivates based on polynomial fitting for correcting nonlinearity, thus resulting in a more robust method under noisy conditions.

A different approach for phase retrieval, different from interferometric and defocus (TIE) methods, consists of the use of ptychography [37, 38]. In this label-free technique, a coherent illuminating beam moves with respect to the object, which yields a sequential array of overlapping illuminated regions. For each illuminated region, the light scattered as it passes through the object is registered as a diffraction pattern on a detector (camera). Then, the diffraction patterns are processed by an iterative phase retrieval algorithm. Unlike DHM, ptychography is able to recover both the phase and amplitude of the field scattered by an object without requiring a reference wave. A variant of ptychography is Fourier ptychographic microscopy [39, 40], which iteratively combines in Fourier domain differently illuminated low-resolution intensity images, i.e. by using a LED array to control the spatial frequency scanning, in order to produce a wide-field and high-contrast image. Although providing a good performance (high resolution and wide field of view), the ptychographic methods (as well as other scanning illumination based QPI techniques) are slow in acquisition and processing, so they are not appropriate for the study of dynamic objects.

The actual trend of QPI is the reconstruction of the 3D refractive index (RI) distribution of an object. Indeed, it allows obtaining valuable quantitative information about the object structure, shape, mass, volume, density and their evolution in the natural cell environment. Further, in the case of a biological cell, its RI can provide other biophysical information such as the local concentration of certain chemicals (e.g. the hemoglobin density, as shown in Ref. [41]). Most biological samples (i.e. cells and tissue slices) can be considered as transparent samples with little absorption (close to the so-called phase objects). Let us define the RI of the sample, $n(\mathbf{r},\lambda) = n_{\mathrm{Re}}(\mathbf{r},\lambda) + \mathrm{i}n_{\mathrm{Im}}(\mathbf{r},\lambda)$, where n_{Re} and n_{Im} are the real and imaginary part of the RI, correspondingly, λ stands for the illumination wavelength and $\mathbf{r}$ is a 3D position vector. For weakly absorbing objects, the component n_{Re} (related to the phase) prevails over n_{Im} (associated with the sample absorption). We recall that pure phase transparent objects (as compared to absorbing objects) do not affect the amplitude of the illumination waves transmitted through them.

To achieve the 3D RI reconstruction of an object, two main approaches can be considered: computerized tomography (CT) [42] and optical diffraction tomography (ODT) [43], both of them compatible with wide-field microscopy. These approaches were established in 50th-70th of the last century but their relevant applications in microscopy have started only after the development of proper optoelectronic devices, powerful computers and efficient

signal processing algorithms.

CT and ODT require illuminating the object from different sides. For instance, the variation of the illumination angle in wide-field microscopy is usually achieved by scanning point by point the condenser aperture diaphragm [44, 45]. Thus the sample is sequentially illuminated by spatially coherent *plane waves* propagated in different directions. The larger the condenser and objective numerical apertures (NAs), the broader the angular interval allowed for the object inspection. For every illumination angle, the complex field amplitude of light passing through the sample is recovered by interferometric, TIE, iterative or any other method. Finally, the 3D distribution of the RI contrast $\Delta n(\mathbf{r}) = n_s(\mathbf{r}) - n_m$ of the 3D object is recovered, where n_m is the RI of the surrounding medium in which the object is immersed.

The principal difference between CT [44–46] and ODT [47–53] lies in the posterior processing of the measured intensity distributions of the light transmitted by the sample. In CT framework the eikonal approximation is assumed. In this case, from the phase of the optical field, the object thickness is obtained along each possible illumination direction. Later, the back filtered projection or other tomographic algorithms are applied to recover the distribution of the RI contrast $\triangle n(\mathbf{r})$ of the object [45]. However, the eikonal approximation is only valid when the size (l) of the inhomogeneities of the RI is significantly larger than the wavelength λ and the width of the sample L satisfies the following condition $\sqrt{\lambda L} \ll l$, that for visible wavelength range means approximately $l > 5\,\mu$m and $L \ll 50\,\mu$m [54]. Therefore, it can not be used for analysis of object details of around $1\,\mu$m size. In contrast, ODT [47–49, 51, 53, 55–57] takes into account the diffraction phenomena that in high resolution microscopy allows for inspecting smaller object details than in CT [50, 58]. For this reason, in the scope of this thesis we focus only on ODT since we mainly treat with biological samples (containing tiny organelles below $1\,\mu$m) illuminated in the visible range ($\lambda = 400 - 700\,$nm), thus diffraction effects can not be neglected. Within ODT one finds techniques which benefit from coherent illumination, whereas others apply partially coherent illumination. With respect to 3D imaging applications, it is worth pointing out that the image obtained with highly coherent illumination endures a severe cross-talk caused by objects placed in the same or surrounding depth layers encompassed by the sample. The use of quasi-monochromatic partially coherent illumination (light with partial temporal and spatial coherence) circumvents such drawbacks as well as enables speckle noise mitigation. For instance, the light diffracted by sample layers separated by a distance larger than the temporal coherence length do not interfere each other at the imaging plane. Hence, this coherence gating effect allows for enhanced depth discrimination and out-of-focus information removal [59]. The partial spatial coherence of the illumination also plays an important role in the image formation process in optical microscopy [60] as we will further study in Chapter 3.

The first proposal of application of coherent ODT in wide-field microscopy was published in 2013 (see [52]). Today, coherent ODT has been incorporated into devices comprising especially designed holographic microscopes (including a Mach-Zehnder configuration) operating in transmission. So far, there are two companies, Tomocube [61] and Nanolive [62], providing coherent ODT technology as a 3D imaging tool for biologists and clinicians requiring marker-free imaging.

As a summary, 3D label-free microscopy has gained increased attention thanks to its

capability of revealing cell structural information (shape, organelles, density and composition) without using exogenous agents such as chemical or fluorescent dyes. This type of computational RI imaging technique based on ODT [43] has turned into a widespread alternative to staining (i.e. fluorescence) techniques. Indeed, label-free microscopy techniques enable to image the specimen in its natural environment or with minimal preparation, obtained with a harmless illumination source. Our ODT technique, based on partially coherent illumination, has been developed for standard wide-field microscopes with low coherent illumination and it can be applied using high numerical aperture (NA) objective lenses enabling high resolution imaging.

1.2 Objectives and organization of the thesis

After the comparative analysis of the state of the art about phase tomography and coherent ODT techniques along with the seminal works of N. Streibl [60] on 3D image formation in wide-field transmission microscopy with partially coherent illumination (PCI), published 35 years ago, the latter approach has been chosen as a basis of our research. This approach, forgotten for a long time, can be considered as a mainstay for the generalization of ODT developed for coherent sample illumination (C-ODT) to the partially coherent case (PC-ODT). The goal of this thesis is to develop an affordable and fast technique, compatible with conventional wide-field transmission microscopes, for reconstruction of the 3D refractive index (label-free imaging) of weakly absorbing samples (e.g. biological cells) by using PCI. To this end, the following objectives were set up:

1. Establishment of the theoretical background, supported by the corresponding development of algorithms and software, for high-resolution RI tomography from a single stack of through-focus intensity measurements. In particular, this work includes the analysis of the microscope optical transfer functions, the design of an appropriate illumination able to balance the low and high spatial frequencies transmitted by the microscope, the choice of the proper deconvolution method and the numerical verification of the proposed reconstruction scheme.

2. The experimental implementation of PC-ODT, by means of an affordable setup compatible with commercial wide-field microscopes and, at the same time, fast enough to enable video rate 3D RI reconstruction of dynamic micro-objects such as living cells and bacteria.

3. The application of the developed PC-ODT technique to solve real-world problems in the area of biomedicine and biophysics.

The thesis is organized as it follows. In the first section of this introductory **Chapter 1**, we have briefly introduced the field of label-free imaging, from the first 2D phase retrieval techniques to the 3D microscopy based on tomographic reconstruction of the sample's RI distribution, which has gained increased attention thanks to its capability of revealing cell structural information (shape, organelles, density and composition) without using exogenous agents such as chemical or fluorescent dyes.

In **Chapter 2**, the C-ODT technique is introduced, which allows the recovering of the complex RI. C-ODT implementations are based on digital holography and apply temporally and spatially coherent illumination sources (lasers). Particularly, we review the theoretical

fundamentals (further linked to PC-ODT background), the required experimental setup, the strengths and the downsides of C-ODT.

In **Chapter 3**, we propose an alternative to the C-ODT technique by using partially coherent illumination: PC-ODT. After the introduction of the theoretical fundamentals of this technique and the analysis of the phase and amplitude transfer fucntions (POTF and AOTF, correspondingly) of high resolution wide-field microscope, we establish a simple method for the 3D reconstruction of the RI real part from a single stack of through-focus intensity measurements. The advantages and drawbacks of PC-ODT are underlined after its comparison with C-ODT. The proposed PC-ODT scheme is verified by numerical simulations.

Chapter 4 describes the proposed setup for the experimental implementation of PC-ODT. It involves a wide-field microscope, working under partially coherent illumination, and attached to an optical refocusing module (ORM) that in turn comprises an electrically tunable lens (ETL) for high-speed optical axially scan of the sample, which provides the required intensity images recorded by a digital camera. Two different configurations of the ORMs are considered. They are affordable and can be easily incorporated in conventional wide-field microscopes, and synchronized with the digital camera by a final user non familiarized with optics (i.e. clinicians and biologists). Further, in this Chapter our PC-ODT implementation is tested with well-known samples (diatoms, red blood cells, etc.).

Chapter 5 is devoted to the optimization of the OTF, by means of the PCI design, in order to enhance the quality of reconstructed RI with PC-ODT by only using a single stack of through-focus images. The OTF strongly depends upon the shape of the intensity distribution in the aperture plane of the microscope condenser lens. Consequently, we aim at designing an illumination, different from the conventional bright-field one, for alleviating the low value region of the POTF. To this end, we have explored several illumination patterns and we found that, by replacing conventional BFI with a properly designed gaussian illumination, a better balance between the transmitted low and high frequencies is obtained along with a more uniform OTF. Also, we have considered the use of more realistic OTFs, which have been calculated by considering the real experimental illumination conditions. The comparative numerical and experimental study of different illumination schemes are carried out.

In **Chapter 6** we demonstrate the use of PC-ODT for the analysis of dynamic micro-objects such as freely swimming and optically manipulated bacteria as well as the intracellular dynamics of mammalian cells by reconstructing their 3D RI distributions at video-rate. The optical manipulation of bacteria is achieved by adding an unconventional holographic optical tweezers module to the microscope. These studies involve fast sampling (e.g. 10 RI stacks per second) of the sample attainable by the use of the ETL and is actually limited by the camera frame rate.

The **Chapter 7** is devoted to real-life applications of PC-ODT in the field of biomedicine. In particular, we focus on the 3D RI reconstruction of cells with PC-ODT for applications such as disease diagnosis as well as for estimation of the cell dry mass, among others. It has been demonstrated that, by using the 3D RI distribution obtained with PC-ODT (and parameters derived thereof such as the dry mass concentration), it is possible to study a wide variety of biological physiological changes such as cell parasitization, cell malfunctioning induced by pharmacology and necrosis. In this fashion, we envision that PC-ODT can be

an affordable and powerful alternative to C-ODT in a wide variety of studies in which the RI works as a biomarker.

As a summary, the main contributions derived from this work are outlined in **Chapter 8**, along with future research lines that could enhance PC-ODT in the near future.

Finally, several appendices are also included, where the details of important equation derivations (Appendices A-B), the experimental estimation of the modulation transfer function (Appendix C), the results of additional experiments of RI reconstruction (Appendix D), the protocols for biological sample preparation (Appendix E) and the statistical tests (Appendix F) are provided.

Chapter 2

COHERENT OPTICAL DIFFRACTION TOMOGRAPHY (C-ODT)

2.1 Introduction

The current trend in wide-field label-free microscopy of low absorption samples is not only obtaining high contrast images but also recovering from them quantitative information about the 3D object structure (form, size or composition) directly related to its RI $n_s(\mathbf{r})$, where $\mathbf{r} = (x, y, z)^t$ is a 3D position vector. In general, thanks to the development of computational optics and, more in particular, digital holography, it has been possible to solve the inverse problem that aims at recovering the complex field amplitude of the light scattered by a sample and therefore its RI from a sequence of recorded intensity images. Finally, the 3D distribution of the RI contrast $\Delta n(\mathbf{r}) = n_s(\mathbf{r}) - n_m$ of the 3D object is recovered, where n_m is the RI of the surrounding medium in which the object is immersed.

Throughout this Chapter, the fundamentals and the state of the art of ODT based on coherent illumination, hereinafter referred to as C-ODT, are treated. While the first proposal of application of the C-ODT in wide-field microscopy was published in 2013 (see [52]), nowadays there exist several companies (Tomocube, NanoLive) applying it in especially designed holographic microscopes.

2.2 Basic equations for light propagation in inhomogeneous medium

In order to establish the principles of ODT, let us first consider the propagation of a monochromatic electromagnetic field with harmonic time dependence $e^{-i\omega t}$ (which is dropped henceforward) through a linear, isotropic and inhomogeneous medium. The medium is characterized by its refractive index distribution,

$$n(\mathbf{r}) = \sqrt{\mu_r(\mathbf{r})\varepsilon_r(\mathbf{r})}, \tag{2.1}$$

where μ_r and ε_r represents the relative permeability and the relative permittivity, respectively. From now on we consider non-magnetic materials with $\mu_r = 1$. The propagation of the complex field amplitude of the electric field, $u(\mathbf{r})$, in a medium like that is described by the inhomogeneous scalar Helmholtz equation [42, 43, 63], as

$$\left(\nabla^2 + k^2(\mathbf{r})\right) u(\mathbf{r}) = 0, \tag{2.2}$$

where $k(\mathbf{r}) = k_0 n(\mathbf{r}) = 2\pi n(\mathbf{r})/\lambda_0$ is the wavenumber, λ_0 is the light wavelength in vacuum and ∇^2 is a Laplacian operator comprises the second-order partial derivatives of $\mathbf{r}$ with respect to each independent variable (x, y, z).

By introducing the RI of the surrounding medium (n_m), the Helmholtz equation in Eq. 2.2 can be rewritten as

$$\left(\nabla^2 + k_m^2\right) u(\mathbf{r}) = -V(\mathbf{r}) u(\mathbf{r}), \tag{2.3}$$

where $V(\mathbf{r}) = k_0^2(n^2(\mathbf{r}) - n_m^2)$ is the so called scattering potential and $k_m = k_0 n_m$. From the knowledge of the solution $u_0(\mathbf{r})$ for the homogeneous Helmhotz equation ($V(\mathbf{r}) = 0$) and the knowledge of a Green's function G defined as

$$G(\mathbf{r} - \mathbf{r}') = \frac{-\exp\left(\mathrm{i} k_m |\mathbf{r} - \mathbf{r}'|\right)}{4\pi |\mathbf{r} - \mathbf{r}'|}, \tag{2.4}$$

which satisfies the Helmhotz equation for a point scatterer source $\delta(\mathbf{r} - \mathbf{r}')$,

$$\left(\nabla^2 + k_m^2\right) G(\mathbf{r} - \mathbf{r}') = -\delta(\mathbf{r} - \mathbf{r}'), \tag{2.5}$$

the solution of Eq. (2.3) can be written in the integral form as

$$u(\mathbf{r}) = u_0(\mathbf{r}) + \int G(\mathbf{r} - \mathbf{r}') V(\mathbf{r}') u(\mathbf{r}') \mathrm{d}\mathbf{r}'. \tag{2.6}$$

By writing the total complex field amplitude as a linear superposition $u(\mathbf{r}) = u_0(\mathbf{r}) + u_s(\mathbf{r})$, where $u_0(\mathbf{r})$ and $u_s(\mathbf{r})$ respectively describe the incident and scattered field, it is obtained

$$u_s(\mathbf{r}) = \int G(\mathbf{r} - \mathbf{r}') V(\mathbf{r}') u(\mathbf{r}') \mathrm{d}\mathbf{r}'. \tag{2.7}$$

Eq. 2.7 (strictly speaking is a Fredholm equation of the second kind) provides the solution of the scattered field in terms of the total field, $u(\mathbf{r})$. In order to solve it, two approximations have been considered in the literature: Born and Rytov.

The Born approximation is also known as the small field perturbation method. By representing the total field passing through the sample as the sum of the incident and the scattered fields, $u(\mathbf{r}) = u_0(\mathbf{r}) + u_s(\mathbf{r})$, Eq. (2.7) turns into,

$$u_s(\mathbf{r}) = \int G(\mathbf{r} - \mathbf{r}') V(\mathbf{r}') u_0(\mathbf{r}') \mathrm{d}\mathbf{r}' + \int G(\mathbf{r} - \mathbf{r}') V(\mathbf{r}') u_s(\mathbf{r}') \mathrm{d}\mathbf{r}'. \tag{2.8}$$

If the weak-scattering condition in the first-order Born approximation is considered, then $u_s(\mathbf{r})$ is only a small perturbation and the contribution of the second integral Eq. (2.8)

can be disregarded, thus Eq. 2.7 is transformed into a convolution operation (denoted by the operator $\otimes$):

$$u_s(\mathbf{r}) \overset{\text{Born}}{=} u_{B(1)}(\mathbf{r}) = \int G(\mathbf{r}-\mathbf{r}')V(\mathbf{r}')u_0(\mathbf{r}')\mathrm{d}\mathbf{r}' = [V(\mathbf{r})u_0(\mathbf{r})] \otimes G(\mathbf{r}). \tag{2.9}$$

Then, the total complex field amplitude of the optical field passing through the sample is given by

$$u(\mathbf{r}) \overset{\text{Born}}{=} u_0(\mathbf{r}) + u_{B(1)}(\mathbf{r}) = u_0(\mathbf{r}) + [V(\mathbf{r})u_0(\mathbf{r})] \otimes G(\mathbf{r}), \tag{2.10}$$

where $u_{B(1)}$ represents the field scattered within first-order Born approximation. Note that this first-order Born approximation only takes into account the undiffracted light and its interference with once-scattered light, thus excluding multiple scattering [64]. Let us now consider the intensity distribution, defined as: $I(\mathbf{r}) = |u(\mathbf{r})|^2 = |u_0(\mathbf{r})|^2 + |u_s(\mathbf{r})|^2 + 2\mathrm{Re}\left\{u_0^*(\mathbf{r})u_s(\mathbf{r})\right\}$. In general, for a better estimate of the scattered field higher order Born approximations can be used [65]. By following the first Born approximation we find that the term $|u_s(\mathbf{r})|^2$ can be ignored, so the intensity expression becomes

$$I(\mathbf{r}) \overset{\text{Born}}{=} |u_0(\mathbf{r})|^2 + 2\mathrm{Re}\left\{u_0^*(\mathbf{r})u_s(\mathbf{r})\right\}. \tag{2.11}$$

Instead of Born approximation, Rytov approximation can be applied to solve Eq. 2.2 [50, 66, 67]. In that case, the overall field is represented like $u(\mathbf{r}) = e^{\phi(\mathbf{r})}$, where $\phi(\mathbf{r}) = \phi_0(\mathbf{r}) + \phi_s(\mathbf{r})$ is a complex function in which ϕ_0 and ϕ_s are associated with the incident and scattered fields, correspondingly. In this case, the solution of the wave equation Eq. 2.2 is obtained under the assumption that

$$[(\nabla\phi_s(\mathbf{r}))^2 + V(\mathbf{r})] \approx V(\mathbf{r}), \tag{2.12}$$

which in turn leads to the following relation linking the first Born and Rytov approximations [65],

$$\phi_s(\mathbf{r}) = \frac{u_{B(1)}(\mathbf{r})}{u_0(\mathbf{r})}. \tag{2.13}$$

By introducing in the expression of the transmitted field in Eq. 2.13 one obtains,

$$u(\mathbf{r}) = u_0(\mathbf{r})exp\left(u_{B(1)}(\mathbf{r})/u_0(\mathbf{r})\right). \tag{2.14}$$

Let us now discuss the validity of both approximations which is still a controversial question in the literature. The Born approximation holds in the case when contribution (both in amplitude and in phase) of the scattered field u_s is small in comparison with the incident plane wave u_0, so $u_0(\mathbf{r}) + u_s(\mathbf{r}) \approx u_0(\mathbf{r})$. Since u_0 and u_s are complex functions, an object meets the requirements of first-order Born approximation when its absorption (related to the RI imaginary part) is negligible at the illumination wavelength (λ_0) and the introduced scattering, linked to the real part of the RI, is weak. If one considers a sample with homogeneous RI n_s and a known thickness t, then the phase change of the scattered wave (ψ) can be estimated as,

$$\Delta\psi(\mathbf{r}) = \frac{2\pi}{\lambda_0}\Delta n(\mathbf{r})t. \tag{2.15}$$

The interpretation of Eq. 2.15 is straightforward as the comparison of the phase change over a period of 2π with the variation of the optical path length ($t\Delta n$) over one wavelength [53, 68, 69]. Only optically thin samples in which $\Delta\phi \ll 2\pi$, or equivalently $t\,\Delta n \ll \lambda_0$, are feasible to be treated with Born approximation. Some authors state that Born approximation is accurate when the product of the scatter size and the RI contrast is less than one-quarter wavelength [69].

The Rytov approximation is true if $V(\mathbf{r}) = k_0^2(n^2(\mathbf{r}) - n_m^2) \gg (\nabla\phi_s(\mathbf{r}))^2$ according to Eq. 2.12. When the local variation Δn is small compared to n_m, then the term $(\Delta n)^2$ may be omitted leading to the following approximation for the scattering potential,

$$V(\mathbf{r}) \approx 2k_0^2 n_m \Delta n. \tag{2.16}$$

Then, the Rytov approximation is valid when the following condition is satisfied,

$$\Delta n(\mathbf{r}) \gg \left(\frac{\lambda\nabla\phi_s(\mathbf{r})}{2\pi}\right)^2, \tag{2.17}$$

according to which the variation of ϕ_s over a single wavelength has to be small. This also explains the alternative name of Rytov approximation: slow perturbation method. Thus, the Rytov approximation is also valid for optically thick samples because it does not rely on the overall phase delay but on its gradient within the sample. However, since in this thesis we consider the implementation of the ODT with high-numerical aperture optics enabling high resolution imaging of small object details, the Born approximation is a proper choice thanks to the consideration of optically thin specimen and a small Δn (by considering a RI of surrounding medium close to the one of the sample) .

2.3 C-ODT in wide-field microscopy

The first stage of C-ODT consists of the sequential illumination of the sample from different dirrections by using spatially-coherent plane waves and the subsequent recovery of the complex field amplitude (CFA) of the transmitted field for each illumination direction. The object rotation can be used for this purpose (see [46, 70, 71]), however, it is a challenging task for small living organisms. Alternatively, the scanning illumination is achieved by the variation of the position of a laser spot onto the back focal plane of the condenser lens (e.g., see [52, 67]). Note that the larger the NA of the condenser lens, the wider is the angular interval available for object inspection. We start from the consideration of the illumination scanning approach.

Under plane-wave illumination $u_0(\mathbf{r}\,|\mathbf{s}) = a(|\mathbf{s})\exp(\mathrm{i}k_m\mathbf{s}\mathbf{r})$, where $\mathbf{s} = (s_x, s_y, s_z)^t = \left(s_x, s_y, \sqrt{1 - s_x^2 - s_y^2}\right)^t$ is a unit vector in the direction of the wave propagation and $a(|\mathbf{s})$ stands for its amplitude, the complex field amplitude passed through the sample is obtained,

according to Eq. 2.10, as

$$u(\mathbf{r}\,|\mathbf{s}) = u_0(\mathbf{r}\,|\mathbf{s}) + u_s(\mathbf{r}\,|\mathbf{s}) = a(|\mathbf{s})\exp(\mathrm{i}k_m\mathbf{s}\mathbf{r}) + a(|\mathbf{s})[V(\mathbf{r})\exp(\mathrm{i}k_m\mathbf{s}\mathbf{r})] \otimes G(\mathbf{r}). \quad (2.18)$$

Note that here and further the symbol $|\mathbf{s}$ indicates the parameter associated with the considered illumination direction. The objective lens collects the transmitted waves thus yielding the convolution with its point spread function (PSF) $h_o(\mathbf{r})$ as it follows:

$$u(\mathbf{r}\,|\mathbf{s}) \;\; = \;\; a(|\mathbf{s})\big\{\exp(\mathrm{i}k_m\mathbf{s}\mathbf{r}) \otimes h_o(\mathbf{r}) + [V(\mathbf{r})\exp(\mathrm{i}k_m\mathbf{s}\mathbf{r})] \otimes G(\mathbf{r}) \otimes h_o(\mathbf{r})\big\}. \quad (2.19)$$

Here, the Green's function from Eq. 2.4 can be simplified by considering the far field (when r is large enough) in which the approximation $|\mathbf{r}-\mathbf{r}'| \sim r - \mathbf{s}\cdot\mathbf{r}'$ is valid. Then, by calculating the 3D FT, $\widehat{u}(\mathbf{p}\,|\mathbf{s}) = \int u(\mathbf{r}'\,|\mathbf{s})\exp\left(-\mathrm{i}2\pi\mathbf{r}'\mathbf{p}^t\right)\mathrm{d}\mathbf{r}'$, Eq. 2.19 can be rewritten in Fourier domain as:

$$\widehat{u}(\mathbf{p}\,|\mathbf{s}) = a(|\mathbf{s})H_o(\mathbf{p})\delta(\mathbf{p}-\kappa_m\mathbf{s}) + a(|\mathbf{s})H_o(\mathbf{p})\widehat{G}(\mathbf{p})\hat{V}(\mathbf{p}-\kappa_m\mathbf{s}), \quad (2.20)$$

where $\mathbf{p} = (p_x, p_y, p_z)$ is a 3D spatial frequency vector, $2\pi\kappa_m = k_m$ and $H_o(\mathbf{p})$ is the transfer function of the objective lens. In the case of a microscope objective lens with a circular aperture its transfer function can be approximated by [72],

$$H_o(\mathbf{p}) = \mathrm{circ}\left(\frac{\lambda\sqrt{p_x^2+p_y^2}}{\mathrm{NA_o}}\right)\mathrm{step}\left(\frac{p_z}{\kappa_m}\right), \quad (2.21)$$

where $\mathrm{NA_o}$ accounts for the numerical aperture of the objective lens. Alternatively, instead of using the analytical expression from Eq. 2.21, the coherent transfer function (CTF) given by $H_o(\mathbf{p})\widehat{G}(\mathbf{p})$ can be experimentally measured [47, 52].

According to Eq. 2.20, the spectrum of the amplitude of the scattered wave in the illumination direction given by vector $\mathbf{s}$ (referred to as $\widehat{u}(\mathbf{p}\,|\mathbf{s})$) depends on only the contribution $\hat{V}(\mathbf{p}-\kappa_m\mathbf{s})$ filtered by the Green function. Consequently, with a single illumination direction $\mathbf{s}$ it is not attainable to fully encompass all the original frequencies of the sample. However, Eq. 2.20 allows treating the scattering potential retrieval problem sequentially, as illustrated in Fig. 2.1. It is possible to reconstruct $\hat{V}(\mathbf{p})$ by successively changing the ilumination direction $\mathbf{s}$ to reach different spectrum regions and subsequently stiching them all. The wave vector of the scattered (diffracted), $\mathbf{q}_d = \mathbf{p} + \mathbf{k}_{ill}$, is related to $\mathbf{p}$ and $\mathbf{k}_{ill} = \kappa_m\mathbf{s} = (\kappa_{x,ill}, \kappa_{y,ill}, \kappa_{z,ill})$ standing for the incident illumination. By considering the elastic scattering constraint, $|\mathbf{k}_{ill}| = |\mathbf{q}_d|$, and expanding both sides of the equation one gets $k_{ill}^2 = \kappa_m^2 = (\kappa_{x,ill}+p_x)^2 + (\kappa_{y,ill}+p_y)^2 + (\kappa_{z,ill}+p_z)^2$. In this way, the locus accessible object frequencies is the so-called Ewald sphere of radius κ_m with its center at $\kappa_m\mathbf{s}$ [63, 73, 74]. According to the sphere equation, the two solutions must satisfy the relation $p_z = -\kappa_{z,ill} \pm \sqrt{\kappa_{z,ill}^2 - (p_x^2+p_y^2) + 2(\kappa_{x,ill}\,p_x + \kappa_{y,ill}\,p_y)}$ to contribute to image formation, where the $\pm$ sign accounts for the transmission and reflection detection schemes, respectively. Throughout this work we focus exclusively on transmission approach, since the light scattered by the sample is collected after passing through it. Note that in Fig. 2.1

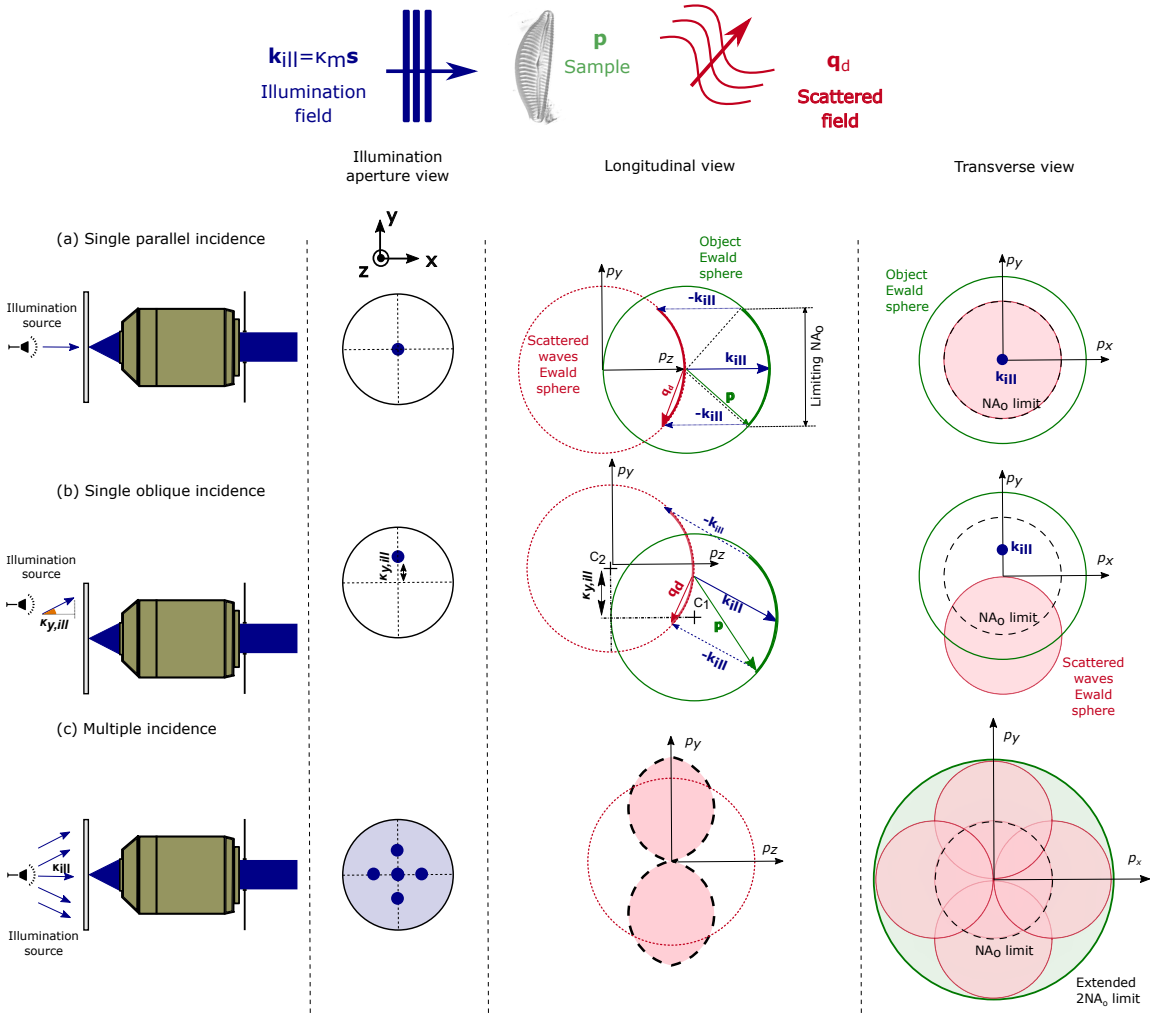

Figure 2.1: Sequential illumination scanning performed in C-ODT to reconstruct the scattering potential of the sample, by assuming an identical NA for condenser and objective lenses of the microscope. (a-b) A single plane wave illumination, either parallel (a) or tilted (b) with respect to the optical axis, is only able to recover a small portion of the sample spectrum corresponding to a cap of the Ewald sphere (corresponding to an arc in the 2D view of the figure) of the sample spectrum. (c) Multiple illumination directions are needed to obtain a better coverage of sample Fourier spectrum. The attainable frequencies lie within a new extended sphere of radius $2\mathrm{NA}_\mathrm{o}$.

identical objective and condenser apertures have been considered. The Ewald sphere of sample frequencies is coloured in green, while the red sphere corresponds to the scattered waves and the black dashed line stands for the maximum frequencies attainable according to NA_o limit. As summarized in Fig. 2.1 (a), if a single plane wave illumination parallel to the optical axis is used, for example a single centered spot of light onto the condenser back focal plane (BFP), then only a cap of the Ewald sphere (shown as a 2D bold arc in Fig.2.1 (a) in $p_y - p_z$ view) can be detected due to the limited objective lens NA. Then, after the deconvolution procedure (see Eq. 2.20) given by

$$\hat{V}(\mathbf{p}\,|\mathbf{s}) = \frac{\widehat{u}(\mathbf{p}+\kappa_m\mathbf{s}\,|\mathbf{s}) - a(|\mathbf{s})H_o(\mathbf{p}+\kappa_m\mathbf{s})\delta(\mathbf{p})}{a(|\mathbf{s})H_o(\mathbf{p}+\kappa_m\mathbf{s})\widehat{G}(\mathbf{p}+\kappa_m\mathbf{s})}. \tag{2.22}$$

only a part of the scattering potential spectrum can be recovered. Nevertheless, the variation of the incident wave direction $\mathbf{s}$ yields a displacement of the cap center given by $\mathbf{k}_{ill}$, see Fig. 2.1 (b), and therefore it permits enlarging the area of the spectral domain to be recovered. Indeed, by tilting the illumination a different part of the object spectrum is mapped onto the Ewald sphere defined by the objective NA. Therefore, thanks to tilted illumination, higher frequencies can be collected by the objective. The proper assembling of the gathered spectral components $\hat{V}(\mathbf{p}\,|\mathbf{s})$ allows recovering the entire $\hat{V}(\mathbf{p})$ that makes possible the reconstruction of the scattering potential via its 3D inverse FT. Ideally, the whole condenser aperture must be scanned point by point, that allows for the extended frequency support displayed in Fig. 2.1 (c). All the collected frequency regions (illustrated as the red circles from Fig. 2.1 (c), in the $p_x - p_y$ view, each one corresponding to a different illumination direction) are combined to obtain $\hat{V}(\mathbf{p})$. However, the limited angular coverage of the condenser lens aperture (usually it is not extended more than 60º with respect to the optical axis) yields an incomplete coverage of $\hat{V}(\mathbf{p})$, responsible for the missing cone (MC) problem, as later explained in Section 2.4. Moreover, the available axial frequency (p_z) content is smaller than that of the transverse direction. Consequently, several artifacts such as axial elongation are present in the reconstructed 3D RI distribution, which can be mitigated by using post-processing algorithms, based on prior knowledge of the sample or other constraints [67, 75, 76].

Note that the scattering potential is, in general, a complex valued function

$$\begin{aligned} V(\mathbf{r}) &= P(\mathbf{r}) + \mathrm{i}A(\mathbf{r}), \\ P(\mathbf{r}) &= k_0^2\,(n_{\mathrm{Re}}^2 - n_{\mathrm{Im}}^2 - n_m^2), \\ A(\mathbf{r}) &= 2\,k_0^2 n_{\mathrm{Re}} n_{\mathrm{Im}}, \end{aligned} \tag{2.23}$$

whose real and imaginary parts, $P(\mathbf{r})$ and $A(\mathbf{r})$ respectively, are related to the real (n_{Re}) and imaginary (n_{Im}) parts of the sample RI ($n_s = n_{\mathrm{Re}} + i\; n_{\mathrm{Im}}$) which can be easily found from $V(\mathbf{r})$. Here, n_m corresponds to the surrounding medium RI in which the object is immersed and it is supposed to be real. However, in ODT microscopy weak absorbing samples (negligible n_{Im}) are usually considered, therefore it is n_{Re} (further also denoted as n_s) which reveals the object structure.

A typical scheme for 3D RI reconstruction in the case of C-ODT is displayed in Fig. 2.2. It starts with the acquisition of one or several intensity distributions for a certain plane-wave illumination, $\mathbf{s}_i$, which is required for the recovery of the CFA of the light transmitted by the microscope corresponding to a single plane of the sample, z_0. The type of intensity measurement, either hologram(s) or refocused images, depends on the method used for phase retrieval (digital holography, TIE, iterative algorithms). When using a method based on digital holography (DH), the mentioned intensity distributions correspond to holograms from which the required complex-field amplitudes can be retrieved. For instance, in the case of off-line holographic setups, one hologram per tilted illumination is, in general, sufficient to retrieve the corresponding complex-field amplitude. On the other hand, in the

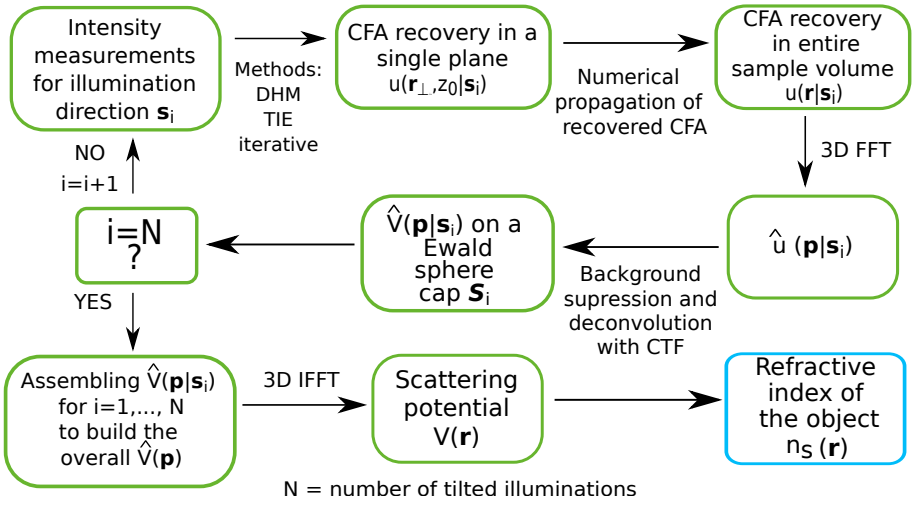

Figure 2.2: Flowchart of the information processing approach used in C-ODT for reconstructing the 3D RI.

case of on-line holography it is necessary to measure at least four holograms (by using phase-shifting setup) to retrieve each CFA. Alternatively, TIE or iterative methods can be used instead of DH, in which case such intensity distributions correspond to $4-10$ optically refocused images. The numerical refocusing of the CFA retrieved at z_0 allows for the recovery of an optical field in the entire sample volume. Then, the 3D FT of such a CFA stack is calculated. The background suppression is applied in this step (or, alternatively, previously in the $\mathbf{r}$ domain). Note that the deconvolution described by Eq. (2.22) only provides the accessible content of the scattering potential spectrum $\hat{V}(\mathbf{p}|\mathbf{s}_i)$ lying on the captured cap of the Ewald sphere defined by $\mathbf{s}_i$ and NA_o. Afterwards, the described process is repeated for each illumination direction until reaching a predetermined number (N). Ideally, the whole condenser aperture diaphragm must be scanned point by point providing all the possible illumination directions. Nevertheless, in order to make more practical such a time-multiplexing approach, a scanning reduced to spiral trajectories have been proposed [67], thus achieving a good trade-off between accuracy and speed of the RI reconstruction. Finally, all the acquired pieces of the 3D scattering potential spectrum, $\hat{V}(\mathbf{p}|\mathbf{s}_i)$ (with $i=1,...,N$) that have been obtained separately, are assembled together to build the overall 3D scattering potential spectra $\hat{V}(\mathbf{p})$. From the latter one, and after performing an inverse 3D FT (IFFT), one gets the scattering potential in the spatial domain, $V(\mathbf{r})$, from which the 3D RI image reconstruction is straightforward following the expression Eq. (2.23).

Alternatively, the so-called filtered backpropagation algorithm (not be confused with filtered backprojection algorithm used in CT [68, 77, 78]) can be used for the recovery of $V(\mathbf{r})$ in C-ODT. However, the deconvolution method considered here allows easily taking into account the microscope transfer function. Both of these C-ODT approaches can be applied for Born and Rytov approximations.

2.4 Frequency support for different illumination schemes in ODT

In wide-field microscopy not all the illumination directions are accessible and therefore it yields incomplete reconstruction of the 3D object spectrum. Indeed, the possible illumination angles are limited by the NA of the microscope condenser and objective lenses, thus the collection of scattered fields is incomplete. This limitation leads to missing data in the object angular spectrum in form of the missing cone (MC) problem or the missing apple core problem. In this Section we review different illumination schemes in ODT and how they cope with these limitations.

Single plane-wave illumination provides incomplete mapping of the observed object frequency support, regardless of whether a transmission or reflection configuration is chosen. As aforementioned, by changing the illumination wavevector one is able to recover object frequencies that were not initially accessible in the Ewald sphere. Conventionally, this step has been achieved by three different techniques: illumination rotation, sample rotation and the combination of both of them. A comparison of accessible frequency support for each case is drawn in Fig. 2.3. Taken into account that the resolution is strongly anisotropic and depends upon the considered direction, the theoretical transverse ($\Delta x = 1/2p_x^{\text{cut}}$, $\Delta y = 1/2p_y^{\text{cut}}$) and axial ($\Delta z = 1/2p_z^{\text{cut}}$) Nyquist distances [71, 79] are often used for the estimation of the spatial resolution limits of ODT, where p_x^{cut}, p_y^{cut}, p_z^{cut} are the maximum spatial frequency pertaining to the frequency support (see for example [51]). As an example, the frequency support limits attainable for different illumination methods in holographic tomography are included in Table 2.1, in which it has been considered that $\text{NA}_\text{c} = \text{NA}_\text{o} = \text{n}_\text{imm}\sin(\theta)$, where θ stands for half–angle admitted by the acceptance cone and n_{imm} is the immersion RI. Let us briefly review each case.

- Fixed sample and a single plane wave illumination only enables the retrieval of a single cap of Ewald sphere, as shown in Fig. 2.1, insufficient to reconstruct the 3D RI.

- Illumination rotation with fixed sample, represented in Fig.2.3(a). This approach offers the advantage of being easily implemented by changing the position of a laser spot onto the back focal plane of the condenser lens (e.g., see [52, 67]), thus modifying the illumination incidence angle. By using several illumination directions, tilted with regard to the optical axis, one shifts portions of the object frequency support formerly not transmitted by the microscope towards positions that can be imaged. Thus, by sequentially illuminating the sample with many illuminations (ideally one must scan point by point the entire microscope condenser aperture) and then combining them all to create a synthetic aperture [80, 81], one extends the original frequency support. Therefore, it provides a good lateral resolution but in turn it suffers from a restrained resolution along optical axis. This latter problem is better known as MC and it originates artifacts, underestimation of the RI and stretching of the reconstructed sample along the optical axis [67]. By means of this illumination scheme, which is the one applied throughout this work, the Nyquist lateral distance is $\Delta x = \Delta y = \lambda_0/\left[2(\text{NA}_\text{c} + \text{NA}_\text{o})\right]$ and the Nyquist axial distance is given by

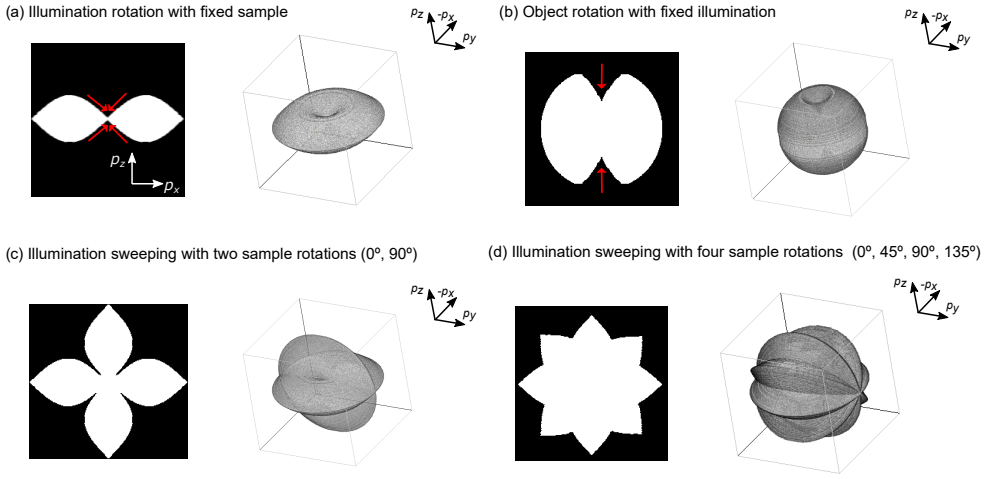

Figure 2.3: Comparison of the frequency support covered by different illumination and rotation approaches. (a) Illumination rotation with fixed sample. Note the strong anisotropy of the frequency support along with the missing cone region (marked by red arrows) around the origin of p_z axis. (b) Sample rotation with fixed illumination is able to achieve a more isotropic frequency support. In return, the maximum frequency reached in the traverse direction is slightly reduced and an empty region remains (the so-called missing apple core indicated by red arrows). (c-d) Illumination scanning with 2 and 4 object rotations to combine the advantages from (a) and (b) methods in order to provide a larger frequency coverage.

$\Delta z = \lambda_0 / \left[2(n_{imm} - (n_{imm}^2 - \mathrm{NA}_o^2)^{1/2}\right])$, where λ_0 is the illumination wavelength and n_{imm} is the RI of the immersion medium.

- Sample rotation (about y-axis, in this case) with single illumination, illustrated in Fig.2.3 (b), provides a fairly isotropic frequency support (almost spherical) even though is less extended than in illumination rotation approach. Moreover, there remains a subset of captured frequencies around the rotation axis suffering from high attenuation (or even untransmitted). The shape of the frequency support resembles that of an apple core, in an analogous manner to MC in fixed sample ODT [70]. Furthermore, typically many rotations are needed to fill all the frequency support, so this approach is difficult to implement. For example, the rotation may be performed optically by means of optical tweezers [82], or mechanically rotation by embedding the sample within a micropippete [44]. In this way, the missing apple-core lessens the resolution in that axial direction.

- Hybrid approach, combining both illumination and sample rotations as displayed in Figs. 2.3(c-d) for illumination rotation with 2 and 4 object rotations, respectively. The more object rotations are applied, the broader the covered frequency support becomes. This configuration allows to combine the advantages of each of the previous techniques, thus theoretically obtaining an extended and isotropic 3D frequency coverage. Nevertheless, in practice only a few object rotations are performed, which

Illumination scheme	p_x^{cut}	p_y^{cut}	p_z^{cut}
Single illumination and fixed sample (*)	$\frac{2n_{imm}\sin(\theta)}{\lambda_0}$		$\frac{n_{imm}(1-\cos(\theta))}{\lambda_0}$
Illumination rotation and fixed sample	$\frac{4n_{imm}\sin(\theta)}{\lambda_0}$		$\frac{2n_{imm}(1-\cos(\theta))}{\lambda_0}$
Single illumination and sample rotation	$\frac{4n_{imm}\sin(\theta/2)}{\lambda_0}$	$\frac{2n_{imm}\sin(\theta)}{\lambda_0}$	$\frac{4n_{imm}\sin(\theta/2)}{\lambda_0}$
Combined illumination and sample rotations	$\frac{4n_{imm}\sin(\theta)}{\lambda_0}$		

Table 2.1: Theoretical frequency resolution limits, given in lateral (p_x^{cut} and p_y^{cut}) and axial (p_z^{cut}) directions, reached by different illumination and rotation ODT configurations wherein the sample is rotated about y-axis and θ is the maximum angle between the optical axis direction and the direction of the incident plane wave being transmitted through the objective aperture according to $\text{NA}_\text{c} = \text{NA}_\text{o} = n_{imm}\sin(\theta)$. (*) Not suitable for ODT.

yields a not truly isotropic 3D resolution but it is enough to fill most of the frequency support. The downside of this configuration is the larger datasets to be processed and higher computational complexity of reconstruction algorithms [71, 83].

We have seen that C-ODT can be combined with rotation of the object in order to effectively mitigate MC artifacts, thereby providing a more isotropic spatial resolution [44, 46, 70, 71]. However, the rotation approach significantly increases the data acquisition time, thus making challenging real-time imaging. Therefore, in practice, the C-ODT is commonly applied without object rotation but further including post-processing iterative algorithms to mitigate possible artifacts arising from the MC [67, 75, 76, 84].

2.5 Implementations of C-ODT

The experimental setup of C-ODT consists of, apart from a microscope, two additional modules: one that provides the illumination control over the sample and another one for the measurement of the required intensity distributions. Both modules have to be programmable and fast switchable, which is specially needed when ODT is applied for analysis of dynamic objects such as living cells. This section covers some relevant ODT schemes already settled in the state of the art as well as some new proposals based on modifications in either the illumination or measurement setups.

Nowadays, the modality of interferometric C-ODT is a well-established technique often used for 3D RI imaging of biological specimens. Several specially designed commercial holographic microscopes are available for its implementation. A basic scheme of the experimental setup typically required for interferometric C-ODT [45, 50, 52] is displayed in Fig. 2.4. In this case, a collimated laser beam is divided into two components referred to as illumination and reference beams. The illumination beam is redirected by using a turning mirror in order to sequentially scan the back focal plane of the condenser lens. This scan provides the set of tilted illuminations required in C-ODT as it has been previously described. For each illumination direction a hologram is recorded by the digital camera. The interferometric setup depicted in Fig. 2.4 corresponds to an off-axis configuration where a second turning mirror is used to preserve the interference angle between the reference

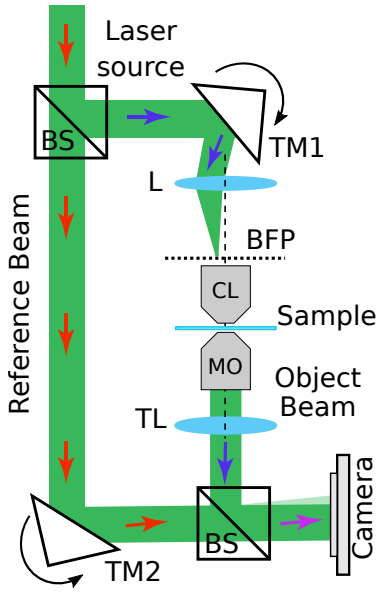

Figure 2.4: Sketch of an interferometric setup for implementation of the C-ODT technique in a holographic microscope.

and object beams during the illumination scanning process. The first turning mirror (TM1) controls the illumination scanning process while the second one (TM2) is used to preserve the interference angle between the reference and object beams. Note that an input collimated laser beam is divided by using a beam splitter (BS) while the object and reference beams are recombined by a BS mounted in front of the camera (e.g. sCMOS). A convergent lens (L) is used for focusing the collimated illumination beam onto the BFP of the condenser lens (CL). The microscope objective lens (MO) collects the laser beam passing by the sample (object beam) at a given scanning position. Then the tube lens (TL) images the object beam into the detector plane of the camera. In general, hundreds of holograms are required to reconstruct the 3D RI of the object by using the C-ODT algorithm explained in the previous section, see the flowchart sketched in Fig. 2.2. Note that other DH techniques such as phase-shifting interferometry can be used instead, however, it requires at least four holograms for each scanning position making slower the C-ODT reconstruction process [85].

C-ODT techniques have been successfully incorporated into commercial devices. As previously introduced in Chapter 1, there are two companies, Tomocube [61] and Nanolive [62], that have developed 3D RI imaging tools mainly devoted to biologists and clinicians requiring marker-free imaging. For this reason, both companies pay special attention to minimize photoxicity risks by injecting very low energy to the sample ($\approx 0.2\,\mathrm{nW}/\mu\mathrm{m}^2$). Either Tomocube and Nanolive implement a similar experimental setup: a laser source is splitted into a reference and a sample beam (similarly to Mach-Zehnder configuration, as depicted in Fig. 2.4), and then recombined to produce a 2D hologram recorded by a camera. Moreover, the illumination beam rotates around the microscope objective optical axis to acquire a series of holograms from all (360º) viewing points. Furthermore, each company provides its own software to perform post-processing over the retrieved tomogram, thus

allowing segmentation and digital staining procedures to the final user.

The particular implementation and capabilities of the system from each company are slightly different. On the one hand, Tomocube HT-2 patented system uses the digital micromirror device (DMD) instead of a moving (galvanometric) mirror. The DMD provides a fast, reliable and stable control of the beam path, enabling a 3D imaging speed of 2.5 fps. According to the technical specification, the optical resolution achieved by the system is $\Delta x = 166\,\text{nm}$ and $\Delta z = 332\,\text{nm}$ in the traverse and axial directions, correspondingly, with a $60\times$ magnification objective lens. Furthermore, it is able to image a field of view of $80\,\mu\text{m}$ with $40\,\mu\text{m}$ depth of field. On the other hand, Nanolive 3D Cell Explorer's technology enables a larger stage over the object and facilitating its manipulation. Besides, it offers a similar scanning volume ($85 \times 85 \times 30\,\mu\text{m}^3$) but with slightly worse resolution ($\Delta x = 200\,\text{nm}$ and $\Delta z = 400\,\text{nm}$) and a lower frame-rate for 3D imaging (0.5 fps) compared to Tomocube. Finally, it is worth remarking that Nanolive guarantees a RI precision of ± 0.001.

2.6 Conclusions

Several research groups have demonstrated the feasibility of 3D mapping of RI of cells by using a tomographic interference technique often referred to as coherent optical diffraction tomography [44, 45, 52, 53]. Specifically, C-ODT allows for the computational reconstruction of the 3D RI by recovering of the complex field amplitudes of light scattered by the cell for a set of illumination angles. Note that C-ODT is able to reconstruct the object RI from a synthetically assembled 3D angular spectrum, by computing hundreds of digital holograms and by performing 3D deconvolution with the complex optical transfer function of the microscope. This complex acquisition and processing, which is characteristic of C-ODT, turns out to be computationally demanding and needs an interferometric setup with specialized hardware: e.g., fast galvanometer-controller mirrors to change the angle of incidence (beam rotation) and a high-speed camera recording the holograms. In addition, the interferometric setups necessarily require specially designed holographic microscopes. Moreover, C-ODT suffers from inherent limitations due to the coherent laser illumination such as speckle-noise and parasite interference degrading the RI reconstruction. In spite of these difficulties, several commercially available holographic microscopes based on C-ODT have been recently developed providing reliable 3D RI at low video rates (typically at $0.5 - 2.5$ fps according to manufacturer data, Nanolive SA and Tomocube Inc.) suited for long-term cell observation. An option for increasing the acquisition rate in C-ODT is to reduce the number of illumination angles achieving rates up to 60 Hz, but at expense of the spatial resolution and quality of the 3D RI reconstruction [49] due to increased missing-angle artifacts. In this context, there is still a need in the field of 3D RI tomography of an imaging tool with a simpler and faster reconstruction method while compatible with conventional wide-field microscopes and providing a quality similar to C-ODT. The following Chapter proposes a ODT technique based on partially coherent illumination which addresses this problem.

Chapter 3

PARTIALLY COHERENT OPTICAL DIFFRACTION TOMOGRAPHY (PC-ODT)

The goal of ODT is to obtain quantitative information from the sample's 3D RI. As we have reviewed in the previous Chapter, C-ODT requires sequentially illuminating the sample from different directions and a complex reconstruction process for the RI recovery. As an alternative, in this Chapter we introduce the fundamentals of ODT using partially coherent light, a technique further referred to as PC-ODT and conceived to be easily implemented in commercially available wide-field microscopes. Thus, PC-ODT is intended to provide a more affordable and straightforward ODT alternative to C-ODT which requires specially designed holographic microscopes. PC-ODT provides direct reconstruction of the 3D RI from a stack of through-focus intensity measurements, via a deconvolution process with the microscope optical transfer function. Finally, several numerical simulations are conducted in order to evaluate the accuracy and the reliability of the PC-ODT technique.

3.1 Introduction

As aforementioned in the previous chapter, the main goal of ODT is the RI reconstruction from the optical scattering potential, which is defined by the function $V(\mathbf{r}) = k_0^2(n^2(\mathbf{r}) - n_m^2)$, where: $\mathbf{r} = (x,y,z)$, $k_0 = 2\pi/\lambda_0$ with λ_0 being the free-space wavelength, while $n(\mathbf{r})$ and n_m are the refractive index of the specimen and its surrounding medium, correspondingly. The function $V(\mathbf{r})$ is real in the lossless case when the sample only modulates the phase of the transmitted field, $V(\mathbf{r}) = P(\mathbf{r})$, while it is a complex function $V(\mathbf{r}) = P(\mathbf{r}) + \mathrm{i}A(\mathbf{r})$ if the sample absorption has to be taken into account.

Unlike C-ODT, PC-ODT studied in this Chapter does not require coherent illumination scanning because the entire back focal plane of the microscope condenser is illuminated simultaneously providing all the possible illumination directions corresponding with partially coherent illumination (PCI). The PC-ODT approach benefits from PCI, which can significantly reduce the data acquisition time because it only requires a single exposure to the illumination (it suffices that a single stack of refocused intensity images is measured).

In this way, the use of PCI simplifies the reconstruction process, as it does not require the combination of different frequency support regions obtained with different illumination states. For low spatial coherent illumination (fully opened condenser aperture) the bright-field microscope transmits the same object spatial-frequency content that C-ODT is able to achieve from multiple illuminations. However, these benefits of PCI are accompanied by a lower image contrast in certain regions of the frequency support, which is probably one of the reasons why the PCI potential has not been completely exploited yet in ODT.

The theoretical fundamentals of PC-ODT technique have been established thirty-five years ago by N. Streibl [60] devoted to 3D partially coherent imaging, where the expression of the phase and absorption optical transfer functions (OTFs) of the wide-field transmission microscope were derived assuming the Born approximation in the paraxial limit. Nevertheless, this work has not been transferred to practice until 2016. In this context, we start working by May 2016 in an experimental setup based on Streibl work, which discloses OTF expressions for the paraxial approximation. The OTFs in nonparaxial aproximation have been reported in the same year [72]. We adopted the nonparaxial OTFs since they are more appropiate for high NA microscopy. Moreover, at that time (October 2016) it was also published the Ref. [86], disclosing the 3D differential phase contrast (DPC) in paraxial approximation for low NA microscopy. DPC implements the method proposed by Streibl in his seminal work [60] for the RI reconstruction of absorbing samples by using multiple asymmetric illuminations. Therefore, DPC is slow for imaging of living cells because it requires the measurement of multiple intensity stacks, which in turn makes complex the reconstruction process.

Taking into account this context of the state of the art, our research first focused on the design of a competitive PC-ODT technique and system for high NA microscopy with the following requirements: fast enough to enable 3D RI imaging of dynamic micro objects such as living cells (weak absorbing samples), and simple in the measurement as well as in the reconstruction process. In the next sections, we introduce the fundamentals of the proposed PC-ODT and analyze its performance via numerical simulations and experimental results (a more detailed description of the PC-ODT setup is provided in Chapter 4). From this analysis we have realized that the performance of PC-ODT can be improved by using a proper design of the PCI different from the uniform bright-field illumination, and it will be further studied in Chapter 5. The implementation of PC-ODT for real-life applications underlying its potential in biomedicine will be demonstrated in Chapter 6 and 7.

3.2 Principle of 3D imaging with partially coherent illumination

Let us introduce the 3D image formation process with partially coherent illumination. In a common microscope, the opening and closing of the condenser diaphragm eventually controls the amount of light reaching the specimen. Moreover, for the case of a wide-field transmission microscope, the spatial coherence of the illumination depends on the aperture of the condenser lens relative to that of the objective. In this way, it is possible to define a ratio of spatial coherence as $SC = \mathrm{NA_c}/\mathrm{NA_o}$, where $\mathrm{NA_c}$ and $\mathrm{NA_o}$ are the numerical

apertures of the condenser and objective lenses, correspondingly. The coherent limit is reached for $SC \to 0$ whereas $SC \to \infty$ corresponds to the incoherent case [60, 87]. For the intermediate SC values, including $SC = 1$ (also known as matched illumination), light is partially coherent. Larger values of SC are obtained when the condenser diaphragm is fully opened.

Instead of using a coherent laser beam, in PC-ODT the spatially incoherent quasi-monochromatic light available in wide-field microscopes (either LED or filtered light from a halogen lamp) is projected onto the back aperture of the condenser lens (position of condenser diaphragm), thus providing the object illumination from all the angles required in C-ODT but simultaneously. Let us assume that the incoherent intensity distribution over the condenser aperture diaphragm is described by $a^2(|\mathbf{s}\rangle)$,where the vector $\mathbf{s}$ stands for the illumination direction. Then, the measured intensity distribution is a sum of all the intensity contributions obtained by the coherent plane wave illumination at different tilting angles. The intensity distribution of the wave scattered by the object when it is illuminated by a plane wave $u_0(\mathbf{r}\,|\mathbf{s}\,) = a(|\mathbf{s}\,)\exp(\mathrm{i}k_m\mathbf{s}\mathbf{r})$ can be found through Eqs. (2.28-2.29):

$$\begin{aligned} I(\mathbf{r}\,|\mathbf{s}\,) = a^2(|\mathbf{s}\,)\Big[&|\exp(\mathrm{i}k_m\mathbf{s}\mathbf{r}) \otimes h_o(\mathbf{r})|^2 \\ &+ [\exp(\mathrm{i}k_m\mathbf{s}\mathbf{r}) \otimes h_o(\mathbf{r})]^* [V(\mathbf{r})\exp(\mathrm{i}k_m\mathbf{s}\mathbf{r})] \otimes G(\mathbf{r}) \otimes h_o(\mathbf{r}) \\ &+ [\exp(\mathrm{i}k_m\mathbf{s}\mathbf{r}) \otimes h_o(\mathbf{r})] \{[V(\mathbf{r})\exp(\mathrm{i}k_m\mathbf{s}\mathbf{r})] \otimes G(\mathbf{r}) \otimes h_o(\mathbf{r})\}^*\Big], \end{aligned} \tag{3.1}$$

where $\otimes$ stands for the convolution operation and h_o represents the point spread function (PSF) of the objective lens. The first term, $I_0(\mathbf{r}\,|\mathbf{s}\,) = a^2(|\mathbf{s}\,)\,|\exp(\mathrm{i}k_m\mathbf{s}\mathbf{r}) \otimes h_o(\mathbf{r})|^2 = a^2(|\mathbf{s}\,)|H_o(k_m\mathbf{s})|^2$, denotes the DC term representing the background intensity. By expanding the scattering potential into its real $P(\mathbf{r})$ and imaginary $A(\mathbf{r})$ contributions, the last two terms of the normalized intensity $J(\mathbf{r}\,|\mathbf{s}\,) = [I(\mathbf{r}\,|\mathbf{s}\,) - I_0(\mathbf{r}\,|\mathbf{s}\,)]\,/a^2(|\mathbf{s}\,)$ can be rewritten as

$$\begin{aligned} J(\mathbf{r}\,|\mathbf{s}\,) = &[\exp(-\mathrm{i}k_m\mathbf{s}\mathbf{r}) \otimes h_o^*(\mathbf{r})] \times [(P(\mathbf{r}) + \mathrm{i}A(\mathbf{r}))\exp(\mathrm{i}k_m\mathbf{s}\mathbf{r})] \otimes G(\mathbf{r}) \otimes h_o(\mathbf{r}) \\ &+ [\exp(\mathrm{i}k_m\mathbf{s}\mathbf{r}) \otimes h_o(\mathbf{r})] \times [(P(\mathbf{r}) - \mathrm{i}A(\mathbf{r}))\exp(-\mathrm{i}k_m\mathbf{s}\mathbf{r})] \otimes G^*(\mathbf{r}) \otimes h_o^*(\mathbf{r}). \end{aligned} \tag{3.2}$$

Afterwards, we take advantage of the Fourier Transform (indicated by the hat ˆ symbol) for simplifying Eq. (3.2). By taking the 3D FT on both sides and introducing the normalized wavevector magnitude $\kappa_m = k_m/(2\pi)$, one obtains:

$$\begin{aligned} \hat{J}(\mathbf{p}\,|\mathbf{s}\,) = \hat{P}(\mathbf{p})\Big[&H_o^*(\kappa_m\mathbf{s})\widehat{G}(\mathbf{p} + \kappa_m\mathbf{s})H_o(\mathbf{p} + \kappa_m\mathbf{s}) \\ &+ H_o(\kappa_m\mathbf{s})\widehat{G}^*(-\mathbf{p} + \kappa_m\mathbf{s})H_o^*(-\mathbf{p} + \kappa_m\mathbf{s})\Big] \\ &+\mathrm{i}\hat{A}(\mathbf{p})\Big[H_o^*(\kappa_m\mathbf{s})\widehat{G}(\mathbf{p} + \kappa_m\mathbf{s})H_o(\mathbf{p} + \kappa_m\mathbf{s}) \\ &- H_o(\kappa_m\mathbf{s})\widehat{G}^*(-\mathbf{p} + \kappa_m\mathbf{s})H_o^*(-\mathbf{p} + \kappa_m\mathbf{s})\Big]. \end{aligned} \tag{3.3}$$

Finally, after an integration over all the possible illumination directions limited by the condenser aperture diaphragm $S(\mathbf{s}) = \mathrm{circ}\left(\sqrt{s_x^2 + s_y^2}/\mathrm{NA_c}\right)\mathrm{step}(s_z)$, the 3D FT of intensity

distribution is obtained as it follows

$$\widehat{I}(\mathbf{p}) \quad = \quad = \int_S \widehat{I}(\mathbf{p}\,|\mathbf{s})\mathrm{d}\mathbf{s} = B\delta(\mathbf{p}) + \hat{A}(\mathbf{p})H_A(\mathbf{p}) + \hat{P}(\mathbf{p})H_P(\mathbf{p}). \tag{3.4}$$

Here, the term $B = \int_S I_0(\mathbf{r}\,|\mathbf{s})\,\mathrm{d}\mathbf{s}$ is the background intensity, $H_A(\mathbf{p})$ and $H_P(\mathbf{p})$ are the so-called absorption (AOTF) and phase (POTF) transfer functions [60] defined by

$$\begin{aligned} H_A(\mathbf{p}) &= \mathrm{i}\int_S a^2(|\mathbf{s})[H_o^*(\kappa_m\mathbf{s})\widehat{G}(\mathbf{p}+\kappa_m\mathbf{s})H_o(\mathbf{p}+\kappa_m\mathbf{s}) \\ &- H_o(\kappa_m\mathbf{s})\widehat{G}^*(-\mathbf{p}+\kappa_m\mathbf{s})H_o^*(-\mathbf{p}+\kappa_m\mathbf{s})]\mathrm{d}\mathbf{s}, \\ H_P(\mathbf{p}) &= \int_S a^2(|\mathbf{s})[H_o^*(\kappa_m\mathbf{s})\widehat{G}(\mathbf{p}+\kappa_m\mathbf{s})H_o(\mathbf{p}+\kappa_m\mathbf{s}) \\ &+ H_o(\kappa_m\mathbf{s})\widehat{G}^*(-\mathbf{p}+\kappa_m\mathbf{s})H_o^*(-\mathbf{p}+\kappa_m\mathbf{s})]\mathrm{d}\mathbf{s}. \end{aligned} \tag{3.5}$$

Note that $H_A^*(\mathbf{p}) = H_A(\mathbf{p})$ while the POTF is a Hermitian function $H_P^*(-\mathbf{p}) = H_P(\mathbf{p})$. Consequently, the AOTF is a real even function whereas the imaginary part of the POTF is odd. In the sake of brevity, the details of Eqs. 3.5 derivation are available in Appendix A.1. Eqs. 3.4-3.5 are the key expressions for describing the imaging model settled down by N. Streibl [60, 88], which is based on imposing Helmholtz equation to the mutual intensity function that can be applied for both coherent (a single plane wave) and partially coherent illumination. Indeed, the 3D image formation can be understood as a filtering process where the OTFs limit the observable object spectrum encoded as the 3D-FT of the scattering potential $\hat{V}(\mathbf{p})$. The analytical expressions for the POTF and AOTFs of a bright-field illumination (BFI), derived from Eqs. 3.5 for the particular case of circular apertures (of both the condenser and the objective lens), are provided in Appendix A.2. We recall that BFI corresponds to an uniform illumination across de condenser's input aperture. In particular, the integrals from Eqs. 3.5 have been calculated for $SC \in [0,1]$ in the paraxial approximation by N. Strebil [60] and more recently by Y. Bao and T. Gaylord [72] for the nonparaxial case. This model is valid in first-order Born approximation and it can be alternatively expressed in the reciprocal spatial domain by applying an 3D inverse Fourier Transform (IFFT) to the Eq. 3.4. In this way, one derives that the 3D intensity image $I(\mathbf{r})$ in a bright-field microscope can be written as a linear superposition of the real and imaginary contributions of the scattering potential convolved with the corresponding PSFs $h_P(\mathbf{r})$ and $h_A(\mathbf{r})$ as it follows

$$I(\mathbf{r}) = B + P(\mathbf{r}) \otimes h_P(\mathbf{r}) + A(\mathbf{r}) \otimes h_A(\mathbf{r}), \tag{3.6}$$

with B being the background intensity (unscattered light). Here, $h_P(\mathbf{r})$ and $h_A(\mathbf{r})$ are the microscope response functions to a point scatter, $V(\mathbf{r}) = \delta(\mathbf{r})$, and to a point absorber, $V(\mathbf{r}) = \mathrm{i}\delta(\mathbf{r})$, respectively. Note that the POTF and the AOTF are the 3D FT of $h_P(\mathbf{r})$ and $h_A(\mathbf{r})$, respectively. In the C-ODT case it exists a similar expression but for the complex field amplitude [45, 52].

We recall that the Eq. 3.6 can be applied for different illumination configurations by using either theoretically calculated or experimentally estimated functions $h_P(\mathbf{r})$ and $h_A(\mathbf{r})$.

3.3 Deconvolution process to obtain the object's RI

In this Section we show how to retrieve the scattering potential, and therefore reconstructing the 3D RI of weakly absorbing samples, by means of our PC-ODT technique. PC-ODT is intended to samples with very low absorption in which the real and imaginary contributions of the refractive index fulfill the condition $n_{\mathrm{Im}}(\mathbf{r}) = \varepsilon n_{\mathrm{Re}}(\mathbf{r})$, where ε takes a small positive value (in the range $10^{-5} - 10^{-2}$ for weak absorption objects, see [89]). This approximation is often considered in a similar way for X-ray phase imaging [90] and is appropriate for weakly absorbing and optically thin samples as the ones considered throughout this thesis. In this context, PC-ODT is able to recover the sample RI by only measuring a single intensity data set $I(\mathbf{r})$ provided by the microscope under low spatially coherent illumination ($SC \approx 0.5 - 0.8$). This approach is equivalent to the introduction of an effective transfer function $H_{\mathrm{EFF}}(\mathbf{p}) = H_P(\mathbf{p}) + 2\varepsilon H_A(\mathbf{p})$, as further explained in Appendix A.3, so that the Eq. (3.4) can be then rewritten as

$$\hat{I}(\mathbf{p}) = B\delta(\mathbf{p}) + 2\varepsilon k_0^2 n_0^2 H_A(\mathbf{p}) + \hat{P}(\mathbf{p}) H_{\mathrm{EFF}}(\mathbf{p}). \tag{3.7}$$

Then a regularized Wiener deconvolution [91] provides an accurate and straightforward RI reconstruction from the following expression:

$$\hat{P}(\mathbf{p}) = \frac{\left[\hat{I}(\mathbf{p}) - B\delta(\mathbf{p}) - 2\varepsilon k_0^2 n_0^2 H_A(\mathbf{p})\right] H_{\mathrm{EFF}}^*(\mathbf{p})}{|H_{\mathrm{EFF}}(\mathbf{p})|^2 + \beta(\mathbf{p})}, \tag{3.8}$$

which has been applied in our first work [89]. Note that the previous equation assumes an ideal detector (camera). This assumption does not hold in practical terms, so one needs to include the modulation transfer function (MTF) of the camera which describes how the contrast of the camera decreases as the spatial frequency of the sample increases. Here, we have taken into account the low-pass filtering associated to the MTF by replacing $\hat{I}(\mathbf{p}) \rightarrow \hat{I}(\mathbf{p})/\mathrm{MTF}(p_x, p_y)$ for every possible p_z. In this way, the Eq. (3.8) leads to

$$\hat{P}(\mathbf{p}) = \frac{\left[\hat{I}'(\mathbf{p}) - B\delta(\mathbf{p})\right] H_{\mathrm{EFF}}^*(\mathbf{p})}{|H_{\mathrm{EFF}}(\mathbf{p})|^2 + \beta(\mathbf{p})}, \tag{3.9}$$

where $\hat{I}'(\mathbf{p}) = \left[\hat{I}(\mathbf{p})/\mathrm{MTF}(p_x, p_y)\right] - 2\varepsilon k_0^2 n_0^2 H_A(\mathbf{p})$ and the regularization parameter $\beta(\mathbf{p}) = 1/\mathrm{SNR}(\mathbf{p})$ depends on the signal to noise ratio (SNR) of the measured intensity images which is typically within the range $\beta \sim 10^{-3} - 10^{-5}$ [73]. Throughout this work the SNR has been estimated by considering that the power spectrum of very high frequencies beyond the system's frequency cuttoff. The real noise power spectrum estimation, $PS_n(\mathbf{p})$, is approximated as an average of the power spectrum of those frequencies ($PS_n(\mathbf{p}) \approx \overline{PS_n}$), and the SNR in Fourier space is computed as $\mathrm{SNR}(\mathbf{p}) = \left[PS_s(\mathbf{p}) - \overline{PS_n}\right]/\overline{PS_n}$ where $PS_s(\mathbf{p})$ is the measured signal power spectrum. More intricate deconvolution algorithms could improve the recovery of $\hat{P}(\mathbf{p})$, but they have to be specifically developed for the considered

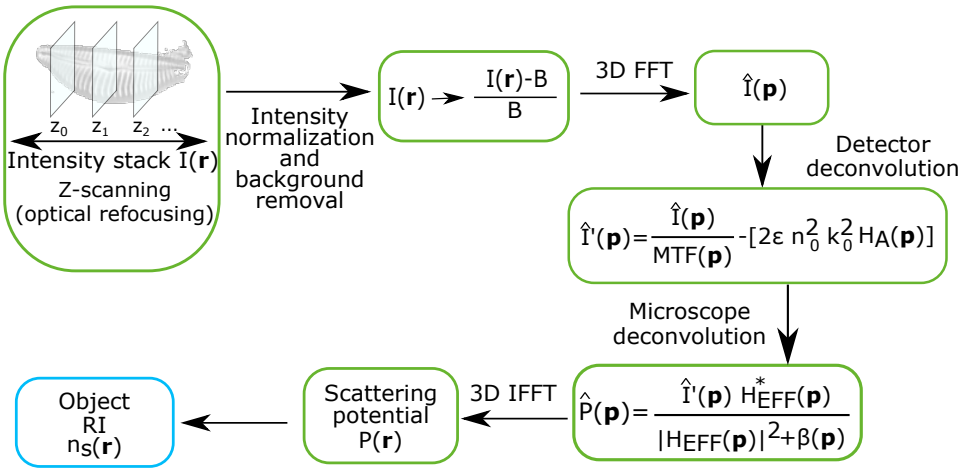

Figure 3.1: Flowchart of the information processing approach used in PC-ODT for reconstruction of the object 3D RI. A 3D intensity stack $I(\mathbf{r})$ of refocused intensity images is measured by optical axial scanning of the sample. Then, a intensity normalization is performed to impose energy conservation, followed by a background removal in $I(\mathbf{r})$. Next, a 3D FT of $I(\mathbf{r})$ is calculated. Later, $\hat{I}(\mathbf{p})$ is deconvolved first by using the detector modulation transfer function, MTF($\mathbf{p}$), and the the remaining background is suppressed in order to obtain $\hat{I}'(\mathbf{p})$. Afterwards, $\hat{I}'(\mathbf{p})$ is deconvolved again by considering the microscope effective transfer function, $H_{\mathrm{EFF}}(\mathbf{p})$, in order to obtain the scattering potential in the spectral domain, $\hat{P}(\mathbf{p})$. Finally, the 3D inverse FT is applied to obtain the scattering potential in the spatial domain from which the RI of the sample is obtained.

bright-field 3D imaging. Note that the available fluorescence deconvolution tools (either with direct or iterative approaches) [91, 92] cannot be applied because they are based on *a-priori* constraints such as non-negativity of the PSF, which do not hold for both C-ODT and PC-ODT quantitative imaging.

Then, according to Eq. 2.24, the real part of the RI distribution is finally obtained:

$$n_{\mathrm{Re}}(\mathbf{r}) = \sqrt{\frac{P(\mathbf{r})k_0^{-2} + n_m^2}{1-\varepsilon^2}}. \tag{3.10}$$

As weak scattering samples are considered, the $n_{\mathrm{Re}}(\mathbf{r})$ provides most of the relevant structural information of the sample. Consequently, henceforth only the real part of the sample RI is considered.

3.4 PC-ODT algorithm

In this Section we describe how the information is processed by the PC-ODT technique to retrieve the 3D RI, as summarized in the flowchart displayed in Fig. 3.1. The first step consists of measuring a stack of intensity images, $I(\mathbf{r})$, obtained by scanning along the optical axis (in this case the z-axis). The next step consists of a background removal (that alternatively can be performed in Fourier domain), followed by the intensity normalization

of the filtered stack to ensure the energy conservation. Afterwards, the deconvolution considering the MTF of the detector (camera) is performed [73, 89], and then $\hat{I}'(\mathbf{p})$ is obtained. The deconvolution Eq. (3.9) is later performed yielding $\hat{P}(\mathbf{p})$ from which the scattering potential $P(\mathbf{r})$ is obtained by calculating the inverse FT of $\hat{P}(\mathbf{p})$. Finally, the 3D RI of the object is recovered from Eq. (3.10).

Finally, let us discuss an important fact about OTF estimation, that is a key point to proceed with PC-ODT and to obtain a reliable RI estimation. In the case of uniform illumination projected over the entire back aperture of the condenser lens, the term $a^2(|\mathbf{s}) = a^2$ is independent on $\mathbf{s}$ and therefore the integrals in Eqs. (3.5) can be analytically calculated either in paraxial [60] or nonparaxial [72] regime. For a high NA objective lens, $\mathrm{NA_o} > 1$, the paraxial OTFs derived by Streibl [60] are not accurate enough as oblique illumination also contributes to image. Hence, in this Chapter we consider nonparaxial case, according to which we apply the following expressions developed in Ref. [72] to calculate the phase and absorption OTF contributions,

$$H_P(p_\perp, p_z) = \frac{i\lambda}{4\pi} \int \hat{O}\left(p'_\perp + \frac{p_\perp}{2}\right) \hat{O}^*\left(p'_\perp - \frac{p_\perp}{2}\right) \times \left[\frac{\hat{S}\left(p'_\perp + \frac{p_\perp}{2}\right)}{\sqrt{1-\lambda^2\left(p'_\perp - \frac{p_\perp}{2}\right)^2}} - \frac{\hat{S}\left(p'_\perp - \frac{p_\perp}{2}\right)}{\sqrt{1-\lambda^2\left(p'_\perp + \frac{p_\perp}{2}\right)^2}} \right] \times \delta\left(p_z + \sqrt{\lambda^{-2} - \left(p'_\perp - \frac{p_\perp}{2}\right)^2} - \sqrt{\lambda^{-2} - \left(p'_\perp + \frac{p_\perp}{2}\right)^2} \right) d^2(p'_\perp) \tag{3.11}$$

and

$$H_A(p_\perp, p_z) = \frac{\lambda}{4\pi} \int \hat{O}\left(p'_\perp + \frac{p_\perp}{2}\right) \hat{O}^*\left(p'_\perp - \frac{p_\perp}{2}\right) \times \left[\frac{\hat{S}\left(p'_\perp + \frac{p_\perp}{2}\right)}{\sqrt{1-\lambda^2\left(p'_\perp - \frac{p_\perp}{2}\right)^2}} + \frac{\hat{S}\left(p'_\perp - \frac{p_\perp}{2}\right)}{\sqrt{1-\lambda^2\left(p'_\perp + \frac{p_\perp}{2}\right)^2}} \right] \times \delta\left(p_z + \sqrt{\lambda^{-2} - \left(p'_\perp - \frac{p_\perp}{2}\right)^2} - \sqrt{\lambda^{-2} - \left(p'_\perp + \frac{p_\perp}{2}\right)^2} \right) d^2(p'_\perp), \tag{3.12}$$

where we have introduced the illumination function $\hat{S}(p_x, p_y)$ and the pupil $\hat{O}(p_x, p_y)$ related to the illumination field over condenser and objective apertures, respectively. Let us recall that $\lambda = \lambda_0 / n_{imm}$ is the normalized wavelength (n_{imm} refers to the RI of the immersion oil of the objective lens). The expressions from Eqs. 3.11-3.12 are the general imaging case. Nevertheless, for the remaining of this Chapter (and the next one) we assume an ideal uniform bright-field illumination and circular apertures (both the condenser and objective) with $SC \in [0, 1]$. In that case, Eqs. 3.11-3.12 can be further simplified, as detailed in Appendix A.2. We remark that the inclusion of OTF concept assumes a linear shift-invariant system [60, 72].

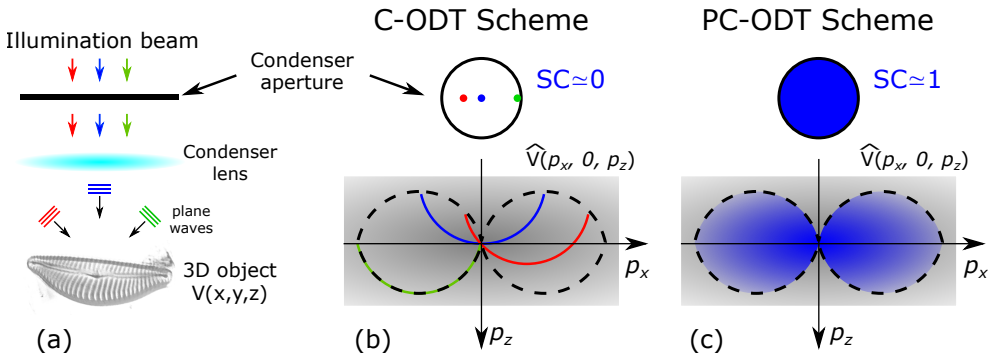

Figure 3.2: (a) Illumination configuration for a transmission wide-field microscope. (b) The C-ODT technique retrieves the complex scattering potential spectrum $\hat{V}(\mathbf{p})$ transmitted by the microscope. An illumination scanning approach (sequential object illumination) is used to gather all the cross sections of the object's spectra with the Ewald sphere (semicircular arcs). As an example, only 3 scanning positions (thus 3 semicircular arcs) have been sketched. Note that the transmitted part of $\hat{V}(\mathbf{p})$ falls inside a 3D horn-torus in the reciprocal space, here only its section $(p_x, 0, p_z)$ has been sketched (dashed curve). (c) The proposed PC-ODT technique collects the same horn-torus region because the illumination of the condenser aperture allows for coverage of all the illumination angles simultaneously.

Nevertheless, it also exists the possibility of using direct experimental measurements of the PSF of a high-NA microscope operating in transmission bright-field, as explored in some works [93], and then deriving the OTF by Fourier Transform. This approach takes into account the imperfections of the imaging system like the effects of slightly off-axis illumination or optical aberrations. However, the direct measurement of PSF suffers from several drawbacks. The choice of a sample mimicking an ideal isolated point scatterer is troublesome. Typically, nanoparticles like calibrated polystyrene beads with size close to the diffraction limit (100 nm diameter, around $\lambda_0/4$, being λ_0 the illumination wavelength) and known RI are used [67, 93]. This approach is prone to noise as in bright-field the background term prevails in the intensity measurement and a weakly scattering sample exhibits poor contrast. Other works rely on PSF estimation obtained by means of deconvolution algorithms [94], but require *a-priori* knowledge of the sample and the reconstructed RI still suffer from artifacts like ringing. Indeed, the intensity stacks from a reference or probe object (i.e. beads of known dimensions or by calibrated by using another technique, so the probe volume contains a single in-focus slice with blurring above and below it according to the PSF of the imaging system) are used together with iterative Landweber least squares method for minimizing the error norm of the PSF calculated in this way [94]. Consequently, in this Chapter we prefer to apply analytical expressions for PSF and OTF. Later, a better OTF estimation is obtained by measuring the experimental illumination in the microscope condenser plane, as detailed in Chapter 5.

3.5 Transmitted spatial frequency content of the object

In ODT, the amount of information transmitted by the imaging system is determined by the illumination and the NA of the microscope lenses (both NA_c and NA_o), which determine the limits (see the dashed curves in Fig. 3.2) of the spatial frequency content of the object that contributes to the image formation. Both C-ODT and PC-ODT provide access to the same spatial frequency content of the 3D object. However, this information is obtained in different ways in PC-ODT in comparison with C-ODT, as illustrated in this Section.

In the case of C-ODT, a laser beam is focused onto the condenser aperture in order to approximate a point light source which is Fourier transformed by the condenser lens into a collimated wave approximating the ideal plane wave reaching the sample, as it is indicated in Fig. 3.2 (a-b). For each illumination angle of the plane wave (that depends on the spot position) only one cross section of the object spectrum $\hat{V}(\mathbf{p})$ and the Ewald sphere can be retrieved. In general, an interferometric measurement (a hologram recorded by a digital camera) is often used to retrieve such a cross-section information (which is a complex field defined by an amplitude and a phase distributions). Specifically, the recovered information located within the transmited Ewald cap (represented in Fig. 3.2 (b) by using a semicircualr arc to help the visualization) is obtained via phase retrieval from the recorded hologram by using numerical refocusing (involving Fresnel beam propagation) and complex amplitude deconvolution. Thus, in C-ODT the spatial frequency support is covered by scanning the laser beam throughout the entire condenser aperture that allows approaching the available frequency content till the limits. In Fig. 3.2 (b) such filling process used in C-ODT has been indicated only for 3 scanning positions (thus resulting in 3 semicircular arcs) to help the visualization. To create the synthetic version of the object's $\hat{V}(\mathbf{p})$ transmitted by the microscope, all the retrieved spectrum cross sections have to be assembled together in the reciprocal 3D space [45, 52].

In contrast to C-ODT, PC-ODT exploits quasi-monochromatic and spatially incoherent light provided by a LED or a halogen lamp to illuminate the entire condenser aperture simultaneously, see Fig. 3.2 (c). Note that numerical refocusing can not be applied for partially coherent illumination. As a result, the object is illuminated by the incoherent sum of plane waves emerging from different directions. Therefore, a similar part of the $\hat{V}(\mathbf{p})$, see Fig. 3.2 (c), transmitted by the microscope can be reconstructed from a single data set $I(\mathbf{r})$ obtained by optical refocusing (axial scanning). Thus, PC-ODT is inherently faster than C-ODT and, in practice, simplifies the measurement and the reconstruction process. An additional advantage is that the low spatial coherent illumination avoids coherent artifacts such as speckle noise, which plagues C-ODT and other coherent light microscopy imaging methods [13]. Moreover, the partially coherent illumination enables compatibility with conventional commercial microscopes.

Let us now analyze the contribution of illuminating plane waves in the total POTF and AOTF, as illustrated in the first and the second row of Fig. 3.3, respectively. Here, the analytical OTF expressions for ideal uniform bright-field illumination have been considered [72], also available in Appendix A.2. In that case, both POTF and AOTF are axially symmetric. Specifically, the parameters chosen for OTF computation are a central wavelength of $\lambda_0 = 450\,\text{nm}$, and numerical apertures of $NA_c = 0.95$ and $NA_o = 1.4$ ($SC \approx 0.7$). In this way, Fig. 3.3 (a-c) correspond to the $(p_x, 0, p_z)$ sections of the OTFs for the fol-

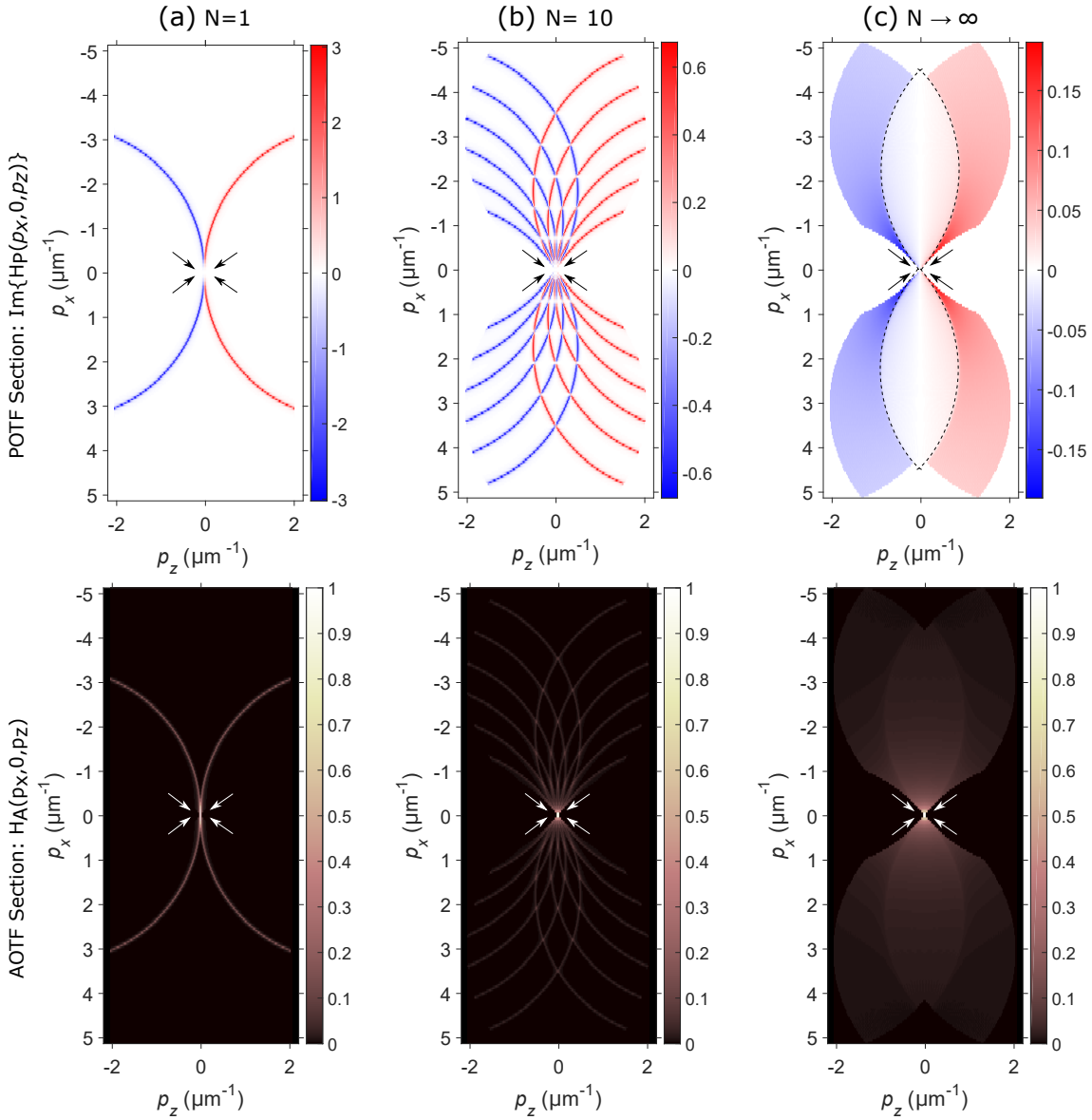

Figure 3.3: Comparison between different 2D xz-sections of the 3D nonparaxial OTF. The first row summarizes different phase OTFs (POTFs), $H_P(\mathbf{p})$, whereas the second row shows the corresponding sections of the absorption transfer function (AOTF), $H_A(\mathbf{p})$. OTFs from (a-c) columns have been calculated with a different number of illumination plane waves (N), ranging from a coherent illumination (a) to almost incoherent illumination (c). All the OTFs have been represented by considering $\lambda_0 = 450\,\text{nm}$, $\text{NA}_\text{c} = 0.95$ and $\text{NA}_\text{o} = 1.4$. The arrows point towards the missing-cone (MC) region in the frequency domain, whereas the dashed line contains the low value (LV) region.

lowing cases: in Fig. 3.3 (a) a plane wave provides coherent illumination (only the central point of the condenser aperture diaphragm has been illuminated, thus $\mathbf{s} = (0,0,1)$), while in Figs. 3.3 (b-c) intermediate (with 10 different illumination directions, so 10 points of the condenser are scanned) and almost incoherent (the whole condenser aperture diaphragm is filled with light) illumination have been deemed, respectively. The case with $N = 1$ shown in Fig. 3.3 (a) is equivalent to coherent illumination, therefore only a couple of arcs (corresponding to Ewald sphere caps in 3D) are reached. When some more condenser positions are scanned, the arcs overlap (see Fig. 3.3 (b)) and the frequency coverage improves, although important empty gaps remain. As observed in Fig. 3.3 (c), if one fills the whole condenser aperture with light (equivalent to a very large number of scanning spots), it yields an extended covered spectrum region. Note that the bright-field microscope (with fully opened condenser aperture) transmits the same object spatial-frequency content that C-ODT is able to achieve from multiple illuminations [89]. We remark that POTF has positive and negative regions, therefore exhibiting a contrast loss around the optical axis ($p_z = 0\,\mu\mathrm{m}^{-1}$) due to destructive overlapping of opposed sign Ewald sphere caps. Conversely, the AOTF is always positive (as every couple of conjugated Ewald sphere caps overlaps additively) and showcases a low-pass behaviour [66]. In this way, we see that the frequency support in PC-ODT is the same that could be reached by considering a number of waves high enough. Note that in the Fig. 3.3 (c), PC-ODT exhibits certain regions of low POTF magnitude (poor contrast). Indeed, the spatial frequencies delimited within the dashed line are further referred to as low-value (LV) region while the missing spatial frequencies marked with arrows are responsible for the well-known MC problem. The MC problem produces artifacts and elongation of the reconstructed sample, as further illustrated in Chapter 4 with experimental examples. This MC problem is a well-known problem, leading to an axial distortion effect which is also present in C-ODT as well as in other quantitative imaging techniques, see for example [67, 86]. However, the LV region and the subsequent contrast loss in certain spatial frequency regions is a new problem and its effects can be mitigated by using a more appropriate design of the illumination over the condenser lens input aperture, different from BFI, as we will further study in Chapter 5.

It is also worth pointing out that the missing-cone problem equally affects both ODT modalities. The missing-cone region is smaller for the larger $\mathrm{NA_c}$ and $\mathrm{NA_o}$, however, it can not be completely filled without applying mechanical rotation of the object discussed for the C-ODT case in Chapter 2. The same analysis is applicable for PC-ODT. The utilization of object rotation [95], multiple angle illumination [66] and even the combined use of both of them [71] have already been experimentally exploited for analysis of static objects. Nevertheless, it results cumbersome for analysis of dynamic objects such as living cells. Some prior assumptions about the object (for instance, *a-priori* knowledge of its shape or imposing the constraint that its RI is higher than the surrounding medium in which it is immersed) or an iterative approach for RI recovery can help to mitigate the artifacts caused by the lack of certain spatial frequency information (e.g. see [67]). Such methods can be applied for both ODT modalities.

So far, we have seen the impact of modifying the illumination coherence (through *SC*) on the POTF frequency support. It is also convenient to illustrate how the illumination wavelength (λ_0) plays also a crucial role in the frequency support. Further, let us now analyze the POTFs for three illumination wavelengths (450, 560 and 630 nm respectively), as

displayed in Fig. 3.4, and a higher coherence ratio ($SC = \mathrm{NA_c}/\mathrm{NA_o} = 1$, with $\mathrm{NA_o} = 1.4$) in comparison with the one from the Fig. 3.3. The magnitude of POTF values has been normalized to the range [-1, 1] for each λ_0. Regardless the λ_0 value, all the POTFs exhibit the LV region around the optical axis. However, in the event of the smallest wavelength ($\lambda_0 = 450\,\mathrm{nm}$), the frequency support extends far away $p_x = 3\,\mu\mathrm{m}^{-1}$ and $p_z = 1.25\,\mu\mathrm{m}^{-1}$. Furthermore, the wavelength produces a scaling effect over the frequency support in PC-ODT according to the results from Fig. 3.4, thus extending the maximum spatial frequencies attainable as long as the wavelength decreases. However, the choice of λ_0 often depends on the absorption of a particular sample, and it is not always possible to select the wavelength that would offer the widest frequency support.

The spatial resolution in ODT, without sample rotation, exhibits a strong anisotropy due to inhomogeneous coverage of the spatial frequency support. For this reason, the Nyquist limits are often used to theoretically compare the OTFs from different imaging system [51, 79]. It is worth remarking that the OTF allows to link diffraction limit and optical resolution concepts [96]. We recall that Nyquist distances in traverse ($\Delta x, \Delta y$) and axial directions (Δz) are respectively given by $\Delta x = \Delta y = \lambda_0 / \left[2(\mathrm{NA_o} + \mathrm{NA_c})\right]$ and $\Delta z = \lambda_0 / \left[2(n_{imm} - (n_{imm}^2 - \mathrm{NA_o^2})^{1/2})\right]$, where n_{imm} is the objective immersion oil (in this case, n_{imm} =1.515 is considered). The Nyquist distances, for both $SC = 0.7$ and $SC = 1$ and the imaging system considered in Fig. 3.3 and Fig. 3.4, are summarized in Table 3.1). Note that Nyquist distances only determine maximum frequency values that can be reached in axial and traverse directions, but do not provide any information about spatial resolution distribution in 3D arbitrary directions. In this way, it is not possible to affirm that broader limits of Δx, Δy, Δz , obtained by a lower λ_0, are always associated with the improvement of the RI quality.

Moreover, by comparing the Fig. 3.3 and Fig. 3.4 one may conclude that working with $S \to 1$ would be better to enlarge the frequency support. Nevertheless, it is easier working with an air (dry) condenser with a moderately high NA (i.e. in the range 0.8-0.95) than using a extremelly high-NA immersion condenser for reaching a *SC* value close to 1, since the air condenser provides larger working distance [97]. Moreover, the frequency content of extremely high frequency that would be reached with a high-NA condenser (above $p_x = 4\,\mu\mathrm{m}^{-1}$, corresponding to sample features below 250 nm) is close to diffraction limit (around half λ_0) and would be severely attenuated. Therefore, this region of frequency mainly contributes to the noise of the reconstruction rather than improving RI quality. In consequence, we typically adopt intermediate-high $SC \approx 0.5 - 0.8$ ratios, as later explained in the experimental implementation in Chapter 4, as a trade-off between frequency support and simplicity in the experimental setup.

3.6 Analysis of PC-ODT performance with numerical simulations

In this Section we perform RI reconstruction with a simulated phantom for testing the reliability of PC-ODT. A good phantom test should provide a sufficient range of different spatial frequency structures. In this case, it consists of a structure based in a Siemens star with a

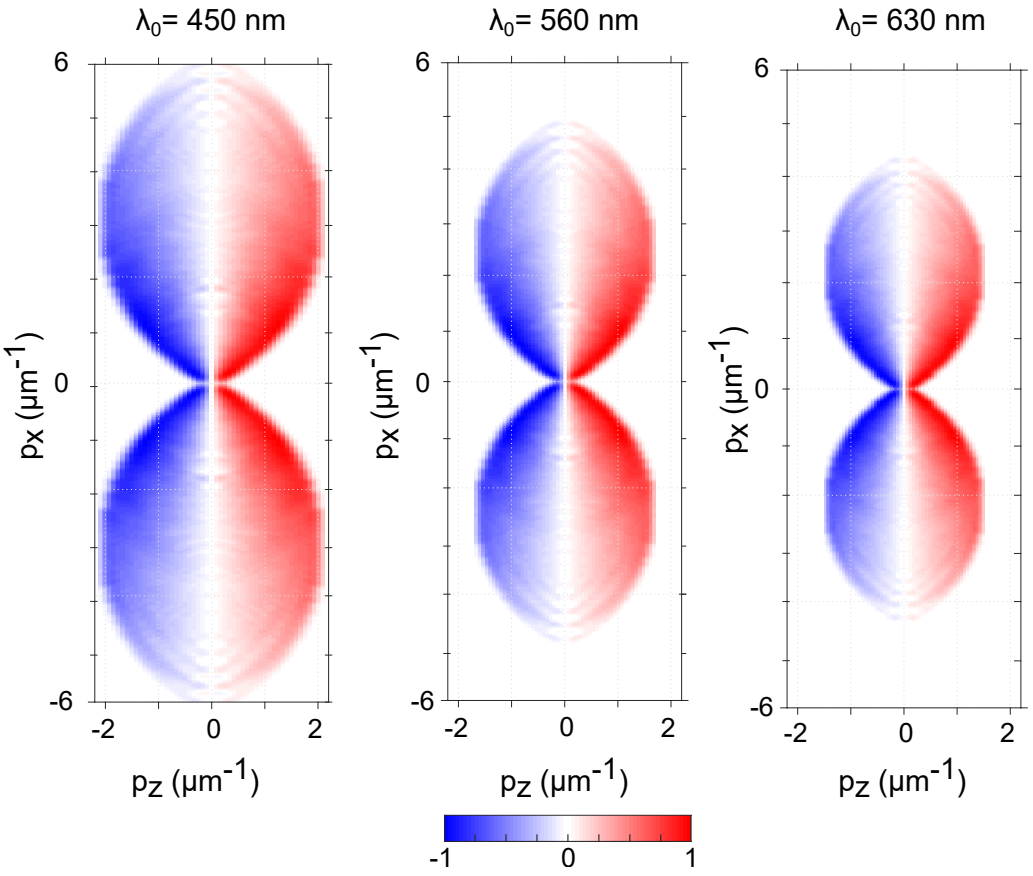

Figure 3.4: 2D xz-slices (fixing $y = 0\,\mu$m) from normalized POTFs obtained in BFI with $\mathrm{NA_o} = 1.4$ and the coherence ratio $SC = \mathrm{NA_c} = \mathrm{NA_o} = 1$ for demonstrating the scaling effect by varying the illumination wavelength (λ_0).

λ_0(nm)	SC	Δx(nm)	Δz(nm)
450	0.95/1.4	96	240
560		119	299
630		134	337
450	1	80	240
560		100	299
630		113	337

Table 3.1: Nyquist distances in the traverse (Δx) and axial (Δz) directions, depending on the chosen wavelength (λ_0) and the spatial coherence ratio (SC) with $\mathrm{NA_o} = 1.4$.

diameter of 16 μm and arranged as a spiral staircase (of 3 different steps in z-direction) while the central area is a solid cylindrical pillar crowned with four concentric cylinders of decreasing radii. In this way, the object provides low and high spatial frequencies, so it is a suitable benchmark for 3D imaging techniques assessment. The simulations have been perfomed assuming first Born aproximation (according to Eq. 3.7) and applying the Wiener deconvolution procedure described in Section 3.3. In all cases, it has been simulated $\mathrm{NA_c} = 0.95$ and $\mathrm{NA_o} = 1.4$. Further, three representative examples have been considered to study the effects of absorption, noise and object rotation on PC-ODT performance.

3.6.1 Absorption effects under Born approximation

We recall that we have assumed a linear dependance of absorptivity with phase RI according to $n(\mathbf{r}) = n_{\mathrm{Re}} + in_{\mathrm{Im}} \approx n_{\mathrm{Re}}(1 + i\varepsilon)$ that is convenient for weak scattering and optically thin samples under Born approximation. Nevertheless, the value of imaginary part of RI (also known as extinction coefficient) is scarcely available in the literature for most of biological samples that have been studied throughout this thesis. For example, at $\lambda_0 = 560\,\mathrm{nm}$ the extinction coefficient is $3.55 \cdot 10^{-3}$ for human liver cells [98] (it is expected to be around this value for most eukaryotic cells) whereas $n_{\mathrm{Im}} = 2.38 \cdot 10^{-3}$ for SiO_2 (the main material of diatom samples studied in next Chapter) at $\lambda_0 = 450\,\mathrm{nm}$ [99]. We have already mentioned that the absorption could be estimated by using multiple illuminations, as explained in Ref. [86]. However, it enlarges the data acquisition and brings new problems in LV regions of the corresponding OTFs. In our PC-ODT realization, the choice of ε is taken as an *a-priori* value in agreement with literature. Here, our goal is to quantify how much distortion is introduced in the real part of reconstructed RI if an inaccurate absorption value is considered.

Let us consider a Siemens star phantom ($373 \times 373 \times 51$ pixels) with complex RI of $n_p = 1.35 \cdot (1 + i \cdot 10^{-3})$, illuminated with BFI ($\lambda_0 = 560\,\mathrm{nm}$), in which n_{Im} has been chosen to mimic typical extinction values for mammalian cells in the visible range. In Fig. 3.5(a-c) the real part of the RI recovered by PC-ODT (with Wiener deconvolution and fixed regularization parameter of $\beta = 10^{-7}$ for all cases) has been displayed for different absorption parameters, including $\varepsilon = 0$ (disregarding all absorption effects), the correct value ($\varepsilon = 10^{-3}$) and an order of magnitude higher and below the appropriate one. Note that the central pillar of the Siemens star, corresponding to low spatial frequencies and delimited withing dashed lines in Fig. 3.5(a, c), is almost hollow when a pure phase sample is assumed. Moreover, a strong halo effect is present when $\varepsilon = 0$ is taken, thus presenting some values below the immersion RI (in dark blue) and a radial degradation along each star spoke of the structure particularly noticeable near the central cylinder, due to the LV region. Oppositely, when $\varepsilon > 0$ is considered, this missing part of the pillar is filled. However, when absorption is underrated (see the case $\varepsilon = 10^{-4}$ in Fig. 3.5) a strong halo remains with out-of-focus information and the real part of the structure RI is, in general, underestimated (values around 1.344), therefore producing a high relative error (4.47 %). When the proper ε value is found the computed RI (around 1.348) is closer to the ground truth (the measured relative error decreases up to 1.29 %) and the halo effect is ostensibly reduced. Finally, if an excessive absorption is considered ($\varepsilon = 10^{-2}$) the real part of reconstructed RI remains virtually unaltered except for a halo that appears again, thus producing a slightly higher

relative error (1.37 %). Despite this, one concludes that it is better to consider a certain degree of absorption than ignoring its effects at all, because the designed phantom includes an absorptive component which is retrieved (at least partially) by the AOTF, thereby obtaining additional information for a more reliable reconstruction. A comparison of the same line profile, labeled as (1) in Fig. 3.5(a), reconstructed with several values of ε is displayed in Fig. 3.5(d), which confirms that as ε approaches the correct value the profile tends to the phantom one. Finally, Fig. 3.5(e) compares the 3D RI of the phantom and the recovered version with PC-ODT when the correct value of ε is taken, in which we observe that the morphology of the phantom has been accurately retrieved.

By considering the absorption effects we also mitigate the effects of the LV region of the POTF. Very low frequencies around the axis $p_z = 0$ that are formerly attenuated by the POTF can be better retrieved if AOTF is included due to the fact that precisely in such region AOTF exhibits large magnitude values. To summarize, a hybrid OTF including both AOTF and POTF effects enhances the quality of the reconstructed 3D object in comparison with $\varepsilon = 0$, even if the estimation of the absorption parameter is not completely accurate. When the absorption is unknown, we may assume a small value of ε parameter to enhance RI reconstruction.

3.6.2 Noise effects in RI reconstruction

Let us now discuss about the effects of RI reconstruction degradation in Wiener deconvolution due to the noise. The main component of noise accompanied the intensity measurements is typically modeled as a Poisson distribution [100, 101], $\kappa^n e^{-\kappa}/n!$, where n (integer value) and κ accounts for photon arrivals at the detector plane (i.e. camera sensor) and the rate thereof, respectively. Despite other sources of noise involved in digitalization (e.g. Gaussian noise in different electronic and thermal process) also contributes to the uncertainty in the acquired raw data, the Poisson noise has been reported to prevail [101] and for this reason in this study it is considered as a dominant noise source.

We simulate again the RI recovery of a weakly absorbing phantom of Siemens star (a stack with $373 \times 373 \times 85$ pixels) with complex RI of $n_p = 1.35 \cdot (1 + i \cdot 10^{-3})$, illuminated with BFI ($\lambda_0 = 560\,\text{nm}$). After computing the simulated noise-free intensity images then we apply a scaled Poisson noise ($\kappa = 1.5$) and estimate the SNR to quantify the intensity degradation. We recall that according to Wiener deconvolution $\beta(\mathrm{p})$ is a regularization parameter whose value depends on the SNR of each spatial frequency. Nevertheless, in practice the reference image is unavailable to compute the SNR properly. For this reason, the general Wiener filter is often simplified to a fixed and small positive β value, which is also known as Tikhonov deconvolution [73]. In practice, the noise can be estimated from a region of very high frequencies beyond the OTF frequency support as the object frequency content is not transmitted away from the OTF limits. Consequently, very high frequencies are prone to carry mostly noise, as formerly explained in Section 3.3.

The results of the reconstruction with a low amount of Poisson noise that allows an intensity SNR of 22.66 dB are shown in Fig. 3.6 while the outcomes with a larger amount of noise leading to a smaller SNR of 16.42 dB are displayed in Fig. 3.7. As observed in Fig. 3.6, a low value of $\beta = 10^{-6}$ leads to an average Siemens star RI (≈ 1.346) as well as a reasonably uniform reconstruction (the whole structure takes a RI value within a very

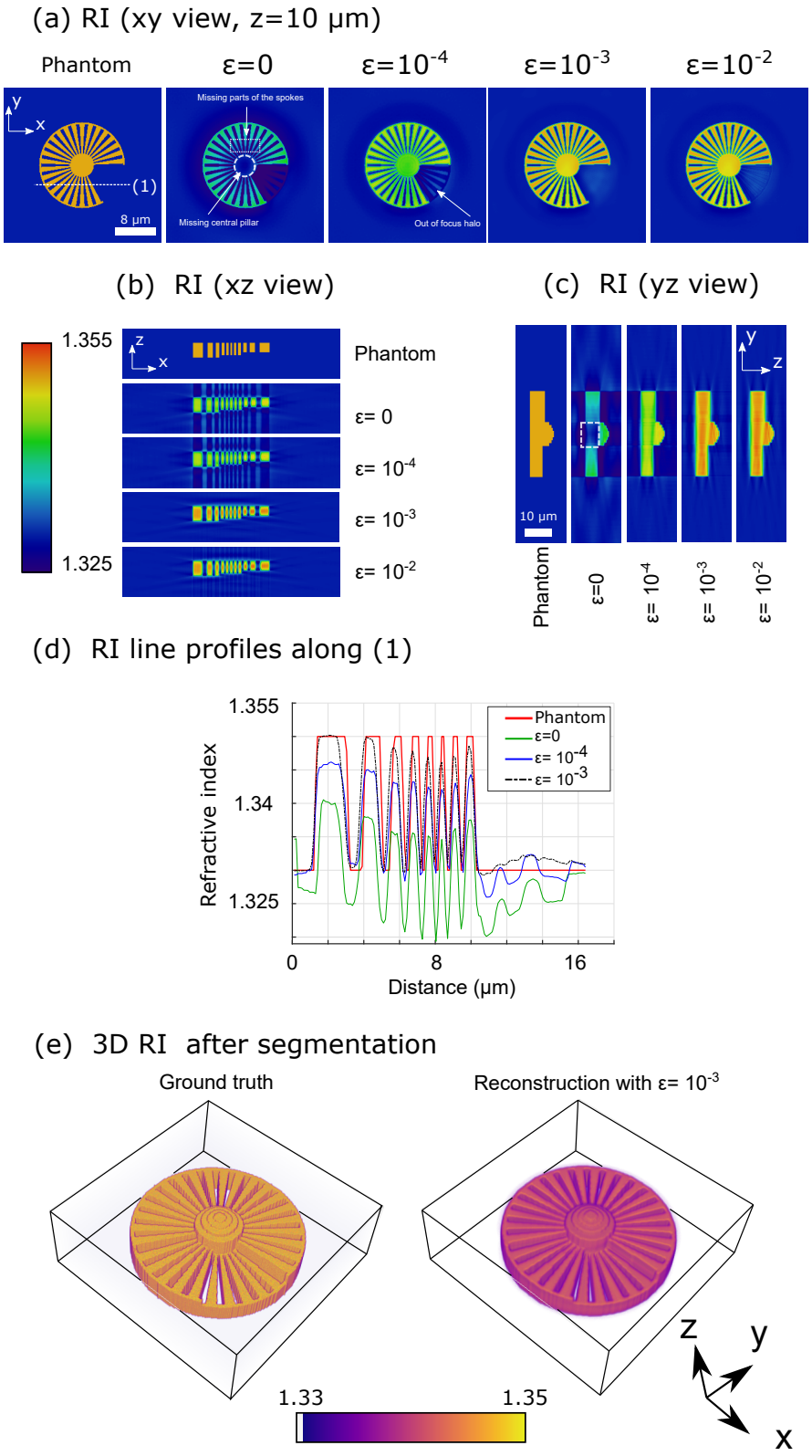

Figure 3.5: Simulation results for a weakly absorbing phantom. (a-c) Different 2D slices when different absorption ε is considered. (d) Line profiles of the reconstructed RI. (e) 3D RI reconstructions after background segmentation based on gradient. Only the real part of RI has been displayed.

limited range between $1.345 - 1.348$). Otherwise, the noise effects have not been completely supressed from the background, which lead us to test a higher value of β. Hence, for $\beta = 10^{-4}$ the Poisson noise is effectively removed at the expense of RI underestimation and a lower degree of uniformity within Siemens star structure, notably the middle pillar RI (around 1.335) is much lower than that of the outer boundaries (≈ 1.340). We note that Tikhonov deconvolution can strongly distort the information at frequencies within the LV region, corresponding in this case mostly with the central cylinder of the star. Then, Wiener filter offers the best trade-off between noise compensation and accurate average RI retrieval within the structure of the star (≈ 1.344, a bit worse than in $\beta = 10^{-6}$ case). We see that Wiener filter removes the noise as effectively as $\beta = 10^{-4}$ without sacrificing RI uniformity, as well as it mitigates halo artifacts (see Fig. 3.6(c-d)). We also conclude that the best β choice for Tikhonov regularization is the lowest value that guarantees the noise removal to avoid sample blur and underestimation. The same study has been repeated with worse noise conditions, as shown in Fig. 3.7, obtaining similar results but being unable to remove completely the noise. Besides, when β value is too small (see the case with $\beta = 10^{-6}$) and the noise level is significant the deconvolution even yields overestimated RI (between $1.352 - 1.354$). Even though the star is recognizable in this hard conditions, the background noise persists and it would be necessary a postprocessing stage to extract reliable quantitative information (i.e. the object's RI). Conversely, when Wiener is applied we obtain a reconstruction with similar average RI (≈ 1.343) despite having 6.24 dB more of noise, which demostrates that it is a more robust deconvolution method.

Apart from the relative error, for measuring RI reconstructions quality assessment it is also possible to use feature similarity (FSIM), which better fits with the perception of the human visual system [102]. When the reference (noise-free) image is known, FSIM measures the structural similarity between it and the reconstructed one and assigns a score within the range $[0, 1]$, with FSIM $= 1$ being the case of perfect reconstruction. FSIM considers both the phase congruency (a contrast invariant magnitude that accounts for the significance of a local feature of the reconstructed image and how it matches the structure of the original one) and the RI image gradient magnitude. More information about FSIM can be found elsewhere [102, 103]. Both the relative error and average FSIM for the previous noisy simulations are summarized in Table 3.2. Note that FSIM is always quite high (above 0.84) which means that the overall structure of the sample is observable. Moreover, for the reconstruction in which the central pillar is partially faded and radial degradation exists (with $\beta = 10^{-4}$) the lowest FSIM score is obtained which proves that FSIM decreases when the morphology of the phantom is not properly recovered regardless the noise level. Otherwise, the highest relative error is obtained for β=10^{-6} which indicates that this metric is more suitable for the assessment of image noise degradation rather than detecting morphological errors. For a fair comparison between different simulations, we give the FSIM along with the relative error, for evaluating both the structure and accuracy of reconstructed RI.

It is also possible to analyze the phantom in z-direction (optical axis) to verify the quality of reconstructed structure, for example by computing the FSIM for each z-slice as displayed in Fig. 3.8. We recall that the whole z-stack comprises 85 planes ($\approx 22\,\mu$m) and that there is a padding equivalent to $2\,\mu$m on both sides in that direction to avoid windowing artifacts during data manipulation. Note that for the central z-slices, corresponding

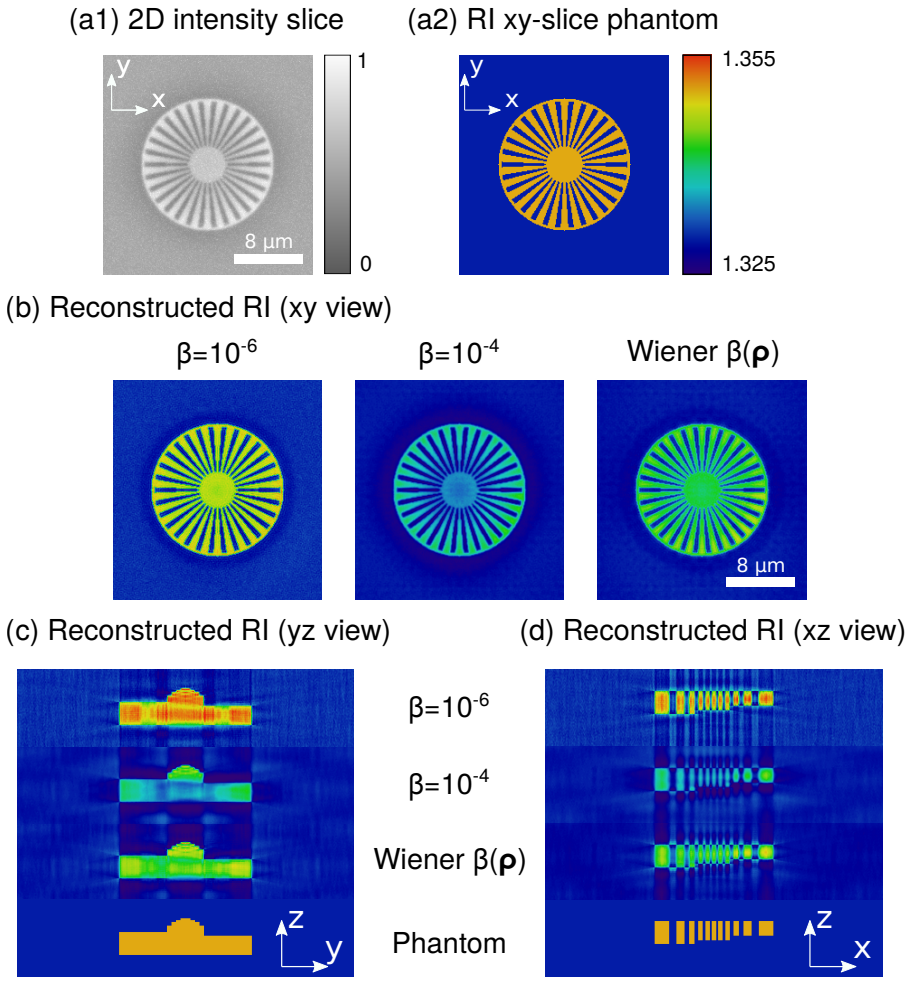

Figure 3.6: Simulation results for a weakly absorbing phantom under low noise conditions. (a1) Noisy intensity slice with SNR $= 22.66$ dB. (a2) 2D xy-slice of the phantom. (b-d) 2D slices of the reconstructed RI with different regularization: Tikhonov deconvolution with $\beta = 10^{-6}$, Tikhonov deconvolution with $\beta = 10^{-4}$ and Wiener deconvolution with $\beta(\mathbf{p}) = 1/\mathrm{SNR}(\mathbf{p})$. Only the real part of the RI is displayed.

SNR (dB)	Regularization β	Relative error (%)	FSIM
22.66	10^{-6}	6.59	0.902
	10^{-4}	5.16	0.873
	Wiener $\beta(\mathbf{p})$	3.75	0.913
16.42	10^{-6}	11.41	0.858
	10^{-4}	5.81	0.849
	Wiener $\beta(\mathbf{p})$	5.77	0.871

Table 3.2: Relative error and average FSIM score for noisy image stacks of Siemens star phantom considered in the PC-ODT simulation.

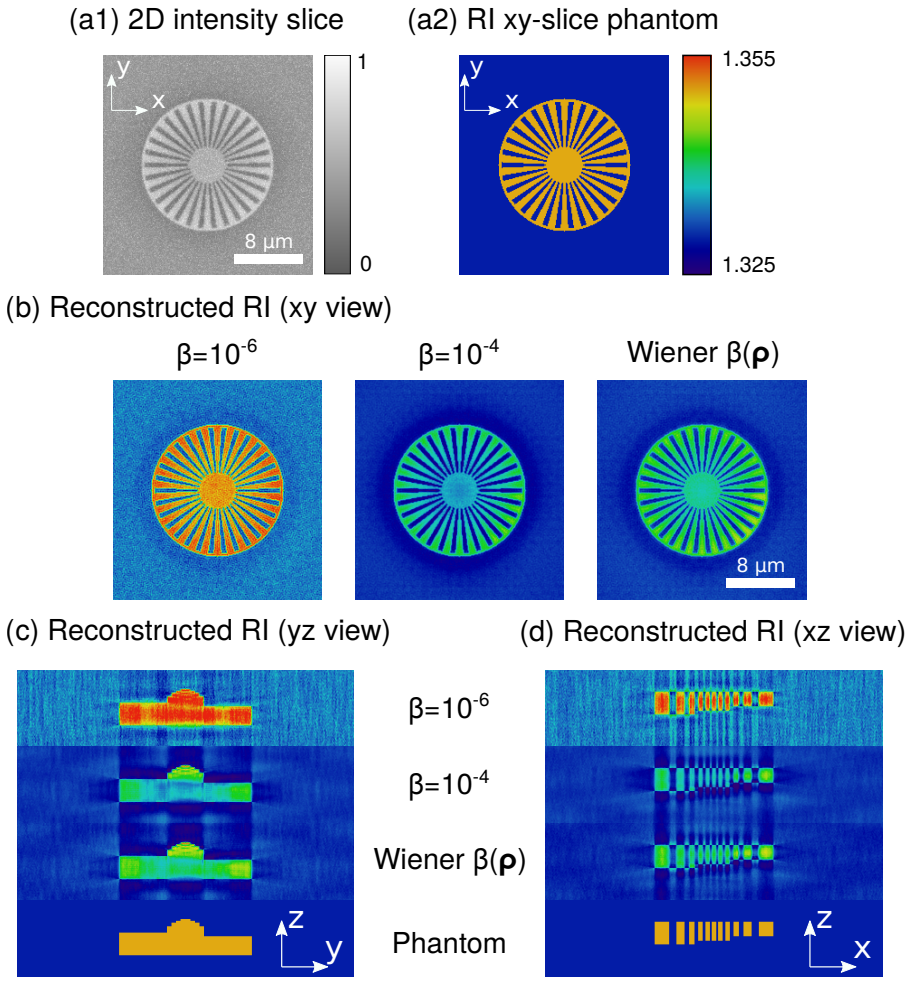

Figure 3.7: Simulation results for a weakly absorbing phantom under high noise conditions. (a1) Noisy intensity slice with SNR $= 16.42$ dB. (a2) 2D xy-slice of the phantom. (b-d) 2D slices of the reconstructed RI with different regularization: Tikhonov deconvolution with $\beta = 10^{-6}$, Tikhonov deconvolution with $\beta = 10^{-4}$ and Wiener deconvolution with $\beta(\mathbf{p}) = 1/\mathrm{SNR}(\mathbf{p})$.

to depths around $10\,\mu$m in Figs. 3.8(b-c), the FSIM reaches extremely high values (above 0.88) regardless the considered noise level. However, important differences arises when we look at peripheral z-slices that should be completely filled by a medium of uniform RI. This analysis provides useful knowledge about the halos and defocus artifacts in RI reconstruction. First, we notice that outer z-slices FSIM decays more rapidly in high noise case (even reaching values below 0.7) in comparison with their low noise counterpart, which confirms the presence of more halos and artifacts as previously shown in Fig. 3.7. Second, we verify that Wiener deconvolution is robust as it overperforms Tikhonov for both noise levels, but it is even more noticeable when the input intensity exhibits a poor SNR. Lastly, by comparing Fig. 3.7(b) and Fig. 3.7(c) we corroborate that, in general, a larger amount of noise deteriorates FSIM as phantom structure tends to be more difficult to perceive.

We recall that many different criteria have been applied to assess image quality aside

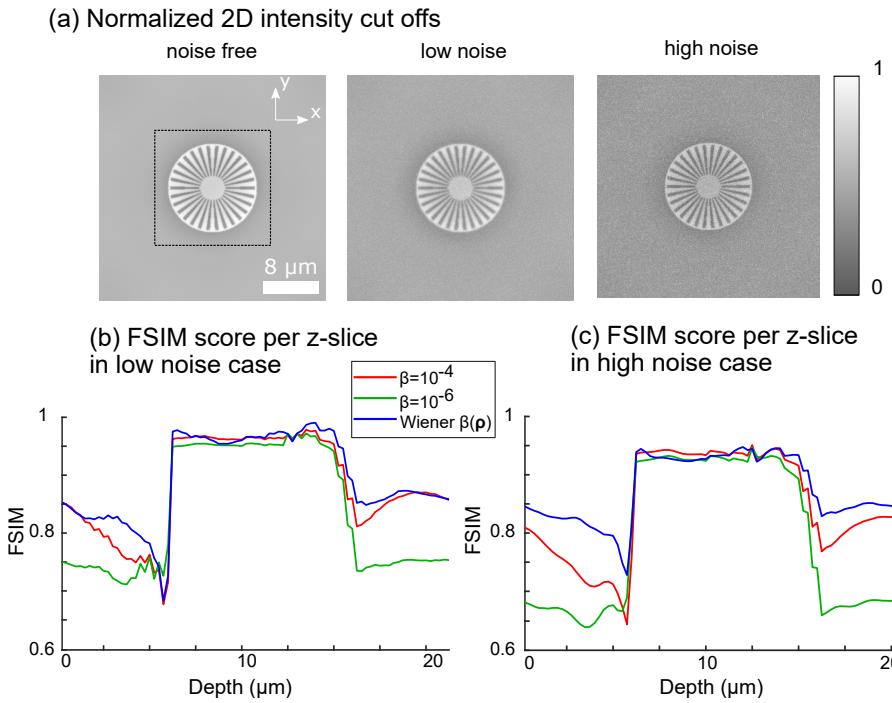

Figure 3.8: (a) 2D intensity slices in different noise cases: noise-free (infinite SNR), low noise (SNR = 22.66 dB) and high noise (SNR = 16.42 dB). (b-c) FSIM score for the reconstructed RI within the region delimited by the dashed box depending on regularization parameter, with low and high noise conditions respectively.

from relative error, root mean squared error (RMSE) or structural methods like FSIM, and no one is foolproof. Consequently, here we have considered several error metrics as well as comparison between RI slices and relevant profiles to better explain the discrepancies between phantom and reconstructed samples. Nevertheless, in the experiment, all these quality measurements would require an accurate reference model of the sample, for instance by characterizing it with scanning electron microscope, atomic force microscope or any other method with higher resolution limits than ODT. This point has been troublesome in ODT literature during years, as an appropriate phantom has not been available until the development of 3D microprinting technology. Rather recently, Ziemczonok et at. [104] have manufactured a phantom that mimics some structures of a cell by using the 3D microprinting system Professional GT (from Nanoscribe GmbH, that offers a lateral resolution of 200 nm and a axial resolution around 300 nm). In this way, the problem of testing limited-angle tomographic techniques (including those based on ODT) can be addressed.

As a summary, Wiener deconvolution is robust to a moderately-low amount of noise. If the noise severely degradates the image SNR, an excessive regularization parameter ($\approx 10^{-3}$ or above) would be needed, which strongly smooths high-frequency features of the sample and causes the sample RI underestimation. In this fashion, it is convenient to acquire low noise images (for instance, with enough exposure time in the camera or by frame averaging) to achieve a good performance of Wiener algorithm. Moreover, the choice of a variable regularization depending on the SNR of each spatial frequency also improves the

accuracy of reconstructed RI.

3.6.3 Object rotation to mitigate the MC effects: simulation with a known phantom

To avoid the effects of the MC frequencies, the object has to be properly rotated to allow the missing information to be transmitted by the optical system. By rotating the object, its spectral content also rotates and spectral regions suffering from the MC problem are shifted to other regions which may have a higher OTF transmittance (mainly a higher |POTF| value). In this way, portions of the frequency content of the object which are severely attenuated or blocked in the original orientation of the sample can be transmitted after rotation. For instance, if the MC frequencies are constrained to a certain portion of the spectrum, then it would be possible to rotate the object so that said MC spectrum portion shifts to another region allowing its transmission. Data assembling of the spectral components collected under different rotation angles is performed in Fourier space [71, 105]. We recall that, for implementing such a data fusion procedure, previously all the datasets must be aligned (registered) to reconstruct the object's RI as previously explained. Then, a Wiener deconvolution (with the same or different OTF) is applied to this intensity stack.

Here we study the benefits of the object rotation in PC-ODT and try to find out the minimal number of rotations required to significantly mitigate the MC effects. However, the minimal number of rotations depends on the frequency spectrum of the objects and the distribution of untransmitted object frequencies. An excessive number of rotations would lead to unnecessary data acquisition, whereas a scarce number of rotations would be unable to mitigate the MC artifacts. In simulation, the optimal number of rotations can be estimated by minimizing the relative error of the reconstruction with regard to the reference phantom. In this Section, the relative error has been computed by averaging the ratio of the pixel-wise difference between n_p and the reconstructed version thereof (n_s) to the reference phantom RI (n_p). However, in experimental conditions this error minimization is not possible (the object is not known *a-priori*), thereby a low number (i.e. 4-8) of rotations is chosen to avoid an excessive complexity of the data fusion procedure [71].

Let us perform a numerical simulation of the Siemens star phantom with homogeneous RI value of $n_p = 1.35$ immersed in a medium with $n_m = 1.33$ (see Fig. 3.9(a)) considered as a phase-only object. In this Section, the size of the intensity stack is 251^3 voxels. By using the conventional PC-ODT technique (without sample rotation) under BFI with $\mathrm{NA_c} = 0.95$ and $\mathrm{NA_o} = 1.4$, then one obtains the RI shown in Fig. 3.9(b1) with a relative error of 3.95 %. It is worth pointing out that the thick central pillar of the sample (see white dashed box in Fig. 3.9(b1)) suffers from a certain vanishing effect as it is mostly associated with missing frequencies contained in MC and LV regions. Note also the halos and artifacts in the background of the reconstruction, due to the missing spatial frequency content of the object. To overcome these problems, the sample has been rotated about y-axis (Ω), thus we have to combine the information collected by two different orientations of the sample (the one with $\Omega = 0$, corresponding to no rotation case, and another tilting value for Ω). In Figs. 3.9(b2-b4) with test which is the best Ω value that, together with no rotation

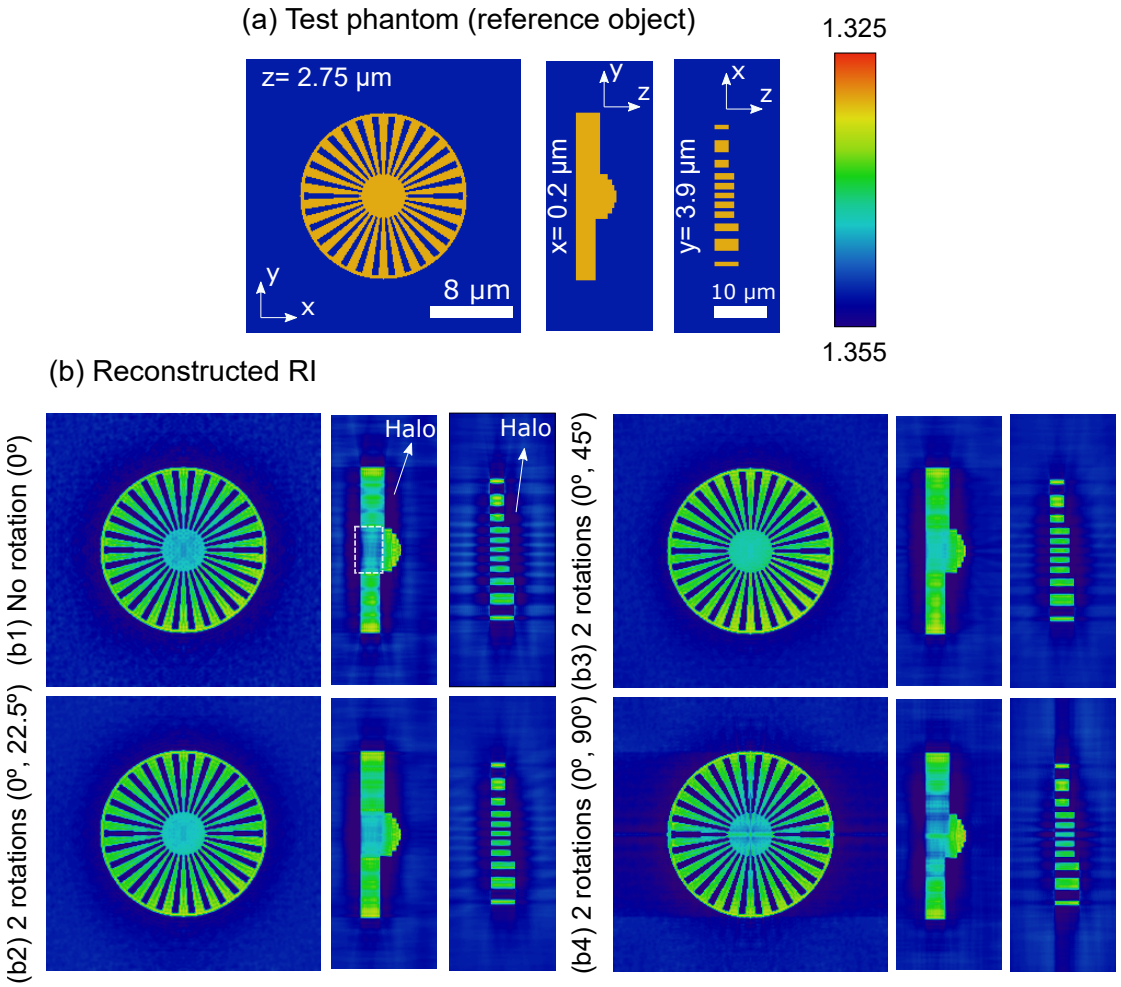

Figure 3.9: Simulation results for object rotation around y-axis (Ω). (a) Siemens star phantom with uniform RI ($n_p = 1.35$). (b) Reconstructed RI with no rotation (b1) and a pair of sample rotations with different tilting angles (b2-b4).

measurement, reaches the best quality in reconstruction. In particular, if only two rotations of this phantom are considered, the best values would be $\Omega = 0$ and $\Omega = 45^{\circ}$ (obtaining a relative error of 3.19 %) although this strongly depends on the frequency content of the sample. From these simulations we confirm that specimen rotation is able to effectively alleviate the MC that suffers single view scheme, even if the reconstruction suffers from a RI underestimation (around 1.345 against the real value of 1.35).

By combining a larger amount of object rotations it is possible a more accurate reconstruction closer to the phantom RI is achievable. With this purpose, the results of Siemens star RI reconstructions by considering multiple equispaced angular increments around y-axis, in the range $\Omega \in [0^{\circ}, 90^{\circ}]$, have been displayed in Fig. 3.10. The relative error measured for 4 and 8 rotations is 2.61 % and 2.32 %, correspondingly. It is worth remarking that, for multiple object rotations, the middle pillar that was barely resolved in the simulations from Fig. 3.9 has been better retrieved. In particular, for 8 rotations the reconstructed RI exhibits a high degree of uniformity and its value (average value around 1.347) is very

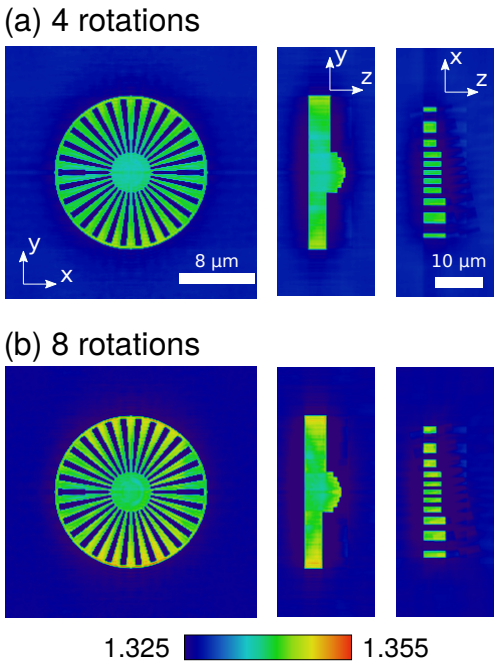

Figure 3.10: Simulation results for multiple object rotations (Ω between $0-90^{o}$ in equispaced angular increments around y-axis) and considering the same phantom as in Fig. 3.9. (a) With 4 object rotations. (b) With 8 object rotations.

close to the phantom RI value. In the latter case one even observes a mitigation of halo effects and other artifacts due to an incomplete collection of the object's spatial frequency information. The reason for this RI reconstruction improvement is that certain regions of the sample frequency content, which has been severely attenuated by the microscope OTF, now can be retrieved by merging the frequency support obtained with several rotations. In this way, the coverage of the object frequency support broadens, thereby obtaining a more reliable reconstruction. Nevertheless, sample rotation requires mechanical action of a stepper motor over the rotation stage or manipulation tools and could produce motion artifacts in subsequent spectrum assembling for different object orientations. To conclude, sample rotation in ODT (for instance, by using optical tweezers) seems a promising future research line as other approaches for surpassing MC limitations rely on iterative refinement of RI (e.g. imposing edge-preserving constraints [105]) or including *a-priori* knowledge of the sample.

3.7 Concluding remarks

Most of the ODT modalities reported in the literature [47, 53, 77] exploit spatially coherent laser illumination along with a illumination scanning process to reconstruct the RI of weak absorbing and scattering objects, from a set of interferometric measurements provided by especially designed holographic microscopes [52, 67, 106, 107]. However, C-ODT requires a long and complex data acquisition and processing of images which suffer from speckle-

noise as well as parasitic interference due to the coherent illumination.

Alternatively, in this Chapter we have provided the theoretical framework of PC-ODT which enables non-interferometric speckle noise-free imaging compatible with conventional wide-field microscopes [86, 89, 108] In PC-ODT the sample is simultaneously illuminated from different directions allowed by wide-field microscopes. Then, the 3D RI reconstruction is directly performed from a stack of through-focus intensity images by applying deconvolution with the effective OTF of the system (comprising both absorption and phase contributions) [60].

By comparing the coherent and partially coherent schemes for 3D RI recovery, we see that both of them provide the same frequency support. However, the PC-ODT method is simpler than C-ODT as it does not require intermediate recovery of complex-field amplitude and the complicated gathering procedure of the scattering potential spectrum. Indeed, PC-ODT applies a direct Wiener deconvolution to recover the RI distributions from intensity measurements. As a result, PC-ODT needs less data processing as well as less computation time than the C-ODT counterpart. This makes PC-ODT more suited for almost real-time quantitative 3D imaging. However, the PC-ODT scheme presented in Fig. 3.1 assumes a non absorbing sample or the proportionality between the real and imaginary parts of the RI. Otherwise, an additional stack of intensity distribution acquired for different illumination conditions ($a(|\mathbf{s})$ distribution) is required to obtain $n(\mathbf{r})$ [86]. On the other hand, the C-ODT method allows recovering the complex scattering potential, both phase and absorption contributions, from the same data set. It is also worth remarking that, unlike the CTF associated with C-ODT, the OTFs of PC-ODT are not uniform due to contrast attenuation exhibited by certain frequencies (LV region). However, a proper design of the illumination, different from the conventional BFI, may provide a higher uniformity to the OTF. This problem will be addressed in Chapter 5.

Further, we have performed several numerical simulations to study how the uncertainty in absorption estimation and the noise may impact on the object reconstruction. Indeed, according to the experimental simulations (see again Fig. 3.6.1) we find that an estimated low value of absorption (ε) is better than the pure phase hypothesis ($\varepsilon = 0$) provided that a weakly absorbing object is considered. For this reason, even if the correct ε value is not known (which is the typical case in practice), it is convenient to introduce a reasonable initial guess (i.e. ε in the range $10^{-4} - 10^{-2}$) to include information about the absorptive part of the RI retrieved by the AOTF. These conclusions have also been verified under noisy imaging conditions. When the SNR is very small, the Wiener deconvolution procedure is prone to artifacts and errors. Consequently, the choice of an appropriate value of the regularization parameter (β), with an SNR varying across different frequency regions, is a crucial task to be considered. Finally, we also analyzed how the object frequency content untransmitted by the OTF with $SC \to 1$ can be collected by means of object rotation. From our simulation results we conclude that a few (typically no more than 4-8 in the range $0 - 90^{\circ}$ about the traverse xy-plane) object rotations are enough to significantly mitigate the MC problem, as illustrated in Fig. 3.10

Chapter 4

EXPERIMENTAL IMPLEMENTATION OF PC-ODT

In this Chapter we describe experimental setups designed for PC-ODT implementation. Briefly, they comprise a wide-field transmission microscope attached to an optical refocusing module (ORM) and a detector (camera). The refocusing required for the through-focus intensity measurement in PC-ODT can be obtained in two different ways: mechanically or optically.

The mechanical refocusing consists of changing the distance between the stage of the sample and the objective lenses (for instance, with a motorized piezo-stage [72]), thereby providing a constant NA for all refocused intensity slices. Conversely, the ORM considered here for PC-ODT allows for axial scanning of the sample without moving it physically. In this way, the ORM enables a fast measuring of a through-focus intensity stack $I(\mathbf{r})$ without any mechanical axial movement of the microscope's sample stage. This method is inherently faster and more robust than the mechanical stage control of the commercial microscopes, so it has been applied throughout this thesis. Specifically, an electrically tunable lens (ETL) with variable focal length has been used for designing this optical refocusing module. However, the optical refocusing is responsible for a slight NA variation between different refocused intensity slices, which is not relevant for our PC-ODT implementation as explained in Appendix B.1.

Throughout this Chapter, the two main elements of the setup are introduced: the microscope and the ORM. Two different configurations of the ORM are discussed, depending on the size of the transverse field of view (FOV) to be scanned. The PC-ODT technique is experimentally demonstrated on different examples: diatom cells (biosilica shells), polystyrene micro-spheres and different cell samples. We demonstrate that the use of high NA of the objective and condenser lenses, together with the optical refocusing, are main issues for achieving fast and reliable 3D RI reconstruction of weak absorbing objects. The results confirm the straightforward 3D-RI reconstruction of the samples providing valuable quantitative information for their analysis.

4.1 Wide-field transmission microscope

The experimental setup comprises a wide-field microscope, which at least includes: a quasi-monochromatic incoherent illumination source (e.g. LED), a condenser lens, a sample placed onto a moving stage, an infinity-corrected objective lens (collecting the illumination scattered by the sample after passing through thereof) and a tube lens. In particular, the microscope comprises a fine adjustment knob and a coarse adjustment knob which ensure a precise focusing. Further, it is also convenient to have an aperture diaphragm to control the diameter of the illumination beam passing through the condenser lens, linked to the coherence ratio as formerly discussed in Chapter 3. The microscope uses Köhler illumination to evenly illuminate the desired field of view, with a uniform intensity [109]. Moreover, the microscope is equipped with high NA lenses (both the condenser and the objective) to guarantee high resolution in the RI reconstruction.

In this thesis, two different wide-field microscopes have been tested: a customized inverted microscope which has been built in the laboratory and a commercially available Nikon Eclipse Ti-U inverted microscope. The first one has been used during the development of the PC-ODT technique because it enables to adjust more parameters (i.e. illumination shaping, as later explained in Chapter 5). The second microscope has been applied to demonstrate that the PC-ODT can be easily adopted with a commercial wide-field microscope just by attaching the ORM to it.

4.2 Optical refocusing module (ORM)

The optical refocusing module, whose main element is the ETL, plays a crucial role in PC-ODT implementation. In this case, we use Optotune EL-10-30-C-VIS-LD ETL model, whose focal length can be changed within milliseconds by applying different electric currents. This varifocal lens includes a container coated with an elastic polymer membrane and filled with optical fluid. An electromagnetic actuator exerts pressure on the container, thus controlling the deflection of the lens membrane (changing the focal length). Moreover, it incorporates a driver (Lens Driver 4) with a digital signal generator, so the driving signal for the ETL can be conveniently tuned or even used as an external trigger source required for synchronization with the camera.

In this way, the user configures the current sent to the ETL actuator. The lens shape depends on gravity due to elastic membrane of the fluid container. Consequently, in order to minimize coma aberration the manufacturer recommends to mount the lens with the optical axis along vertical direction (hence, the ETL placed lying horizontally). It is also advisable to stabilize the temperature to avoid heating up effects of the ETL, such as the expansion of the fluid or the variation of its RI (see [110] for more details). This type of ETL has been succesfully applied in different imaging techniques such as confocal microscopy [111] or light-sheet microscopy [112]. Here, we benefit from the ETL to obtain a stack of refocused intensity images corresponding to an optically scanned 3D volume of the sample, which in turn is used as an input data $I(\mathbf{r})$ for the PC-ODT. Two different configurations of the ORM are discussed below.

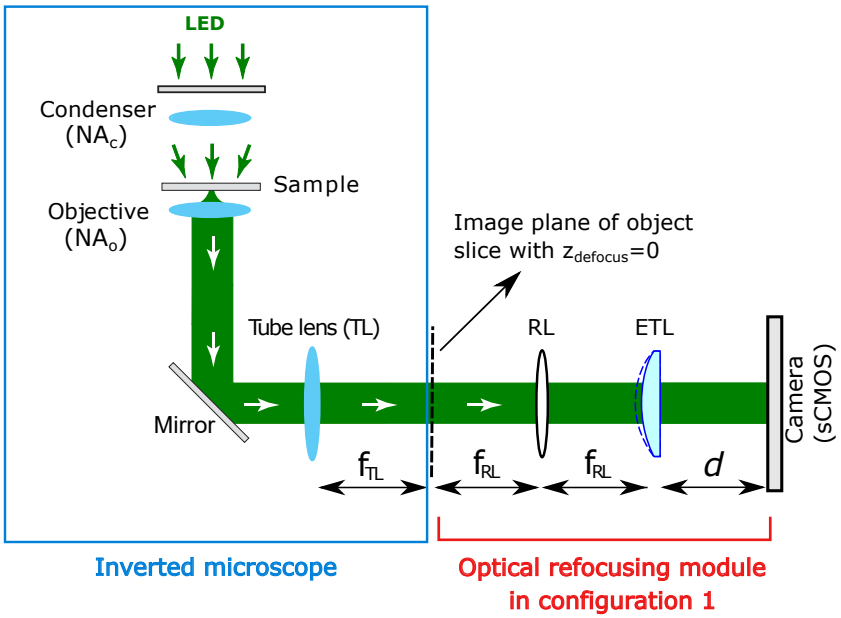

Figure 4.1: Sketch of the experimental setup for the measurement of the stack of intensity images $I(\mathbf{r})$. The sample is imaged by the objective lens and the tube lens. The obtained 3D image is then axially scanned by using the optical refocusing module in configuration 1 comprising the relay lens (RL) with fixed focal length and the ETL lens with a varying focal length.

4.2.1 ORM in configuration 1

A first experimental configuration of the ORM suitable for PC-ODT is displayed in Fig. 4.1. The ORM is sketched along with a wide-field microscope comprising an Abbe condenser lens (with numerical aperture $\mathrm{NA_c}$) providing the uniform sample illumination with light supplied by a quasi-monochromatic LED source, and the sample imaging is obtained by using a high NA objective lens (characterized by a magnification M_{obj}, and a numerical aperture of $\mathrm{NA_o}$). As the objective lens is infinity-corrected (its image distance is set to infinity), then a tube lens (TL, with a focal length $\mathrm{f_{TL}}$) has been placed to provide the 3D intensity image of the sample. The camera sensor records a 2D image (intensity distribution) corresponding to the *xy*-object slice located in the microscope's focal plane (defocus distance $z_{defocus} = 0\,\mu$m). The position of this focused plane can be optically shifted by using the ETL, therefore yielding the axial z-scanning of the sample. Indeed, the optical refocusing (axial z-scanning) can be performed almost in real time by using the telescopic configuration provided by the relay lens (RL) along with the high-speed ETL located in the Fourier conjugated plane respect to the intermediate image (central slice, $z_{defocus} = 0\,\mu$m) (see Fig. 4.1). Finally, $I(\mathbf{r})$ is acquired by a sCMOS camera and stored in a computer for its processing.

The shift of the imaged plane ($z_{defocus}$) depends on the magnification M of the considered microscope, as well as the relay lenses projecting the image onto the camera detector. Specifically, as it follows from the ABCD-matrix analysis of the optical system (see Appendix B.2), the shift distance is given by [59, 113]

$$z_{defocus} = \frac{n_m \mathrm{f}_{\mathrm{RL}}^2}{M^2}\left(\frac{1}{d} - \mathrm{P}_{\mathrm{ETL}}\right), \tag{4.1}$$

where n_m is the refractive index of the surrounding medium of the sample (e.g. water), f_{RL} corresponds to the focal length of the RL, $\mathrm{P}_{\mathrm{ETL}} = 1/\mathrm{f}_{\mathrm{ETL}}$ is the optical power of the ETL, and d stands for the distance between the ETL and the detector. When a current is applied to the ETL, its focal length ($\mathrm{f}_{\mathrm{ETL}}$) changes and the sample is scanned with regard to the focal plane of the objective. Note that the $z_{defocus}$ and the optical power of the ETL ($\mathrm{P}_{\mathrm{ETL}} = 1/\mathrm{f}_{\mathrm{ETL}}$) are linearly proportional to one another. The maximum scanned interval depends on the $\mathrm{P}_{\mathrm{ETL}}$ variation range, $\mathrm{P}_{\mathrm{ETL}} \in [\mathrm{P}_{\mathrm{ETL}}^{\mathrm{min}}, \mathrm{P}_{\mathrm{ETL}}^{\mathrm{max}}]$, as

$$z_{scan} = \frac{n_m \mathrm{f}_{\mathrm{RL}}^2}{M^2}\left(\mathrm{P}_{\mathrm{ETL}}^{\mathrm{max}} - \mathrm{P}_{\mathrm{ETL}}^{\mathrm{min}}\right). \tag{4.2}$$

In the ORM in configuration 1, the ETL device is used, with $\mathrm{f}_{\mathrm{ETL}} \in [100, 200]$ mm corresponding to a range of $\mathrm{P}_{\mathrm{ETL}} \in [+5, +10]$ dpt. Note that the magnification of the microscope is $M = M_{obj}$ when the focal length f_{TL} of the tube lens coincides with the one recommended by the manufacturer of the objective lens. For example, a tube lens focal length of $\mathrm{f}_{\mathrm{Olympus}}$=180 mm corresponds to the case of an Olympus objective lens. In our case we have used a Olympus objective with $M_{obj} = 100\times$ and the tube lens with focal length f_{TL}=150 mm, then $M = M_{obj} \times (\mathrm{f}_{\mathrm{TL}}/\mathrm{f}_{\mathrm{Olympus}}) = 83\times$. Note that the magnification of the whole setup is $M_s = M \times (-d/\mathrm{f}_{\mathrm{RL}})$, see Appendix B.2. Thus, the transverse FOV (with magnification M_s) of the image acquired by the camera can be adjusted by changing either M, d or f_{RL}. We underline that this ORM configuration contains a minimum number of lenses and can change the transverse magnification of the entire system if needed.

The magnification M_s can be adjusted so as to capture an image of the whole object according to the camera FOV available. A modification in M_s can be easily achieved by modifying d, but it has an impact on the offset shift of $z_{defocus}$, according to Eq. 4.1 this may lead to the reduction of the NA of this ORM module that might suffer from aberration. To address this problem, a second relay lens can be arranged in the ORM for enabling the adjustment of M_s independently of $z_{defocus}$, as explained in the next Section.

4.2.2 ORM in configuration 2

The second experimental configuration is summarized in Fig. 4.2. The main modification with regard to the ORM configuration 1 consists of inserting a second relay lens (RL2) in the setup, thus the ETL is now placed between both relay lenses in the focal plane of RL1. In the ORM in configuration 2, the EL-10-30-C-VIS-LD-MV ETL device is used, with $\mathrm{f}_{\mathrm{ETL}} \in [-667, +286]$ mm corresponding to a range of $\mathrm{P}_{\mathrm{ETL}} \in [-1.5, +3.5]$ dpt. In this case, as it follows from the ABCD-matrix analysis of the optical system (see Appendix B.3), the shift along the optical axis in the object space is given by

$$z_{defocus} = \frac{-n_m \mathrm{f}_{\mathrm{RL1}}^2 \mathrm{P}_{\mathrm{ETL}}}{M^2}, \tag{4.3}$$

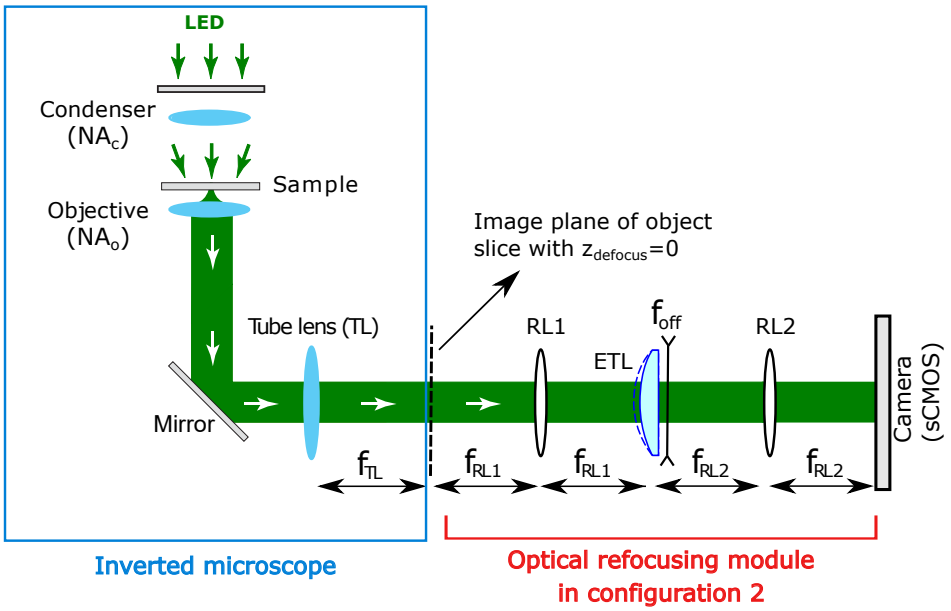

Figure 4.2: Experimental setup for PC-ODT with the optical refocusing module in configuration 2, including an ETL with an integrated divergent offset lens and a additional relay lens (RL2) to create a 4f imaging configuration between the tube lens and the camera.

and does not depend on the distance between the ETL and sCMOS detector of the camera. Again, the $z_{defocus}$ and the effective optical power of the ETL ($\mathrm{P_{ETL}}$) are linearly proportional to one another and

$$z_{scan} = \frac{n_m \mathrm{f_{RL1}^2}}{M^2}\left(\mathrm{P_{ETL}^{max}} - \mathrm{P_{ETL}^{min}}\right). \tag{4.4}$$

From the ABCD-matrix analysis, it is also obtained the global magnification of the system as $M_s = M \times (-\mathrm{f_{RL2}}/\mathrm{f_{RL1}})$. Unlike the system with the ORM in configuration 1, in this case it is possible to adjust M_s without changing a target $z_{defocus}$ value just by modifying $\mathrm{f_{RL2}}$. Another difference with the ORM configuration 1 is that the ETL comprises an integrated divergent offset lens so that the overall focal tuning range goes from negative to positive values, making this a more proper choice for combinations with infinity corrected fixed-focus relay lenses (as the considered ones) often required in microscopy imaging setups.

4.3 ETL and camera configuration settings for synchronized image acquisition

The measurement of the stack $I(\mathbf{r})$ of through-focus intensity images, needed in PC-ODT to reconstruct the 3D object's RI, is performed by using a sCMOS camera synchronized with an optical refocusing module comprising a high-speed focus-tunable lens. In this case, the tunable lens (ETL) has been configured to perform a repetitive bidirectional z-scanning by setting a periodic triangular electrical signal in the lens microcontroller (see [110]) while

the sCMOS camera continuously acquires the images during the entire optical scanning process. Let us underline that the measurement process is fully automatic because the ETL triggers the camera acquisition (the first rising edge of the triangular signal serves as an external start trigger for the camera) enabling their synchronization. The light scattered by the sample is collected by the microscope's lenses and then it is redirected to the ORM, which provides the required axial scanning by changing the optical power of the ETL according to the applied electrical current (I_{ETL}).

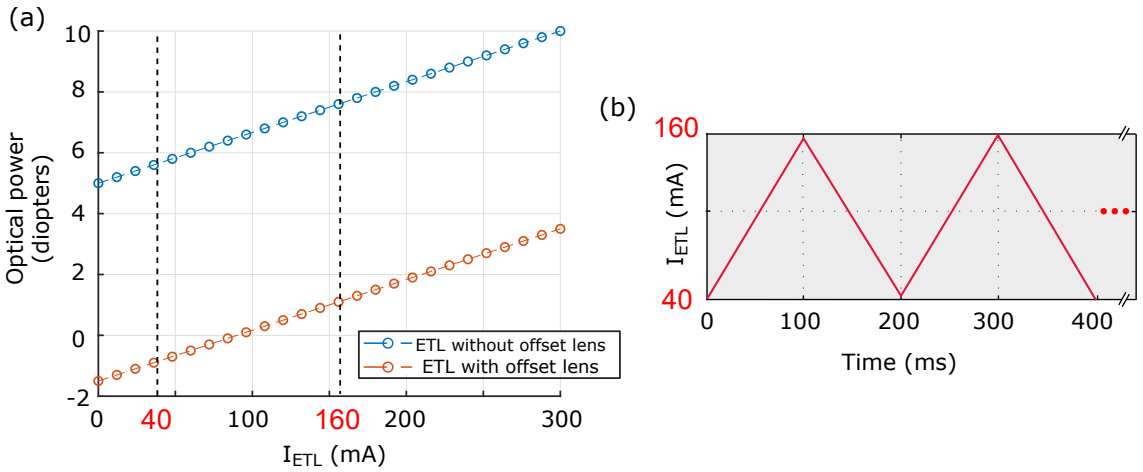

Figure 4.3: (a) Optical power variation of the ETL in both ORM configurations. (b) Periodic electrical signal addressed into the ETL required for optical axial scan with the ORM.

The optical power of the ETL linearly increases with I_{ETL}, as displayed in Fig. 4.3 (a) in both ORM configurations. However, the optical power at zero current exhibits a negative value (-1.5 diopters) in the ETL device equipped with the offset lens (as in ORM configuration 2), whereas for the ETL device without offset lens (as in ORM in configuration 1) the starting point at zero current is +4.8 diopters. In this way, by using the ORM in configuration 2 it is possible to obtain a symmetric scanning around the plane $z_{defocus} = 0$ by setting a proper current range, for example $I_{ETL} \in [0-180]$ mA, which leads to an optical power variation in the range of $P_{ETL} \in$[-1.5, +1.5] diopters (see Fig. 4.3).

When the ORM in configuration 1 is applied, the amplitude of the triangular current signal I_{ETL} is configured between 40-160 mA, as illustrated in Fig. 4.3 (b) in order to obtain a $P_{ETL} \in$[+5.67, +7.67] diopters. This intermediate current range has been selected for the ETL device without offset lens to prevent from an excessive deflection of the ETL membrane. For instance, the frequency of the current signal applied to the ETL (ν_{ETL}) is 5 Hz in order to scan 50 *xy*-slices in 100 ms (camera with an exposure time of 2 ms).

As a rule of thumb, the ETL and the camera must be synchronised fullfiling the following relationship,

$$\frac{\nu_{\text{cam}}}{\nu_{\text{ETL}}} = 2N_z = 2\frac{z_{scan}}{\Delta z_{defocus}}, \tag{4.5}$$

where ν_{ETL} is the frequency of the signal I_{ETL} and ν_{cam} is the acquisition frequency (i.e. frame-rate) of the camera, N_z is the number of *xy*-slices of $I(\mathbf{r})$, z_{scan} is the portion of the

sample thickness which is scanned (scanning interval) and $\Delta z_{defocus}$ is the distance along the optical axis (z) between two consecutive *xy*-slices of $I(\mathbf{r})$. By satisfying Eq. 4.5, the sample scanning along the sample thickness is performed in small enough steps $\Delta z_{defocus} = (2z_{scan}v_{\mathrm{ETL}})/v_{\mathrm{cam}}$. Moreover, in order to take full advantage of microscope frequency support, the axial sampling has to satisfy Nyquist criteria $\Delta z_{defocus} \leq \Delta z$, where $\Delta z = \lambda_0 / \left[2(n_{imm} - (n_{imm}^2 - \mathrm{NA_o^2})^{1/2})\right]$. Let us recall that a higher acquisition frame rate (v_{cam}) is possible just by reducing the size of the transverse FOV of the image or by decreasing the exposure time (t_{exp}), while keeping a reasonably good image SNR.

4.4 Implemented experimental setups

Here, we describe in detail the two implemented experimental setups. In both setups, the white LED source (SugarCUBE Ultra) can be filtered in order to choose the central illumination wavelengths (typical values are $\lambda_0 = 450, 560, 630\,\mathrm{nm}$) depending on the particular sample to be imaged. Furthermore, a sCMOS camera (Hamamatsu, Orca Flash 4.0, 16-bit gray-level, pixel size of $a = 6.5\ \mu\mathrm{m}$) is chosen, due to its high readout speed and resolution. Indeed, this camera is able to acquire 16-bit images of 500×500 pixels at a rate of 500 fps with an exposure time of $t_{exp} = 2$ ms. However, this frame rate decreases if the entire FOV of the camera (2048×2048 pixels) is considered, up to 30 fps. For the sake of a faster acquisition, we limit the camera FOV to no more than 500×500 pixels. Another reason for using a reduced camera FOV is that, even if we acquire the full FOV provided by the camera, then it must be trimmed off to fit within the numerical FOV. Indeed, this latter refers to the size of the intensity stack (in pixels) which can be processed by the computer for RI distribution recovery in a reasonable period of time. In this work, we have used an Intel Xeon E5-1620v3 CPU equipped with a 8 GB DDR4-RAM, so the numerical FOV does not exceed a maximum of $500 \times 500 \times 100$ pixels in order to obtain the 3D RI reconstruction in a few seconds. For this reason, it is very convenient to design an ORM allowing the setting of the magnification (M_s) of the system in order to fit the imaged sample within the numerical FOV with minimal setup reconfiguration.

4.4.1 Setup with the ORM in configuration 1

In this setup, the microscope comprises high NA lenses: a condenser with $\mathrm{NA_c} = 0.95$ (Nikon) and an objective with $\mathrm{NA_o} = 1.4$ (Olympus UPLSAPO, $M_{obj} = 100\times$ with oil immersion Olympus Type F, $n_{imm} = 1.518$). With this microscope configuration, the high NA of both lenses and low degree of light spatial coherence ($SC = \mathrm{NA_c}/\mathrm{NA_o} \sim 0.7$) provide a large spatial spatial frequency transmittance required for 3D imaging as well as reasonably good trade-off between transverse $\Delta x = \Delta y = \lambda_0 / [2(\mathrm{NA_o} + \mathrm{NA_c})] \approx 100$ nm and axial $\Delta z = \lambda_0 / \left[2(n_{imm} - (n_{imm}^2 - \mathrm{NA_o^2})^{1/2})\right] \approx 240$ nm spatial resolution limits (with $\lambda_0 = 450\,\mathrm{nm}$). We recall that the transverse (Δx, Δy) and axial (Δz) Nyquist distances [79] are often used for the estimation of the spatial resolution limits of ODT (see [51]).

With regard to the ORM, the relay lens focal length is $\mathrm{f_{RL}} = 150$ mm and the distance between the ETL and sCMOS detector of the camera is $d = 116$ mm. Note that the objective

manufacturer (Olympus) specifications recommends to use a tube lens with a focal length of $f_{Olympus} = 180\,mm$. Otherwise, a factor $f_{TL}/f_{Olympus}$ needs to be introduced to calculate the image magnification in the intermediate image plane, $M = M_{obj} \times \left(f_{TL}/f_{Olympus}\right)$, taking into account the mismatch in the tube lens in comparison with Olympus specifications. Depending on the magnification required to better match the size of the considered sample within the numerical FOV, in this thesis we use $f_{TL} = 150\,mm$ (thus obtaining $M_s = 64$) or $f_{TL} = 180\,mm$ (thus obtaining $M_s = 83$) for the distance $d = 116\,mm$.

4.4.2 Setup with the ORM in configuration 2

In this setup we use a conventional Nikon Eclipse Ti-U inverted microscope equipped with a quasi-monochromatic LED illumination source filtered with a bandpass filter (depending on the desired working wavelength), a dry condenser lens (CSC2001, Thorlabs, NA_c=0.78), an immersion objective ($M_{obj} = 60\times$, NA_o=1.45, Nikon Plan-Apo with immersion oil n_{imm}=1.515) and a matching tube lens according to the specifications of the objective manufacturer (Nikon designs its microscopes with $f_{TL} = 200\,mm$). The ORM in configuration 2 is used with this microscope where infinity corrected relay lenses with $f_{RL1} = f_{RL2} = 150\,mm$ have been used. The system magnification is $M_s = M_{obj} = 60$. With this microscope configuration, we obtain a low degree of light spatial coherence ($SC = NA_c/NA_o \sim 0.54$) which in turn provides a large spatial frequency transmittance along with a reasonably good trade-off between transverse $\Delta x = \Delta y = \lambda_0/\left[2(NA_o + NA_c)\right] \approx 100$ nm and axial $\Delta z = \lambda_0/\left[2(n_{imm} - (n_{imm}^2 - NA_o^2)^{1/2})\right] \approx 210$ nm spatial resolution limits (with $\lambda_0 = 450\,nm$).

4.4.3 Design criteria for both ORM configurations

In this Section we discuss a proper choice of the lenses from both aforementioned ORM configurations. Let us consider an experimental setup with the ORM, in which the focal length of the relay lens must satisfy the following condition in order to avoid resolution loss when it comes to image a sample [112],

$$f_{RL} \leq f_{TL}\frac{c_{ETL}}{c_{OL}}, \tag{4.6}$$

where $c_{ETL} = 10\,mm$ and $c_{OL} = 6\,mm$ are the full diameter of clear apertures of the ETL and the objective lens (OL), correspondingly [110, 114]. With these values, and if we use a tube lens with $f_{TL} = 180\,mm$, then the maximum value of relay lens focal length would be f_{RL}=300 mm. Indeed, we apply $f_{RL} = 150\,mm$. We remark that, according to Eq.4.6, the spectrum of the image from the back focal plane of the objective lens is projected over the ETL with a scaling factor of f_{RL}/f_{TL}, which in this case is $0.83\times$. For this reason, it is relevant to choose an ETL aperture value (c_{ETL}) large enough to accomodate the spatial frequency support of the sample. Note that if one uses a f_{RL} larger than the maximum value (f_{RL}=300 mm) allowed by the Eq. 4.6, this would be equivalent to a zoom larger than the objective lens magnification, but at the expense of degrading the spatial resolution.

4.5 Experimental test of the PC-ODT

To test the feasibility of the PC-ODT technique, here we consider the setup with the ORM in configuration 1 displayed in Fig. 4.1, with $M_s = 64$ and a LED source (SugarCUBE Ultra) characterized by a central wavelength is $\lambda_0 = 450$ nm and a FWHM of 20 nm. In this way an ample field of view ($52 \times 52 \times 15\,\mu\text{m}^3$). Particularly, a data set $I(\mathbf{r})$ comprising $N_z = 130$ images of 512×512 pixels has been registered in 1.3 s with a camera exposure time of 10 ms. In order to make faster the reconstruction process, a region of interest of $373 \times 373 \times 64$ pixels in the stack $I(\mathbf{r})$ has been processed. The ETL focal length range used in the experiments discussed in this Section corresponds to a $z-$scanning interval of $\sim 15\,\mu$m with an axial step of $\Delta z_{defocus} = 250$ nm in the sample domain. Then, the deconvolution algorithm has been applied with a regularization parameter $\beta = 5 \times 10^{-4}$ according to the estimated average SNR. The MTF of the system was experimentally measured, as detailed in Appendix C.

Our first test comprises diatom samples, which are micro-organisms with transparent cell walls (known as frustule) made of silicon dioxide hydrated with a small amount of water. Such a biosilica frustule, which has a real RI value $n_{\text{Re}} \sim 1.46$ [115], typically consists of two halves called valves containing patterns of pores that allow nutrient and waste exchange with the environment since silica structure is impervious. The frusture pores may vary in the range of $0.1 - 1\,\mu$m, so they have a proper size and geometrical arrangement for testing the PC-ODT. Since this technique has been designed for the weak object approximation, the diatoms need to be immersed in a matching medium with a similar RI to fulfill this condition. Note that PC-ODT can not be applied for diatoms immersed in water ($n_{\text{H}_2\text{O}} \sim 1.33$) due to the high RI contrast ($\Delta n \sim 0.12$) beyond the applied Born approximation. For this reason, the diatoms have been cleaned with hydrogen peroxide (H_2O_2) to remove the highly absorbing algae they harbor inside preserving only the biosilica frustule. In our case, the diatoms have been immersed in oil ($n_m = 1.518$) in order to achieve an appropriate RI contrast: $\Delta n \approx -0.05$. In this case $n_{\text{Re}} < n_m$, but in the examples studied later a contrast $\Delta n > 0$ is considered for the completeness of the technique demonstration.

The correct application of the proposed PC-ODT technique requires high NA_c and NA_o along with high *SC* (corresponding to a low degree of spatial coherence) at the same time. Let us first illustrate this important fact by comparing the results obtained by using the same experimental setup with $\text{NA}_\text{o} = 1.4$ but different coherence states: $SC = 0.34$ ($\text{NA}_\text{c} = 0.48$) and $SC = 0.68$ ($\text{NA}_\text{c} = 0.95$). The measured stack of intensity images along with the reconstructed RI stack are available for each case in Visualization 1 ($SC = 0.34$) and Visualization 2 ($SC = 0.68$) from Ref. [89] (see supplementary material in published work). The Figs. 4.4 (a-d) display representative intensity images and RI slices extracted from such stacks, where a *Cocconeis placentula* diatom [116] is observed along with another rod-like diatom. In Figs. 4.4 (a) and 4.4 (b) the images present severe cross-talk between different layers of the diatoms due to the high spatial coherence achieved for $SC = 0.34$. In contrast, for $SC = 0.68$ the cross-talk effects are suppressed and the diatoms result well distinguished including their characteristic structural features such as the pores observed in the reconstructed RI slices of Fig. 4.4 (d). For example, the detection of a small piece of another diatom wall (labeled as region R1) attached to *Cocconeis placentula* is much better observed for $SC = 0.68$, see Fig. 4.4 (d).

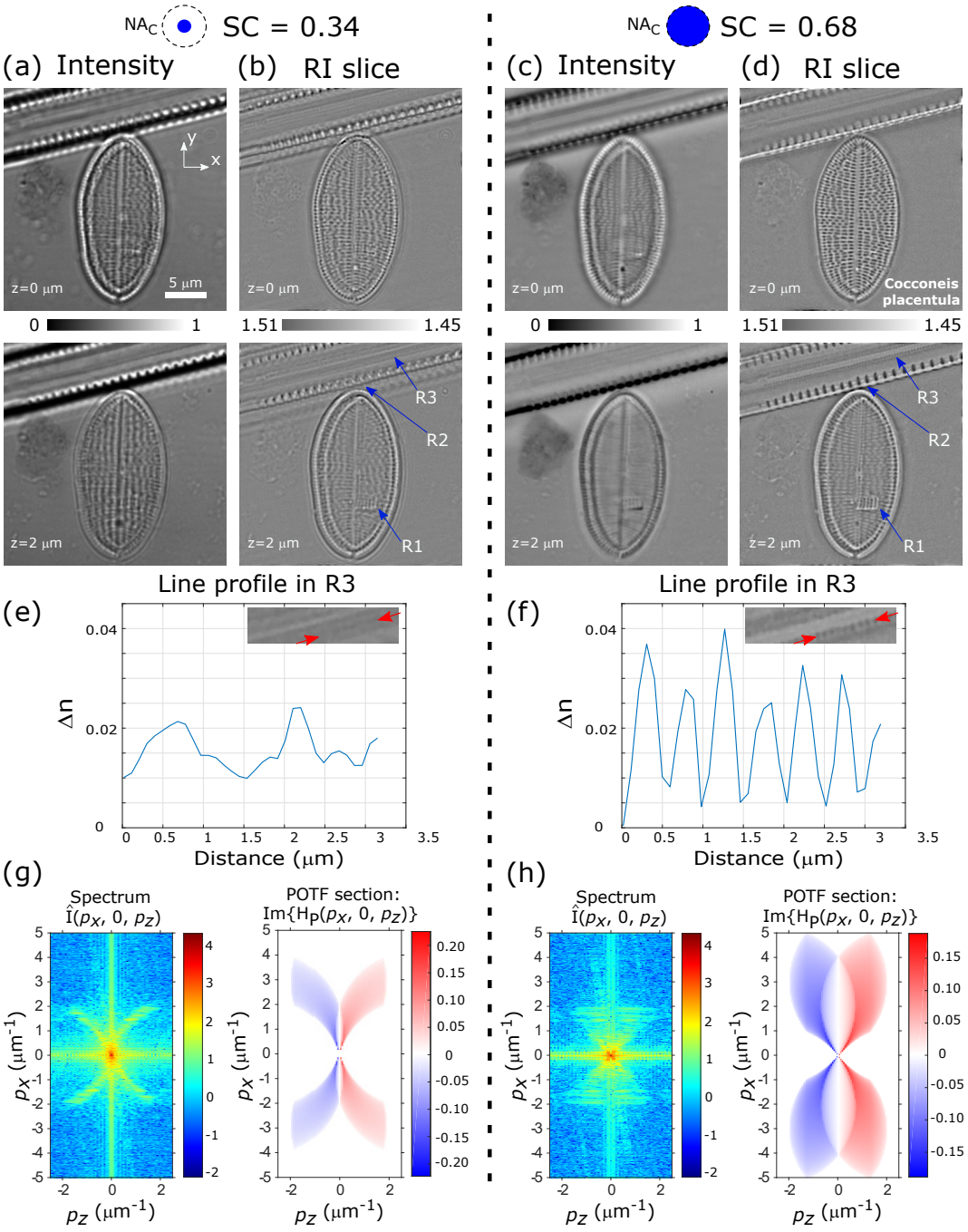

Figure 4.4: Bright-field intensity images (slices extracted from the measured intensity stack $I(\mathbf{r})$) and the corresponding reconstruction of the refractive index (RI) for a *Cocconeis placentula* diatom obtained under two different illumination conditions: $SC = 0.34$ for (a, b) and $SC = 0.68$ for (c, d). The intensity and RI distributions (xy-slices) are displayed for two axial positions z in the first and second row. (e) and (f) display a RI profile along region R3 for $SC = 0.34$ and $SC = 0.68$, correspondingly. (g) and (h) show a 2D section of the object intensity spectrum $\widehat{I}(p_x, 0, p_z)$ together with the POTF section $\mathrm{Im}\{H_P(p_x, 0, p_z)\}$ corresponding to the case $SC = 0.34$ and $SC = 0.68$.

The low spatial coherence also permits well-resolved imaging of other structures such as the rectangular-shaped pores (size of $\sim 300-400$ nm long and ~ 450 nm wide) decorating the frustule of the *Cocconeis placentula,* see Fig. 4.4 (d) at $z = 0$, that almost disappear at $z = 2\,\mu$m where relevant diatom structures such as its dorsal margins and raphe are observed. Moreover, for $SC = 0.34$ the images of both diatoms result overlapped while for $SC = 0.68$ they are correctly separated, see region R2 indicated in Figs. 4.4 (b) and 4.4 (d). From the reconstructed RI distribution it is also possible characterizing tiny diatom structures [see region R3 in Figs. 4.4 (b) and 4.4 (d)] that are hidden in the intensity images and non-resolvable for small values of *SC*. Indeed, by comparing the RI line profile of the region R3 displayed in Figs. 4.4 (e) and 4.4 (f) one realizes that the smallest resolved pores (holes of 250 nm) can only be successfully detected for high *SC* values. Let us highlight that such periodic arrangement of nano-scale pores is imaged in a single $xy-$plane of the RI stack, thus illustrating the better optical sectioning of the system achieved with low spatially coherent illumination, linked with the more extended object frequency content coverage reached by $SC = 0.68$. These results underline the important role played by the low spatial coherence in the imaging process and the RI reconstruction, as the illumination with $SC \rightarrow 1$ enables the collection of more 3D spatial frequency content of the sample.

Let us inspect the 3D intensity spectra and the POTF corresponding to both coherence states, see the Figs. 4.4 (g) and 4.4 (h) where a slice of the spectra $\hat{I}(p_x, 0, p_z)$ and the imaginary part of the POTF $\mathrm{Im}\{H_P(p_x, 0, p_z)\}$ are displayed. Note that the intensity spectra seem to have an axial and transverse spatial frequency cut-off of $2\,\mu\mathrm{m}^{-1}$. The axial frequency limit coincides with the frequency cut-off $p_z^{\mathrm{cut}} = \left[(n_{oil} - (n_{oil}^2 - \mathrm{NA_o^2})^{1/2})\right]/\lambda_0$ determined by the objective lens. However, the transverse frequency limit observed in the spectra is significantly lower than the corresponding cut-off frequency of the optical system ($p_x^{\mathrm{cut}} = (\mathrm{NA_o} + \mathrm{NA_c})/\lambda_0 = 5\,\mu\mathrm{m}^{-1}$). Finally, we must take into account that the intensity measurement is also filtered by the camera (with a representing its pixel size). Note that the frequency cut-off of the camera in the sample plane is given by $p^{\mathrm{cam}} = M_s/(2a) \approx 4.9\,\mu\mathrm{m}^{-1}$. In this way, the spectral content beyond p^{cam} is likely to be noise contribution, which is used to compute the SNR as previously explained in Chapter 3 (Section 3.3).

It is well-known from scanning electron microscope images of diatoms that they are typically decorated with structures [116] in the scale of $0.1 - 1\,\mu$m (in Fig. 4.4 (d) the pores of about $0.25 - 0.8\,\mu$m are distinguished) as well as with nano-scale structures $5 - 10$ nm beyond the optical resolution limit. Thus, the observed spatial frequency limits are in good agreement with the expected ones for diatoms. Note that for a low value of *SC* the intensity spectrum has the shape of two thin semicircular arcs that fit in with the form of the corresponding POTF, see left panel of Fig. 4.4 (g). Only the frequency content that lies within non-zero POTF region is transmitted by the bright-field microscope. In the case of low spatial coherence [$SC = 0.68$, see Fig. 4.4 (h)] there is a significantly improved lateral resolution limit $p_x^{\mathrm{cut}} = 5\,\mu\mathrm{m}^{-1}$ compared with $p_x^{\mathrm{cut}} = 3.9\,\mu\mathrm{m}^{-1}$ reached for $SC = 0.34$. Moreover, the axial cone of missing frequencies in the POTF is significantly smaller for $SC = 0.68$. We recall that the well-known missing cone effect (see for example [67]) is responsible for an artificial object elongation along the optical axis and for the artifacts in the image and RI values deviating from the expected values. Note that the cross-talk effects

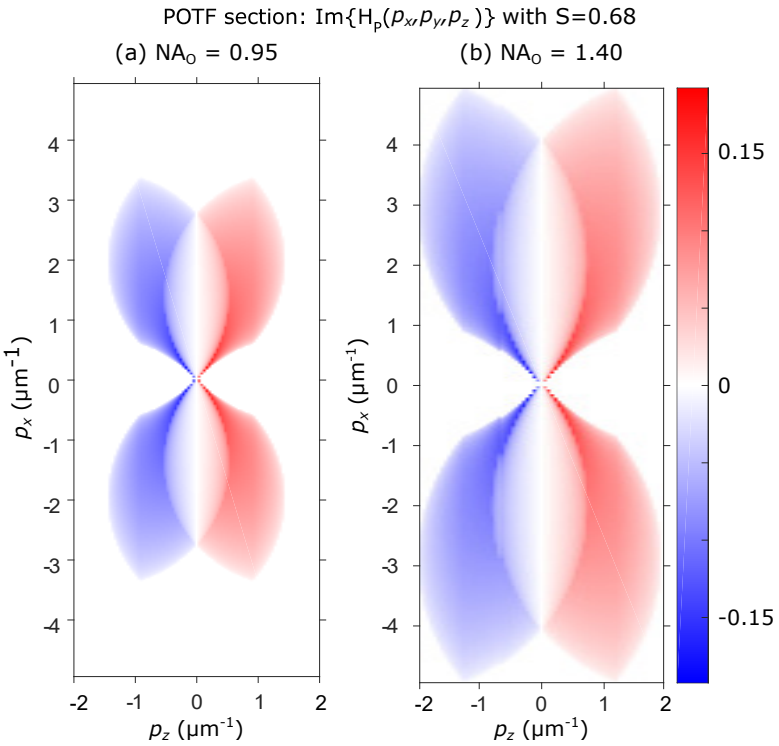

Figure 4.5: Comparison between 2D xz-slices of the 3D nonparaxial POTF obtained in bright-field illumination for the same coherence ratio ($SC = 0.68$) but different $\mathrm{NA_c}$and $\mathrm{NA_o}$.

are more severe for higher spatial coherence and for larger object size, thus underlying the need of using a low spatially coherent illumination ($SC \to 1$) to obtain more reliable RI information. As observed in the POTF sections displayed in Figs. 4.4 (g, h), $\mathrm{Im}\{H_P\}$ is a function that has opposite sign for positive and negative frequencies in the axial direction p_z.

From the previous analysis it follows that a high SC ratio is needed for obtaining a large frequency support in the POTF. Nevertheless, it is also required that the NAs are as large as possible. To give an example, Fig.4.5 compares the POTF in bright-field with the same coherence ratio ($SC = 0.68$) but different objective and condenser apertures: Fig. 4.5 (a) accounts for $\mathrm{NA_c} = 0.65$ and $\mathrm{NA_o} = 0.95$ whereas Fig. 4.5 (b) represents the case with $\mathrm{NA_c} = 0.95$ and $\mathrm{NA_o} = 1.4$. It is noticeable that a larger system NA aperture ($\mathrm{NA_c} + \mathrm{NA_o}$) enables a broader frequency content, therefore a better sample reconstruction would be obtained. Nevertheless, the fact of working with dry condenser is preferable to enable simpler sample manipulation and a larger field depth. Consequently, the use of moderate-high SC ratio (around $0.5 - 0.8$) allows a trade-off between resolution, optical sectioning and simplicity in the experimental setup. If higher SC are demanded, an immersion condenser would be necessary.

For the remainder of the examples, $SC = 0.68$, $\mathrm{NA_c} = 0.95$ and $\mathrm{NA_o} = 1.4$ are considered. To further test the performance of the proposed PC-ODT technique, we have also considered a sample comprising polystyrene spheres (bead diameter of 3.73 μm, $n_{\mathrm{Re}} = 1.6$

at $\lambda_0 = 450$ nm, Spherotech Lot. AD01) immersed in oil ($n_m = 1.56$, Cargille Labs Series A) as a surrounding medium. Fig. 4.6 displays transverse and axial slices of the measured intensity and reconstructed RI distributions.The RI value of the polystyrene bead has been properly determined ($n_{\mathrm{Re}} = 1.59 \pm 0.01$) as well as the reconstructed shape of the sphere in the middle plane. Particularly, the measured diameter of the sphere $3.8 \pm 0.1\,\mu$m is close to the expected value of $3.7\,\mu$m. However, the reconstructed bead suffers from some elongation along the axial direction due to the missing-cone issue which is associated with a lack of low axial frequencies transmitted by the microscope [67,86,117]. This well-known axial distortion (longitudinal stretching) effect is also present in C-ODT as well as in other quantitative imaging techniques, see for example [67,86] where dielectric spheres of similar size have been studied. The halo observed around the sphere is also attributed to this problem. Such missing-cone issue is more severe for higher spatial coherence. We recall that this MC problem can be mitigated by object rotation or partially mitigated by using iterative post-processing algorithms, based on a prior knowledge of the sample properties [67].

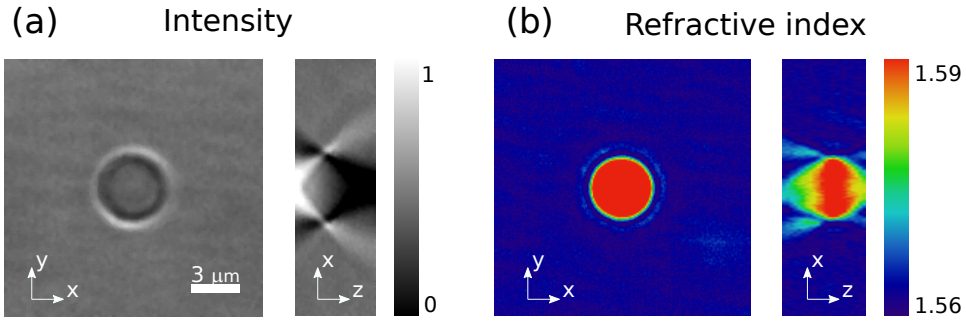

Figure 4.6: (a) $xy-$slice of the bright-field intensity for a polystyrene sphere (bead diameter of $3.8 \pm 0.1\,\mu$m, $n_{\mathrm{Re}} = 1.59 \pm 0.01$, Spherotech Lot. AD01) immersed in oil ($n_m = 1.56$, Cargille Labs Series A). (b) Reconstructed refractive index for the same $xy-$slice.

Another example of the PC-ODT technique that has been included in Fig. 4.7 displays the RI rendered as a 3D volume corresponding to two different diatoms: *Cymbella subturgidula* [Fig. 4.7 (a)] and *Diploneis elliptica* [Fig. 4.7 (b)] specimens. The *Cymbella subturgidula* diatom has dorsi-ventral valves and exhibits bluntly rounded and barely protracted apices. Moreover, the dorsal margin of this diatom is strongly arched whereas the middle striae is slightly convex as displayed in Fig. 4.7 (a). The curvature of the radiate striae (finely punctate) as well as tiny features such as isolated stigmata (~ 350 nm diameter, see zoom inset) have been also successfully reconstructed. This 3D structural information is particularly useful for the specimen taxonomy and classification apart from the study of other biological characteristics. The size of the *Cymbella subturgidula* is about $20\,\mu$m long and $8\,\mu$m wide, which is in good agreement with the typical dimensions measured by using a scanning electron microscope (SEM) [116]. Figure 4.7 (b) shows a symmetrical *Diploneis elliptica* diatom of $32.5\,\mu$m long and $17.3\,\mu$m wide exhibiting a density of 8 resolvable radiate striae along 10μm, that is also in good agreement with SEM data [116]. Indeed, the striae are radiate mid-valve, becoming arched towards the valve apices. Furthermore, the terminal *raphe* fissures deflect near of the valve margin [see the diatom apices in Fig. 4.7 (b)]. The stack of intensity images alongside the corresponding RI slices are given

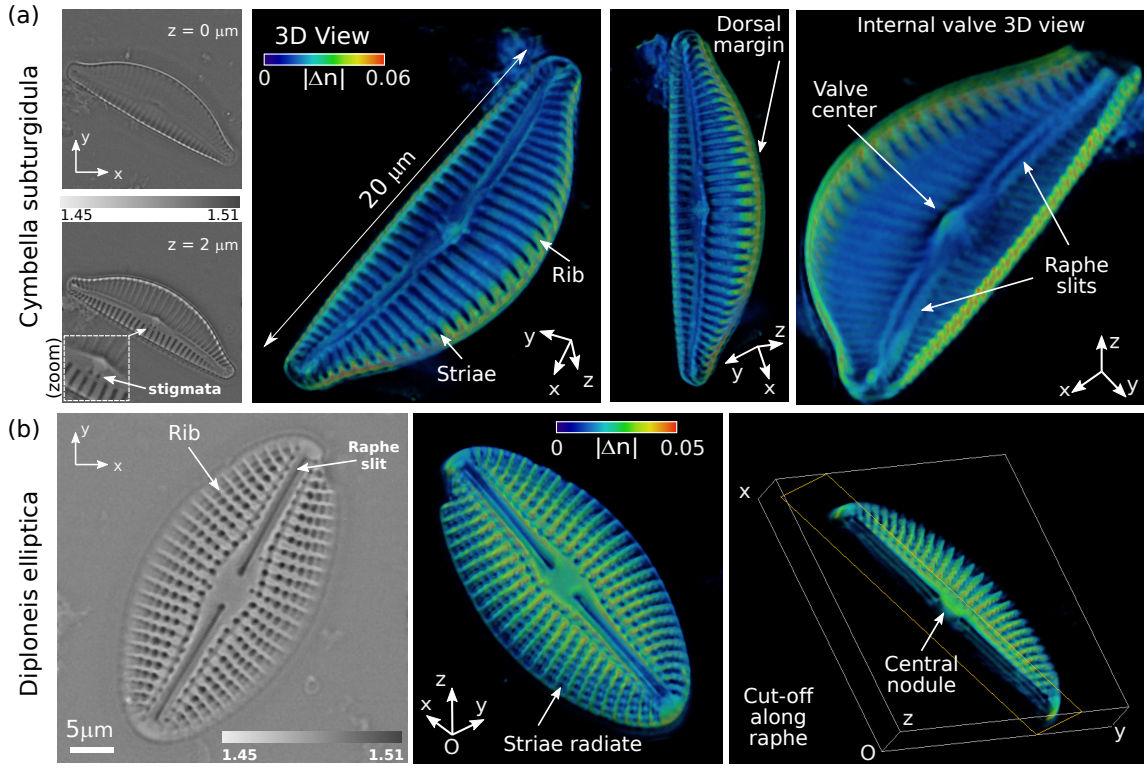

Figure 4.7: (a) Reconstructed RI for a *Cymbella subturgidula* diatom. The frustule made of biosilica exhibits distinct structures such as slits and striae comprising the valves. Two $xy-$RI slices are presented in the first column where two tiny *stigmata* are observed close to the valve center, at $z = 2\,\mu$m. The following three columns are different points of view for 3D-RI ($|\Delta n| = |n_{\mathrm{Re}} - n_m|$) where different structures of the diatom are observed. (b) Reconstructed RI for a *Diploneis elliptica* diatom. In the first column, the $xy-$RI slice reveals detailed structures such as the *raphe* slits and the pores comprising the diatom striae. The next two columns include different perspectives of the 3D-RI $|\Delta n|$, in which it is observed a rounded central area (*nodule*) located in the middle of a longitudinal canal (*raphe*).

in Visualization 3 from Ref. [89]. Moreover, a 3D animated version of these diatoms (RI volume) is provided in Visualization 4 and Visualization 5 from Ref. [89], correspondingly.

The RI values (n_{Re} in the range $1.45 - 1.47$) obtained for the biosilica wall of the diatoms are consistent with those reported in the literature [115]. In this case, by using immersion oil as surrounding medium, the maximum $|\Delta n| \sim 0.04 - 0.06$ is obtained which is reasonably good for a weak object in the Born approximation. Nevertheless, these values vary depending on the diatom region: $n_{\mathrm{Re}} \sim 1.51$ in the striae, $n_{\mathrm{Re}} \sim 1.46 - 1.48$ in the ribs and $n_{\mathrm{Re}} \sim 1.45 - 1.46$ in the dorsal margin. This fact can be explained by the diversity of perforations present in the diatom structure. Indeed, the immersion oil fills the larger pores (in the striae) and thus yields an artificial increase of the RI comparing with the non-porous zones. Therefore, we think that the more reliable values of the frustule RI are found in the more homogeneous biosilica regions such as the dorsal margin for the *Cymbella subturgidula* specimen [corresponding to $|\Delta n| = 0.05$ and $n_{\mathrm{Re}} = 1.46$, see Fig. 4.7 (a)] or the

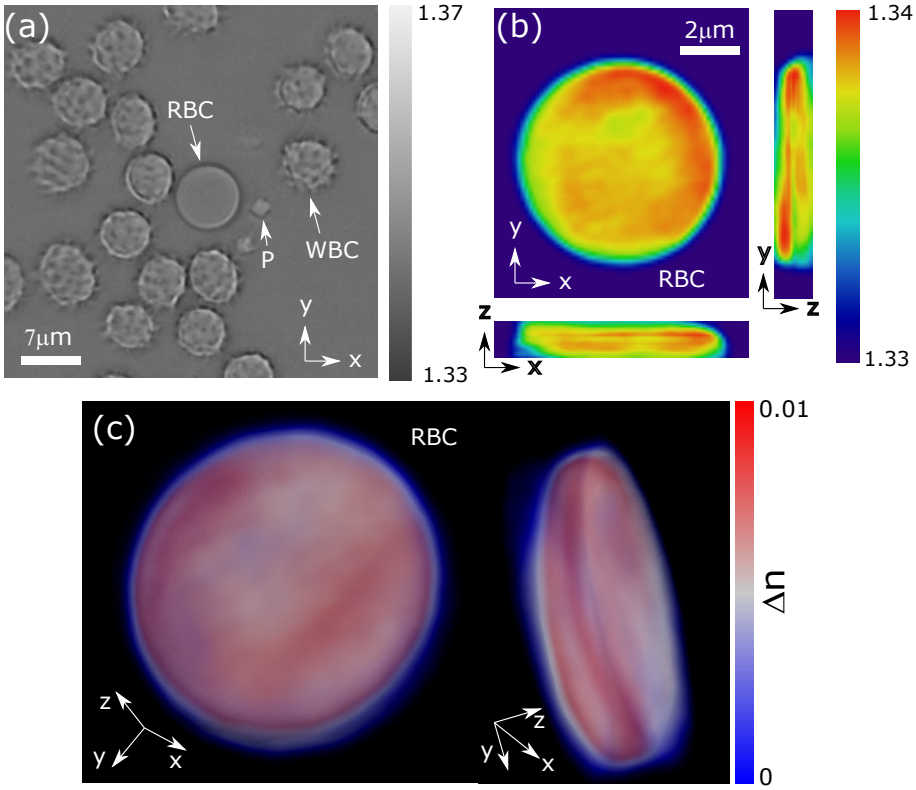

Figure 4.8: (a) Refractive index slice of a blood smear where red blood cell (RBC), white blood cells (WBC) and platelets (P) are observed. (b) Close-up view of the refractive index slice of the RBC along $xy-$, $yz-$, and $xz-$planes. (c) 3D refractive index distribution (Δn) of the RBC exhibiting its characteristic biconcave disc-like shape.

central nodule of the *Diploneis elliptica* [corresponding to $|\Delta n| = 0.04$ and $n_{\mathrm{Re}} = 1.47$, Fig. 4.7 (b)]. The proposed technique is useful to reconstruct relevant structural features of the diatoms required for the analysis and classification of such micro-organisms, which is important for example to gather information about the environment where they live [116].

Finally, we study the performance of the PC-ODT technique for free-label analysis of a human blood sample just immediately after its extraction. The RI slice displayed in Fig. 4.8 (a) shows red blood cells (RBCs), white blood cells (WBCs) and platelets (P) immersed in the blood plasma. Note that in this case $\Delta n > 0$. The reconstructed RI (n_{Re}) values are $n_{\mathrm{RBC}} = 1.34$ for the RBC and $n_{\mathrm{WBC}} = 1.36$ for the WBC. These results are in good agreement with those obtained by other reference techniques including C-ODT [118]. The RI slices displayed in Fig. 4.8 (b) and the 3D RI reconstruction shown in Fig. 4.8 (c) demonstrate the typical biconcave disc shape of a healthy human RBC. Note that in this case the axial stretching effect, caused by the mising-cone issue, is not so evident as in the case of the polystyrene micro-sphere previoulsy described.

The 3D RI recovery of RBCs turns out to be particularly interesting as a diagnosis tool. For instance, it can be used to track abnormalities in their shape or changes in their chemical properties allowing for detection of certain illnesses [119]. Other samples used for calibration and test of PC-ODT techniques are shown in Appendix D.1.

The real word applications of PC-ODT in biomedicine, including imaging and diagnosis are later considered in Chapter 7.

4.6 Conclusions

In this Chapter we have experimentally demonstrated that 3D quantitative imaging of weak scattering and absorbing objects is possible by using a standard bright-field transmission microscope thanks to a straightforward PC-ODT technique. The measurement is performed by an ETL and a sCMOS camera that allow for fast programmable and automatic acquisition of a single stack of bright-field intensity images, which is required for 3D reconstruction of the object RI. It has been proven that the high NA of the condenser and objective lenses, as well as the low spatial coherence of the illumination, provide the required spatial resolution and optical sectioning crucial for 3D quantitative imaging. The dynamic range of the digital camera along with its MTF and the SNR have also been taken into account in order to deconvolve intensity images to recover the RI.

Here two experimental setups, with the ORM in configuration 1 and 2, have been disclosed for PC-ODT implementation. In both configurations, the ETL and the camera must be synchronized. The ORM in configuration 2 can be used for the study of both optically thin and thick samples (up to $\sim 70\,\mu$m), however, it requires more optical elements than the configuration 1 which is recommended only for thin samples (up to $\sim 15\,\mu$m). In this Chapter we have considered optically thin samples and the ORM in configuration 1 to test PC-ODT. Later, the Chapter 6 is devoted to the study of living cells, both optically thin and thick samples, where the ORM in configuration 2 is also applied.

It is worth pointing out that the reconstruction with PC-ODT is fast and the computation time thereof can be further reduced with hardware and software improvements. For instance, in the diatom reconstruction examples from the Section 4.5, the measurement is performed in 1.3 s with an exposure time of 10 ms while the computational reconstruction of the 3D RI of the object was typically achieved in a time of 8 s. A rate of about 10 3D frames per second can be achieved by using a lower exposure time of 2 ms, which is compatible with further development of video-rate 3D imaging as later discussed in Chapter 6. Furthermore the exposure time can be reduced or alternatively a smaller region can be measured if faster video rate visualization is needed. Finally, the computation time of the described direct reconstruction method (involving the Fast Fourier Transform) can be significantly reduced from 1.5 s to a few milliseconds by harnessing the power of the current graphics processing unit (GPU, e.g. NVIDIA's CUDA parallel computing architecture) available in personal computers and workstations.

Chapter 5

ILLUMINATION ENGINEERING IN PC-ODT

PC-ODT provides fast non-interferometric speckle noise-free imaging compatible with conventional wide-field transmission microscopes, but suffers from two principal inconveniences. One of them is the missing cone problem, which is a common drawback for all tomographic modalities with limited-angle inspection, including interferometric coherent ODT. The second one, considered in this Chapter, is a non-homogeneous OTF contrast for different spatial frequency regions, which is particularly noticeable in BFI and even leading to the LV region of untransmitted spatial frequencies. There are different strategies to mitigate these drawbacks and to improve the performance of PC-ODT. One of them consists of exploiting the illumination diversity [86, 120] which requires a collection of sample reconstructions under different illuminations and the subsequent assembling of data. The use of multiple 2D illumination patterns in PC-ODT has been also considered for different purposes, for example, to recover the complex RI (such as the differential phase contrast [86]) or to enhance the gathering of high frequencies of pure-phase objects (by using two circular and one complementary annular illuminations, as proposed in Ref. [120]). The main drawback of using multiple illuminations is the increased number of measurements resulting in a time-consuming approach incompatible with the study of dynamic objects such as live cells. Consequently, in practice such methods [86, 120] are limited to the study of static objects due to the number of required 3D intensity stacks (one per illumination), the amount of time needed for their acquisition and the complexity of reconstruction algorithms. Another approach, studied here, aims at designing a proper illumination which provides a more homogeneous OTF coverage without requiring multiple illuminations.

This last approach, further referred to as illumination engineering, enables fast 3D RI reconstruction intended to monitoring of dynamic objects. With this purpose, first we analyze the microscope 3D OTFs for several illuminations over the condenser aperture, apart from the conventional BFI, by conducting numerical simulations. In this way, we aim to gain knowledge about the interplay between illumination shaping and the resulting OTF. We came to a simple yet effective solution consisting in designing a gaussian illumination leading to an OTF with a wide frequency support and partially filling the frequency gaps in the LV region. Moreover, we demonstrate a more homogeneous 3D RI contrast provided by a proper gaussian illumination allowing for a better balance between low and high spatial

frequencies contributions transmitted by the microscope. Further, we disclose an experimental setup suitable for testing the more convenient OTF design obtained by the previous numerical simulations. Finally, we demonstrate that a more realistic OTF can be obtained by using the measured experimental intensity distribution on the condenser aperture instead of assuming an ideal distribution thereof.

5.1 Optical transfer function design in PC-ODT

The analysis of the POTF obtained with BFI for the case of high NA objective and condenser lenses has revealed a LV region around the zero axial frequency that can alter the RI reconstruction apart from the well-known MC problem (see Fig. 3.3 from Section 3.5). We analyze different types of illumination to improve the homogeneity of the POTF and therefore the viability of PC-ODT technique. It is assumed that light at the back focal plane of the condenser is spatially incoherent, and the coherence degree of light illuminating a specimen is described by the Fourier transform of its intensity distribution according to the Van Cittert-Zernike theorem [121]. Since the ODT technique is mainly applied to low absorbing objects, we pay more attention to the POTF during the discussion.

The 3D POTF of a perfectly aligned microscope with rotationally symmetric illumination is a pure imaginary function also exhibiting rotational symmetry along the axial frequency axis p_z. This allows us considering a real function corresponding to its imaginary part further referred to as $\mathrm{P} = \mathrm{Im}\{H_P\}$. The plane $p_z = 0$ divides the P-section into two symmetric halves with opposite signs, so that $\mathrm{P}(p_x, p_y, p_z) = -\mathrm{P}(p_x, p_y, -p_z)$. Taking into account these symmetry properties, only a section $\mathrm{P}(p_x, 0, p_z)$ is analyzed in Fig. 5.1, where (p_x, p_y, p_z) denotes the spatial frequency vector. In particular, Fig. 5.1 displays the $\mathrm{P}(p_x, 0, p_z)$ sections corresponding to an objective with $\mathrm{NA_o} = 1.4$ and different illumination patterns (with $\lambda_0 = 450\,\mathrm{nm}$) projected on the condenser back focal plane. Among the tested patterns included in Fig. 5.1, one finds BFI with two different condensers ($\mathrm{NA_c} = 1.2$ in (a) and $\mathrm{NA_c} = 0.5$ in (b)), a binary ring (c), an inverse gaussian illumination (IGI) as displayed in (d), two combinations of gaussian illumination (GI) and ring (e,f) and finally two GI with different widths (σ) of $\sigma = 0.5\,\mathrm{NA_c}$ and $\sigma = 0.75\,\mathrm{NA_c}$ (with $\mathrm{NA_c} = 1.2$) respectively. Note that for each case, the |POTF| has been normalized to the range $[-1, 1]$. We recall that regardless of the illumination pattern, there always exists a MC frequency region around the p_z axis which is a well-known drawback of wide-field microscopy. This MC region can create artifacts such as halos and longitudinal stretching in the reconstructed 3D object [67, 122], in both C-ODT and PC-ODT modalities. For a same objective lens, by considering a larger $\mathrm{NA_c}$, the MC is smaller and the maximum transverse resolution is higher, as observed in Figs. 5.1 (a, b) corresponding to the BFI with $\mathrm{NA_c} = 1.2$ and $\mathrm{NA_c} = 0.5$, respectively. However, these advantages of high $\mathrm{NA_c}$ are accompanied by a wider area (around the line $p_z = 0$) where the absolute values of the POTF are almost negligible. We recall that such frequency domain is the LV region, formerly introduced in Chapter 3. The ideal POTF would have the MC region as small as possible and almost uniform distribution of its modulus, |POTF|. Therefore, the key question is: Can it be achieved by using an illumination distinct from the BFI? [123]

To answer the previous question, let us first compare the POTFs for different illumi-

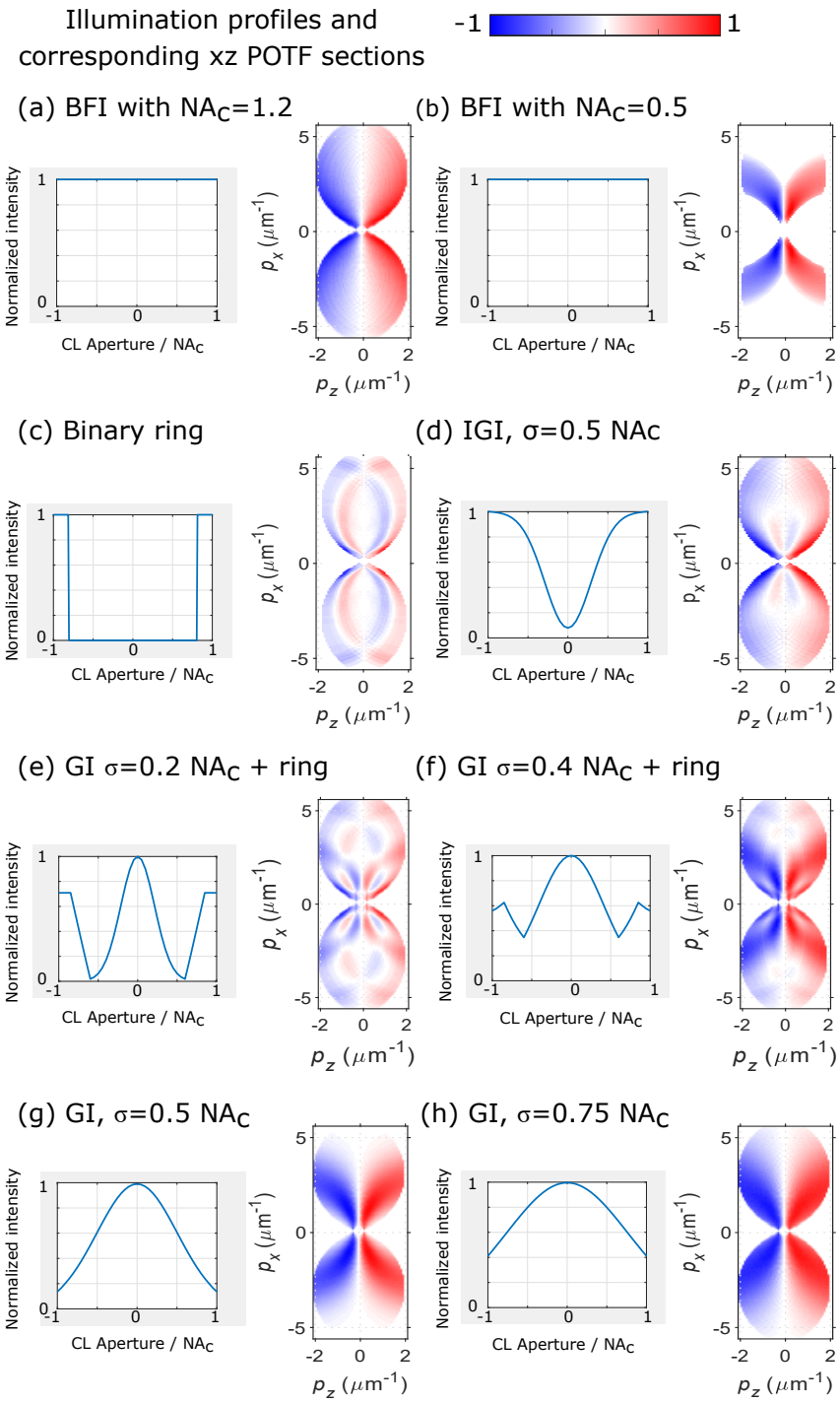

Figure 5.1: Sections of imaginary part of the normalized POTFs for different illumination distributions in the condenser aperture, along with the corresponding normalized intensity profiles. (a) BFI with $\mathrm{NA_c} = 1.2$, (b) BFI with $\mathrm{NA_c} = 0.5$, (c) Binary ring, (d) IGI with $\sigma = 0.5\,\mathrm{NA_c}$, (e) combination of GI with $\sigma = 0.2\,\mathrm{NA_c}$ and binary ring, (f) combination of GI with $\sigma = 0.4\,\mathrm{NA_c}$ and binary ring, (g) GI with $\sigma = 0.5\,\mathrm{NA_c}$ and (h) GI with $\sigma = 0.75\,\mathrm{NA_c}$. Except in (b), in which $\mathrm{NA_c} = 0.5$, the remaining cases have been computed with $\mathrm{NA_c} = 1.2$. All cases consider $\mathrm{NA_o} = 1.4$.

nations. For this purpose, apart from Fig. 5.1, we also show in Fig. 5.2 the POTF moduli together with their corresponding histograms, which are better suited for their homogeneity analysis. The histograms for each illumination are compared with respect to the BFI case for $\mathrm{NA_c} = 1.2$, that is considered as a reference illumination. Since a high $\mathrm{NA_c}$ is considered it is good to preserve the high resolution usually associated with the periphery illumination of the condenser aperture. Then, we start our analysis by considering an annular illumination, as shown in Figs. 5.1 (c-d), defined by an internal radius of $R_{int} = 0.75\,\mathrm{NA_c}$ and an external radius of $R_{ext} = \mathrm{NA_c}$. In this case we observe that the |POTF| distribution is even less uniform than in the reference BFI. Moreover, as it can be seen in Fig. 5.1 (c) there exist sign changes into the same half of the P-section. This effect is undesired because the result of sign mismatching between the ideal (theoretical) and experimental ring POTFs could lead to severe artifacts in RI reconstruction.

Let us now find whether or not the smoothing of the illumination ring boundary helps to yield a more uniform POTF. For this reason, we now consider an IGI defined as $I(\mathbf{r}_\mathrm{c}) = I_0\left(1-\exp\left(-r_\mathrm{c}^2/2\sigma^2\right)\right)\mathrm{circ}\,(r_\mathrm{c}/\mathrm{NA_c})$, where $\mathbf{r}_\mathrm{c} = (r_x, r_y)$ is a dimensionless coordinate vector (contained in the diaphragm plane of the condenser lens) and I_0 is the intensity maximum value (see Figs. 5.1(d, e)). We have found a slight improvement in the histogram values with respect to the ring illumination: the peak of |POTF| low values around 0.1 have decreased from a 40 % in the ring illumination to a 30 % in IGI. However, this is not significantly better than the BFI case. Then, our next guess is to combine in a single illumination the advantages from the ring illumination and a low $\mathrm{NA_c}$ BFI, since as we mentioned before such BFI exhibits a lower LV region for the low and middle transverse frequency range. The superposition of both the annular illumination and a low $\mathrm{NA_c}$ BFI followed by a smoothing (to avoid sudden intensity changes) corresponds to a gaussian pattern. In particular, the Figs. 5.1 (e,f) and Figs. 5.2 (f, g) illustrate two different combinations of a GI and a ring illumination (with a common center), being the ring delimited between $R_{int} = 0.6\,\mathrm{NA_c}$ and $R_{ext} = \mathrm{NA_c}$. Here the Gaussian illumination is given by $I(r_\mathrm{c}) = I_0 \exp\left(-r_\mathrm{c}^2/2\sigma^2\right)\mathrm{circ}\,(r_\mathrm{c}/\mathrm{NA_c})$. We observe that the homogeneity of the POTF modulus has not been improved with regard to the BFI. Moreover, there is a complex structure of the POTF sign changes. especially appreciable in Fig. 5.1 (e), accompanied by zero-value curves (corresponding to surfaces of the full 3D POTF). From the analysis of all the aforementioned illuminations we decide to impose an additional constraint for the illumination: same POTF sign for positive (negative) axial frequencies of each P-section half.

Let us return to the first considered illuminations, BFI with $\mathrm{NA_c} = 1.2$ and $\mathrm{NA_c} = 0.5$, as displayed in Fig. 5.1 (a-b) respectively. The first one exhibits a low MC but pronounced LV regions whereas the second one shows large MC but small LV area. Therefore, a smoothed superposition of both BFI could result in a more homogeneous POTF. In this way, a GI can be used for such combination. Two cases of GI with different width values ($\sigma = 0.5\,\mathrm{NA_c}$ and $\sigma = 0.75\,\mathrm{NA_c}$, respectively, where $\mathrm{NA_c} = 1.2$) are displayed in Fig. 5.1 (g, h) and Fig. 5.2 (h, i). Note that no sign changes exist into the same half of P-section with this illumination. We observe that the GI with the width $\sigma = 0.75\,\mathrm{NA_c}$ provides a relevant improvement in |POTF| homogeneity and a reduction of the LV area. As a counterpart, the GI presents further attenuation of the very high frequency region which in any case could not be properly resolved with the BFI due to low contrast.

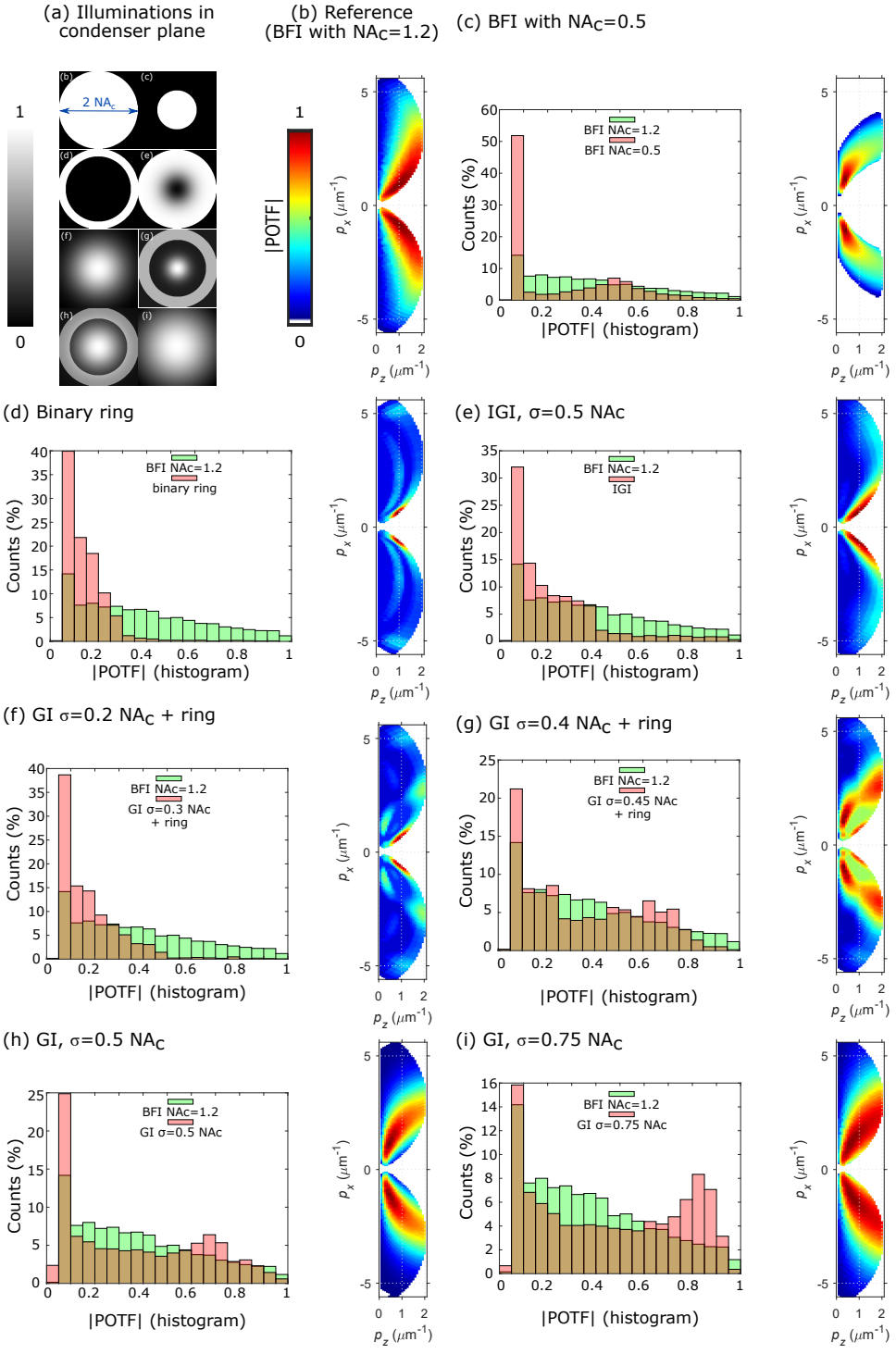

Figure 5.2: Normalized POTF magnitude (only the section of positive axial frequencies is presented) for several illuminations, along with the |POTF| histogram comparing each case (rose color) with BFI $NA_c = 1.2$ (green color). (a) Illumination projected in the condenser aperture. (b) BFI with $NA_c = 1.2$ (reference illumination), (c) BFI with $NA_c = 0.5$, (d) Binary ring, (e) GI with $\sigma = 0.75\,NA_c$. Except in (c), in which $NA_c = 0.5$, the remaining cases are computed with $NA_c = 1.2$. All cases use $NA_o = 1.4$.

We recall that the complex degree of coherence at the sample area is related to the Fourier transform of illumination pattern at the condenser back focal plane, according to the Van Cittert-Zernike theorem. The degree of coherence is gaussian-shaped under GI, while in the case of BFI (i.e. uniform illumination pattern) it is described by a besinc function with multiple secondary peaks [63]. Since the OTFs usually considered for ODT are calculated following the first Born approximation, thereby neglecting the interference between different scatterers (see Eq. 2.5), we believe that the coherence degree of a narrower gaussian shape is better suited for this model than one described by the besinc function, where undesired interference of scattered light from two separated scatterers could produce significant contribution. Thus, a Gaussian illumination (GI) whose intensity distribution in the diaphragm plane of the condenser lens, given by $I(\mathbf{r}_c) = I_0 \exp\left(-r_c^2/2\sigma^2\right) \mathrm{circ}\left(r_c/\mathrm{NA}_c\right)$, can be well suited for this purpose. We underline that $\sigma/\mathrm{NA}_c = 0.75$ is not a fixed value, similar results are obtained for 0.75 ± 0.05 (similar histogram of the |POTF| values are obtained in those cases). This range of σ/NA_c has been verified for $\mathrm{NA}_c \in [0.9, 1.4]$.

Another example with a different NA_c value is shown in Fig. 5.3, in which $\mathrm{NA}_c = \mathrm{NA}_o = 1.4$. Fig. 5.3 corresponds to the BFI case while Fig. 5.3 (b) is obtained for a GI with $\sigma = 0.75\,\mathrm{NA}_c = 1.05$. Note that the modulus |POTF| is normalized to its corresponding maximum value to help the comparison between the considered cases. Indeed, as observed in Fig. 5.3 (b), in the GI case the corresponding LV region in the POTF is significantly narrowed around the plane $p_z = 0$. This LV region is determined by the absolute values below a cut-off threshold value of 0.2, which is often considered in the analysis of OTFs of imaging systems. Moreover, the middle-high values of the |POTF| (range $0.5-1$, indicated by the green-yellow-red colormap) are now distributed in a larger region, thus resulting in a significantly improved transmission of the object's spatial spectrum. Such a redistribution is also clearly observed in the histogram of |POTF| values displayed in Fig. 5.3 (c) for GI and BFI. From these histograms it is possible quantitatively estimating the gain of GI with respect to BFI. Indeed, for BFI the 21 % of the |POTF| values are in the range $0.5-1$ while for GI it is the 42 %, which is a gain factor of $2\times$ for GI with respect to BFI. This is a relevant improvement that could increase the accuracy of the object's RI reconstruction in PC-ODT.

With regard to the AOTF, it is less sensitive to the illumination modification unlike the POTF. This aspect can be verified in Fig. 5.4, where the AOTF forms for the more representative illuminations considered during POTF analysis are displayed. The AOTF of each illumination has been normalized to its maximum value. The AOTF of a system presenting rotational symmetry is positive and symmetric about the plane $p_z = 0$, that allows us considering only the AOTF section $\mathrm{A}(p_x, 0, p_z)$ for non-negative axial frequencies. In contrast to POTF, the maximum AOTF values are concentrated around the axis $p_z = 0$. Most of normalized AOTF values are below 0.3 as can be seen from the histograms presented in Fig. 5.4. The spatial frequency region with AOTF magnitude values above 0.4 is more elongated along the $p_z = 0$ for BFI with $\mathrm{NA}_c = 0.5$ (Fig. 5.4 (c)) and GI (see Fig. 5.4 (e)) in comparison with BFI ($\mathrm{NA}_c = 1.2$), see Fig. 5.4 (b). On the other side, the ring-like illuminations tend to yield a more symmetric filling of the low frequency region as shown in Fig. 5.4 (d). We conclude that the changes in AOTF are irrelevant specially when weakly absorbing objects are considered. This also supports our proposal of applying the gaussian illumination with $\sigma = 0.75\,\mathrm{NA}_c$ for PC-ODT instead of conventional BFI.

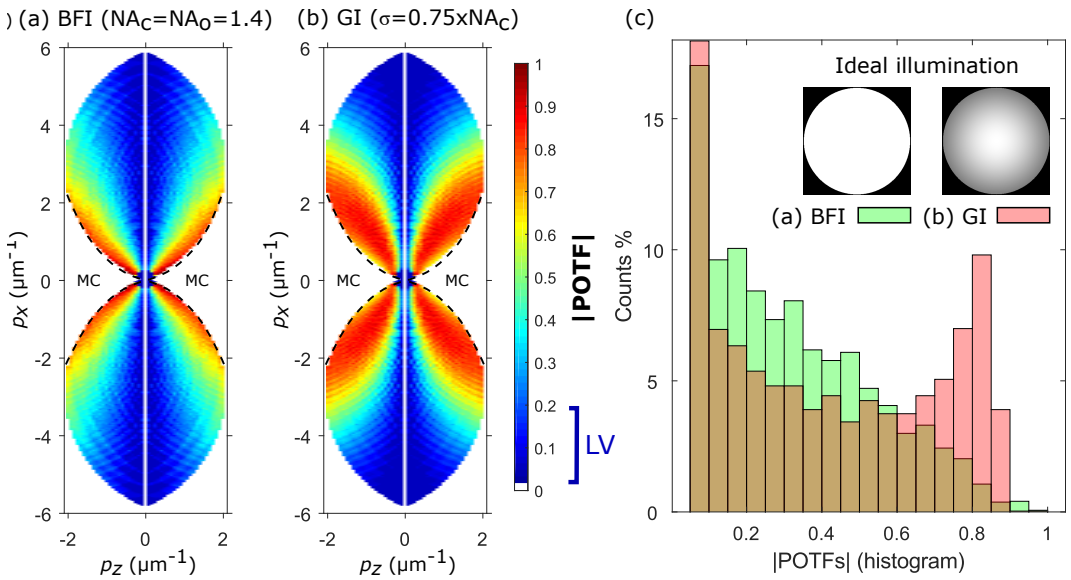

Figure 5.3: |POTF| sections of (a) 3D BFI-POTFs with $\mathrm{NA_c} = \mathrm{NA_o} = 1.4$. (b) GI-POTF for $\sigma = 0.75\,\mathrm{NA_c}$ (where $\mathrm{NA_c} = \mathrm{NA_o} = 1.4$). (c) Histograms of the |POTF| values for BFI in (a) and GI in (b). MC indicates the missing cone region.

In summary, with the study of this Section we have verified that Gaussian illumination (GI) overperforms BFI in terms of POTF homogeneity [123, 124], therefore providing a better balance between low and high spatial frequencies contributions transmitted by the microscope.

5.2 Comparative analysis of PC-ODT with BFI and Gaussian illumination: numerical simulations

In this Section, the advantages of using the GI have also been verified by the following numerical simulations. In this case, the OTFs correspond to $\mathrm{NA_c} = 0.95$, $\mathrm{NA_o} = 1.4$ and $\sigma = 0.75\,\mathrm{NA_c}$. In Fig. 5.5 (a) is displayed a non-absorbing test object with a known non uniform RI distribution (indicated as n_{TO}) that has been used for the comparison of the performance of PC-ODT in the RI reconstruction with the BFI-POTF and GI-POTF shown in Fig. 5.5 (b, c), respectively. This object consists of an array of 25 perforated micro-pillars ($10\,\mu$m long, with a diameter of 800 nm and inner hole of 250 nm) immersed in a surrounding medium of $n_m = 1.33$ yielding a RI contrast $|\Delta n| = |n_{\mathrm{TO}} - n_m| \sim 0.06$. Specifically, we have numerically calculated the stack of intensity images obtained using the POTFs for ideal BFI and GI and then, from this stack, performed the deconvolution and RI reconstruction process as explained in Section 3.4. The reconstructed 3D RI distribution for GI (indicated as n_{GI}) is in good agreement with the test object's n_{TO}. While, it is evident that a degradation exists in the reconstructed object's shape (n_{BFI}) for BFI, especially in the axial direction (see $yz-$slices), which is due to the effect of the LV region of the BFI-POTF. Moreover, in Fig. 5.5 (d) a comparison of RI profiles along the y-axis dashed line is drawn

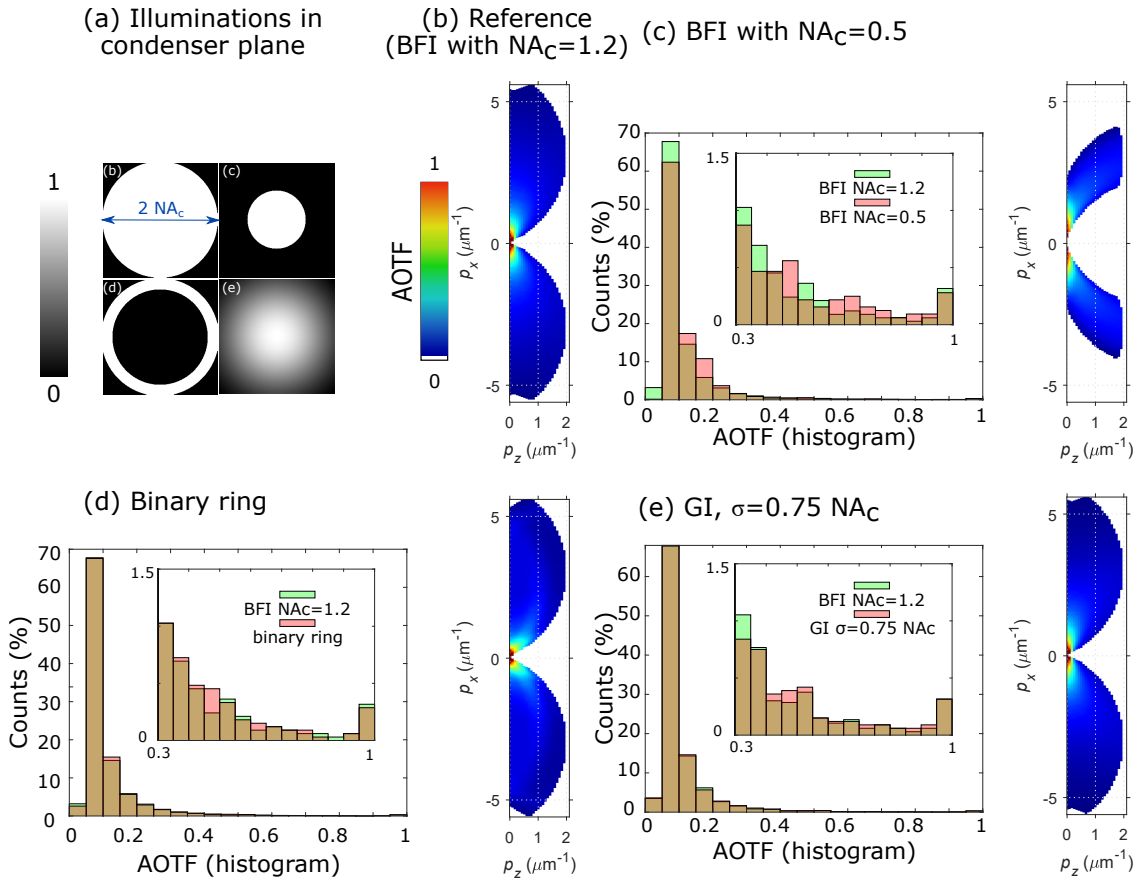

Figure 5.4: Normalized AOTF (only the section of positive axial frequencies is presented) for several illuminations, along with the AOTF histogram comparing each case (rose color) with BFI $\mathrm{NA_c} = 1.2$ (green color). (a) Illumination projected in the condenser aperture. (b) BFI with $\mathrm{NA_c} = 1.2$ (reference illumination), (c) BFI with $\mathrm{NA_c} = 0.5$, (d) Binary ring, (e) GI with $\sigma = 0.75\,\mathrm{NA_c}$. Except in (c), in which $\mathrm{NA_c} = 0.5$, the remaining cases have been computed with $\mathrm{NA_c} = 1.2$. All cases use $\mathrm{NA_o} = 1.4$.

in order to compare the accuracy of the reconstructed RI in the case of BFI and GI. Note that n_{GI} is closer to the theoretical one (n_{TO}), whereas n_{BFI} suffers from underestimation along with contrast lost. Indeed, we remark that the perforations of the micro-pillars have a RI value close to n_m and the entire object exhibits a better contrast in the reconstructed RI with GI. The RI histograms displayed in Fig. 5.5 (e) also enable a fair comparison between the reconstructions obtained with each illumination and the theoretical object RI. Note that a deviation between the n_{BFI} values with respect to n_{TO} exists, resulting in histogram mismatch in the left panel of the Fig. 5.5 (e). For instance, the object regions with a RI above 1.375 which represent almost the 30 % of the histogram counts according to the theoretical object (blue histogram) are severely underestimated. Indeed, only around 2 % of the RI counts from n_{BFI} histogram corresponds to values above 1.375. Conversely, n_{GI} exhibits a histogram very similar to the theoretical one n_{TO}, which confirms the more reliable RI reconstruction obtained thanks to gaussian illumination. Thus, the considered numerical simulation proves the advantage of GI over BFI due to the reduction of the LV

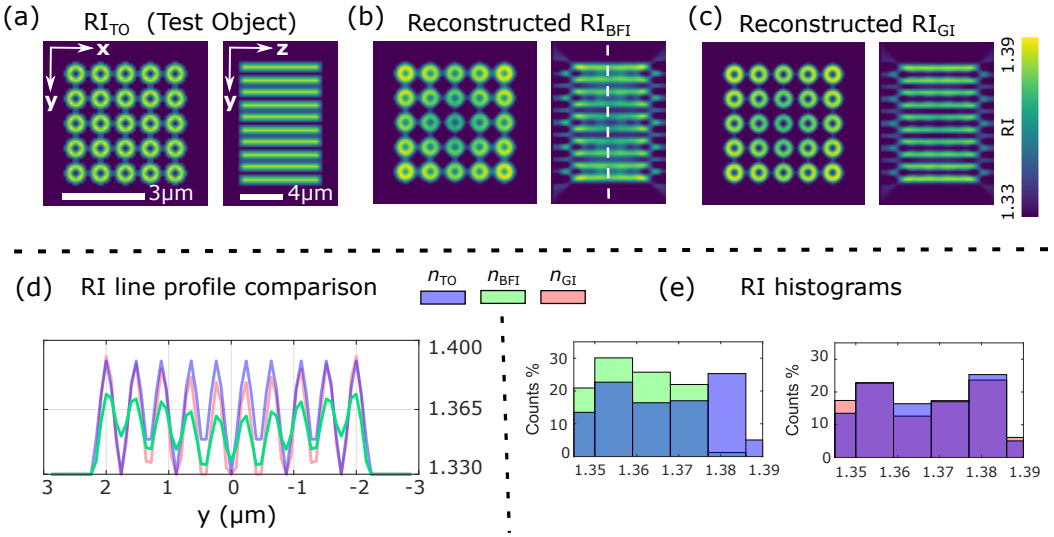

Figure 5.5: (a) RI of a test object (array of 25 microperforated tubes of known and non homogeneous RI distribution). (b-c) The reconstructed RI (numerical simulation) for the case of ideal BFI (b) and GI (c). (d) Line profiles along y-axis dashed line comparing different illumination schemes. (e) Histogram comparison for RI values.

region and redistribution of the POTF values as it has been previously discussed.

5.3 Experimental setup equipped with an illumination control module

Here we disclose an experimental setup suitable for testing the illumination patterns analyzed in the Sections 5.1 and 5.2, as shown in Fig. 5.6. This setup is similar to the ones introduced in Section 4.2 (bright-field microscope with $NA_c = 0.95$, $NA_o = 1.4$, $f_{TL} = 180$ mm) but it further comprises a programmable system for illumination control [113]. This module consists of a digital light processing (DLP) projector (LG PA70G, 750 ANSI lumens of power) whose projection lens has been replaced by a 4-f setup. Incoherence is provided by the extended LED source of the DLP. The DLP allows obtaining a real image of the digital mirror device (DMD, manufactured by Texas Instruments) display onto a static ground glass diffuser (GGD, Thorlabs N-BK7 glass), that warrants for a further homogeneous incoherent illumination of the condenser plane. Indeed, the diffuser plane (e.g. the green circle of Fig. 5.6) is then relayed onto the back focal plane of the condenser lens by using two convergent lenses (RL1 and RL2). The DLP projector enables the illumination engineering, providing fast switchable multi-wavelength and shaping design. In this way, the DLP projector provides dynamic generation of desired images onto the condenser back focal plane. The refocusing module comprises a relay lens (RL3) and the varifocal ETL, as explained in Section 4.2. Finally, the required axially scanned images are measured by using a high speed camera (e.g. sCMOS). All the relay lenses ($f_{RL1}, f_{RL2}, f_{RL3}$) are achromatic doublets with focal length of 150 mm.

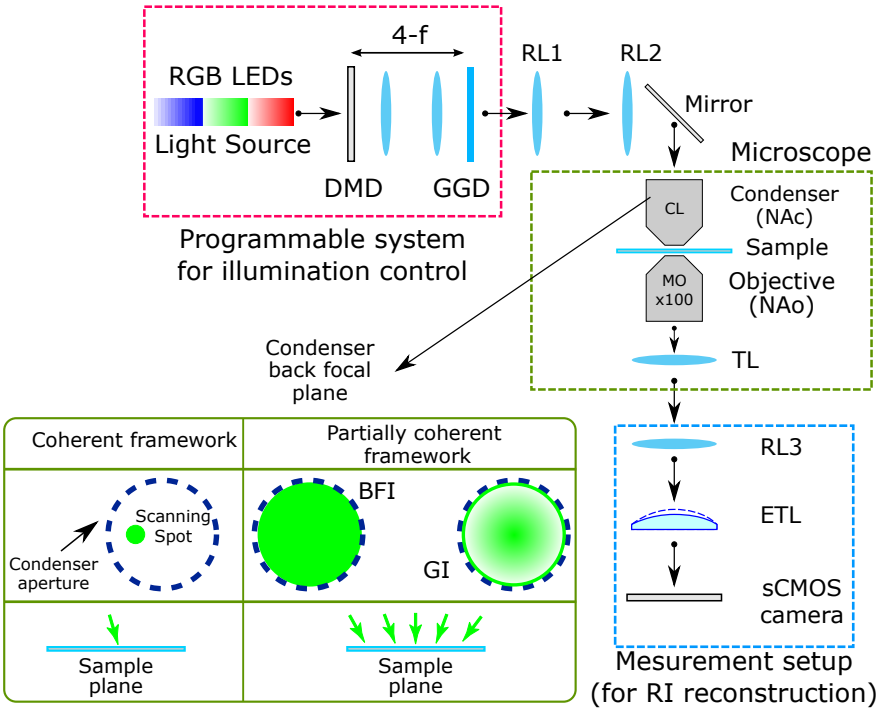

Figure 5.6: Experimental setup for PC-ODT including the microscope, the optical refocusing module and an additional programmable system for illumination control.

In this way, the experimental setup proposed in Fig. 5.6 is useful to test the best illuminations (in terms of uniformity and filling of the spatial frequency space to be transmitted by the microscope) devised from the theoretical simulations proposed in the previous Section. A practical advantage of the GI is that it can be easily incorporated into conventional wide-field microscopes just by using a commercial Gaussian apodizing filter placed over the condenser's diaphragm plane, instead of using the DLP setup. Once the desired illumination (i.e. the GI with $\sigma = 0.75\mathrm{NA_c}$, which is the best option among the studied patterns) is found, the programmable system for illumination control is no longer needed. For this reason, to experimentally test the proposed illumination, it is possible to alternatively consider the setup with the ORM in configuration 1 previously described in Section 4.2, but with the Gaussian apodizing filter inserted in the condenser plane. Advantageously, this approach is simpler, more affordable and convenient for living samples imaging than the DLP since its refresh rate (60 Hz) is typically lower than the sCMOS camera frame rate (e.g. 100 fps) required for fast PC-ODT.

5.4 Towards a realistic experimental estimation of the OTF

In this Section we experimentally demonstrate the benefits of applying more realistic OTFs that better take into account the experimental illumination conditions. They have been numerically calculated using Eqs. 3.5 and the illumination pattern measured in the back focal plane of the condenser lens. Note that this approach allows computing the OTFs

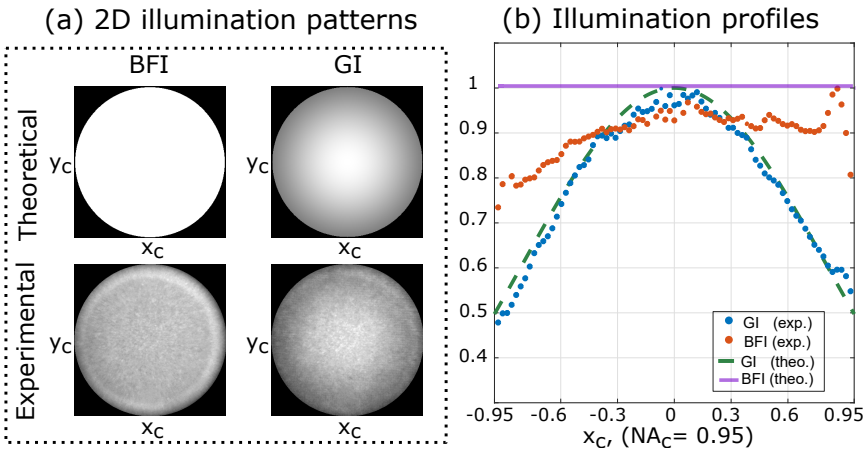

Figure 5.7: (a) Ilumination in the condenser plane for BFI and GI, both theoretical and experimentally measured. (b) Radial profiles for the analyzed illuminations.

for arbitrary illumination patterns for which the analytical expressions of the OTFs are not available. The use of better approximated OTFs has been previously considered in PC-ODT for the particular case of BFI [66], where the measured BFI pattern has been fitted as a rotational symmetric function ignoring the possible asymmetries of the experimental BFI (originated by misalignments between condenser and objective lenses or aberrations). Conversely, in this Section we compute the OTF by using Eq. 3.5 and considering the experimental measurement of the incoherent intensity distribution over the condenser aperture diaphragm given by $a^2(|\mathbf{s}|)$, as illustrated in Fig. 5.7.

A more realistic coherent transfer function has also been applied in C-ODT modality [47, 125]. It is worth pointing out that the method to obtain a more realistic OTFs for PC-ODT is completely different from the one reported for C-ODT [47]. In particular, a realistic CTF for C-ODT requires the measurement of the complex field amplitude for each illumination plane wave in order to better approximate the CTF of the experimental setup and therefore compensating possible wavefront aberrations in the optical train of the microscope. Consequently, this results in a more difficult task than the OTFs estimation in PC-ODT case where only one measurement of the intensity distribution of the illumination at the aperture plane of the condenser lens is needed.

Let us now proceed with experimental validation of the GI approach, by using the imaging setup with the ORM in configuration 1 previously described in Section 4.2, but with a spatial filter inserted in the condenser plane according to the Section 5.3. The intensity distribution in the condenser aperture, see Fig. 5.7 (a), has been measured for both BFI and GI cases and compared with the theoretical ones. For a better comparison among different illuminations, Fig. 5.7 (b) displays the radial profiles for each of them. Note that experimental illuminations are asymmetric, for this reason several profiles have been averaged in order to help the visualization of the plot displayed in Fig. 5.7 (b). It is also worth remarking that the OTFs derived from these experimental illuminations are not rotationally symmetric, which constitutes a more realistic model of the imaging process given the experimental conditions.

The |POTF| corresponding to this microscope experimental configuration for BFI and GI are respectively displayed in Figs. 5.8 (a-b), along with the corresponding |POTF| histograms in Fig. 5.8 (c). Only 32 % of the |POTF| values are in the range $0.5-1$ for the case of BFI while for GI (for $\sigma = 0.75\,\mathrm{NA_c} = 0.72$) the ratio is 46 %, thus resulting in a gain factor of $1.44\times$. The realistic POTF, see Fig. 5.8 (d-e), have been calculated using the measured illumination patterns for BFI and GI, respectively. These illumination patterns are displayed in Fig. 5.8 (f) along with the corresponding histograms of the 3D |POTF| for each case. We observe that for the case of GI the reduction of the LV region for low/mid-range frequencies is slightly smaller in the realistic POTF. Moreover, the realistic POTFs are no longer symmetric because the experimental illumination patterns are not circularly symmetric. In particular, the asymmetry is highly manifested in the realistic BFI-POTF, see Fig. 5.8 (d) and the Visualization 1 from Ref. [124] (available online) of the 3D POTF z-stack. The redistribution of the frequency weights in the realistic GI-POTF, see Fig. 5.8 (e), does not significantly alter the symmetry because the experimental GI fits reasonably well to the ideal one. For the realistic GI-POTF the values in the range $0.5-1$ decreased to a ratio of 35 % while for the realistic BFI-POTF the ratio is 22 %, see Fig. 5.8 (f).

As an example, we compare the reconstructed RI for the diatom sample displayed in Fig. 5.9 by using both the BFI and GI, and for each one, either the ideal and the more realistic OTF. This diatom exhibits a periodic porous pattern in its biosilica shell resulting in a nearly phase structure with a n_D value in the range 1.47 ± 0.01 at $\lambda_0 = 450$ nm, when it is immersed in oil with $n_{imm} = 1.51$ to obtain a maximum RI contrast value of $|\Delta n| = |n_D - n_{oil}| \sim 0.06$. The real part of the reconstructed RI distribution (n_D) of the diatom is displayed in Figs. 5.9 (a, b) for the case of ideal BFI and GI, respectively. The transverse xy-RI slices show a structure with circular-like perforations ranging in size from 240 nm to 450 nm. The reconstructed n_D distribution is more homogeneous for the GI than for BFI. Moreover, it is more evident for the GI case that the micro-perforated channels ($\sim 10\,\mu$m long) indeed are crossing the entire diatom wall, see the RI $yz-$slices in Fig. 5.9. Note that these micro-channels have not been properly resolved using the ideal BFI-POTF. They are better detected, see Fig. 5.9 (c), when using the realistic BFI-POTF because it takes into account the experimental illumination conditions. In the reconstruction with the realistic GI-POTF the LV region has been reduced and therefore the reconstructed micro-channels are less degraded than in the case of BFI-POTF, see Fig. 5.9 (d), as predicted by the numerical simulation Fig. 5.5. The histograms displayed in Fig. 5.9 (e) indicate that the diatom's RI values in the case of realistic BFI-POTF and GI-POTF are more concentrated around the value $\mathrm{n}_D \approx 1.48$ than in the ideal case. Moreover, the RI reconstruction is more accurate for the case of GI than for BFI, as well as has been concluded from the numerical simulation results shown in Fig. 5.5. To help with the observation of the diatom's micro-channels, in Fig. 5.10 (f) and in the Visualization 2 from Ref. [124] a volumetric representation is provided with the diatom's RI reconstructed using the realistic GI-POTF and renderized with Drishti open-source software [126]. Finally, we also compare BFI and GI schemes by using a eukaryotic sample, particularly human cheek cell attached to a epithelial layer included in Appendix D.2 which also corroborates that GI outperforms BFI, especially when tiny object features are present.

We conclude that the use of both GI and more realistic OTFs (that consider the experimental illumination in the back focal plane of the microscope condenser instead of the

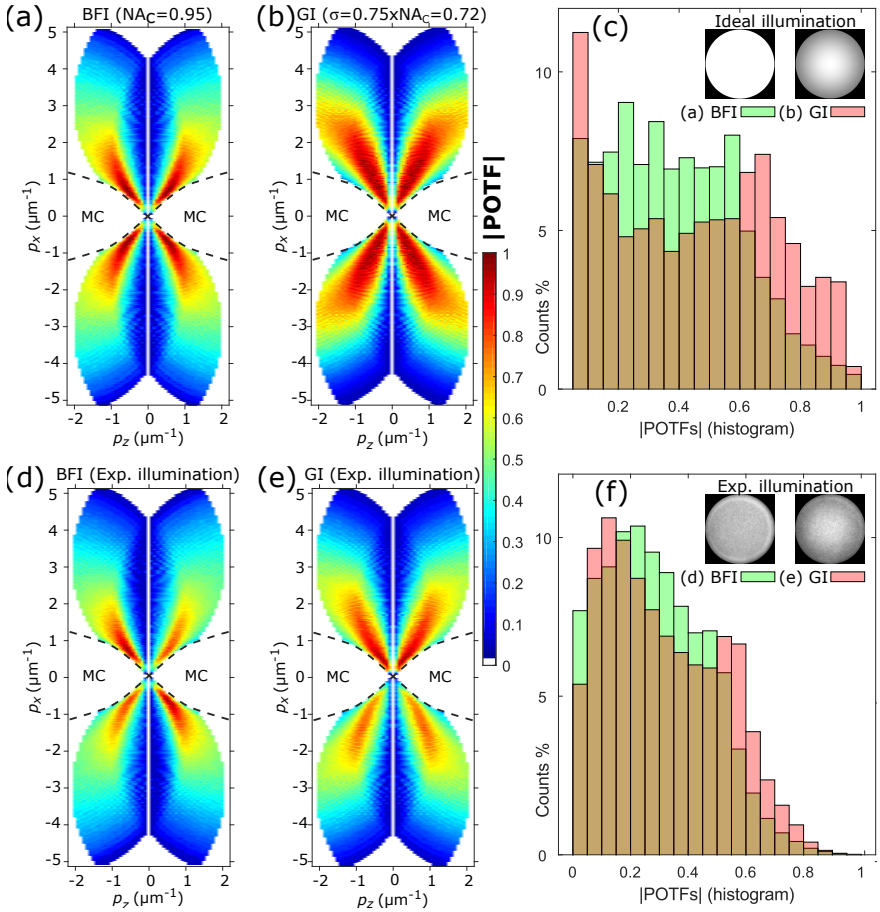

Figure 5.8: |POTF| sections calculated for ideal (theoretical) illumination: (a) BFI with $NA_c = 0.95$ and (b) GI with $\sigma = 0.75\,NA_c$, while the corresponding |POTF| histograms are shown in (c). The |POTF| sections displayed in (d) and (e) have been calculated using the measured (experimental) BFI and GI, which have been displayed in (f) along with |POTF| histogram for each case.

ideal distribution) significantly improves the accuracy and the reliability of the 3D RI reconstruction [124]. The numerical simulation and the experimental results prove that GI outperforms BFI in PC-ODT preventing degradation in the RI reconstruction, especially in the axial direction. This is due to the reduction of the LV region in the GI-POTF and the extension of middle-high |POTF| values.

5.5 Conclusions

In this Chapter, the optimization of the POTF via illumination has been considered in order to enhance the quality of reconstructed RI with PC-ODT. The OTF strongly depends upon the shape and distribution of the illumination in the input aperture plane of the condenser lens. Furthermore, we have explored several illumination patterns (gaussian, annular, inverse-gaussian and combinations thereof). In this way, the OTF (mainly POTF)

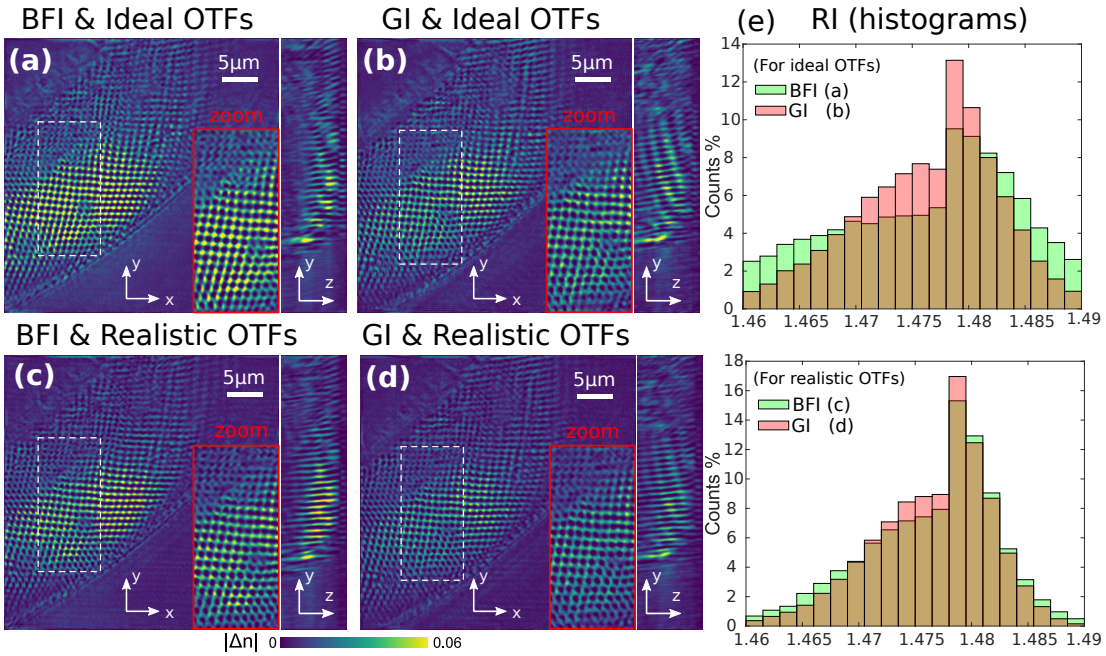

Figure 5.9: RI slices of a diatom reconstructed with ideal (theoretical) OTFs for BFI (a) and GI (b), and realistic OTFs for BFI (c) and GI (d). The histograms of RI values are displayed in (e) for each case. (f) 3D volumetric representation of the diatom's RI obtained with realistic GI-OTFs, see also Visualization 2 from Ref. [124].

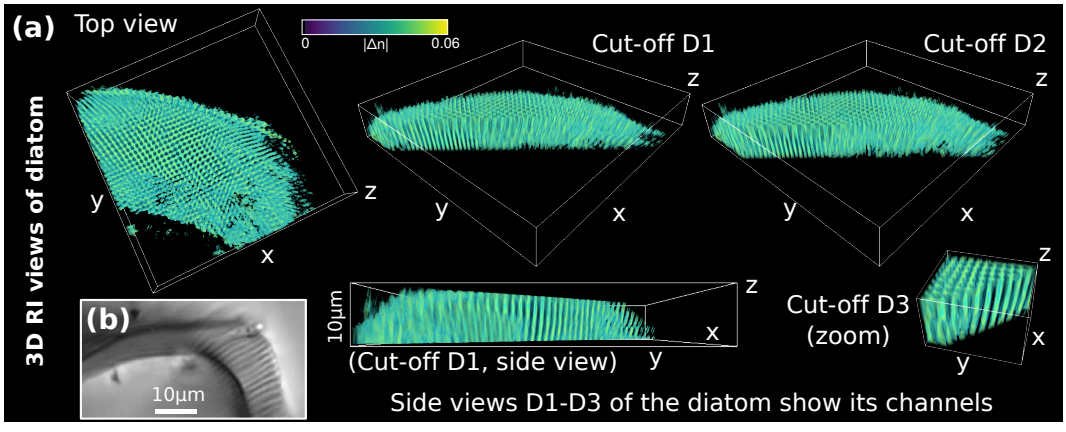

Figure 5.10: (a) Different views of 3D RI reconstruction of diatom obtained with realistic GI OTFs. (b) Intensity side view of the sample in which the micro-channels are observed.

engineering allows to tackle the problem of nonuniformity in the POTF for BFI as well as mitigating the inherent frequency attenuation in LV region. In particular, the replacement of the conventional BFI with a properly designed GI provides a better balance between the transmitted low and high frequencies and yields a more uniform POTF, which in turn results in a higher accuracy of the sample details in its RI reconstruction. The illumination engineering can be further tested experimentally by taking advantage of DLP technology, based on DMD projectors or LED arrays, to provide fast switchable illumination control [113, 127]. Finally, it has been demonstrated that the use of more realistic OTFs, which have been calculated by considering real experimental illumination conditions, significantly increases the accuracy in 3D RI reconstructions.

Chapter 6

FAST PC-ODT ENABLING VIDEO-RATE 3D RI IMAGING OF DYNAMIC OBJECTS AND BIOLOGICAL CELLS

Living biological cells constantly vary their position, shapes, sizes and other biophysical characteristics which analysis results crucial for their study, together with the detection and diagnosis of disease. Tracking the cell motion in real time as well as observing intracellular phenomena in 3D require optical microscopic techniques able to achieve high data acquisition and processing rates while providing enough spatial resolution. Since the cell is mostly transparent its analysis often relies on targeting specific cellular structures by using labeling agents such as fluorescent dyes requiring a high level of illumination intensity, that chemically affect and might damage the cell.

In this Chapter we showcase the use of PC-ODT for the analysis of living samples with fleeting dynamics by reconstructing their 3D RI distributions at video-rate without requiring the use of labeling agents. In these studies, the time is a critical parameter, so the RI measurements must be acquired as fast as possible. The PC-ODT, implemented with the experimental setup comprising the optical refocusing system enables fast video-rate 3D high resolution quantitative imaging. To test its performance for real-life applications, video-rate 3D RI imaging of live bacteria optically transported by different laser traps along prescribed trajectories is experimentally demonstrated. These examples evidence the practical use of fast PC-ODT in optical tweezers experiments, which is a real-life application of current interest in biophysics. Finally, the short-term evolution of live cells (COS-7 kidney cells) is also studied by using video-rate 3D RI imaging providing quantitative information of the cell behaviour revelant in biomedicine.

6.1 Video-rate 3D RI imaging of freely swimming live bacteria

To experimentally demonstrate the performance of the proposed PC-ODT technique for video-rate 3D RI imaging of the sample, here we apply the setup with the ORM in configuration 1 (see Section 4.2). Each stack of intensity images ($400 \times 400 \times 50$ voxels) corresponding to a 3D volume of $40 \times 40 \times 12\,\mu\text{m}^3$ has been measured in 100 ms by using a camera exposure time of $t_{exp} = 2$ ms, thus achieving an acquisition rate of 10 fps for 3D stacks. Since the considered sCMOS camera is able to acquire images of 400×400 pixels at a rate of $\nu_{\text{CCD}} = 1/t_{exp} = 500\,\text{fps}$, the frequency of the triangular electrical signal of the ETL (ν_{ETL}) has been set at 5 Hz (with an amplitude varying between 40-160 mA, see Section 4.3), thereby providing a proper focal length shift to axially scan the region $\triangle z_{defocus} = 12\,\mu\text{m}$ by recording $N_z = 50$ images. We have considered living yeast cells, in particular Schizosaccharomyces pombe (further referred to as S. pombe) bacteria dispersed in aqueous sugared solution. The S. pombe bacteria are rod-shape cells particularly interesting in genetics [128] and well suited for testing quantitative imaging techniques [129]. They exhibit natural swimming motion and have fine cellular features, as shown in the 3D RI reconstruction from Fig. 6.1 without applying any optical trap. These cells were prepared as detailed in Appendix E.1. We have considered a value of $\varepsilon = 0.05$ (parameter linking the real and imaginary part of the RI) for the RI reconstruction with PC-ODT, which has been experimentally proved successful for different biological specimens such as diatoms and blood cells [89].

Fig. 6.1 corresponds to one RI frame of the video-rate 3D RI reconstruction also provided as a video file in Visualization 1 of Ref. [108], which shows S. pombe natural motion for a recording time of 1 s. Note that the reconstructed 3D RI has been rendered as a volume by using open source software, Fiji imaging suite (ImageJ, open-source software) [130]. In Fig. 6.1 we observe the cell division process. The bacteria were going through their reproductive cycle that can be of several hours. This kind of bacterium divides itself by fission yielding two identical daughter cells separated by a medial wall or septum [131, 132]. The daughter cells present a cleavage point in the septum, then they divide and each one subsequently repeat the fission process. The septum is clearly distinguishable in Fig. 6.1 (see the cells located at the center, they have a size of $\sim 3.5\,\mu\text{m}$ long and $\sim 1.5\,\mu\text{m}$ wide). Furthermore, small features such as endoplasmatic organelles (tiny intracellular structures of $250-350$ nm indicated by arrows in Fig. 6.1) are also observed into the cytoplasm and the cell membrane is clearly bounded. The RI of the membrane ($n_{\text{Re}} = 1.40 \pm 0.01$) is higher than that of the cytoplasm ($n_{\text{Re}} = 1.38-1.39$). These RI values are in good agreement with the literature [129] and support the weak object approximation given that the refractive index of the sugared water is close to $n_m = 1.37$, thus the RI contrast between surrounding medium and bacteria is about $\Delta n_{\text{Re}} = 0.03-0.04$. Finally, to observe the typical wobbling and swimming motion [133] exhibited by the S. pombe bacteria the reader is referred to the video file Visualization 1 of Ref. [108].

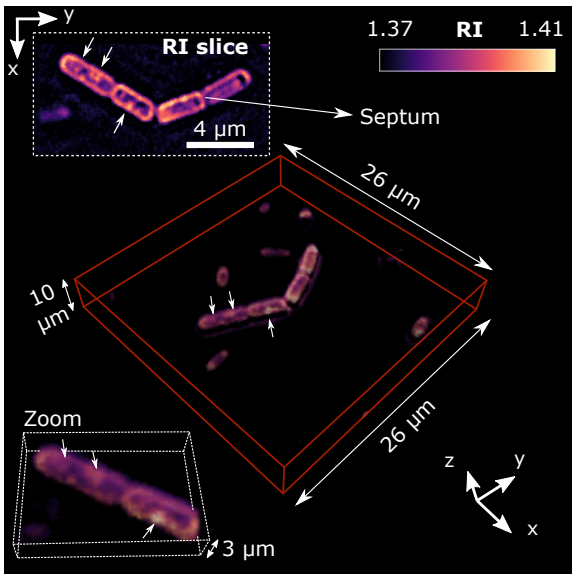

Figure 6.1: 3D RI reconstruction ($\lambda_0 = 450\,\text{nm}$) of multiple S. pombe bacteria freely swimming in sugared solution. The inset displaying a RI *xy*-slice shows four concatenated cells ($\sim 3.5\ \mu\text{m}$ long and $\sim 1.5\ \mu\text{m}$ wide) with well-defined membrane and exhibiting small intracellular structures of $250 - 350$ nm indicated by the arrows. Tiny bacteria, freely swimming in the scanned sample volume, are also observed (see Visualization 1 of Ref. [108]).

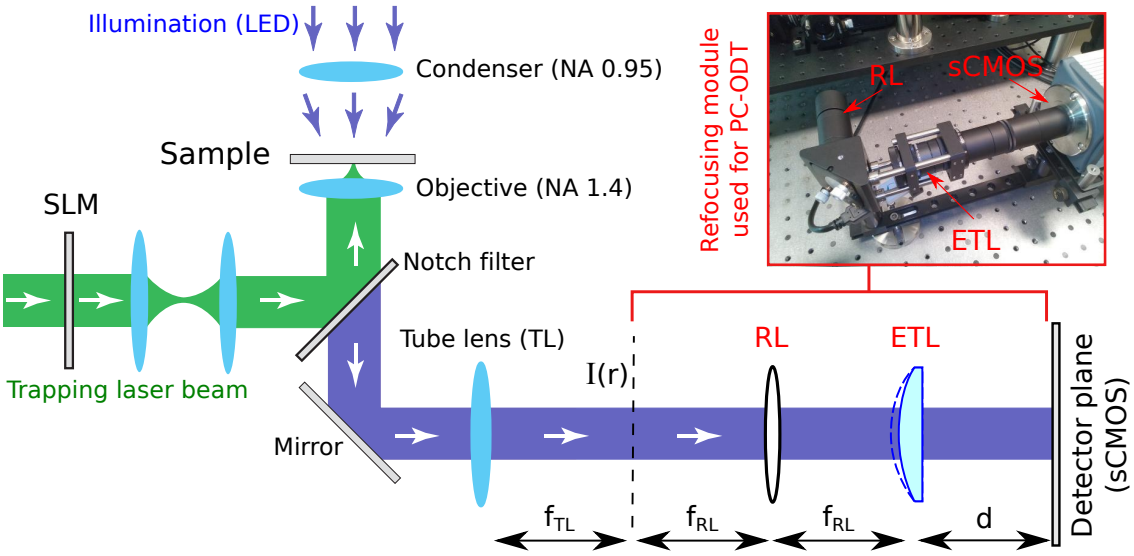

Figure 6.2: Sketch of the experimental setup used for simultaneous video-rate 3D RI imaging (based on PC-ODT) and optical trapping and manipulation of living cells. In the wide-field microscope (comprising the condenser and objective lenses) two systems have been incorporated: the measurement setup required for PC-ODT and the setup for shaping the laser traps (LC-SLM and the laser device). The laser beam modulated by the LC-SLM is relayed onto the back aperture of the objective lens by using a set of two identical convergent lenses working as a $\times 1$ Keplerian telescope.

6.2 Video-rate 3D RI imaging of optically manipulated bacteria

Another relevant achievement is that the PC-ODT technique is fast enough to exploit video-rate 3D RI visualization together with optical manipulation tools (e.g., optical tweezers) for the study of the cell biophysics. Thus, this Section includes optical manipulation of living bacteria by using laser traps providing optical confinement and transport of the cells. Specifically, we have used freestyle laser traps as reported in Ref. [134] to optically confine and transport the bacteria along arbitrary 3D trajectories. Such freestyle laser traps have been experimentally demonstrated for optical manipulation of inorganic samples such as dielectric micro-spheres of 1 μm (silica) and metallic nanoparticles (e.g., gold and silver particles of 100 nm). Here, it is proved that this laser trap allows for optical confinement and transport of living cells along trajectories that can be designed according to the considered application. While the optical transport of multiple living cells is a challenging task by means of conventional optical tweezers (point-like laser traps, see for example [133]), it can be easily achieved by freestyle laser traps which provides an independent light-driven control of their trajectory and speed.

The experimental setup used for conducting simultaneous video-rate 3D RI imaging and optical manipulation of living cells is illustrated in Fig. 6.2. This setup is similar to the one comprising the ORM in configuration 1 described in Section 4.2 and configured as in Section 6.1, but it further includes the equipment required for shaping the laser traps and performing optical trapping, which in turn comprises a laser device and a programmable liquid-crystal spatial light modulator (LC-SLM). The freestyle laser traps require a computer generated hologram addressed into a programmable LC-SLM (Holoeye PLUTO device with pixel size of $8\,\mu$m). Once the laser beam is modulated by the LC-SLM, it is relayed onto the back aperture of the objective lens by using a set of two identical convergent lenses (with focal length of 150 mm) working as a $\times 1$ Keplerian telescope. The freestyle 3D laser traps provide light-driven particle motion along a light curve due to the confinement and propelling forces exerted over the particle which arise from intensity and phase gradients of the beam, respectively. As depicted in Fig. 6.2, a Notch filter (Semrock, dichroic beam splitter for $\lambda = 532$ nm) has been used to redirect the trapping laser beam (Laser Quantum, Ventus, $\lambda = 532$ nm, 170 mW, linearly polarized) towards the objective lens. This filter also avoids imaging the backscattered laser light into sCMOS camera. Note that each cell confined in the considered laser traps receives an optical power of a few mW during a time of about 20 s, thus preventing the cell from being damaged. The reader is referred to Refs. [134, 135] for further details about the design and generation of the considered laser trapping beams and their optical forces that allow confining and propelling the particles.

To illustrate the working principle of the freestyle laser trap and illustrate its performance in manipulating living bacteria, let us first consider a 3D spiral laser trap as the example shown in Fig. 6.3(a). The trapping laser beam has been strongly focused in form of 3D spiral and its high-intensity gradients exert trapping forces confining the bacteria along the curve. While, the phase gradient of the trapping laser beam has been designed to exert an optical propelling force [134–136] that is responsible for the transport of bacteria

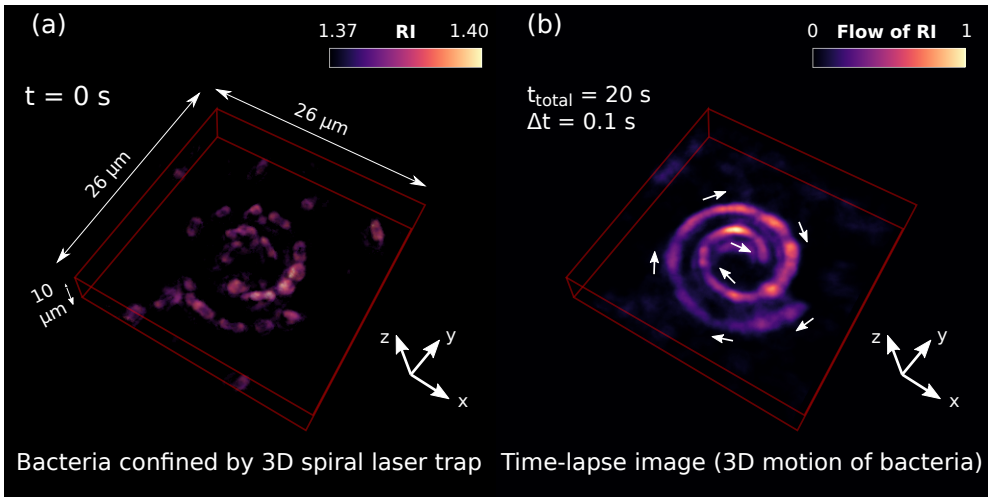

Figure 6.3: (a) A freestyle laser trap in form of 3D spiral is used to optically confine and transport the bacteria along the spiral, see Visualization 2 of Ref. [108]. (b) The trajectory followed by the transported bacteria along the spiral is revealed in the displayed time-lapse image, which has been made by combining all the recorded video frames of Visualization 2 of Ref. [108].

along the curve. Indeed, as observed in the temporal evolution of the reconstructed 3D RI provided in Visualization 2 of Ref. [108], multiple bacteria have been transported from the spiral tail towards its center. The time lapse image displayed in Fig. 6.3(b) has been made by summing all the recorded 3D frames of RI and it reveals the trajectory followed by the trapped bacteria, which coincides with the spiral shape of the optical trap as expected. Note that this kind of time lapse image shows the trajectory followed by the bacteria in form of accumulated RI (normalized at its maximum value) that can be understood as a flow of RI along the curve.

The speed and motion direction of the trapped bacteria can be also optically controlled along 2D curves in real time if needed. For example, Fig. 6.4 (a) and video recording Visualization 3 of Ref. [108] show three bacteria (about 6 μm long and 2 μm wide) confined in a ring trap that sets them into rotation in a programmable way. Note that S. pombe cells spread in the longitudinal direction while remaining at almost constant width [138], as it is observed in Fig. 6.4 (a). Another advantage of reconstructing the video-rate 3D RI is that this permits tracking the cell and estimating its speed as displayed in Fig. 6.4 (b), see also Visualization 3 of Ref. [108]. In particular, the local speed map shown in Fig. 6.4 (b) reveals that the cell labeled as B1 follows a pendulum-like movement along the ring trap reaching a maximum speed of 6 μm/s and a minimum speed of 1 μm/s at the recoil points where its motion has been optically switched [134, 135] from clockwise to counter-clockwise rotation and vice versa. Such a speed map also confirms that the bacteria are stably trapped in the ring trap. The rest of cells also follow a prescribed pendulum-like movement but along a shorter distance. These tracking results have been obtained by using a particle tracking software included in Fiji, *Trackmate* plug-in [139], which is well suited for monitoring of the cell motion.

This optical confinement and transport tool results promising for contactless guiding of

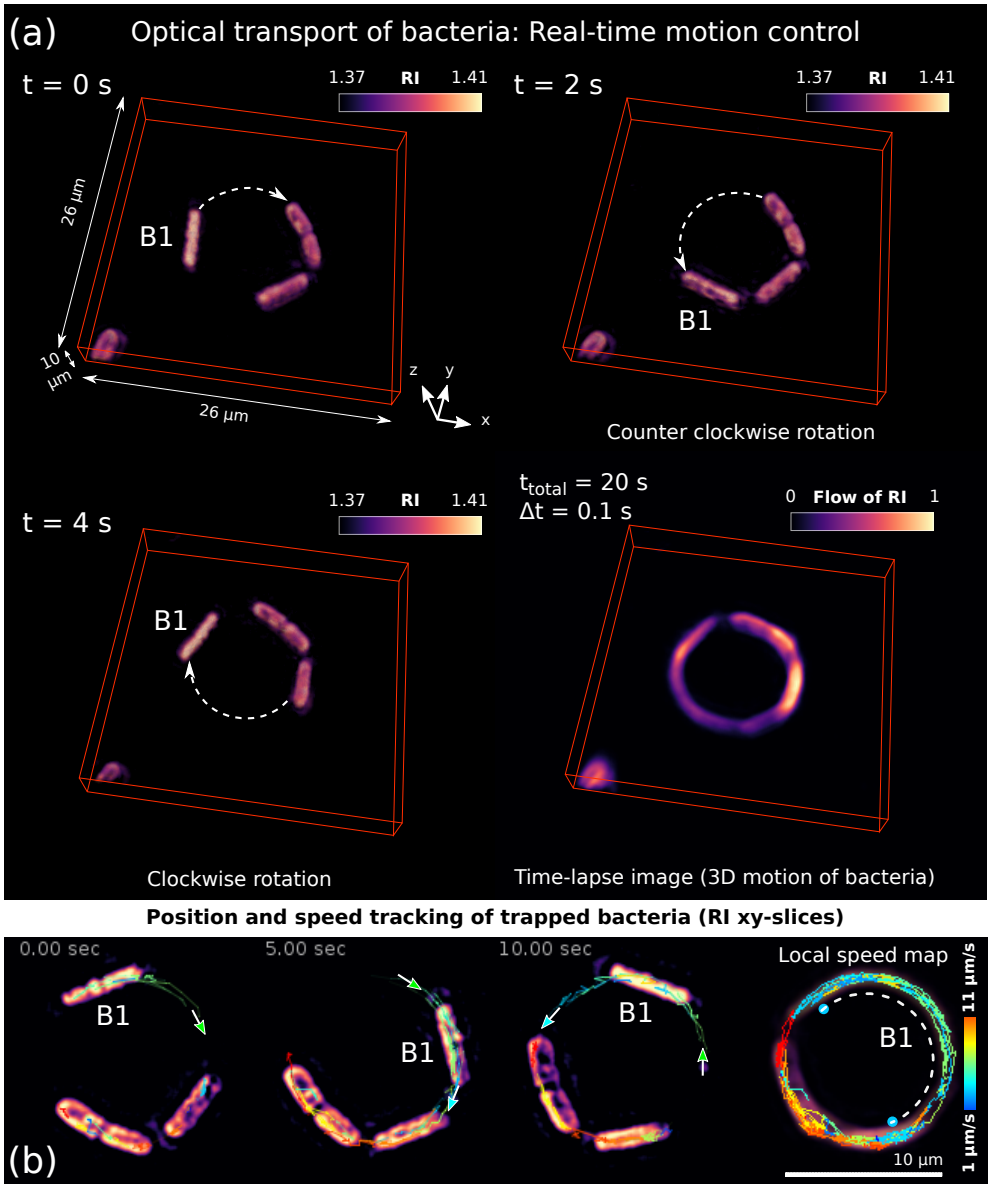

Figure 6.4: (a) Experimental results demonstrating video-rate 3D RI reconstruction of three bacteria (S. pombe, ~ 6 μm long and ~ 2 μm wide) while they have been optically manipulated by using a laser ring trap. This example shows real-time motion control achieved by simultaneously exploiting trapping and propelling optical forces. The cell labeled as B1 optically transported along the ring follows a pendulum-like motion (due to switching the rotation direction) as observed in Visualization 3 of Ref. [108]. The time-lapse image confirms stable 3D confinement of the cells in the ring. (b) The positions of the confined cells have been tracked revealing their trajectory and velocity distribution during this experiment, see the corresponding local speed map. Note that some of these cells are undergoing division cycle with a clearly visible medial cavity. In these experiments the recording time was 20 s with rate of 10 fps (100 ms each 3D frame).

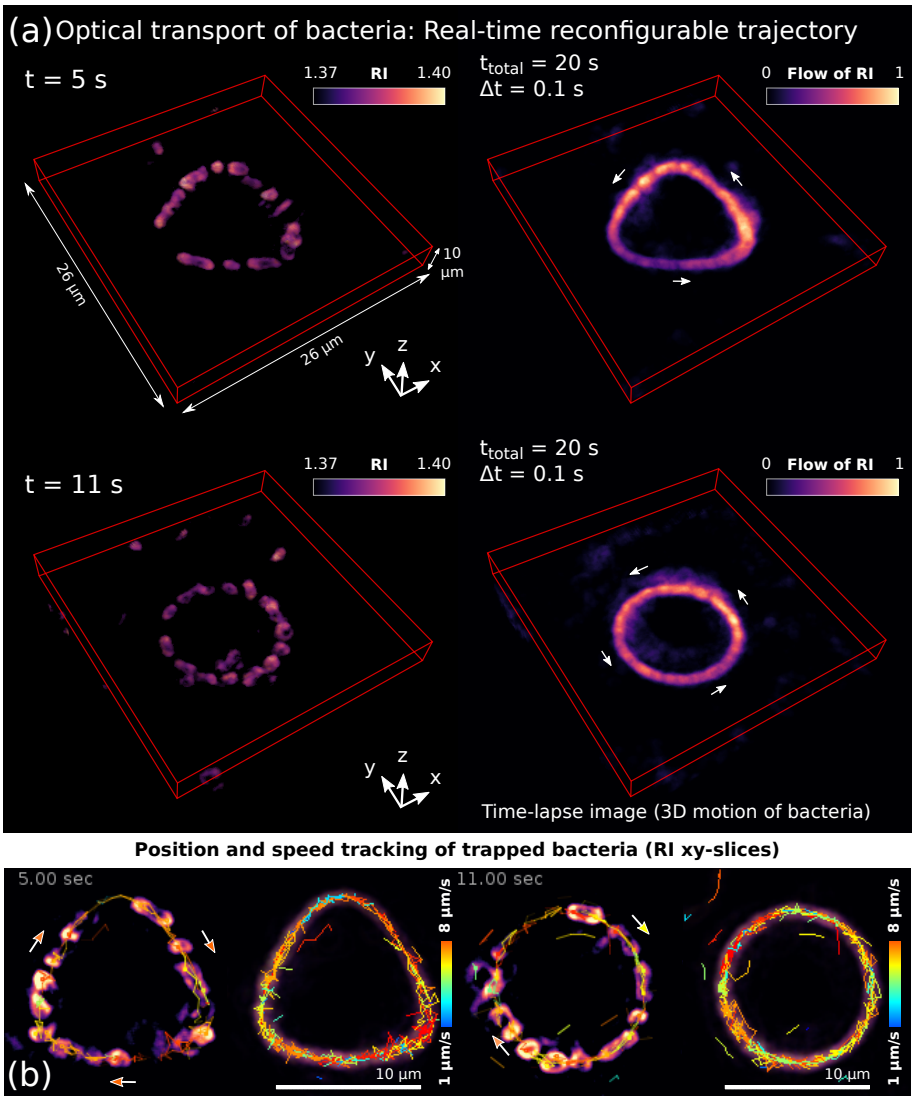

Figure 6.5: (a) Experimental video-rate 3D RI results demonstrating real-time reconfiguration of the transport trajectory of bacteria, switching between triangle and ring laser traps. The time-lapse images reveal the corresponding flows of cells transported along the curves while their tracking confirms a nearly uniform velocity distribution for each case as shown in (b), see also Visualization 4 of Ref. [137]. In these experiments the recording time was 20 s with rate of 10 fps (100 ms each 3D frame).

living cells. To further illustrate its versatility, Fig. 6.5 (a) and Visualization 4 of Ref. [108] show how the trajectory can be reconfigured in real time while keeping the transported cells well confined. In this case the bacteria have been confined in a triangle-shaped trapping laser beam that sets them into rotation along the triangle. After a few seconds the triangular trap has been rapidly switched to a ring trap and consequently the rotating flow of bacteria immediately gets confined in the new trap geometry, as observed in Visualization 4 of Ref. [108]. The corresponding speed maps displayed in Fig. 6.5 (b) indicate stable confinement as expected. Moreover, the velocity distribution is almost uniform along both

curves because in both kind of traps the phase gradient prescribed along the curve is uniform [135], that yields a constant optical force for the ring trap and slightly changing force for the triangular one. These optical forces continuously propel the bacteria. Nevertheless, there also exist hydrodynamic interactions and collisions events between the trapped bacteria responsible for the variations in the velocity distribution observed in Fig. 6.5 (b). We recall that in the case of Figs. 6.4 (a, b) the sign of the phase-gradient force propelling the bacteria has been switched in real time to change the rotation direction of the bacteria along the ring and triangular traps.

All the aforementioned examples demonstrate video rate 3D label-free quantitative imaging that is fast enough even for study 3D optical manipulation of unstained cells, thus resulting in a promising tool for biophysics and biomedicine applications. Such a video-rate 3D visualization of the cell is well suited to study its dynamics while facilities tracking the position, speed, and orientation of the cell in 3D. For example, this allowed us observing the natural wobbling motion of freely swimming bacteria ($1-3$ μm long) as well as characterizing the motion of bacteria optically trapped and transported along 3D curved trajectories. As shown in Fig. 6.5(a) and Visualization 4 of Ref. [108], the trapped bacteria can exhibit continuous reorientation. Particularly, the elongated cell body lies contained into the *xy*-plane (laser curve) but also tends to align along the propagation direction of the trapping beam (*z*-axis). This reorientation seems to be conditioned by random wobbling motion, collisions and hydrodynamic effects apart from complex interactions between the cell body and the laser beam. Nevertheless, more elongated bacteria (~ 6 μm long) as the ones studied in Fig. 6.4 (a) do not exhibit significant wobbling motion and they remained stably aligned along the laser curve (contained in the *xy*-plane) during the entire optical manipulation process. These results illustrate the importance of dynamic 3D label-free quantitative imaging for observing and studying the changes in the structure of cells and their motions in vivo.

6.3 Study of short-term cell dynamics with video-rate 3D RI imaging

The fast monitoring of the sample provided by PC-ODT enables the study of cells with fleeting dynamics, which exhibit noticeable changes in the time scale below 0.5 s. In these studies, the maximum time between two consecutive 3D RI measurements must not exceed 100 ms (equivalent to a frame rate of 10 fps). For evaluating the capability of PC-ODT for the study of cell motion, in this Section we analyze living COS-7 cells, which hail from the African green monkey kidney and typically exhibit a fibroblast-like morphology (see Ref. [140]). We prepare the COS-7 sample following the protocol detailed in Appendix E.2. Afterwards, the cells are immersed in phosphate-buffered saline (PBS) and sealed between cover slips, to prevent evaporation. Then, PC-ODT is carried out and 3D RI images ($500 \times 500 \times 105$ pixels, corresponding to $60 \times 60 \times 28\,\mu$m) are obtained with the ORM in configuration 2 (Section 4.2) equipped with a filter to select $\lambda_0 = 560$nm. Taking into account that we would need the maximum temporal resolution available, we scan $N_z = 105$ z-planes of the sample with 2 ms exposure time each. Note that, in this

case, a much larger z-range of scanning is needed in comparison with samples considered in Chapter 4 and fixed cells that are later studied in Section 7.2. This is due to the relevant motion of the cell in 3D (wobbling, flickering), therefore we would need to guarantee that the whole cell is imaged.

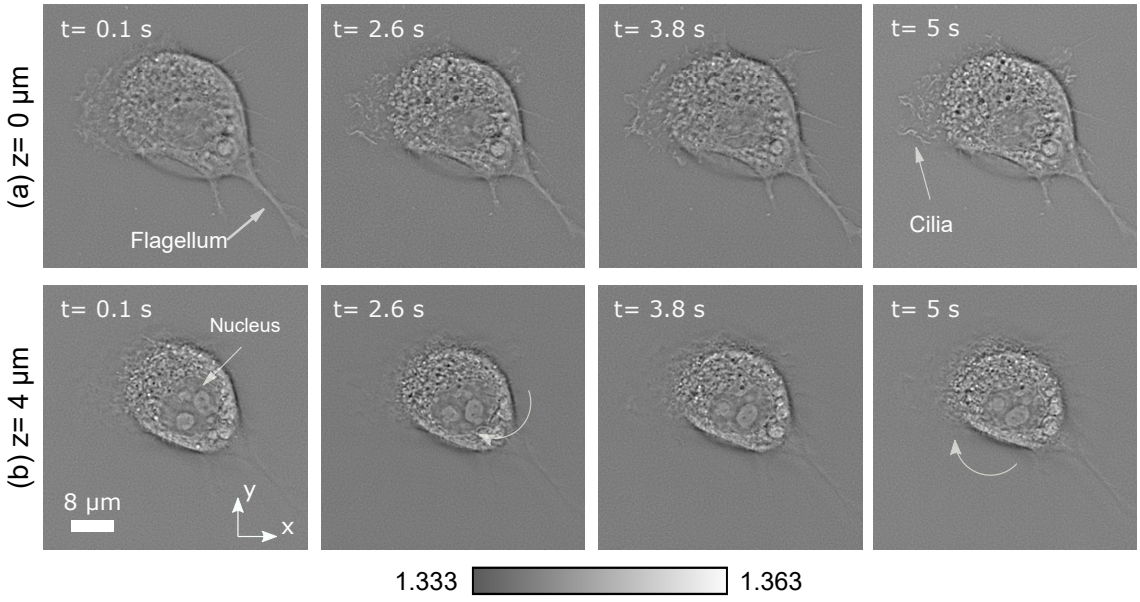

Figure 6.6: Time evolution of two different 2D RI slices of a living COS-7 cell immersed in PBS solution.

As an example of relatively short-term observation, Fig. 6.6 includes the evolution in time (a recording during 5 s) of two characteristic planes at $z = 0\,\mu$m (a) where a flagellum, a wavy membrane and plenty of cilia are seen; and at $z = 4\,\mu$m (b), in which three organelles immersed in the nucleus are observed. Particularly, this cell has initiated its adhesion to the plate at $z = 0\,\mu$m, which explains why the flagellated structure is extended and the lack of relevant motion. Otherwise, in the plane $z = 4\,\mu$m, shown Fig. 6.6 (b), the cell exhibits continuous dynamics like intracellular trafficking, nucleus counterclockwise rotation and nucleus plication.

Furthermore, the underlying dynamics of the cell can be unveiled even at a lower time scale. Let us consider now the Fig. 6.7 where four consecutive frames (each pair separated by only 100 ms) has been analyzed for the previous COS-7 cell, including quiver plots for the velocity maps inside the nucleus for studying the rotation motion of its internal organelles. The speed maps have been obtained by using PIVlab plug-in (a digital particle image velocimetry tool) available for MATLAB [141], that performs a multipass window deformation ensemble correlation widely applied in particle velocimetry applications [142]. Thus, by considering the correlation between consecutive image pairs, we obtain the velocity of each region of the cell. Note that every arrow of Fig. 6.7 corresponds to a block of 7×7 pixels. Thanks to the streamlines of this vector field one is able to characterize the motion of organelles inside entire cell. A higher activity is observed inside the nucleus, in the form of a relatively fast rotation. In particular, it is observed that the speed field magnitude is variable within the range $0-5.4\,\mu$m/s with certain tendency to vorticity

(also measured with PIVlab), particularly noticeable at $z = 4\,\mu$m. This point is interesting, but it requires further research. This example is instructive to demostrate the capability of PC-ODT for biology studies regarding living samples, where high spatial resolution and frame rate are required for an imaging tool.

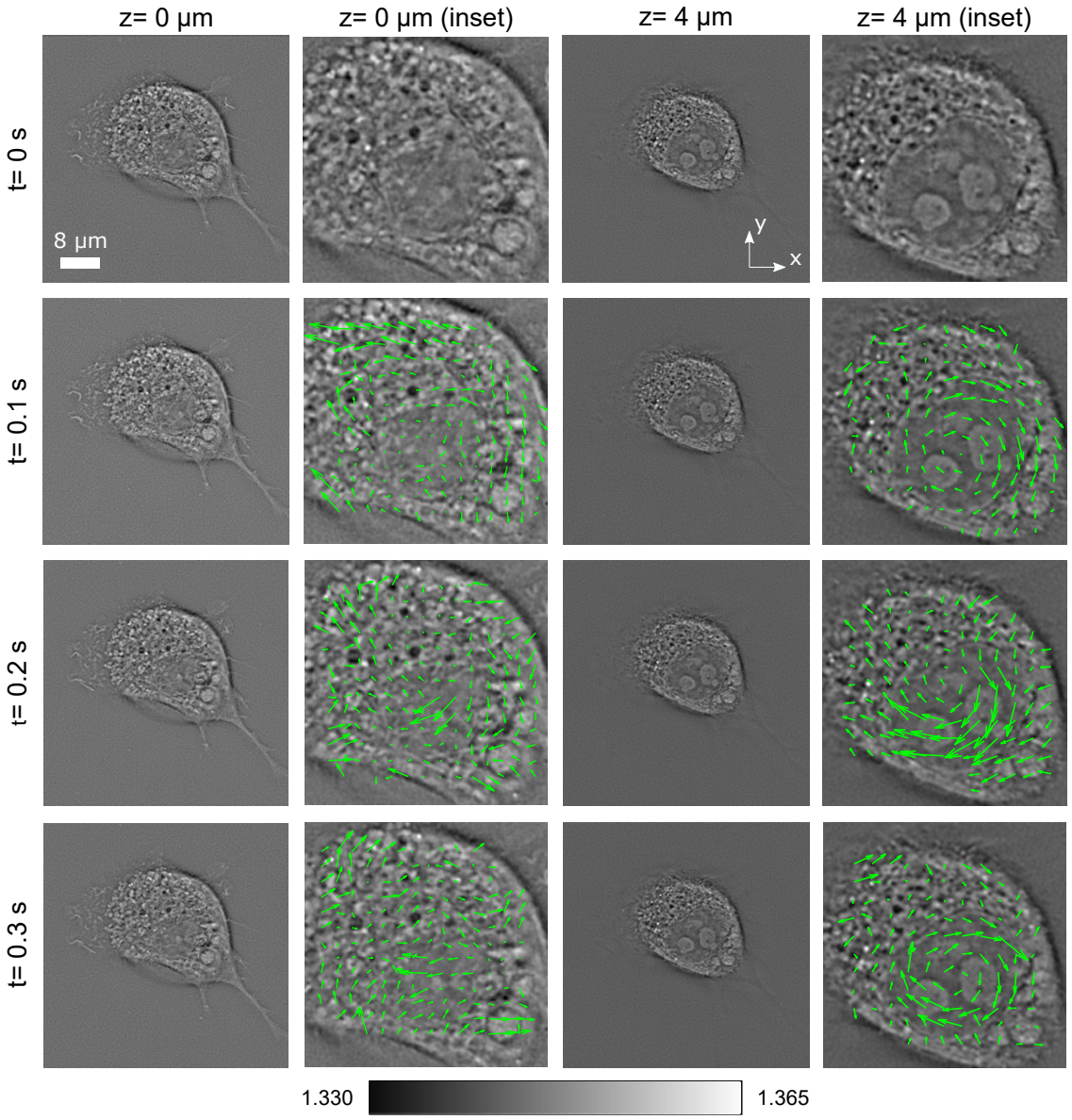

Figure 6.7: Short-term evolution of RI slices of a living COS-7 cell immersed in PBS solution, along with a quiver plot representing the velocity field. It is observed that the speed field magnitude is variable within the range $0-5.4\,\mu$m/s with certain tendency to vorticity, particularly noticeable at $z = 4\,\mu$m.

6.4 Conclusions

In this Chapter we have experimentally proven that PC-ODT provides a 3D data acquisition with a spatial resolution similar to C-ODT but with higher tomography frame rate (e.g. 10 fps in 3D) compared to the current state of the art for C-ODT (2.5 fps and 0.5 fps according to Tomocube [61] and Nanolive [62] companies, respectively). Dynamic 3D RI visualization at video rates results promising in optical manipulation experiments, which often rely on basic imaging methods to study the manipulated objects. Furthermore, we have shown that video-rate 3D RI visualization at 10 fps (region of $40 \times 40 \times 12\,\mu\text{m}^3$ and exposure time of 2 ms) can be sufficient to study optical transport of living cells but it could also be suited for other applications demanding high temporal resolution such as ODT in micro-fluidics [143–146]. Thanks to fast data processing algorithm, each 3D RI volume is computed in around 1.5 s in a conventional laptop. Further, living cell dynamics has been analyzed by using the 3D RI images obtained with PC-ODT together with a velocimetry tool, PIVLab. Therefore, we envision that this technique will serve for video-rate 3D RI study of dynamic objects and living samples (i.e. cells) in future real-time applications.

Chapter 7

3D RI IMAGING AS A TOOL FOR CELL ANALYSIS IN BIOMEDICINE

ODT is a computational imaging technique that allows reconstructing the specimen 3D RI distribution, which has been widely adopted for obtaining quantitative biomedical information such as the shape, density, volume, dry and wet mass, membrane deformability and even chemical composition of cells [41, 118, 147–150].

Thanks to its noninvasive nature, the 3D RI analysis has been recently exploited in several biomedicine applications. For instance, in Ref. [151] RI tomograms have been applied to find morphological and behavioral differences between red blood cells of healthy and diabetic individuals. It has also led to promising results in cancerous epithelial cells bioanalysis [152] and influenza virus presence in human alveolar epithelial cells [153]. Moreover, the RI has been recently exploited in the biomedical research as a diagnostic tool for discerning the metastatic potential of malignant cells [147, 154, 155]. In this way, RI changes have even been considered as a biomarker for the monitorization and diagnosis of certain diseases, such as malaria infection induced by the *Plasmodium falciparum* parasite and detected by blood screening [50, 156, 157].

Nevertheless, most of these applications rely on C-ODT which demands interferometric and expensive setups. In this Chapter, some results of PC-ODT application in biological studies are considered in order to demonstrate the feasibility of this technique as an affordable alternative to conventional C-ODT. As we have previously demonstrated, the developed PC-ODT technique is faster as well as competitive and it is ready for its use in real-life applications. This allowed us to establish several collaborations with reseach groups from different fields including optics (Institut d'Optique, University of Bordeaux, where we carry out most of the experiments with HeLa and COS-7 cells described in this Chapter), medicine (with collaborators from the Faculty of Medicine of the University of Groningen, for studying mitochondria damage induced by certain drugs) and veterinary (with collaborators from the Faculty of Veterinary of the Complutense University of Madrid, in order to carry out a study of *Leishmania* parasite over canine macrophages).

The Chapter is organized as follows. First, the derivation of the dry mass concentration (DMC) of a cell based on its 3D RI is explained. Further, we demonstrate that PC-ODT is able to identify certain cell diseases which induce morphological and RI variations, thereby paving the way to tools of label-free diagnosis. Particularly, PC-ODT has been applied to

reconstruct the RI of fixed samples, parasited and healthy canine macrophage samples. The 3D RI and the global averaged DMC of the samples are compared between healthy and parasited groups in order to identify which macrophages suffer from parasitism. Next, we demonstrate that PC-ODT can be used for the analysis of the 3D RI dispersion, particularly at two different illumination wavelengths, in order to determine its role in the study of the cell. Then, we demonstrate that the DMC analysis is also useful for the analysis of living samples. For this purpose, a long-term study (during several hours) consisting of the monitoring of a living cell under nutrient deprivation conditions is carried out, in order to illustrate that the biophysical changes of the sample can be explained through mean DMC changes. Finally, we have also tested PC-ODT in a pharmacological essay, in which the effects of certain drugs over hepatocyte cells need to be evaluated. In this case, the changes cannot be detected just through a comparison of the averaged RI (or equivalently, the DMC) of the entire cells, because the medicaments may induce subtle changes only in certain regions of the cell. Interestingly, the PC-ODT has revealed that the RI changes are noticeable in a target organelle (the mitochondria of the cell) and this conclusion has been corroborated with clinical trials.

7.1 Dry mass concentration measurement of a cell based on its 3D RI

The dry mass of a cell stands for the mass of all cellular content excluding the water. During the life of a cell, its dry mass changes depending on the health state, the chemical composition or the cell cycle. Consequently, by measuring the biomass variations one obtains valuable knowledge about the sample [140]. As reported in Refs. [41,158,159], for biological samples immersed in an aqueous medium it exists a linear relationship linking the DMC (or density) of the sample and the real part of its RI, as follows

$$\mathrm{DMC}(\mathbf{r}) = \left(\frac{n(\mathbf{r}) - n_w}{\alpha} \right), \tag{7.1}$$

where α represents the so-called specific refractive index increment, n is the sample's RI and n_w is the water RI. We recall that in PC-ODT the refractive index contrast of the cell is $\Delta n(\mathbf{r}) = n(\mathbf{r}) - n_m$, where n_m stands for the RI of the immersion medium surrounding the sample (not necessarily water). As stated by Barer [159], the main solid components of the cell protoplasm are proteins, lipids and carbohydrates (typically conforming complexes with proteins), and other components (such as amino acids or nucleic acids) whose RI is close to that of proteins. Although this chemical composition is variable, an average value around $\alpha = 0.0018$ dL/g is widely accepted within the visible range when nucleated cells are considered [41, 159, 160]. A possibility often applied in the literature to compute the DMC is assuming a particular shape for the sample and extrapolate the dry mass estimation from a single 2D phase image. For instance, the dry mass of E. coli cells have been obtained from a 2D phase image and fitting it to a 3D cylinder, see Ref. [19]. Again, in this latter case the error of the measurement is expected to be important and the shape of the sample is *a-priori* unknown. In this regard, PC-ODT does not need the previous knowledge of

sample structure, as it scans the sample in 3D, and the sample volume can be approximated if a proper number of z-slices is collected.

For accurate sample structure analysis, after performing the PC-ODT technique and obtaining the corresponding 3D RI stack $n(\mathbf{r})$, an additional segmentation step has been performed to separate the sample from the surrounding medium (background). For this purpose, the RI gradient modulus ($|\nabla n|$) has been computed according to Eq. 7.2.

$$|\nabla n(\mathbf{r})| = \sqrt{\left(\frac{n_{x+1,y,z} - n_{x-1,y,z}}{\Delta x}\right)^2 + \left(\frac{n_{x,y+1,z} - n_{x,y-1,z}}{\Delta y}\right)^2 + \left(\frac{n_{x,y,z+1} - n_{x,y,z-1}}{\Delta z}\right)^2}, \tag{7.2}$$

in which the different resolution in transversal (Δx, Δy) and axial (Δz) directions has been taken into account. By normalizing the gradient modulus to the range $[0,1]$ ($|\nabla n_n(\mathbf{r})| = |\nabla n(\mathbf{r})|/\max[|\nabla n(\mathbf{r})|]$ and fixing a low threshold (τ) for $|\nabla n_n(\mathbf{r})|$, one obtains a binary mask, $\mathrm{BM}(\mathbf{r})$ as follows

$$\mathrm{BM}(\mathbf{r}) \rightarrow \begin{cases} 1, & |\nabla n_n(\mathbf{r})| > \tau \text{ and } n(\mathbf{r}) > n_m \\ 0, & \text{elsewhere} \end{cases}, \tag{7.3}$$

where the value of τ (typically in the range $10^{-2} - 10^{-1}$) depends on the background uniformity and SNR. In this way, only the positions of $n(\mathbf{r})$ where $\mathrm{BM}(\mathbf{r}) = 1$ are considered as cell in order to compute the DMC. The more homogeneous the background is, the lower τ value is needed. This RI gradient modulus thresholding technique has been succesfully applied in similar segmentation tasks as it accounts for RI local variations that are different for the background and for sample itself, typically involving little variations in background in comparison with steep changes in the specimen [126, 160–162]. By taking into account the gradient along with the RI itself, one gets a better discrimination of cell structures while removing remaining noise from the deconvolution. For instance, regions with low RI contrast and low normalized RI contrast gradient modulus values ($\Delta n(\mathbf{r}) \rightarrow 0$ and $|\nabla n_n(\mathbf{r})| \rightarrow 0$) correspond to the background. Rather, high RI and high RI gradient modulus are associated with fine details (i.e. if cell samples are considered, tiny features are mainly vesicles and organelles within the cytoplasm). This gradient information can be easily obtained and incorporated to enhance the detection of different sample components. In this way, after $n(\mathbf{r})$ segmentation, the DMC is computed by means of Eq. 7.1. Once the DMC is obtained, it would be possible to calculate the global dry mass of the sample by integration throughout the sample volume.

7.2 Label-free bioanalysis of *Leishmania infantum* using PC-ODT

The goal of this Section is to illustrate the use of RI tomography for quantitative analysis of unstained DH82 cell line (canine blood macrophages) infected with *Leishmania infantum*. The study of *Leishmania* infection has attracted great attention from the scientific community because, according to the World Health Organization, 20000 people die annually from

this disease [163]. Nowadays, this disease is second only to malaria as parasitic infection in the world. To date, there is still no vaccine on the market capable of preventing human leishmaniasis, and although there are vaccines for veterinary use, their effectiveness is quite limited [164]. The antileishmanial treatments present important disadvantages such as the appearance of resistances and their high toxicity making necessary the development of new drugs [165]. Consequently, a tool that provides an accurate intracellular screening of the sample is needed and, in this regard, bioanalysis based on RI emerges as an attractive alternative to traditional staining techniques.

Leishmaniosis is a vector-borne zoonosis widely distributed throughout the world whose responsible etiological agent is a protozoan belonging to the genus *Leishmania* with several species according to their geographical distribution [166]. *Leishmania* is a dimorphic parasite with an intracellular phase called amastigote, and an extracellular flagellated phase known as promastigote. The promastigotes need over a period of 4 to 24 h in order to transform into amastigotes. Thereafter, the infection is sustained by amastigote forms in the infected hosts. The sizes of these intracellular amastigotes typically measures $1-5\,\mu$m in length by $1-2\,\mu$m in width. Vector transmission is carried out from a diptera known as Sandfly and the main species affected are human and canines, whereas more than 50 species have been described worldwide as reservoirs [167].

Here we demonstrate the use of PC-ODT technique, which allows for straightforward 3D label-free imaging of cells, for the monitorization and diagnosis of *Leishmania* infection in canine macrophages. The sample preparation, fixation and the infection protocols have been detailed in Appendix E.3. The sample is fixed with methanol (whose RI is 1.333 at a wavelength of $\lambda_0 = 450\,$nm and 300 K of temperature according to Ref. [168]) and immersed in a matching medium (Dulbecco's Phosphate Buffered Saline, further referred to as PBS) for imaging. The unstained samples of DH82 cells were divided into four categories, according to the presence of the parasite (parasited, P or healthy, H) and the period of time (24 h or 72 h) from the preparation, and labelled as P24, H24, P72 and H72 respectively.

The four groups (P24, H24, P72 and H72) have been analyzed with the same microscope's configuration, particularly the one comprising the ORM in configuration 1, by considering stained and unstained cells separately. The chosen illumination source is the microscope LED source filtered with a color filter (central wavelength $\lambda_0 = 450\,$nm and FWHM of 20 nm). Moreover, as explained in Section 5.3, a gaussian illumination has been used as it allows for a proper collection of relevant object spatial frecuency content otherwise attenuated by the microscope OTF when bright-field illumination is applied. Each measurement of the intensity stack of axially scanned images has a size of $400 \times 400 \times 50$ voxels, that corresponds to a 3D volume of $40 \times 40 \times 12\,\mu\text{m}^3$. We recall that the OTFs have been computed taking into account the illumination pattern measured in the back focal plane of the condenser lens (see Section 5.4), thus better approximating the experimental conditions of the microscope. After RI computation with PC-ODT, it has been segmented according to the RI gradient given by Eq. 7.3 with a threshold value of $\tau = 0.01$. Finally, the DMC has been estimated following Eq. 7.1 which is applied to cell analysis.

In conventional clinical practice, staining techniques are considered mandatory when it comes to *Leishmania* study. Straightforward inspection of unstained samples intensity distribution obtained with an optical microscope (e.g. under conventional bright field il-

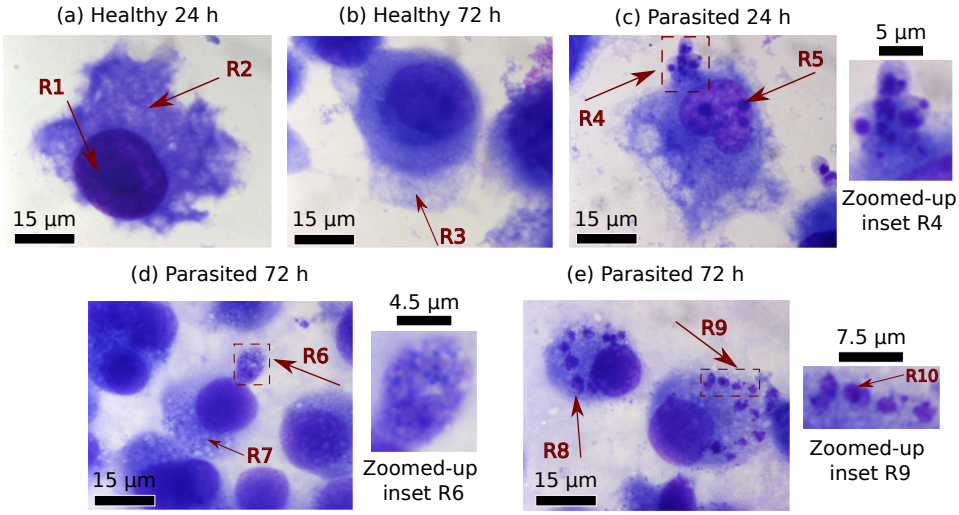

Figure 7.1: DH82 cell images, corresponding to the healthy control (a-b) and parasited groups (c-e). Cells were infected with promastigotes of *Leishmania infantum* BCN150 at a ratio 10:1 (parasites:cells). After 24 h (a, c) or 72 h (b, d, e) cells were fixed in methanol, stained with Giemsa and evaluated by optical microscopy (100x magnification, $\mathrm{NA_c} = 1.4$). Particular features of the cells are marked with red arrows while a close-up view of the intracellular amastigotes within the dashed boxes have been shown in the insets (c-e).

lumination) does not provide enough contrast to enable the parasite observation without post processing corresponding to the PC-ODT. For this reason, we first consider stained samples, usually observed for clinical diagnosis of *Leishmania*, which are displayed in Fig. 7.1. In this case, they have been acquired with a conventional CMOS camera (Thorlabs DCC1240C, exposure time 10 ms). We underline that either the nucleus, some intracellular structures and the parasites are dyed by Giemsa in a purple bluish color. The familiar stained samples will serve as an optional reference to compare with the RI data provided by the PC-ODT.

Once the sample structure has been inspected, let us move forward to the analysis of unstained cells via 3D RI contrast distribution. In this case, the surrounding medium is PBS with $n_m = 1.333$ [168]. Note that other works (for example Ref. [169]) have reported slightly different values of n_m for the same wavelength and temperature. In our analysis we have considered the 3D refractive index contrast of the cell in order to avoid possible uncertainties arising from a tabulated value of n_m. The 3D RI contrast, $\Delta n(\mathbf{r})$, has been represented in Fig. 7.2. Specifically, Fig. 7.2 (a, c) displays two xy-slices of the RI contrast corresponding to healthy macrophages belonging to H24 and H72 groups respectively, while Fig. 7.2 (b,d) shows the 3D RI distribution over the whole studied volume of these samples. One identifies characteristic cell structures such as a rounded nucleus (M1 region within the dashed line circle), long-thin pseudopods (M2), fine cell membrane (M3), nuclear envelope (M4) and the typical surface roughness of membrane projections (M5), which have also been recognized in 2D stained images shown in Fig. 7.1 (b).

Note that in our case the resulting cell volume is about $20 \times 20 \times 12\,\mu\mathrm{m}^3$. We observed

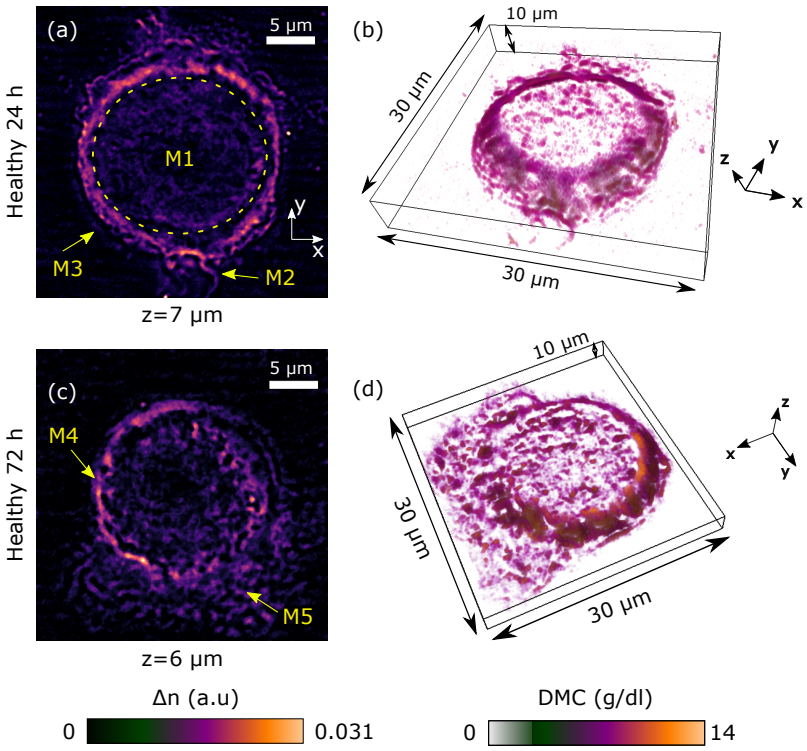

Figure 7.2: Results of healthy DH82 samples. 2D *xy*-slices of the RI contrast distribution for H24 and H72 macrophages are shown in (a) and (c) respectively, while the corresponding 3D DMC reconstructions are displayed in (b, d). The boxes in (b, d) represent the same volume of $30 \times 30 \times 10\,\mu\text{m}^3$.

that this region covers most of the cell's structure and therefore is good enough for the proposed analysis based on the calculation of the average DMC of this region. The live (not fixed) cells could have bigger size and therefore would require an extended axial scanning range, which also can be achieved by using the considered setup. The 3D DMC distributions are displayed in Figs. 7.2 (b, d), which have been created by using the open-source Drishti volumetric visualization software [126]. The inspection of the RI contrast in 3D enables the detection of local variations of the cell's DMC. It was found that the DMC values in the nuclear membrane (above $12\,\text{g/dL}$) are significantly larger than in the rest of the structure ($3-3.5\,\text{g/dL}$) for both healthy groups. From this preliminary analysis we conclude that no relevant differences between healthy cells H24 and H72 arise with regard to their RI contrast and average DMC.

In the case of DH82 cells infected by *Leishmania*, the most remarkable difference in their structure lies in cellular fragmentation and presence of apoptotic blebs (as indicated by blue arrows in Fig. 7.2) that do not appear in healthy samples. These apoptosis evidences can appear as early as 24 h after the infection, see Fig. 7.2 (a), and have also been recognized in the bright-field intensity images of the stained cells displayed in Figs. 7.1 (c-d). From the RI contrast, it is possible to achieve a direct detection of intracellular amastigotes exhibiting high RI contrast values (above 0.03, colored in orange in the first column of

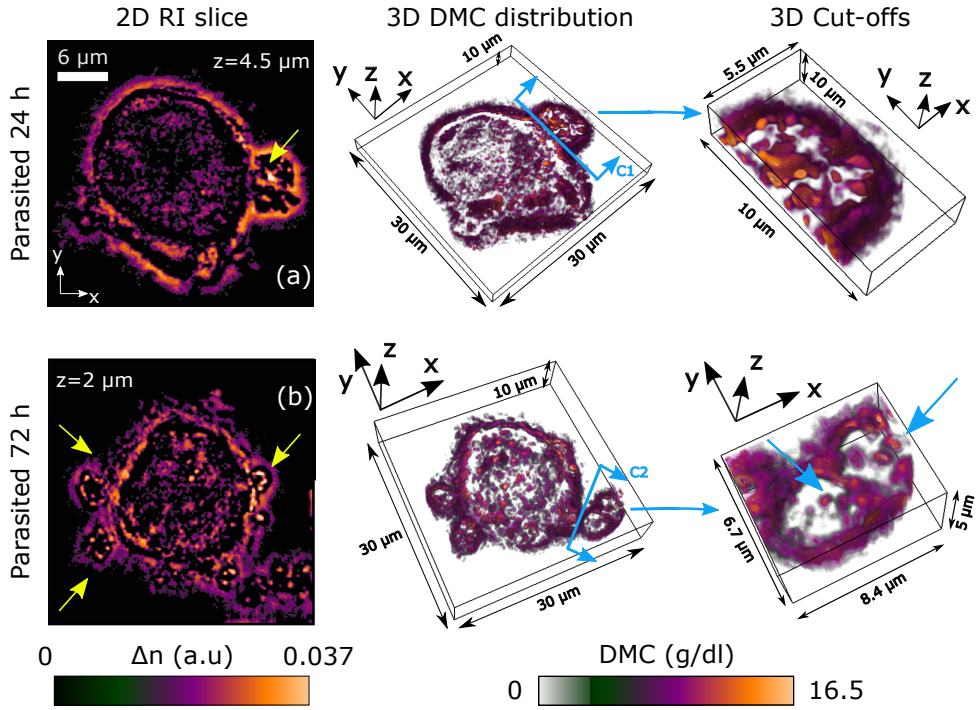

Figure 7.3: Results of parasited DH82 samples, for P24 (a) and P72 (b). For each cell three graphs are included: a 2D *xy*-slice of the RI contrast (first column, in which yellow arrows point towards apoptosis blebs), a view of the 3D DMC reconstruction (second column) and the corresponding magnified regions of the latter (third column) cut by planes C1 and C2 respectively, for highlighting the location of some parasite amastigotes within the membrane blebs.

Fig. 7.2) and located within the blebs. We recall that such blebs are used for spreading the parasitical infection to neighbour cells.

The reconstructed RI-contrast maps also enable a quantitative estimation of the modifications induced by the parasite such as DMC changes in certain cell regions and its evolution as the infection progresses. We have found that the DMC (see Fig. 7.2, second and third columns) of parasited macrophages nucleus membrane (between $14-15\,\mathrm{g/dL}$) is higher than that of the healthy samples (between $12-13\,\mathrm{g/dL}$). Again, as in healthy samples, the DMC of nucleus membrane is superior to the one from the rest of infected cell structure. The rise of average DMC in parasited samples in comparison with the healthy ones can be explained because apoptotic bodies (that typically contain nuclear material and actin cytoskeleton fragments) are shed within the cell [170], thus changing its DMC.

Let us now analyze the temporal evolution of the mean DMC for healthy and infected groups. 40 cells from each group (H24, H72, P24 and P72) have been considered and their mean DMC has been calculated for the scanned cell region (see Fig. 7.2). Relevant differences emerge between the infected and control groups. Both uninfected samples show similar ranges of averaged DMC: H24 presents DMC values of $2.639-3.947\,\mathrm{g/dL}$ (median of $3.189\,\mathrm{g/dL}$) whereas H72 exhibits a DMC of $2.793-4.717\,\mathrm{g/dL}$ (median of $3.172\,\mathrm{g/dL}$). Nevertheless, when the P24 group is considered, a slight rise in median DMC

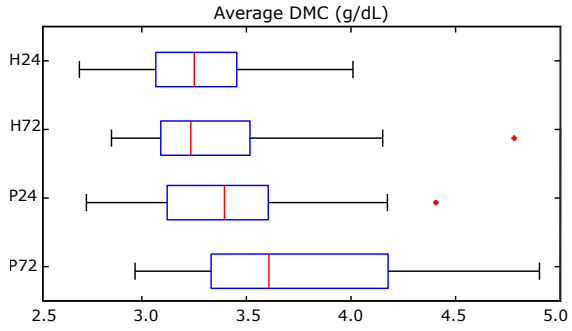

Figure 7.4: Boxplot of the average DMC for the four groups of samples: H24 (healthy 24h), H72 (healthy 72h), P24 (parasited 24h) and P72 (parasited 72h). The red line stands for the median DMC value and outliers are marked with red crosses.

Test	Significant differences?	p-value
H24 vs P24	Yes	0.0214
H72 vs P72	Yes	0.0026
P24 vs P72	Yes	0.0048

Table 7.1: Results from statistical t-tests carried out to verify the relationship between DMC changes and *Leishmania* presence in DH82 cells.

value ($3.383\,\mathrm{g/dL}$) is observed in comparison with any of the healthy cases. This increment is even more noticeable for P72 cells, for which DMC reaches a median value of $3.595\,\mathrm{g/dL}$ and it spans over the interval $2.956 - 4.889\,\mathrm{g/dL}$. This fact suggests that a DMC increase is associated with the presence of *Leishmania* and this change is more remarkable as the time since infection increases. Moreover, as explained in Ref. [171], the communication between *Leishmania* and the macrophages is regulated by proteins, so their effect is expected to prevail in the overall cell RI and subsequently in its DMC.

In order to statistically validate this conclusion, also pointed out by the visual inspection of 3D DMC reconstructions, two hypothesis must be validated. First, we need to test whether the healthy groups DMC (H24 and H72) significantly differs from that of parasited samples (P24 and P72). Secondly, we check if the course of the infection induces changes in DMC by comparing P24 and P72 groups with each other. Each of these statements have been corroborated by conducting an independent sample t-tests [172] over DMC data, as summarized in Table 7.1. Further details about this statistical test are summarized in Appendix F.1. Taken altogether, the results confirm that average DMC can be applied as a reliable parameter for analyzing both the health state of the host cell and the development of *Leishmania* infection.

The heterogeneity of the refractive index contrast values can be another parameter to study as a diagnostic tool apart from the DMC. Indeed, the RI contrast histograms displayed in Fig. 7.5 for healthy and parasited cells evidence a significant heterogeneity in the case of parasited cells. We recall that high $\Delta n(\mathbf{r})$ values (above 0.015) are more frequent in parasited samples, and this is specially more noticeable as *Leishmania* proliferates 72 h after infection.

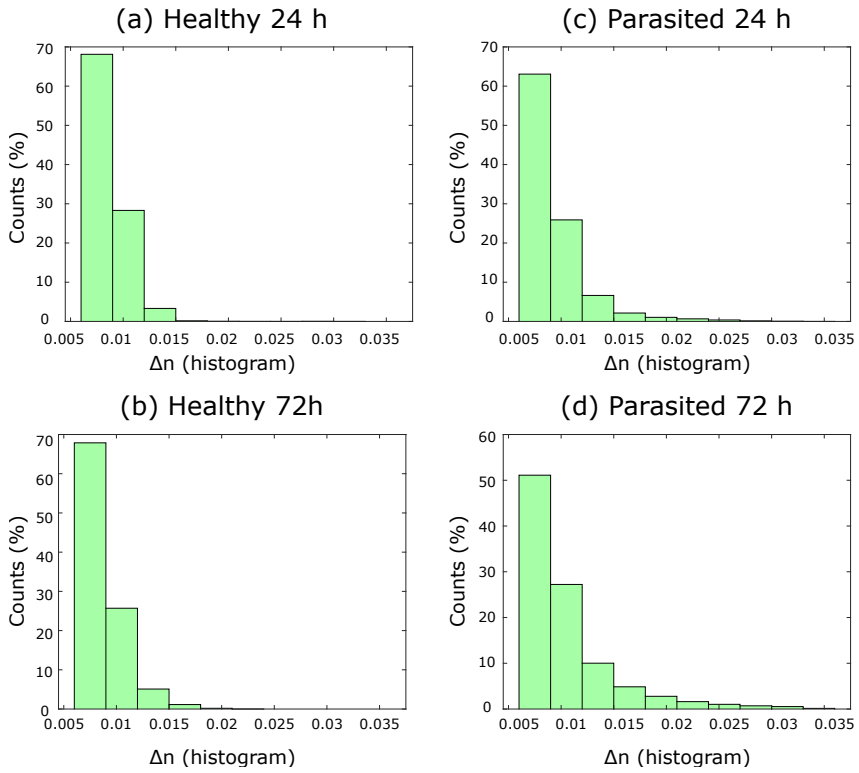

Figure 7.5: Histograms of RI contrast values (Δn) within the cytoplasm of healthy (a-b) and parasited (c-d) macrophages.

To recapitulate, the cell RI is a biophysical parameter that represents the intracellular mass and its concentration providing important insight for the study, diagnosis and assessment of cell health state. Based on PC-ODT technique, in this Section we have performed a quantitative analysis of both healthy and *Leishmania* infected macrophages. We have demonstrated that the cell 3D RI distribution is useful to detect relevant morphological changes in the infected cells such as apoptosis blebs. Our main finding is that the cell DMC (directly obtained from the cell RI) reveals key quantitative information required to gain knowledge about the *Leishmania* spreading. It allows reliable detection and time-lapse monitoring of the parasite proliferation into the cell volume. According to the experimental results, non-infected cells do not significantly change their DMC between 24-72 h from the preparation. Conversely, the infected cells exhibit higher mean DMC than the healthy cultures and this fact becomes even more evident as infection progresses. These experimental results are in good agreement with the known life cycle of the *Leishmania infantum* and its proliferation into the host macrophages. Thus, in comparison with a merely qualitative study over a stained sample, the proposed label-free technique based on RI tomography provides a valuable quantitative measurement to characterize the infection and its temporal evolution.

Note that throughout this *Leishmania* study the sample is fixed but it is also possible to apply PC-ODT technique over live cells. In this way, PC-ODT is appropriate for better taking advantage of temporal changes induced by the parasite in the cell RI. We envision that the increase in DMC could be further exploited to anticipate the development of *Leish-*

mania infection. For instance, it could be applied in the assessment of antileishmanial drug efficacy or even integrated in a medical diagnosis protocol. The considered PC-ODT technique is inherently compatible with a conventional wide-field microscope and allows for straightforward and fast RI tomography (typically at a video rate of 10 fps), which are crucial advantages demanded in the clinical diagnosis protocols.

7.3 Dual wavelength PC-ODT for the analysis of the RI dispersion of biological samples

In this Section we demonstrate that PC-ODT can be used for the analysis of the 3D RI dispersion, in order to determine its role in the study of the cell. For this purpose, we analyze two different types of cells: HeLa and COS-7. HeLa cells are cancerous cells from a human patient suffering from cervical carcinoma. The COS-7 cells, derived from monkey kidney, have been previously introduced in Section 6.3. Both types of cells are widely studied by biologists, therefore in this section we test PC-ODT with them. The culture and preparation procedures, for both HeLa and COS-7 cells, have been summarized in Appendix E.2. Afterwards, the fixation with PFA 4 % (formalin solution) and 0.5 % glutaraldehyde was carried out during 10 min. Finally, they were washed gently with PBS three times to remove fixation and then immersed in PBS and imaged with PC-ODT microscope. We apply the experimental setup with the ORM in configuration 2 with 60x magnification objective ($NA_o = 1.45$) and $NA_c = 0.78$. The broadband LED source of the microscope is filtered with bandpass filters depending on the desired wavelength ($\lambda_1 = 560\,\text{nm}$ and $\lambda_2 = 630\,\text{nm}$, FWHM $= 30\,\text{nm}$). For each sample, a volume of $500 \times 500 \times 95$ voxels ($\approx 60 \times 60 \times 20\,\mu\text{m}^3$) is scanned at room temperature (25 ºC). As the samples have been fixed with formalin, then the measurement time is not as limiting as in live cell imaging. In this case, we may take advantage of intensity averaging to enhance SNR, by scanning 25 times each z-slice. The results are summarized in Fig. 7.6 for both HeLa and COS-7 cells.

The RI of these cells lies in the typical range for eukaryotic cells (1.33-1.36, with the largest values corresponding to tiny organelles immersed in the cytoplasm) and both of them exhibit a big nucleus. In Fig. 7.6 (a) we observe different layers of extremelly confluent HeLa cells, being able to optically discriminate different nucleoli. Note that the out-of-focus sample almost disappear (for example, look at nucleoli pointed by arrow A and B and how they are removed in out-of-focus image). Except for the nucleoli, the intranuclear cytosol shows a lower RI than the rest of the cell (around 1.35), close to the immersion medium RI. Similar results are obtained for COS-7 cell, illustrated in Fig. 7.6 (b), where different delicate membrane protusions (pointed by the arrows A and B) vanish in few microns depth scanning, as also happens with some organelles immersed in cytoplasm.

Once the morphology of HeLa and COS-7 cells has been inspected with a single wavelength, as shown in Fig. 7.6, we recover the RI for two different illumination wavelengths, 560 nm and 630 nm. Note that we have chosen these wavelengths far enough from the absorption maxima exhibited by nucleic acids and proteins (with particularly important peaks between $275 - 280\,\text{nm}$). In this way, the absorption contribution is negligible, thus the obtained RI changes are due to the RI real part [173]. The results provide relevant

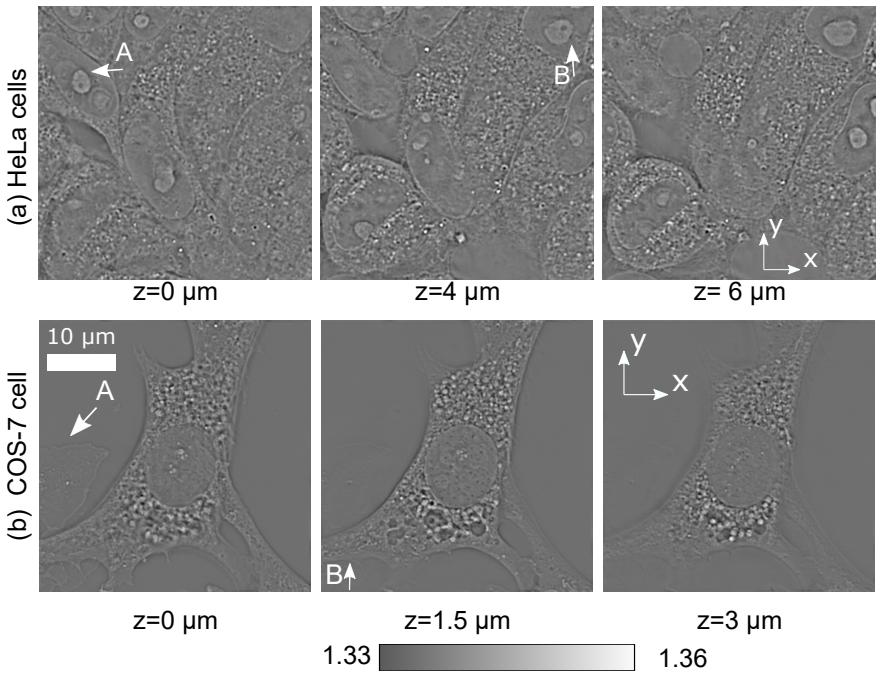

Figure 7.6: 2D RI slices of (a) HeLa and (b) COS-7 cell samples, fixed with formalin solution ($\lambda_0 = 630\,\text{nm}$) and measured at different depths.

information about RI dispersion that could be linked to the chemical composition of the sample [41, 51, 174, 175]. Two groups of samples: monkey kidney COS-7 cells (N=20 samples) and HeLa cells (N=15 samples) immersed in PBS solution have been studied and their 3D RI distributions have been recovered for both wavelengths applying the PC-ODT technique, as shown in Fig. 7.7.

The *xy*-slices of the RI contrast distributions $\Delta n(\mathbf{r},\lambda) = n_s(\mathbf{r},\lambda) - n_m(\lambda)$ corresponding to the same sample transverse plane for two wavelengths are displayed in Figs. 7.8 (a-b). While both images of the same cell display the same features (big nucleus and organelles dispersed in cytoplasm), the absolute values of the $\Delta n(\lambda)$ are different as it can be seen from the color scale bar. We observe that $\Delta n(\lambda)$ is slightly larger for the smaller wavelength. Here the PBS dispersion has been also taken into account [176]: $n_m(\lambda_1) = 1.3357$ and $n_m(\lambda_2) = 1.3336$. It means that the dry components of the cell have larger dispersion than the PBS in this spectral region. It is worth remarking that there is a little difference in RI spatial resolution. Indeed, the Nyquist distances are $\Delta x = 125\,\text{nm}$ and $\Delta z = 260\,\text{nm}$ for λ_1 against $\Delta x = 140\,\text{nm}$ and $\Delta z = 290\,\text{nm}$ for λ_2. It is demonstrated on the spectrum sections limited by the OTF boundaries, displayed in Figs. 7.8 (c-d), that a larger frequency region is filled at λ_1 in comparison with λ_2. Nevertheless, these discrepancies mainly affect high frequency content (small organelles) with little relevance in overall DMC.

After 3D PBS-sample RI contrast recovery, an image segmentation is performed to separate the cell from the background. From now on, only the image regions corresponding to the cell sample are considered. The averaged cell RI contrast with respect to the PBS has been calculated for every sample and wavelength, as displayed in Fig. 7.9 (a) for COS-7 samples and in Fig. 7.9 (b) for HeLa cells. Note that the RI contrast is slightly higher for λ_1

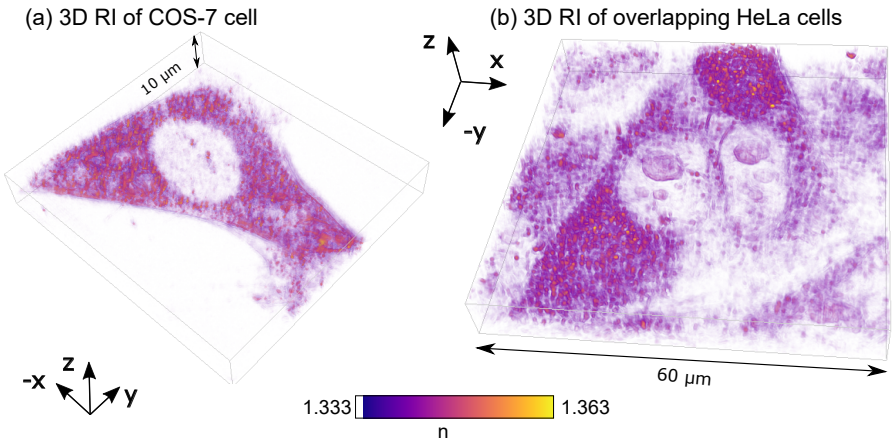

Figure 7.7: 3D RI reconstructions of samples for dual wavelength analysis, both of them immersed in PBS: (a) COS-7 cell and (b) Overlapping HeLa cells layers, both of them measured at 560 nm.

than for λ_2 for both considered cell groups, and proves RI contrast sensibility with regard to wavelength. The boxplots of the averaged RI contrast between the sample and the PBS, for both cell types and wavelengths, are shown in Fig. 7.9 (c). In particular, for COS-7 cells Δn decreases from $(6.60 \pm 0.05) \cdot 10^{-3}$ at λ_1 up to $(5.60 \pm 0.06) \cdot 10^{-3}$ at λ_2. In a similar way, for HeLa cells the difference is more noticeable, with a Δn of $(7.12 \pm 0.05) \cdot 10^{-3}$ at λ_1 versus $(6.11 \pm 0.04) \cdot 10^{-3}$ at λ_2.

As we have mentioned in Section 7.1, for biological samples immersed in an aqueous medium there exists a linear relationship linking the sample DMC and its RI contrast, see Eq. 7.1 [177]. We recall that a refractive increment of cell solids, α, depends on the wavelength, temperature, PH and sample chemical composition, among other parameters. In this Section we only consider its dependence on the wavelength $\alpha(\lambda)$, thus the Eq. Eq. 7.1 can be rewritten for the average DMC as $\overline{\text{DMC}}\,(\text{g/dL}) = [\overline{n_s(\lambda)} - n_w(\lambda)]/(\alpha(\lambda)$, where $n_w(\lambda)$ is the water RI ($n_w(\lambda_1) = 1.3330$, $n_w(\lambda_2) = 1.3318$ and $\overline{n_s(\lambda)}$ is the mean RI of the sample, as stated in [178]).

However, in the literature α is usually taken as a constant value independent on λ. Indeed, a tabulated value of $0.180 - 0.190$ ml/g $\pm 2\%$ is often considered as correct [159,174], since the experimental refractometric measurement of it would require an ultracentrifugation procedure totally destructive for the sample. Here, we aim to clarify whether this approximation is accurate or not, since the PC-ODT is sensitive to α variations linked to wavelength changes. Note that the RI contrast, Δn, has been calculated with respect to PBS. We recall that the formulae of RI changes depending on protein concentration has been developed for pure water as a solvent. Nevertheless, here we use PBS as immersion medium whose RI does not match with the water [176]. The RI contrast between water and PBS is corrected, at both measured wavelengths, with an offset which accounts for the RI mismatch between them. In this way, we obtain the RI contrast between the sample and the water.

Taking into account that the DMC does not depend on λ and must be preserved (as we are measuring the same sample with two wavelengths in a very short period of time),

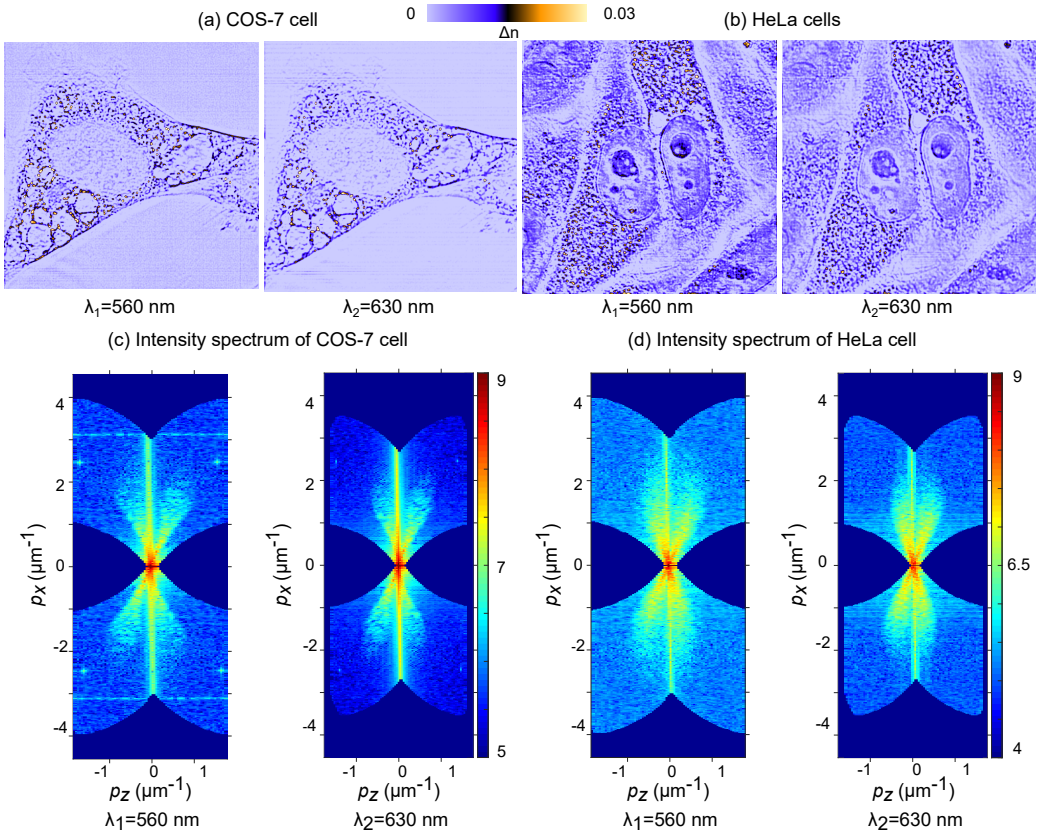

Figure 7.8: 2D RI slices for (a) COS-7 cell and (b) HeLa cells samples. (c-d) $p_x - p_z$ sections of the 3D intensity spectra distributions corresponding to (a-b), in logarithmic scale and multiplied by a binary mask of spatial frequencies transmitted by the microscope. All the samples have been measured at two different wavelengths: 560 nm and 630 nm.

we estimate the ratio $R = \alpha(\lambda_1)/\alpha(\lambda_2)$ from the averaged cell-water RI contrast. Using these data we obtain, as illustrated in the boxplots from Fig. 7.9 (d), experimental values of $R_{exp} = 1.024 \pm 0.005$ and $R_{exp} = 1.020 \pm 0.006$ for COS-7 and HeLa cells, correspondingly. These values reasonably agree with the prediction for pure proteins immersed in water ($R_{theo} = 1.013$) calculated from the Cauchy relation proposed by Perlmann and Longsworth [179], $\alpha(\lambda) = \alpha(\lambda = 578\,\text{nm}) \times \left(0.940 + 2 \cdot 10^4 \text{nm}^2/\lambda^2\right)$, in which the wavelength is measured in nm and is valid for accounting wavelength dependence of α within the visible range. The experimental R is higher than the theoretical one predicted for pure protein solutions. A possible explanation could be that the cell includes other components (nucleic acids, polysaccharides, lipids, etc.) whose solubility is different. However, the amount of nucleic acids immersed in mammalian cells typically do not exceed the 5% and biomolecules like lipids present lower dispersion, thus the protein content is expected to be the main source of RI dispersion [180, 181].

Although the experimental results do not completely agree with the theoretical prediction for R based on the Cauchy relationship, they support the fact that the absorption increases as the wavelength decreases. Note that a slight disagreement with theoretical estimation of R has also been reported by another experimental study [180], where a value of

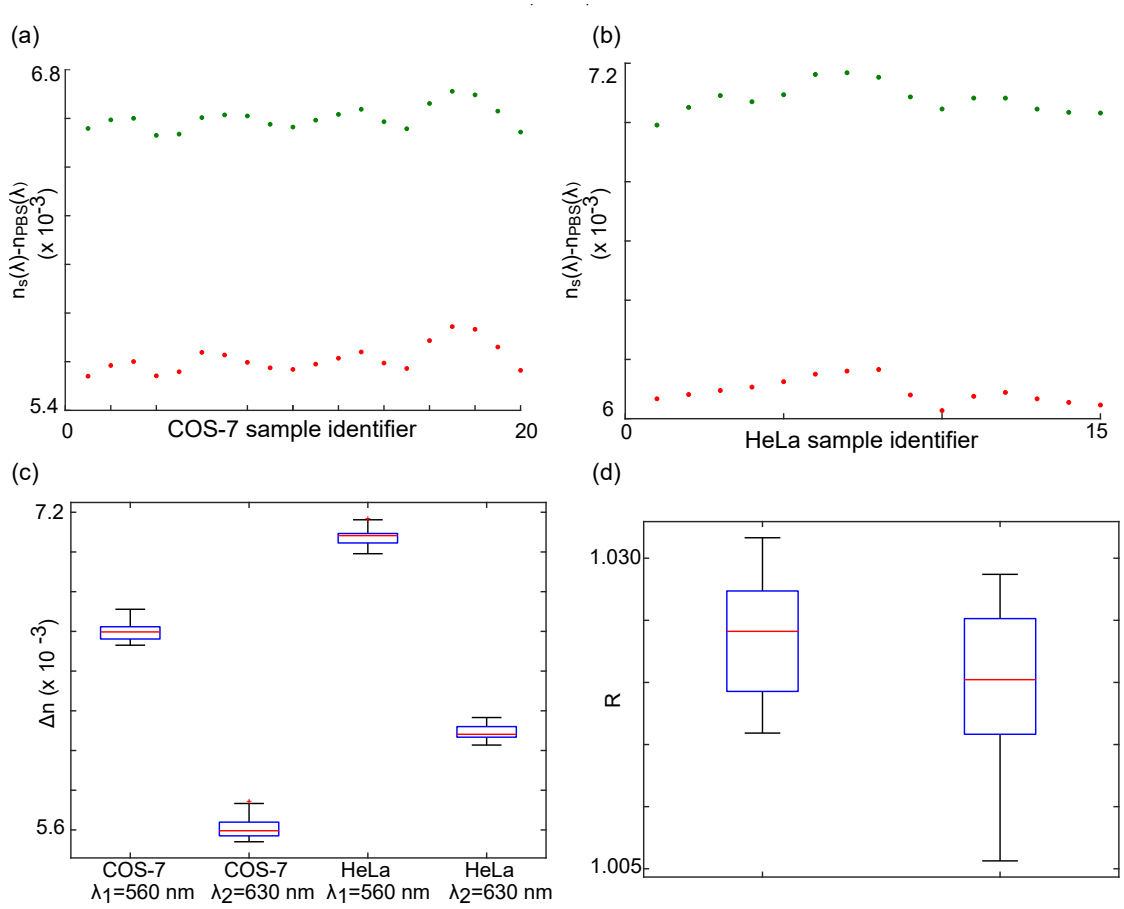

Figure 7.9: Dual wavelength analysis. (a) Averaged sample-PBS RI contrast, for each COS-7 cell sample (N=20). (b) Averaged sample-PBS RI contrast for each HeLa sample (N=15). In (a-b) the red dots account for measurement at 630 nm while the green dots correspond to 560 nm. (c) Boxplots of sample-PBS RI contrast according to each cell group and wavelength. (d) Boxplots of ratio R representing the protein RI increment between two wavelengths: 560 and 630 nm.

$R = 1.088 \pm 0.013$ is obtained for living HeLa cells measured between 310 nm and 400 nm (and based on phase measurements), while the Cauchy relation would lead to $R = 1.078$.

We conclude that the knowledge of $\alpha(\lambda)$ for different types of organic material (proteins, fat, amino acids, etc.) and individual cell organelles is very important for accurate calculation of the cell DMC and dry mass, therefore more studies in this field would be required. Our results demonstrate that the PC-ODT is sensitive to the cell dispersion and can be used for estimation of the corresponding parameters. It is also worth remarking that further research with broader wavelength spectrum would lead to a better sample inspection. Moreover, the authors from Ref. [180] recognized that the high speckle noise was a limiting factor for the accuracy of their results, and the use of partially incoherent source as in PC-ODT removes said speckle noise. Finally, it would be also very convenient to update the Cauchy relation as it has been stated almost 70 years ago. Nowadays, more precise RI measurements can be obtained thanks to the enhancement of label-free imaging.

7.4 Study of the cell death monitored with long-term 3D RI

Another possibility for testing PC-ODT is the study of induced cell necrosis (death), in particular we consider COS-7 cells under nutrient deprivation and immersed in PBS. The cell death is a process that can take minutes or even several hours, so it requires a long-term observation. We apply the experimental setup with the ORM in configuration 2, as formerly described in Chapter 4, because we scan a large field of view ($60 \times 60 \times 16\,\mu\text{m}^3$). Unlike the apoptosis we studied before in Section 7.2, necrosis is a pathological cell death triggered by some external disturbance such as inappropriate temperature, PH changes or hypoxia, among others [182].

For this study, we acquire a 3D intensity measurement in 5 min regular intervals. As shown in Fig. 7.10 (a), two different slices of the sample have been imaged for 2 h: at $z = 0\,\mu$m one sees how the sample attaches to the culture plate with membrane protusions while at $z = 4\,\mu$m a double nucleus has been observed, which means that the cell was undergoing mitosis when extracted from the incubation chamber.

By using PC-ODT, the 3D RI reconstructions are obtained, as shown in Fig. 7.10 (b). It is worth remarking that different phases of the cell cycle have been observed. First, the cell starts to swell progressively (from t=0 min up to t=60 min, Figs. 7.10 (a1-a3)) until reaching a maximum size, while the averaged cytosol RI becomes larger (from $\backsim$ 1.340 at t=0 min until reaching $\backsim$ 1.347 one hour later). Note also that as time passes, the nuclear envelope breaks down and the RI value inside and outside the nucleus becomes more homogeneous due to the degradation of envelope proteins by caspases. This phenomenon is topic of interest in the literature (i.e. Ref. [183]) and PC-ODT is a suitable tool to quantify the disintegration of the nucleus during necrosis. Then, the disruption of the outer membrane starts and progressively the cell shrinkages, resulting in the efflux of intracellular contents and a dramatic loss of cell volume (compare RI slices in Figs. 7.10 (a3-a4)).

Moreover, the average DMC has proved to be useful to assess these cell changes. To obtain the average DMC, the reconstructed RI stack must be split into cell and background (surrounding medium). For this reason, a segmentation algorithm according to Eq. 7.3 is performed, and those image regions that simultaneously satisfy $|\nabla n_n(\mathbf{r})| > 2 \cdot 10^{-3}$ and $n(\mathbf{r}) > 1.333$ are considered as the cell sample ($\text{BM}(\mathbf{r}) = 1$). Only the RI values belonging to those regions are introduced in Eq. 7.1 and averaged to obtain the mean DMC, as shown in Fig. 7.10 (c). During the 1 h of experiment the DMC significantly decreases (from $2.422\,\text{g/dL}$ at t=5 min to $1.685\,\text{g/dL}$ at t=60 min) as the volume of the cell grows remarkably, but the outer membrane of the sample remains structurally intact, so the overall dry mass is preserved. We remark that several z-slices have been analyzed to corroborate that similar DMC variations take place in other layers of the sample. Nevertheless, after 1 h of experiment the DMC reaches a plateau around 1.65 g/dL that can be interpreted in terms of two processes with opposing effects: the outer membrane breaks down and the cell tends to shrinkage, which should increase again DMC, but at the same time all the cell content leaks into the extracellular space.

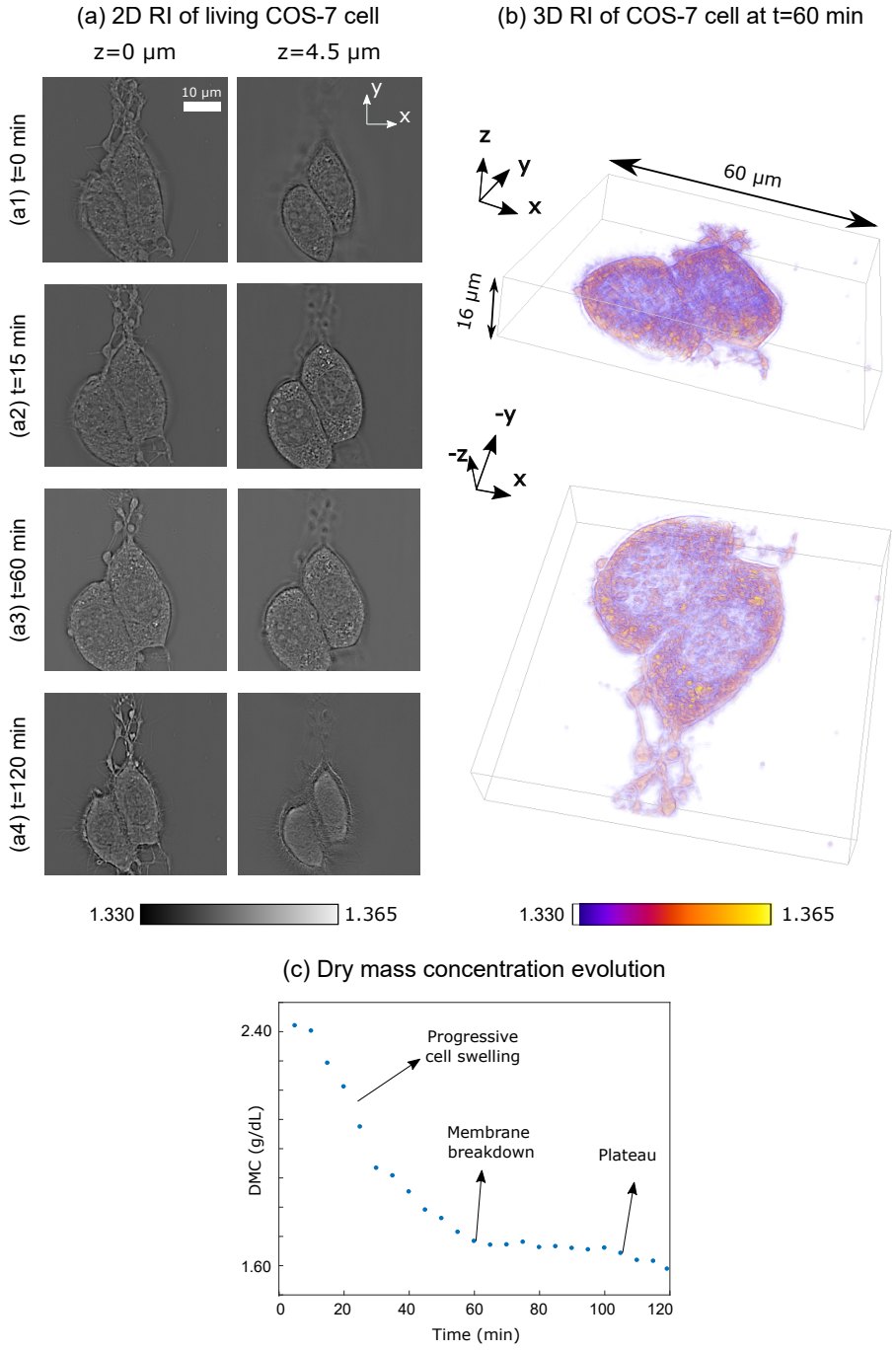

Figure 7.10: RI analysis of a COS-7 cell undergoing necrosis. (a) 2D slices of the RI at two different planes from the sample. (b) 3D RI renderization. (c) Dry mass concentration evolution during the experiment, which enables the identification of two different cell behaviour during the necrosis: an initial progressive cell swelling (characterized by an approximately linear decrease of the average DMC, as the volume grows while the dry mass is preserved) and a plateau region (after membrane breakdown the cell content leaks into the extracellular space).

7.5 Drug screening and pharmacological damage study

In this Section we consider the application of PC-ODT for a pharmacological study. This work has been done in collaboration with researchers from the Faculty of Medical Sciences of Groningen University. Possible damage on the cellular level induced by Diclofenac (DF) has been analysed by means of 3D RI reconstructions. This nonsteroidal anti-inflammatory drug is widely used to treat mild to moderate pain. Although there is no consensus of a toxic dose in the liver, chronic or excessive consumption can lead to drug-induced liver injury typically within the first three months of starting a medication [184].

The mechanism of DF-induced liver injury has been partially elucidated and involves oxidative molecules, mitochondrial and reticule endoplasmic injury in hepatocytes [185]. Previously, it has been reported that cyclic adenosine monophosphate (cAMP), which is a derivative of energy production that hightly governs diverse physiologic processes (e.g. metabolism, secretion, cell fat), can protect hepatocytes against DF toxicity [186]. Moreover, this exchange of protein directly activated by cAMP (EPAC) has been hypothesized to have a target organelle, the mitochondria, better known for producing the energy of the cell in the form of adenosine triphosphate (ATP). Intracellular mitochondria typically display a rod-like shape and are distributed in a mitochondrial network. Conversely, isolated mitochondria are quasi-spherical. Hepatocytes that had interconnected mitochondria network are defined as fused. Fusing is the mechanism that damaged mitochondria apply to repair themselves, so that one damaged mitochondrion could fuse with a healthy one to keep working. Another possibility is a fission mechanism, in which a healthy mitochondrion split into two and send an apoptosis signal to the injured one.

The morphology of the mitochondria has been widely studied (see Ref. [187]) and it strongly depends on the oxidative stress suffered by the cells [188], so it reveals important information about its health state and normal operation. Metformin (ME) is a natural product that is primarily used to treat type-2 diabetes mellitus [189] and is also thought to be mediated by cAMP. A protective effect against DF-induced liver damage in primary rat hepatocytes has been reported for ME (even preventing DF-induced apoptosis [190]) but little is known on how EPAC is involved in this process.

The preparation protocol for the culture is summarized in Appendix E.4. The typical image analysis (see Fig. 7.11 (a), acquired by a LEICA DM 4000B microscope equipped with 40x objective) involves a fluorescence study and dying the samples with DAPI (4',6-diamidino-2-phenylindole), which is the blue stain as observed in Fig. 7.11, that helps to visualize nuclear DNA in order to determine the number of nuclei and identify single cells. DAPI stains nuclei specifically, with little or no cytoplasmic labeling. The second green dye is the immunofluorescence, so fluorescent antibodies are attached to specific molecules to analyze the mitochondrial expression of antioxidant superoxide dismutase. The metformin prevents the depletion of manganese superoxide dismutase caused by diclofenac in primary rat hepatocytes. Furthermore, another fluorescence study of DAPI-stained hepatocytes, see Fig. 7.11 (b), has been carried out by using mitoSOX (Invitrogen). Indeed, mitoSOX is a red probe for detecting manganese superoxide dismutase (MnSOD, a mitochondrial antioxidant), in order to detect mitochondria and confirm the results from the immunofluorescence. From Fig. 7.11 (a) one concludes that metformin partially prevents DF-induced leakage of manganese superoxide dismutase in primary rat hepatocytes. Typi-

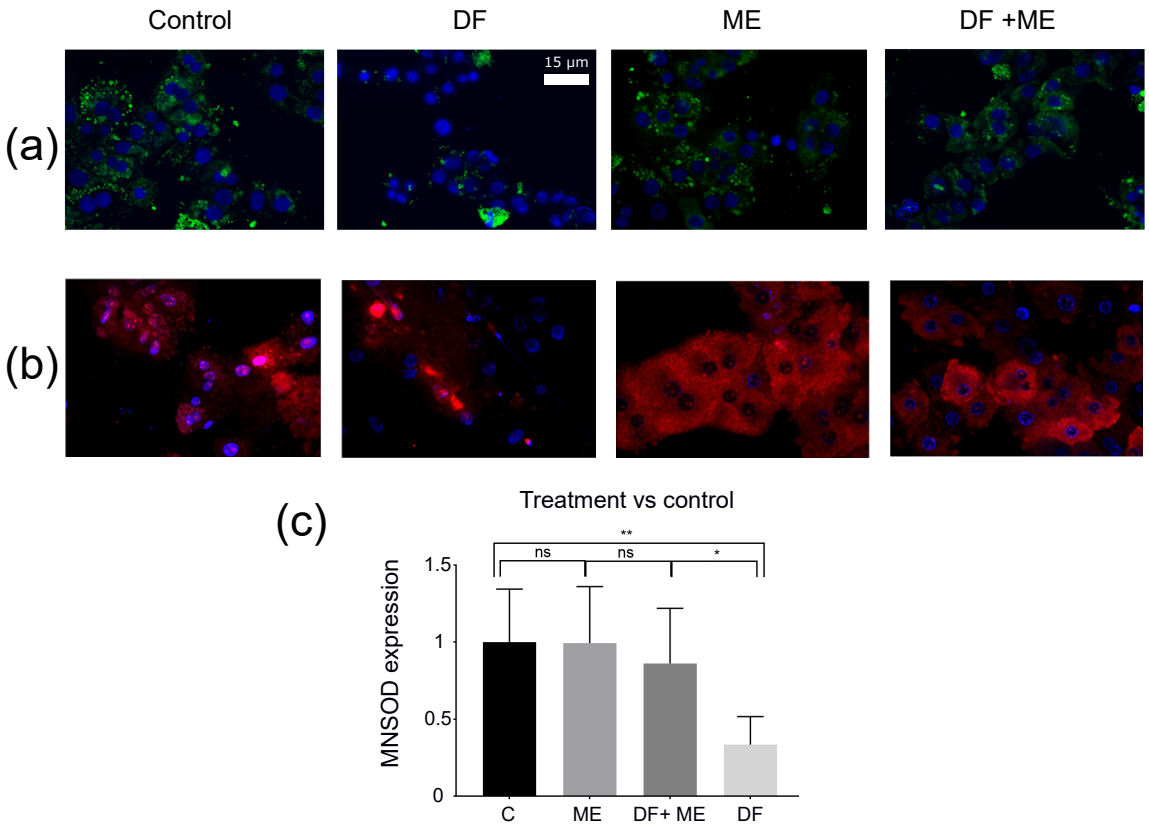

Figure 7.11: Fluorescence intensity images from different cell groups: control, diclofenac (DF), metformin (ME) and a combination of DF and ME. (a) DAPI staining and immunofluorescence. (b) DAPI stained samples and mitoSOX. (c) Fold change of manganese superoxide dismutase (MnSOD) expression. The symbol * represents $p < 0.05$, ** is $p < 0.01$ and ns accounts for non significant comparison. At least 3 independent experiments have been conducted in all cases.

cally, in these studies (see Fig. 7.11 (c)) the fold change of MnSOD and caspase-3 protein activity (that regulates apoptosis) expression among tested drugs is computed to verify the effect of different treatments. It is worth remarking that the MnSOD expression falls ostensibly between the control and DF group, which is linked to oxidative stress suffered by the mitochondria. Conversely, if ME is added to countervail DF effect, MnSOD expression evinces a similar level compared to control group.

The goal of this research is to unravel the relation of EPAC in the ME-DF interaction within mitochondrion, thereby exploring the mitochondria network of the hepatocyte by using PC-ODT. Moreover, quantitative information (like the averaged mitochondria RI) can be assessed to find out the consequences of different drugs over the hepatocytes and even to evaluate their health state. Consequently, the multidisciplinary approach combining PC-ODT, fluorescence microscopy along with chemical tests pave the way in pharmacology field to diagnose mitochondrial dysfunction. It would be very useful to test if PC-ODT is able to obtain complementary information to support evidences pointed out by immunofluorescence tests.

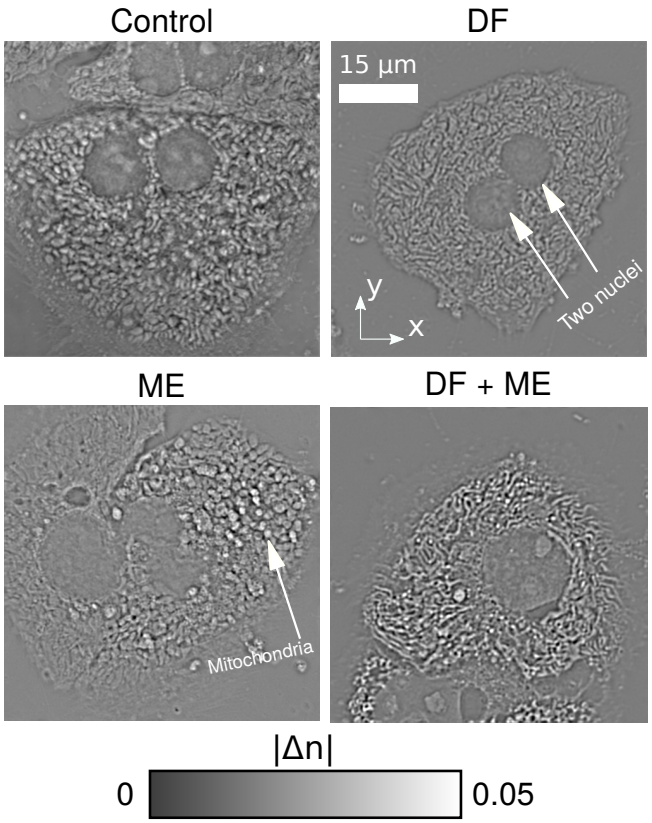

Figure 7.12: RI analysis of primary rat hepatocytes, including 2D RI slices from different cell groups: control, diclofenac (DF), metformin (ME) and a combination of DF and ME.

With this purpose, we arrange the experimental setup with the ORM in configuration 2 in which the illumination has been filtered with a Nikon filter (Texas Red, central wavelength λ_0=560 nm, 30 nm FWHM). For each 3D measurement a volume of $500 \times 500 \times 95$ pixels (corresponding to $62.5 \times 62.5 \times 25\,\mu m^3$) is scanned. Then, the intensity stack registered by the microscope is collected by the sCMOS camera with an exposure time of 2 ms ($2\,ms \times 95$ z-planes per volume). In order to further improve the signal-to-noise (SNR) ratio, 25 stacks have been averaged for each case, thus obtaining a 5 fold SNR enhancement. The samples are mounted in Vectashield Antifade Mounting Medium with DAPI (Vector Laboratories®), characterized by RI of 1.450 ± 0.001 and then sealed between coverslips.

Afterwards, the 3D RI of cells belonging to 10 different hepatocyte groups (20 cells in each group) has been reconstructed by PC-ODT. As an example, some relevant 2D RI contrast slices from several hepatocyte groups are displayed in Fig. 7.12. All cells exhibit big rounded nuclei and they are generally binucleated. We determine that the maximum absolute difference in RI contrast is around $|\Delta n| = 0.03 - 0.04$ and corresponds to small organelles (including mitochondria, of approximate diameter of $1 - 2\,\mu m$ and really heterogeneous in shape and size). Note that the absolute Δn has been considered in this case as the RI of the surrounding medium is higher than the sample's RI. Thus, the mitochondria RI vary between $1.41 - 1.42$, that is in good agreement with previously reported values with other reference techniques like DIC [191] and the combination of phase shifting and

atomic force microscopy [85]. For the sake of brevity, only four cell groups have been included in Fig. 7.12. These groups comprise DF and ME treatments, which have been already reported [190]. The reader is referred to Appendix D.3 for the remaining hepatocyte groups analyzed in this Chapter, like ESI-05 (ES) and CE3FA (CE), which are EPAC inhibitors applied in order to test whether the protective effect of metformin is abolished or not. However, they require further analysis for establishing a link between RI changes and the mitochondria damage associated with the treatment.

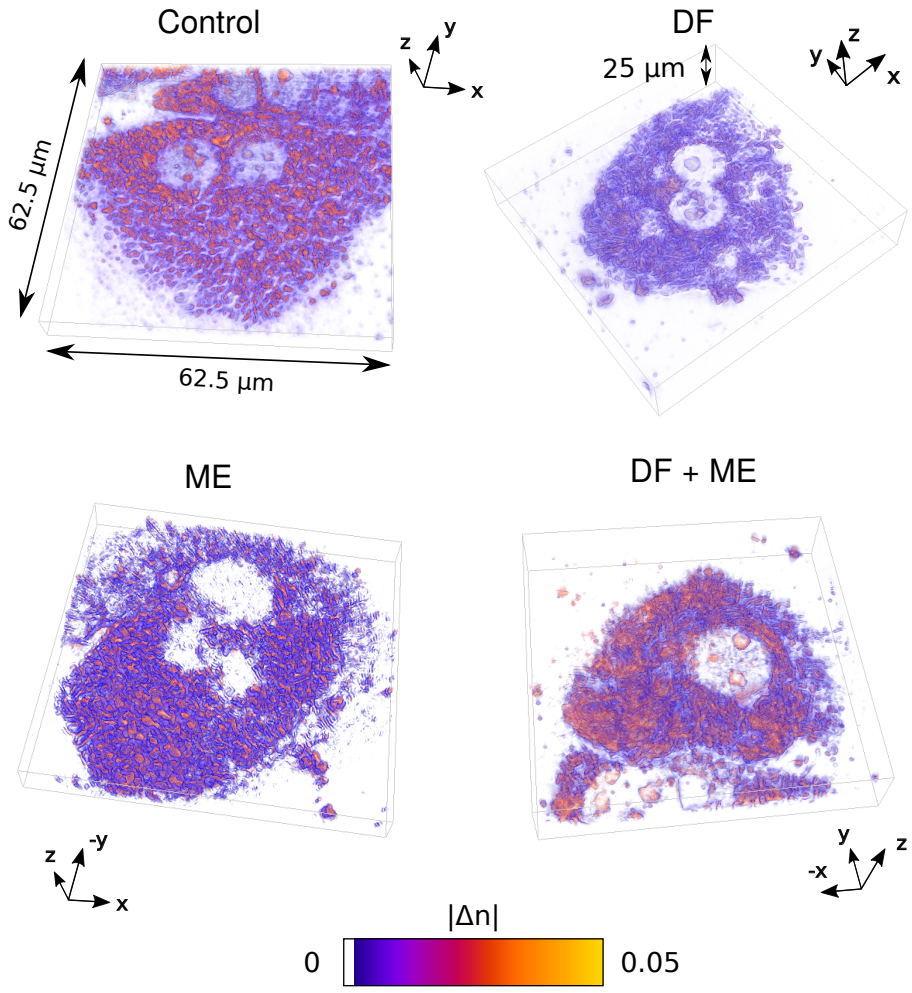

Figure 7.13: RI analysis of primary rat hepatocytes, immersed in mounting medium with $n_m = 1.45$, including 3D RI slices from different cell groups: control, diclofenac (DF), metformin (ME) and a combination of DF and ME. Note that the 3D RI enables the inspection of mitochondria network distribution in all the scanned volume of the cell.

By visual inspection of 2D RI slices from Fig. 7.12 we also conclude that the groups DF, CE or ES (which do not contain metformin) exhibit isolated mitochondria, whereas when ME is incorporated it is more likely to preserve a mitochondria network. Furthermore, the mitochondria damaged by DF, CE or ES become densely packed, and show higher RI (corresponding to low values of $|\Delta n|$). Conversely, the control group and those ones in

which ME has been added usually display more fused and interconnected mitochondria network, as well as higher values of $|\Delta n|$.

The 3D RI distribution of the cells shown in Fig. 7.12 have been displayed in Fig. 7.13. This 3D RI enables the inspection of the mitochondria network in the scanned volume of the cell. Once the 3D RI tomogram is obtained, the segmentation step explained in Section 7.1 and based on RI gradient information has been performed to separate the cell from the surrounding medium (see in Fig. 7.13 the volumetric rendering of the 3D RI made with Tomviz software [192]). Thanks to the 3D RI it is possible to evaluate the global structure of the cell and to conclude whether it is in a good health state or not, for instance, damaged cells displays a depletion of their structure.

First, the whole cells have been considered and their averaged RI contrast ($|\Delta n_{\text{cell}}|$) is obtained, as displayed in Fig. 7.14. Secondly, the analysis has been limited to the cell mitochondria, and the mitochondria RI constrast ($|\Delta n_{\text{mit}}|$) is recovered as shown in Fig. 7.15. In this second case, the RI contrast of five mitochondria have been studied for each of the 20 cells belonging to every hepatocyte group. In this way, we assess the significance of differences involving mitochondria and entire cell RI contrasts. Table 7.2 summarizes the median values of both $|\Delta n_{\text{cell}}|$ and $|\Delta n_{\text{mit}}|$ for hepatocyte samples.

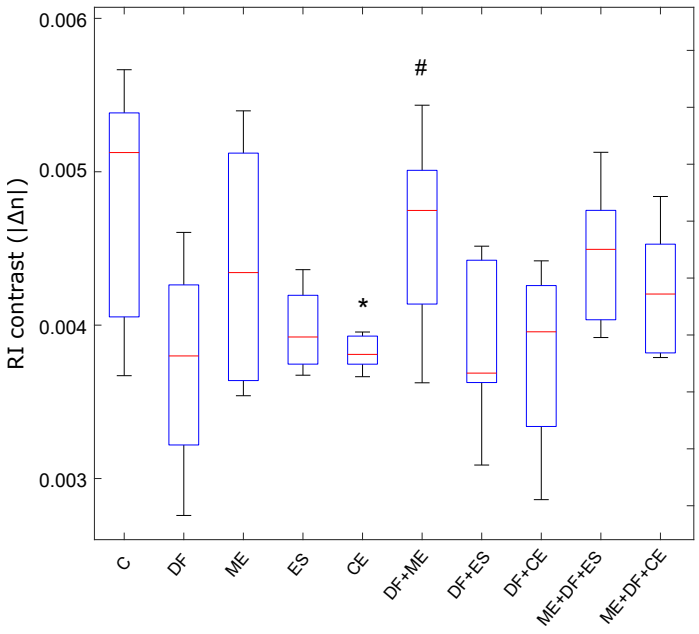

Figure 7.14: Boxplots of averaged entire cell RI contrast (Δn_{cell}) of all primary rat hepatocytes groups, including control (C), diclofenac (DF), metformin (ME), ESI-05 (ES), CE3F4 (CE) and combinations thereof. The symbols * and # corresponds to $p < 0.05$ significance compared to C and DF groups, respectively.

For statistically confirming the differences pointed by the results displayed in Figs. 7.14-7.15, a multiple non-parametric Mann-Whitney-U test (also known as Wilcoxon rank-sum test, further described in Appendix F.2) has been conducted to study the averaged RI contrast among different hepatocyte groups. As expected, no particular differences were found

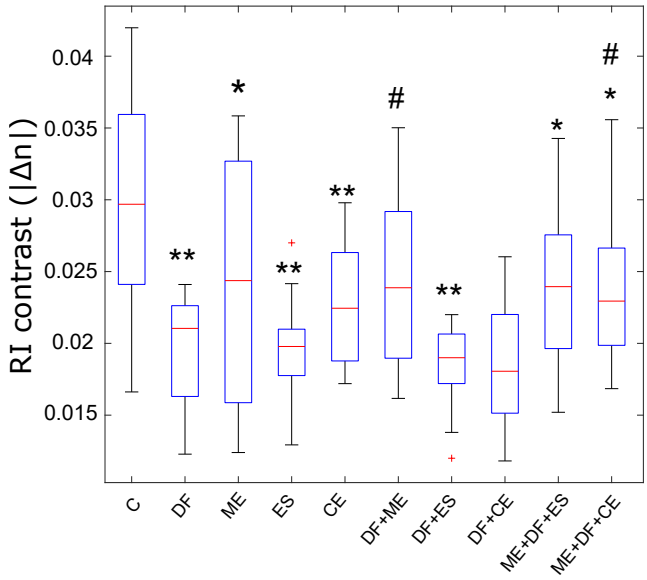

Figure 7.15: Boxplots of averaged mitochondria RI contrast ($|\Delta n_{\text{mit}}|$) of all primary rat hepatocyte groups, including control (C), diclofenac (DF), metformin (ME), ESI-05 (ES), CE3F4 (CE) and combinations thereof. The symbols * and # corresponds to $p < 0.05$ compared to C and DF groups, while ** denotes $p < 0.01$ referred to C group.

by comparison of the averaged Δn_{cell} even if some tendencies have arisen. For instance, some discrepancies have been found between control and diclofenac groups ($p = 0.1091$), control and CE3F4 ($p = 0.0221$), DF against ME ($p = 0.0401$), or ME versus ME + DF+ CE group ($p = 0.0571$). Significant differences are considered when p-value is below 0.05.

Cell group	Median of $\lvert\Delta n_{\text{cell}}\rvert$	Median of $\lvert\Delta n_{\text{mit}}\rvert$
Control	0.0051	0.0297
DF	0.0038	0.0210
ME	0.0043	0.0244
ES	0.0039	0.0198
CE	0.0038	0.0224
DF + ME	0.0047	0.0239
DF + ES	0.0037	0.0191
DF + CE3FA	0.0040	0.0181
ME + DF + ES	0.0045	0.0239
ME + DF + CE	0.0042	0.0242

Table 7.2: Median values of averaged RI contrasts for the entire cell ($|\Delta n_{\text{cell}}|$) and the mitochondria ($|\Delta n_{\text{mit}}|$), respectively, for each hepatocyte group.

The averaged Δn_{cell} takes into account all the cell content (the cytosol and organelles, including the mitochondria). However, for this study the more remarkable difference lies in Δn_{mit} and this value does not significantly impact on Δn_{cell} due to the small size of

mitochondria and the limited proportion thereof with regard to entire cell volume. In this way, significant differences have been found when only Δn_{mit} is considered (see Fig. 7.15). Mitochondria were segmented from the rest of the image by using mitochondria RI contrast and its gradient (see Eq. 7.2) in proper ranges of values, as it follows: $|\Delta n_{\text{mit}}| \in [0.015 - 0.045]$ and $|\nabla n_n(\mathbf{r})| > 0.15$. The RI contrast range is determined by the visual inspection of the sample 3D RI (see Fig. 7.13) performed by an expert biologist over a small amount of samples (at least three of each hepatocyte group). The biologist identifies the mitochondria according to their shape and size. The normalized gradient range is chosen by taking into account that the mitochondria RI values are different from their surroundings, thereby being characterized by a locally large gradient which enables their identification. In this way, the RI segmentation enables the isolation of mitochondria.

From the boxplots outcomes represented in Fig. 7.15 and Table 7.2, statistical differences between control group and some damaged groups (DF, ES, CE) have been observed. We recall that only differences with p-value lower than 0.05 are considered statistically significant as it indicates strong evidence (with at least 95 % probability) against the null hypothesis (according to which the observed differences between groups are random). Note also that the resolution of Δn values provided by PC-ODT is ± 0.002. In particular, a relevant reduction of the median $|\Delta n_{\text{mit}}|$ value is found in DF samples (0.0210) in comparison with the control group (0.0297), which is a decrease around 30 % (with $p < 0.01$). This result is in good agreement with Fig. 7.13 where higher $|\Delta n_{\text{mit}}|$ values (coloured in orange) occur more frequently in control group, whereas the DF-treated sample barely exhibits $|\Delta n_{\text{mit}}|$ values larger than 0.03. Similar conclusions are drawn by comparing the ES and the DF+ES groups with regard to the control (see also the 3D RI reconstructions from Appendix D.3). Moreover, it is observed that the median value of $|\Delta n_{\text{mit}}|$ in DF+ME group (0.0239) is significantly larger (about 13 %) from the samples only treated with DF. We remark that the treatment with ME yields $|\Delta n_{\text{mit}}|$ values more similar to the control group. Furthermore, by visual inspection of Fig. 7.13 one observes that the DF+ME samples comprise large $|\Delta n_{\text{mit}}|$ values (above 0.03). Note that the group treated only with ME exhibits a $|\Delta n_{\text{mit}}|$ value (0.0244), a 20 % lower than the healthy group. However, in this ME case, the 3D RI reconstruction (Fig. 7.13) exhibits a clear mitochondria network with $|\Delta n_{\text{mit}}|$ values larger than 0.03. From this study we conclude that the mitochondria damage undergone after certain drugs application (particularly the diclofenac and ESI-5) can be detected and quantified straightforwardly through $|\Delta n_{\text{mit}}|$ analysis. However, as shown in Fig. 7.15, the mitochondria RI contrast linked to the metformin exhibit a large variability, thus requiring further validation or additional analysis to evaluate ME impact on the cell. Despite this, what is clear is that this study also demonstrates that metformin partially mitigates the $|\Delta n_{\text{mit}}|$ variations introduced by diclofenac.

It is worth pointing out that PC-ODT analysis has been complemented with immunofluorescence and other chemical analysis. The RI analysis results have also been verified by respiration assays (see preparation protocol in Appendix E.4) which measure the amount of ATP that the mitochondria are able to produce. In particular, the oxygen consumption rate (OCR) of four cell groups is displayed in Fig. 7.16. Healthier cells are expected to consume more oxygen during respiration in comparison with damaged samples, so OCR is an indicator for mitochondrial function assessment [193]. Indeed, DF induces a mean decrease of OCR by 40.3 pmol/min compared to control group. Furthermore, no relevant

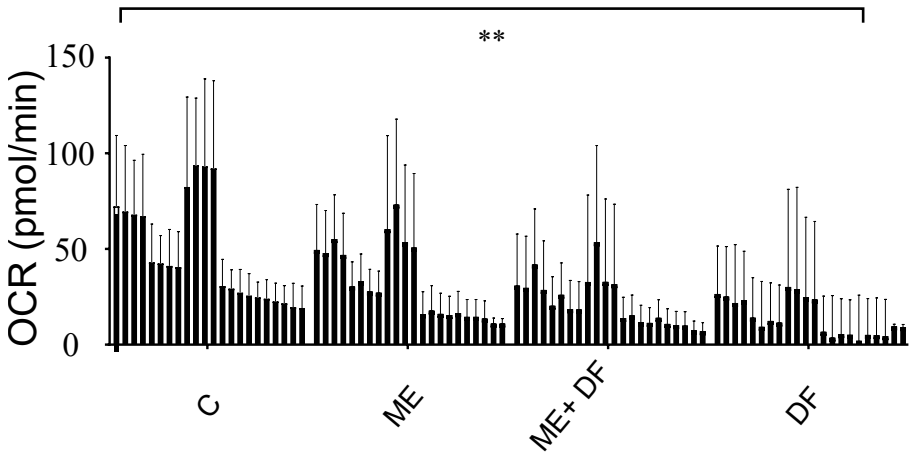

Figure 7.16: Oxygen consumption rate (OCR) for every cell of four hepatocyte groups, including: control (C), metformin (ME), a combination of diclofenac and metformin (ME + DF) and diclofenac (DF). The symbol ** corresponds to p-value $p < 0.01$ referred to control group, correspondingly. Each data bar is presented as the mean ± standard deviation of the mean of three independent measurements.

differences in OCR are observed between control and ME groups, therefore suggesting that no damage has been induced by ME. By contrasting these preliminary outcomes with the boxplots from Fig. 7.15 it suggests that lower $|\Delta n_{\text{mit}}|$ values are correlated with low ATP production rates. However, further research is needed in this direction, including evaluation of mitochondrial activity along with ATP production.

In conclusion, the applicability of the PC-ODT to drug screening problems has been demostrated, particularly when a target organelle (in this case, the mitochondria) can be identified. The RI values obtained for these organelles are reliable and in good agreement with previously reported literature.

7.6 Conclusions

In this Chapter PC-ODT technique has been tested with different biological samples to recover their 3D RI distributions and parameters derived thereof (i.e. the DMC). First, fixed samples have been studied, including macrophages infected with *Leishmania*, COS-7 and HeLa cells. With regard to *Leishmania* analysis, the experimental results demonstrate that the cell DMC obtained from the RI allows for reliable detection and quantitative characterization of the infection and monitoring its temporal evolution. The 3D RI distribution provides important insight for studying morphological changes, particularly membrane blebbing linked to an apoptosis (cell death) process induced by the disease. Moreover, the results evidence that infected DH82 cells exhibit a higher DMC than healthy samples. These findings open up promising perspectives for clinical diagnosis of *Leishmania*. Afterwards, dual wavelength analysis of HeLa and COS-7 cells have been carried out in order to prove that PC-ODT is sensitive to cell dispersion, which is linked to its chemical composition. Further, the PC-ODT is useful not only for fixed cell experiments but also for living cells.

Indeed, the evolution of DMC in living specimen experiments provides valuable information about the health state of the cells sample, as demonstrated with the COS-7 necrosis analysis from the Section 7.4.

Finally, the results from drug screening analysis demonstrate clear RI changes within mitochondria between healthy and chemically damaged samples, as displayed in Fig. 7.15. Consequently, the RI can be applied as a biomarker, together with oxygen consumption (Fig. 7.16) and MnSOD expression from fluorescence analysis (Fig. 7.11), for detecting injured mitochondria in hepathocytes. Indeed, mitochondria exhibit particular RI contrast values and can be effectively segmented despite using a label-free and unspecific technique. Finally, this study has demonstrated that ME treatment is effective against mitochondria damage induced by DF.

Chapter 8

CONCLUSIONS AND OUTLOOK

In this Section, concluding remarks are provided to underline the main achievements of this thesis. Finally, future perspectives of this research are briefly discussed.

8.1 Conclusions

The main research objective of this work has been to develop and implement an affordable and fast technique for reconstruction of the 3D refractive index of weakly absorbing samples (e.g., biological cells). After the comparative analysis of the state of the art about phase tomography techniques along with the seminal works of N. Streibl on 3D image formation in wide-field transmission microscopy [60, 88], published 35 years ago, the latter approach has been chosen as a basis to achieve our goal. Streibl's formulation, forgotten for a long time, can be considered as a mainstay for the generalization of optical diffraction tomography (ODT) developed for coherent sample illumination (C-ODT) to the partially coherent case (PC-ODT). Our PC-ODT technique has been developed for standard wide-field transmission microscopes with low coherent illumination and it can be applied using low as well as high numerical aperture (NA) objective lenses enabling high resolution imaging. Specifically, this PC-ODT technique takes advantage from spatially PCI which avoids speckle noise and other artifacts characteristic of coherent illumination (e.g., laser) used in conventional C-ODT techniques. The main achievements from this thesis are the following.

1. It has been shown that PC-ODT is a viable alternative to C-ODT in high resolution quantitative microscopic imaging of weakly absorbing and scattering samples. In contrast to widely used C-ODT, which requires specially designed holographic setups, PC-ODT is compatible with conventional wide-field microscope. PC-ODT is inherently simple and fast since it avoids the rather time consuming and complex processes of the illumination scanning, phase recovery and further data assembling, required in C-ODT. In PC-ODT the sample is simultaneously illuminated from different directions allowed by the wide-field microscope. The direct 3D RI reconstruction from a single stack of through-focus intensity images, by applying deconvolution with the introduced effective OTF adapted to the non-paraxial case, has been introduced and applied in this thesis. The proposed algorithm for PC-ODT has been verified by numerical simulations and experimental reconstruction

of the RI of well-known test samples previously characterized by other imaging techniques (i.e., blood cells, diatoms, etc.). It has been demonstrated that the same 3D spatial frequency content of the studied sample is recovered in both ODT modalities. However, the OTF in the case of PC-ODT is not uniform that might make it difficult to obtain a correct RI recovery due to low absolute values of the OTF. Taking into account that the OTF strongly depends upon the illumination distribution, its optimization has been performed to mitigate this nonuniformity problem. In particular, we have found that the replacement of the conventional bright-field illumination with a properly designed gaussian illumination provides a better trade-off between the transmitted low and high spatial frequencies, thus yielding a more uniform OTF and eventually increasing the reliability of the sample 3D RI reconstruction. Note that such filter can be easily acquired and incorporated in the microscope. Further, it has been demonstrated that the use of more realistic OTFs, calculated by considering the experimental illumination conditions (i.e. measuring the intensity distribution in the aperture plane of the condenser lens of the microscope), significantly improves the 3D RI recovery.

2. For a fast and easy implementation of the developed PC-ODT technique in a transmission wide-field microscope, an optical refocusing module (ORM) comprising an electrically tunable lens (ETL) with variable focal length has been designed and built. This programmable module synchronized with the digital camera can be easily attached to the commercial microscope as it has been demonstrated in the experimental studies considered throughout the thesis. This PC-ODT implementation is fast, so that it enables video-rate 3D RI actually limited by the frame rate of the camera and target image SNR, providing higher tomography frame rate (e.g., 10 fps in 3D) in comparison with the current state of the art for C-ODT (2.5 fps and 0.5 fps for Tomocube and Nanolive setups [61, 62], respectively). The performance of the setup has been experimentally tested with dynamic micro-objects such as living cells and even bacteria optically manipulated (transported) by using unconventional laser tweezers. It has been shown that it can be also used for the analysis of intracellular motion.

3. The developed PC-ODT technique has been applied to solve real-world problems in biomedicine, in collaboration with international research groups from other fields (medicine and veterinary). It has been demonstrated that, by using the 3D RI distribution obtained with PC-ODT (and parameters derived thereof such as the dry mass concentration), it is possible to study a wide variety of biological physiological changes such as cell parasitization, cell malfunctioning induced by pharmacology and necrosis. Particularly, we have demonstrated that canine macrophages infected with *Leishmania infantum* can be identified through RI changes linked to the cell death process induced by the disease. Also, PC-ODT has been tested in a drug screening assay which reveals RI changes in mitochondria of healthy and chemically damaged hepatocytes. Consequently, the RI can be applied as a biomarker for detecting injured mitochondria in hepathocytes. Indeed, mitochondria exhibit particular RI contrast values and can be effectively segmentated despite using a label-free technique. Further, the evolution of dry mass concentration in living specimen (e.g. HeLa cell) has been applied as a monitorization tool of its health state. We also carry out a dual wavelength analysis of HeLa and COS-7 cells in order to prove that PC-ODT is sensitive to cell dispersion, which in turn might be linked to its chemical composition.

Finally, the development of this thesis has implied gaining knowledge about technology

transfer, from the conception of an idea to its application. It is worth remarking that this work has involved theoretical study, simulation validation in computer and experimental work in the laboratory, with test samples. Finally, the experimental validation of the technique in real-life problems has been carried out. We envision that the PC-ODT will serve for video-rate 3D RI study of both fixed and living samples (i.e. cells) in future real-time applications.

8.2 Future perspectives

In this work a label-free technique for tomographic imaging of weakly absorbing and scattering samples has been established and experimentally proved. However, some open problems still remain and require further research.

The proposed PC-ODT technique does not apply object rotation, which can mitigate the missing cone problem of wide-field microscopy as it has been shown in numerical simulations (see Section 3.6.3 and Ref. [71, 105]). However, mechanical rotation of the sample chamber requires the incorporation of additional arrangement to the microscope. Optical tweezers or more advanced laser traps [108, 134] could be applied to optically induce the required cell rotation without mechanical chamber manipulation. The incorporation of the optical manipulation module in the PC-ODT setup has been experimentally demonstrated for video-rate RI 3D imaging of bacteria optically transported along arbitrary trajectories. This combined setup is suited for other optical manipulation experiments including cell rotation that will be studied in our future works. Apart from optical transport and rotation of cells [108, 194], laser traps also allow exerting controlled forces on the cell which is required for studying its mechanical properties [195–197], where PC-ODT can be applied as well.

Despite the numerical simulations demonstate the viability of the PC-ODT technique, the experimental validation with well-calibrated phantom object is required. For this reason, we have designed a Siemens star phantom (see Section 3.6) with a variety of different spatial frequencies, devised to be a proper test for different imaging techniques, including PC-ODT. Then, we have tried to fabricate the phantom by using a 3D microprinting system (Professional GT from Nanoscribe GmbH, that offers a lateral resolution of 200 nm and a axial resolution around 300 nm). However, the real spatial resolution of the printing system was not sufficient. At the same time, Ziemczonok et at. [104] have successfully manufactured a cell phantom, so we expect to apply it in order to further test PC-ODT. Moreover, the PC-ODT can be fairly compared with the C-ODT technique by reconstructing an identical phantom object with both of them. Such comparison will also verify the practical limitations of the assumption of linear relation between the real and imaginary parts of the RI, n_{Re} and n_{Im} respectively. We remind that in C-ODT the n_{Re} and n_{Im} can be recovered simultaneously, however, there are only a few publications where results about the imaginary part has been reported [86].

Furthermore, PC-ODT could be extended to strong scattering samples as reported in some C-ODT studies [198]. Beyond weak scattering sample approximation, multiple scattering inside the object must be considered, therefore leading to a nonlinear inversion imaging model to reconstruct the scattering potential. This model may involve beam-

propagation method accounting for the total field slice-by-slice along the optical axis direction, thus yielding highly demanding optimization algorithms for image reconstruction and subsequent regularization to enfoce *a-priori* constraints on the object [199]. Other authors prefer the use of complex deep learning techniques, like convolutional neural network, for processing of the intensity measurements and derive the corresponding RI stack [200].

In this thesis, a study with dual wavelength has been carried out in order to evaluate whether PC-ODT is sensitive to object dispersion. In the near future, multiple-wavelength PC-ODT can be further exploited for samples with moderate absorption in order to gain knowledge about their composition. Additionally, the relationship between the concentration of different chemicals and the damage induced in mitochondria of certain cells will be evaluated, as a continuation of the research outlined in Chapter 7. This study will pave the way to interesting applications in pharmacological imaging, for instance, the 3D imaging of the mitochondria network as an exploratory tool for detecting damage in treated cells.

8.3 Published works

The results derived from this dissertation have been published in international journals:

- J. Soto, J. Rodrigo, and T. Alieva, *Label-free quantitative 3D tomographic imaging for partially coherent light microscopy*, Opt. Express 25, 15699-15712 (2017). [89]
- J. Rodrigo, J. Soto, and T. Alieva, *Fast label-free microscopy technique for 3D dynamic quantitative imaging of living cells*, Biomed. Opt. Express 8, 5507-5517 (2017). [108]
- J. Soto, J. Rodrigo, and T. Alieva, *Optical diffraction tomography with fully and partially coherent illumination in high numerical aperture label-free microscopy [Invited]*, Appl. Opt. 57, A205-A214 (2018). [137]
- J. Soto, J. Rodrigo, and T. Alieva, *Partially coherent illumination engineering for enhanced refractive index tomography*, Opt. Lett. 43, 4699-4702 (2018). [124]
- J. Soto, A. Mas, J. Rodrigo, T. Alieva, G. Domínguez-Bernal. *Label-free bioanalysis of Leishmania infantum using refractive index tomography with partially coherent illumination*. J. Biophotonics. 12:e201900030 (2019). [162]

Moreover, the contributions of this work have been disclosed in several international conferences:

- J. M. Soto, J. A. Rodrigo, and T. Alieva, *Dual-wavelength cell's refractive index analysis with partially coherent optical diffraction tomography*, in Imaging and Applied Optics Congress, OSA Technical Digest (Optical Society of America, 2020), paper CF3C.3. [201]
- J. Rodrigo, J. Soto, and T. Alieva, *Fast label-free optical diffraction tomography compatible with conventional wide-field microscopes*, Proc. SPIE 11060, Optical Methods for Inspection, Characterization, and Imaging of Biomaterials IV, 1106016 (2019). [123]

- J. Soto, J. Rodrigo, and T. Alieva, *Achieving Fast 3D Label-free Microscopy for Optical Tweezers Experiments*, Imaging and Applied Optics 2018 DH, OSA Technical Digest (Optical Society of America, 2018), paper DM2F.4 (2018). [202]

- J. Rodrigo, J. Soto, and T. Alieva, *Quantitative imaging with partially coherent illumination: problems and solutions*, Digital Holography and Three-Dimensional Imaging, OSA Technical Digest (Optical Society of America, 2017), paper W4A.2 (2017). [203]

- J. M. Soto, J. A. Rodrigo and T. Alieva, *Partially coherent optical diffraction tomography for label-free quantitative microscopy,* 2017 16th Workshop on Information Optics (WIO), Interlaken, 2017, pp. 1-3. [204]

Appendix A

Mathematical development of relevant expressions

A more detailed discussion about some formulae from the thesis is carried out in this appendix.

A.1 Derivations of expressions for phase and absorption OTFs

In this Section we further explain how to derive the Eq. 3.5 of the thesis [137]. By considering plane wave illumination, the complex field amplitude scattered by the sample and passing through the objective lens with PSF $h_o(\mathbf{r})$ is given by $u(\mathbf{r}\,|\mathbf{s}) = a(|\mathbf{s})\exp(\mathrm{i}k_m\mathbf{sr}) + a(|\mathbf{s})[V(\mathbf{r})\exp(\mathrm{i}k_m\mathbf{sr})]\otimes G(\mathbf{r})$, thereby corresponding to the intensity $I(\mathbf{r}\,|\mathbf{s}) = u(\mathbf{r}\,|\mathbf{s})u^*(\mathbf{r}\,|\mathbf{s})$ and

$$I(\mathbf{r}\,|\mathbf{s}) = a^2(\mathbf{s})\,|\exp(ik_m\mathbf{sr})\otimes h_o(\mathbf{r}) + [V(\mathbf{r})\exp(ik_m\mathbf{sr})]\otimes G(\mathbf{r})\otimes h_o(\mathbf{r})|^2. \tag{A.1}$$

By expanding the previous equation one gets

$$\begin{aligned} I(\mathbf{r}\,|\mathbf{s}) &= a^2(\mathbf{s})\,|\exp(ik_m\mathbf{sr})\otimes h_o(\mathbf{r})|^2 \\ &+ [\exp(ik_m\mathbf{sr})\otimes h_o(\mathbf{r})]^*\,[V(\mathbf{r})\exp(ik_m\mathbf{sr})]\otimes G(\mathbf{r})\otimes h_o(\mathbf{r}) \\ &\times [\exp(ik_m\mathbf{sr})\otimes h_o(\mathbf{r})]\,\{[V(\mathbf{r})\exp(ik_m\mathbf{sr})]\otimes G(\mathbf{r})\otimes h_o(\mathbf{r})\}^*. \end{aligned} \tag{A.2}$$

Let us now rename the last term from right-hand side of Eq. A.2 as $J(\mathbf{r}\,|\mathbf{s})$ and then split up the scattering potential into real and imaginary contributions, $V(\mathbf{r}) = P(\mathbf{r}) + iA(\mathbf{r})$, as follows,

$$\begin{aligned} J(\mathbf{r}\,|\mathbf{s}) &= [\exp(-ik_m\mathbf{sr})\otimes h_o^*(\mathbf{r})]\,[(P(\mathbf{r}) + iA(\mathbf{r}))\exp(ik_m\mathbf{sr})]\otimes G(\mathbf{r})\otimes h_o(\mathbf{r}) \\ &+ [\exp(ik_m\mathbf{sr})\otimes h_o(\mathbf{r})]\,[(P(\mathbf{r}) - iA(\mathbf{r}))\exp(-ik_m\mathbf{sr})]\otimes G^*(\mathbf{r})\otimes h_o^*(\mathbf{r}). \end{aligned} \tag{A.3}$$

In this way, we proceed with the expansion of Eq. A.3 in frequency domain, by introducing $\hat{P}$ and $\hat{A}$ as the Fourier transform from the real and imaginary parts of the scattering potential, respectively, and $2\pi\kappa_m = k_m$ to obtain

$$\begin{aligned}
\hat{J}(\mathbf{p}\,|\mathbf{s}) &= [\delta(\mathbf{p}+\kappa_m\mathbf{s})\,H_o^*(-\mathbf{p})] \otimes \left[\left(\hat{P}(\mathbf{p}) + iA(\mathbf{p})\right) \otimes \delta(\mathbf{p}-\kappa_m\mathbf{s})\right] \widehat{G}(\mathbf{p})H_o(\mathbf{p}) \\
&+ [\delta(\mathbf{p}-\kappa_m\mathbf{s})\,H_o(\mathbf{p})] \otimes \left[\left(\hat{P}(\mathbf{p}) - iA(\mathbf{p})\right) \otimes \delta(\mathbf{p}+\kappa_m\mathbf{s})\right] \widehat{G}^*(-\mathbf{p})H_o^*(-\mathbf{p}) \\
&= [\delta(\mathbf{p}+\kappa_m\mathbf{s})\,H_o^*(-\mathbf{p})] \otimes \left[\left(\hat{P}(\mathbf{p}-\kappa_m\mathbf{s}) + iA(\mathbf{p}-\kappa_m\mathbf{s})\right) \widehat{G}(\mathbf{p})H_o(\mathbf{p})\right] \\
&+ [\delta(\mathbf{p}-\kappa_m\mathbf{s})\,H_o(\mathbf{p})] \otimes \left[\left(\hat{P}(\mathbf{p}+\kappa_m\mathbf{s}) - iA(\mathbf{p}+k_m\mathbf{s})\right) \widehat{G}^*(-\mathbf{p})H_o^*(-\mathbf{p})\right] \\
&= H_o^*(\kappa_m\mathbf{s})\left(\hat{P}(\mathbf{p}) + i\hat{A}(\mathbf{p})\right) \widehat{G}(\mathbf{p}+\kappa_m\mathbf{s})H_o(\mathbf{p}+\kappa_m\mathbf{s}) \\
&+ H_o(\kappa_m\mathbf{s})\left(\hat{P}(\mathbf{p}) - i\hat{A}(\mathbf{p})\right) \widehat{G}^*(-\mathbf{p}+\kappa_m\mathbf{s})H_o^*(-\mathbf{p}+\kappa_m\mathbf{s}),
\end{aligned} \tag{A.4}$$

where $\int h_o(\mathbf{r})\exp(-i2\pi\mathbf{rp})\,\mathrm{d}\mathbf{p} = H_o(\mathbf{p})$, thus $\int h_o^*(\mathbf{r})\exp(-i2\pi\mathbf{rp})\,\mathrm{d}\mathbf{p} = \mathrm{H_o^*}(-\mathbf{p})$. It is worth also remarking that in the previous expansion we have considered the following identities,

$$\begin{aligned}
[\delta(\mathbf{p}-\kappa_m\mathbf{s})\,H_o(\mathbf{p})] \otimes \left[\hat{P}(\mathbf{p}+\kappa_m\mathbf{s})\widehat{G}^*(-\mathbf{p})\right] &= \\
\int \delta(\mathbf{p}-\kappa_m\mathbf{s}-\mathbf{p}')\,H_o(\mathbf{p}-\mathbf{p}')\hat{P}(\mathbf{p}'+\kappa_m\mathbf{s})\widehat{G}^*(-\mathbf{p}')\mathrm{d}\mathbf{p}' &= \\
H_o(\kappa_m\mathbf{s})\hat{P}(\mathbf{p})\widehat{G}^*(-\mathbf{p}+\kappa_m\mathbf{s}),
\end{aligned} \tag{A.5}$$

along with

$$\begin{aligned}
[\delta(\mathbf{p}+\kappa_m\mathbf{s})\,H_o^*(-\mathbf{p})] \otimes \left[\hat{P}(\mathbf{p}-\kappa_m\mathbf{s})\widehat{G}(\mathbf{p}))\right] &= \\
\int \delta(\mathbf{p}'+\kappa_m\mathbf{s})\,H_o^*(-\mathbf{p}')\hat{P}(\mathbf{p}-\mathbf{p}'-\kappa_m\mathbf{s})\widehat{G}(\mathbf{p}-\mathbf{p}')\mathrm{d}\mathbf{p}' &= \\
H_o^*(\kappa_m\mathbf{s})\hat{P}(\mathbf{p})\widehat{G}(\mathbf{p}+\kappa_m\mathbf{s}).
\end{aligned} \tag{A.6}$$

Finally, by grouping common terms one obtains,

$$\begin{aligned}
\hat{J}(\mathbf{p}\,|\mathbf{s}) &= \hat{P}(\mathbf{p})\left[H_o^*(\kappa_m\mathbf{s})\widehat{G}(\mathbf{p}+\kappa_m\mathbf{s})H_o(\mathbf{p}+\kappa_m\mathbf{s}) + \right. \\
&+ \left. H_o(\kappa_m\mathbf{s})\widehat{G}^*(-\mathbf{p}+\kappa_m\mathbf{s})H_o^*(-\mathbf{p}+\kappa_m\mathbf{s})\right] \\
&+ i\hat{A}(\mathbf{p})\left[H_o^*(\kappa_m\mathbf{s})\widehat{G}(\mathbf{p}+\kappa_m\mathbf{s})H_o(\mathbf{p}+\kappa_m\mathbf{s})\right. \\
&- \left. H_o(\kappa_m\mathbf{s})\widehat{G}^*(-\mathbf{p}+\kappa_m\mathbf{s})H_o^*(-\mathbf{p}+\kappa_m\mathbf{s})\right].
\end{aligned} \tag{A.7}$$

Next, we consider the Streibl forward model for partially-coherent imaging [60] that includes both phase (H_P) and absorption (H_A) OTFs terms, as follows

$$\hat{I}(\mathbf{p}) = \int_S \widehat{I}(\mathbf{p}\,|\mathbf{s})\mathrm{d}\mathbf{s} = B\delta(\mathbf{p}) + \hat{P}(\mathbf{p})\,H_P(\mathbf{p}) + \hat{A}(\mathbf{p})\,H_\mathrm{A}(\mathbf{p}), \tag{A.8}$$

where B is a background term and $\hat{I}$ is the intensity spectrum. Finally, by inserting Eq. A.7 in Eq. A.2 and then identifying each term of the resulting expression with Eq. A.8 one gets the expressions for POTF and AOTF that are extensively used for PC-ODT implementation,

$$\begin{aligned} H_A(\mathbf{p}) &= \mathrm{i}\int_S a^2(|\mathbf{s})[H_o^*(\kappa_m\mathbf{s})\widehat{G}(\mathbf{p}+\kappa_m\mathbf{s})H_o(\mathbf{p}+\kappa_m\mathbf{s}) \\ &- H_o(\kappa_m\mathbf{s})\widehat{G}^*(-\mathbf{p}+\kappa_m\mathbf{s})H_o^*(-\mathbf{p}+\kappa_m\mathbf{s})]\mathrm{d}\mathbf{s}, \\ H_P(\mathbf{p}) &= \int_S a^2(|\mathbf{s})[H_o^*(\kappa_m\mathbf{s})\widehat{G}(\mathbf{p}+\kappa_m\mathbf{s})H_o(\mathbf{p}+\kappa_m\mathbf{s}) \\ &+ H_o(\kappa_m\mathbf{s})\widehat{G}^*(-\mathbf{p}+\kappa_m\mathbf{s})H_o^*(-\mathbf{p}+\kappa_m\mathbf{s})]\mathrm{d}\mathbf{s}, \end{aligned} \tag{A.9}$$

where the integration domain encompasses all the condenser aperture diaphragm (S).

A.2 OTF for ideal bright-field illumination and circular apertures

In this Section we summarize the expressions corresponding to ideal OTF for BFI illumination and circular apertures in both condenser and objective lenses, as derived in Ref. [72].

$$H_P(p_\perp,p_z) = \frac{\mathrm{i}\lambda}{4\pi}\left[F(p_\perp,p_z)-F(p_\perp,-p_z)\right], \tag{A.10}$$

$$H_A(p_\perp,p_z) = \frac{\lambda}{4\pi}\left[F(p_\perp,p_z)+F(p_\perp,-p_z)\right], \tag{A.11}$$

where $p_\perp=\sqrt{p_x^2+p_y^2}$ denotes the radial transverse frequency, p_z is the axial frequency,

$$F(p_\perp,p_z)=\frac{p_\perp^2\psi}{p^2p_z}\sqrt{\lambda^{-2}-\frac{p^2}{4}-\frac{p^2\psi^2}{p_z^2}}+\left(\sqrt{\lambda^{-2}-\frac{p^2}{4}}-\frac{p_z^2}{2p}\right)\arccos\left(\frac{p\psi}{p_z\sqrt{\lambda^{-2}-p^2/4}}\right), \tag{A.12}$$

and $p=\sqrt{p_x^2+p_y^2+p_z^2}$ stands for the modulus of frequency vector. According to Appendix B from Ref. [72], the parameter ψ is described by a piecewise function depending on the frequency region. Let us introduce the maximum normalized spatial frequency allowed by the illumination source (circular aperture diaphragm of the condenser) and imaging (objective lens) pupils, $p_S=\mathrm{NA_c}/\lambda_0$ and $p_P=\mathrm{NA_o}/\lambda_0$ respectively. Moreover, we also assume $p_P\geq p_S$. Then, when $0<p_\perp<p_P-p_S$, ψ is given by

$$\psi = \begin{cases} \frac{p_z}{p_\perp}\left(\frac{p_z}{2} - \sqrt{\lambda^{-2} - p_S^2}\right) \\ \text{If}\left[\sqrt{\lambda^{-2} - p_S^2} - \sqrt{\lambda^{-2} - (p_S - p_\perp)^2} \leq p_z \leq \sqrt{\lambda^{-2} - p_S^2} - \sqrt{\lambda^{-2} - (p_S + p_\perp)^2}\right] \end{cases}, \tag{A.13}$$

whereas for $p_P - p_S < p_\perp < p_P + p_S$ it holds that

$$\psi = \begin{cases} \frac{p_z}{p_\perp}\left(\frac{p_z}{2} - \sqrt{\lambda^{-2} - p_S^2}\right) \\ \text{If}\left[\sqrt{\lambda^{-2} - \rho_S^2} - \sqrt{\lambda^{-2} - (\rho_S - \rho_\perp)^2} \leq \rho_z \leq \sqrt{\lambda^{-2} - \rho_S^2} - \sqrt{\lambda^{-2} - \rho_P^2}\right] \\ \frac{p_z}{p_\perp}\left(-\frac{p_z}{2} - \sqrt{\lambda^{-2} - p_P^2}\right) \\ \text{If}\left[\sqrt{\lambda^{-2} - p_S^2} - \sqrt{\lambda^{-2} - p_P^2} \leq \rho_z \leq \sqrt{\lambda^{-2} - (p_P - p_\perp)^2} - \sqrt{\lambda^{-2} - p_P^2}\right] \end{cases}. \tag{A.14}$$

A.3 Effective OTF expression

For obtaining the effective OTF (H_{EFF}) from Chapter 2 we start with the well-known Streibl model [60],

$$I(\mathbf{r}) = B + P(\mathbf{r}) \otimes h_{\text{P}}(\mathbf{r}) + A(\mathbf{r}) \otimes h_{\text{A}}(\mathbf{r}), \tag{A.15}$$

where $\otimes$ operator stands for convolution and h_P and h_A are the PSF functions. By separating the scattering potential into its real and imaginary parts, $V(\mathbf{r}) = P(\mathbf{r}) + iA(\mathbf{r}) = k_0^2(n^2 - n_m^2)$, where n_m is the purely-real RI of the surrounding medium (no absorption of the medium is assumed) and then expanding the sample's RI ($n = n_{\text{Re}} + i n_{\text{Im}}$), we obtain

$$\begin{array}{ll} P(\mathbf{r}) = & k_0^2(n_{\text{Re}}^2 - n_0^2 - n_{\text{Im}}^2) \\ A(\mathbf{r}) = & 2k_0^2 n_{\text{Re}} n_{\text{Im}} \end{array}. \tag{A.16}$$

Let us now hypothesize that the real and imaginary parts of the RI are connected by a linear relationship $n_{\text{Im}} = \varepsilon n_{\text{Re}}$, with low and positive ε constant (within the range $10^{-3} - 10^{-2}$), which mainly holds for weakly absorbing samples. In this case, Eq. A.16 is further simplified as

$$\begin{array}{ll} P(\mathbf{r}) = & k_0^2\left[(1-\varepsilon^2)n_{\text{Re}}^2 - n_0^2\right] \\ A(\mathbf{r}) = & 2k_0^2 \varepsilon n_{\text{Re}}^2 \end{array}. \tag{A.17}$$

By solving the system from Eq.A.17 one gets,

$$A(\mathbf{r}) = \left(\frac{2\varepsilon}{1-\varepsilon^2}\right) P(\mathbf{r}) + \left(\frac{2k_0^2\varepsilon}{1-\varepsilon^2}\right) n_0^2 \approx 2\varepsilon P(\mathbf{r}) + 2k_0^2\varepsilon n_0^2, \tag{A.18}$$

where the approximation $\varepsilon^2 \to 0$ has been applied. Alternatively, Eq. A.18 can be rewritten in spectrum space by applying Fourier Transform as follows,

$$\hat{A}(\mathbf{p}) = 2\varepsilon\hat{P}(\mathbf{p}) + 2k_0^2\varepsilon n_0^2\delta(\mathbf{p}), \tag{A.19}$$

where $\delta(\mathbf{p})$ is the Dirac delta function. By direct substitution of Eq. A.19 in Eq. A.8, the spectrum of the intensity is expressed as

$$\hat{I}(\mathbf{p}) = \delta(\mathbf{p})\left[B + 2k_0^2\varepsilon n_0^2 H_A(\mathbf{p})\right] + \hat{P}(\mathbf{p})\left[H_P(\mathbf{p}) + 2\varepsilon H_A(\mathbf{p})\right]. \tag{A.20}$$

Finally, we introduce the definition of effective optical transfer function as $H_{EFF}(\mathbf{p}) = H_P(\mathbf{p}) + 2\varepsilon H_A(\mathbf{p})$ to obtain

$$\hat{I}(\mathbf{p}) = B\delta(\mathbf{p}) + 2k_0^2\varepsilon n_0^2 H_A(\mathbf{p}) + \hat{P}(\mathbf{p}) H_{\mathrm{EFF}}(\mathbf{p}), \tag{A.21}$$

where the effective OTF accounts for both absorption and phase effects.

Appendix B

Experimental configurations of the optical refocusing module (ORM)

In this Appendix, some details about the experimental setups for the PC-ODT implementation from Chapter 4 are discussed. In particular, the NA variation linked to the operation of the optical refocusing module (ORM) is considered to verify its possible effects over PC-ODT performance. Further, the analytical derivation of the defocus expressions, for the two experimental ORM configurations described in Chapter 4, is performed by means of the corresponding ABCD matrices.

B.1 Object space scanning

The ORM considered in Chaper 4 forms an image recorded by the camera with slightly different NA_o for different scanning planes. Let us quantify the relevance of such mismatch considering the sketch of Fig. B.1 that represents the object space in which a sample is scanned along the z-axis and imaged by using an objective lens and the ORM. As an example, we assume a surrounding medium ($n_m = 1.518$). The initial focus plane (P1) is changed to the position P2 by applying a displacement $+z_{defocus}$ with the ETL. Consequently, although the initial NA (NA_1) matches with NA_o, the effective NA perceived in P2 (NA_2) changes. Taking into account the definition of NA, it is clear that $NA_1 = n_m \cdot \sin\theta_1$ and by value substitution we derive $\theta_1 \approx 67.26º$. Then, by performing some elemental trigonometry we compute the maximum acceptance angles (θ_1 and θ_2) subtended before and after applying ETL refocusing as $\tan\theta_1 = x/w$ and $\tan\theta_2 = x/(w+z_{defocus})$. Note also that according to the geometry shown in Fig. B.1, $h = \sqrt{w^2 + z_{defocus}^2}$ where the distance w can be written as the ratio of the focal length of the objective lens to the magnification factor (M), so $w = f_{OL}/M$. Let us consider $M = 100$, which leads to $w = 1.8\,\text{mm}$. For the vast majority of samples analized in this thesis, the thickness does not exceed $10\,\mu\text{m}$, so $z_{defocus} << w$ and by direct substitution of values one gets $h = 1.81\,\text{mm}$. The distance x is obtained as follows, $x = w \cdot \tan\theta_1 = (w + z_{defocus}) \cdot \tan\theta_2$, therefore it can be rewritten as

$$\theta_2 = \text{atan}\left[\frac{w \cdot \tan\theta_1}{w + z_{defocus}}\right] \tag{B.1}$$

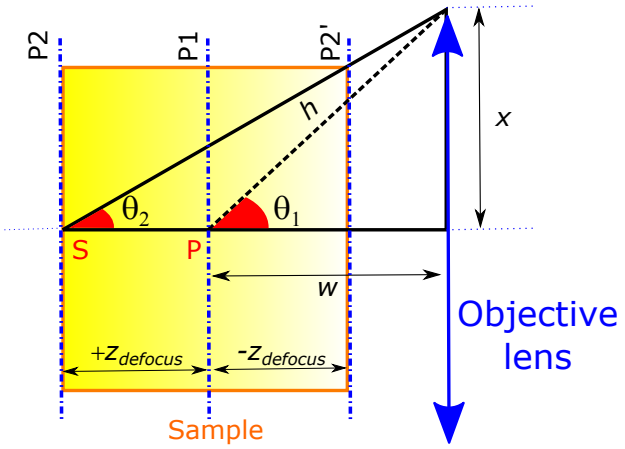

Figure B.1: Object space scanning with optical refocusing module. The ETL scans the sample from an initial focus plane (P1) to another one (P2 or P2′) by axial displacement ($\pm z_{defocus}$), thus changing the effective NA. The variation ΔNA can be computed through acceptance angles modification (from θ_1 to θ_2).

which leads to $\theta_2 = 67.14°$, close to the initial acceptance angle. In that case, the effective numerical aperture is $\mathrm{NA}_2 = n_m \cdot \sin\theta_2 = 1.3988$ and ΔNA only represents 0.086 % of NA_o, thus being an almost negligible effect. This slight ΔNA deviation justifies the shift-invariant OTF hypothesis in the PC-ODT context. Moreover, if one considers the previous analysis with a thicker scan of $z_{defocus} = 100\,\mu$m along optical axis then $\theta_2 = 66.13°$, therefore $\mathrm{NA}_2 = 1.388$ and close to $\Delta\mathrm{NA} \approx 0.01 \cdot \mathrm{NA}_o$, which is still a marginal variation.

B.2 Optical refocusing module in configuration 1

First, let us introduce the experimental setup with the ORM in configuration 1 for implementing PC-ODT, which comprises a wide-field microscope attached to an ETL lens (Optotune EL-10-30-C-LD). To describe the image formation when changing the ETL focal length ($\mathrm{f}_{\mathrm{ETL}}$), the ABCD-matrix $\left(\mathbf{T} = \begin{bmatrix} A & B \\ C & D \end{bmatrix}\right)$ is calculated for the system sketched in Fig. B.2.

We recall that $D_t = \begin{bmatrix} 1 & t \\ 0 & 1 \end{bmatrix}$ is the matrix representation for a slab of free space of thickness t and $L_\mathrm{f} = \begin{bmatrix} 1 & 0 \\ \frac{-1}{\mathrm{f}} & 1 \end{bmatrix}$ is the thin lens transformation matrix with f being the focal length of the corresponding lens (in this case, ETL or RL). Since the position of the camera is fixed, we find the conjugated plane (z distance from the relay lens to the intermediate image corresponding to the image formed by the objective and the tube lens) for every

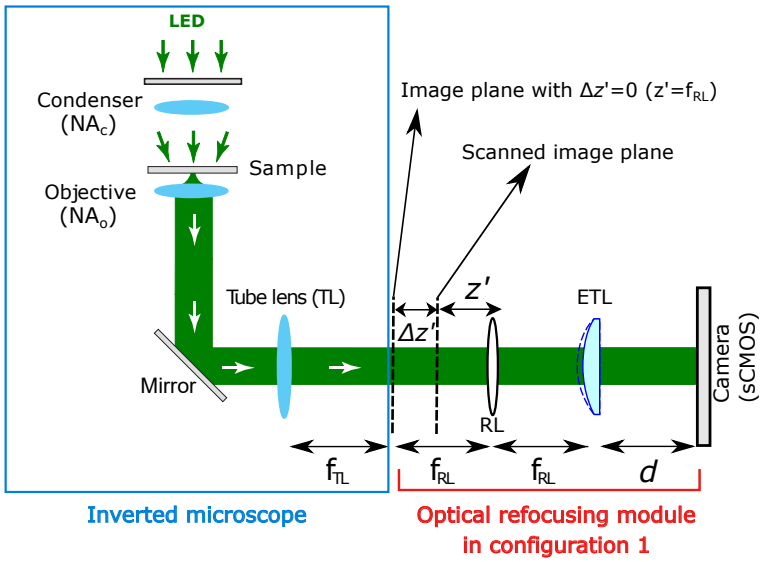

Figure B.2: Experimental setup for PC-ODT, including a wide-field microscope (comprising the condenser and objective lenses) and an optical refocusing module in configuration 1. The latter includes two lenses, TL and RL, working as a Keplerian telescope along with an electrically tunable lens (ETL, with a varying focal length f_{ETL}) that is responsible for the axial scanning of the sample.

value of f_{ETL} as follows

$$\begin{aligned} \mathbf{T} &= [D_d]\,[L_{f_{ETL}}]\,[D_{f_{RL}}]\,[L_{f_{RL}}]\,[D_z] \\ &= \begin{bmatrix} \frac{-d}{f_{RL}} & \left(1-\frac{d}{f_{ETL}}\right) f_{RL} + d\left(1-\frac{z'}{f_{RL}}\right) \\ \frac{-1}{f_{RL}} & \left(1-\frac{z'}{f_{RL}}\right) - \frac{f_{RL}}{f_{ETL}} \end{bmatrix}, \end{aligned} \tag{B.2}$$

in which D_d, $D_{f_{RL}}$ and D_z stands for the light propagation in free space slabs through a section of thickness d, f_{RL} and z', respectively; while $L_{f_{RL}}$ and $L_{f_{ETL}}$ corresponds to the transformation matrix of the RL and the ETL, correspondingly (see Fig. B.2). All the optical elements between the intermediate plane image (corresponding to the image formed by the objective and the tube lens) are included in $\mathbf{T}$. Note that for rays propagating left to right, the matrix elements are written down right to left. If the imaging condition ($B = 0$) is introduced in Eq. B.2, it leads to $f_{RL}(1 - d/f_{ETL}) + d(1 - z'/f_{RL}) = 0$, and gives the distance

$$z' = f_{RL}\left[1 + f_{RL}\left(\frac{1}{d} - \frac{1}{f_{ETL}}\right)\right]. \tag{B.3}$$

Then, the scanning interval in the image space is given by

$$\triangle z' = z' - f_{RL} = f_{RL}^2\left(\frac{1}{d} - \frac{1}{f_{ETL}}\right), \tag{B.4}$$

and the corresponding shift in object space (or defocus distance) is found by taking into account the magnification (M) and the refractive index of the immersion medium (n_m),

$$z_{defocus} = \frac{n_m \triangle z'}{M^2} = \frac{n_m \mathrm{f}_{\mathrm{RL}}^2}{M^2}\left(\frac{1}{d} - \frac{1}{\mathrm{f}_{\mathrm{ETL}}}\right). \tag{B.5}$$

In this way, the $\mathrm{f}_{\mathrm{ETL}}$ variation, which is determined by the applied current to the ETL, is responsible for which plane is imaged onto the camera sensor. Note that M is linked to the global magnification (M_s) of the imaging system as $M_s = M \times (-d/\mathrm{f}_{\mathrm{RL}})$, as derived from the term A of the **T** matrix (see Eq. B.2) accounting for the magnification of the system composed of the relay lenses and the ORM.

B.3 Optical refocusing module in configuration 2

An alternative ORM configuration is displayed in Fig. B.3, that includes an additional relay lens (RL2) and a EL-10-30-C Optotune ETL model (EL-10-30-C-LD-MV). The ETL device comprises an integrated divergent offset lens with focal length $\mathrm{f}_{\mathrm{off}} = -150\,\mathrm{mm}$. Let us now calculate its ABCD matrix as follows,

$$\begin{aligned} \mathbf{T} &= [D_{\mathrm{f}_{\mathrm{RL2}}}]\,[L_{\mathrm{f}_{\mathrm{RL2}}}]\,[D_{\mathrm{f}_{\mathrm{RL2}}}]\,[L_{\mathrm{f}_{\mathrm{ETL}}}]\,[D_{\mathrm{f}_{\mathrm{RL1}}}]\,[L_{\mathrm{f}_{\mathrm{RL1}}}]\,[D_z] \\ &= \begin{bmatrix} -\frac{\mathrm{f}_{\mathrm{RL2}}}{\mathrm{f}_{\mathrm{RL1}}} & \mathrm{f}_{\mathrm{RL_2}}\left(1 - \frac{z'}{\mathrm{f}_{\mathrm{RL1}}} - \frac{\mathrm{f}_{\mathrm{RL1}}}{\mathrm{f}_{\mathrm{ETL}}}\right) \\ 0 & -\frac{\mathrm{f}_{\mathrm{RL1}}}{\mathrm{f}_{\mathrm{RL2}}} \end{bmatrix}, \end{aligned} \tag{B.6}$$

where $D_{\mathrm{f}_{\mathrm{RL1}}}$, $D_{\mathrm{f}_{\mathrm{RL2}}}$ and D_z stands for the light propagation in free space slabs through a section of thickness $\mathrm{f}_{\mathrm{RL1}}$, $\mathrm{f}_{\mathrm{RL2}}$ and z, respectively; while $L_{\mathrm{f}_{\mathrm{RL1}}}$, $L_{\mathrm{f}_{\mathrm{RL2}}}$ and $L_{\mathrm{f}_{\mathrm{ETL}}}$ corresponds to the transformation matrix of the RL1, RL2 and the ETL, correspondingly (see Fig. B.2).

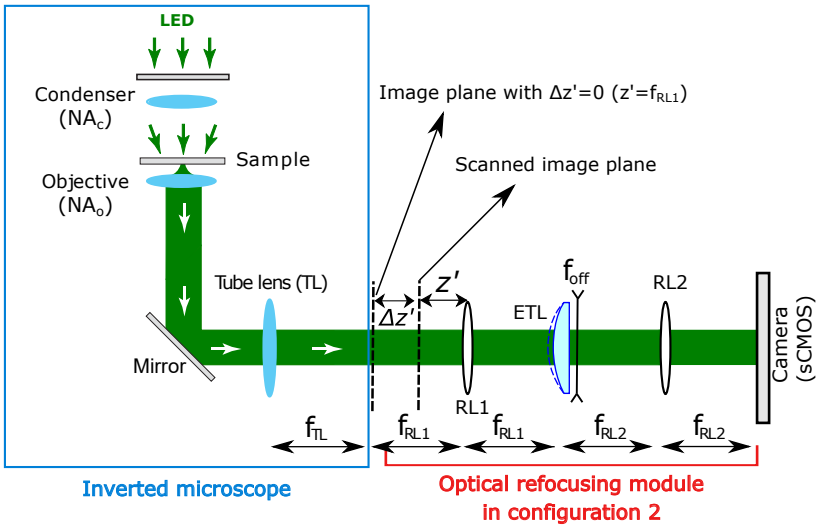

Figure B.3: Experimental setup for PC-ODT with the optical refocusing module in configuration 2, including an additional relay lens (RL2) to create a 4f imaging configuration between the tube lens and the camera and a ETL model which comprises an integrated divergent offset lens with focal length $\mathrm{f}_{\mathrm{off}} = -150\,\mathrm{mm}$.

Again, by considering imaging condition $f_{RL2}\left(1-\frac{z'}{f_{RL1}}-\frac{f_{RL1}}{f_{ETL}}\right)=0$ one gets $z=f_{RL1}-\left(f_{RL1}^2/f_{ETL}\right)$. Therefore, now we have $\Delta z'=z'-f_{RL1}=-f_{RL1}^2/f_{ETL}$ and one gets that the shift of the image of the imaged plane in the object space is given by

$$z_{defocus}=\frac{n_m\triangle z'}{M^2}=\frac{-n_m f_{RL1}^2}{M^2 f_{ETL}}, \tag{B.7}$$

where the magnification $M=M_{obj}\times(f_{RL1}/f_{TL})$.

We also recall that, as pointed out by both Eq. B.5 and Eq. B.7, the more effective way for obtaining a larger scanning range is to lower the magnification of the imaging system, thanks to the quadratic and inversely proportional relationship between $z_{defocus}$ and M. For instance, if one changes a $100\times$ objective to another with $40\times$ magnification, the scanning range is enlarged by a factor of 6.25. Another possibility for expanding the scan range may be using a greater relay lens focal length, respectively f_{RL1} and f_{RL} in the setups with the ORM in configuration 2 and configuration 1. Finally, the global magnification of the system with ORM in configuration 2 is given by $M_s=M\times(-f_{RL2}/f_{RL1})$ according to the term A of the corresponding $\mathbf{T}$ matrix (see Eq. B.6).

Appendix C

Experimental measurement of the modulation transfer function

The modulation transfer function (MTF) characterizes the imaging system accuracy for capturing the sample details and is useful to evaluate its spatial resolution [205, 206]. Briefly, it characterizes how the contrast decreases as the spatial frequency of the sample increases, since an imaging system usually exhibits a low-pass filter behaviour. In this Appendix, we explain how to experimentally measure the MTF of the optical refocusing module, comprising the ETL, the relay lenses and the detector (camera), previously described in the Sections 4.3 and 4.4 of the thesis.

The effective OTF of the microscope, $H_{\mathrm{EFF}}(\mathbf{p})$, considers light propagation from the condenser aperture until reaching the intermediate image plane corresponding to the back focal plane of the microscope objective. Nevertheless, the setups also comprise a 4f-system along with the ETL, therefore it is also important to consider the optical path between the image plane and the detector (camera). Again, by assuming a shift-invariant imaging system, one is able to measure its MTF in order to incorporate relay lenses, ETL and the camera (Hamamatsu Orca Flash 4.0) effects. The OTF and the MTF are simply two filters in series, so the equivalent transfer function in Fourier space would be the product of both.

For measuring the MTF we use a knife-edge method. The target is placed in the back focal plane of the objective and illuminated with an incoherent source. After the derivation of averaged edge response in the intensity distribution recorded by the camera, the line spread function (LSF) is computed and subsequently, its Fourier Transform magnitude leads to MTF [207]. Here, we suppose that the system and therefore the MTF is rotationally symmetric in *xy*-plane.

As shown in Fig. C.1, the MTF plot represents the variation of normalized contrast (visibility) modulation (y-axis) with spatial frequency (x-axis). The spatial frequency can be expressed as $\mu\mathrm{m}^{-1}$, or alternatively as line-pairs per millimeter (lp/mm). The inverse of its limiting value, where MTF value is around 0.1, defines the system resolution. Theoretically, the Hamamatsu camera with pixel size $a = 6.5\,\mu\mathrm{m}$ should be able to resolve a maximum frequency of $1000/(2a) \approx 77\,\mathrm{lp/mm}$ according to Nyquist resolution criterion although from $45\,\mathrm{lp/mm}$ the contrast is extremely poor. A radial profile of the MTF of the ORM in configuration 1 is illustrated in Fig. C.1. We observe that the system is able to transfer the contrast above 0.7 (70 %) for frequencies below $1\,\mu\mathrm{m}^{-1}$. However, the con-

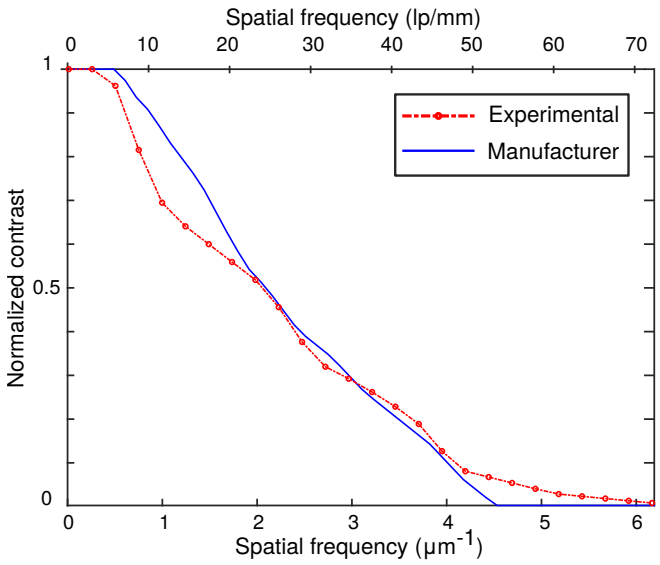

Figure C.1: Modulation transfer function (MTF) characterization of optical refocusing module in configuration 1. The double x-axis represents the spatial frequency both in μm^{-1} and in line pairs per millimeter (lp/mm).

trast transfer capability decreases when higher frequencies are considered, until reaching a threshold below 0.1 (10 % contrast) for those frequencies beyond $4\,\mu$m^{-1} corresponding to sample features below 250 nm.

The measured MTF displayed in Fig. C.1 (red curve) is similar to the manufacturer MTF characterization for the camera (see [208]), therefore we conclude that the latter has a prevailing effect in the MTF of the optical system composed of the ETL, the relay lenses and the camera. Theoretically, the MTF should be verified for each current of the ETL and placing the test (a sharp border) in-focus for each of them. As the experimental characterization of the MTF for every ETL current is a non-viable approach, here we have studied the MTF corresponding to the middle current of the considered range (100 mA) and shift-invariant hypothesis has been supposed for 3D MTF estimation.

Appendix D

Additional examples of RI reconstructions

In this Appendix, the RI reconstructions of different samples considered during the development and test of the PC-ODT are displayed. We note that no post-deconvolution processing has been applied for these reconstructions.

D.1 Diatom analysis

To further demonstrate the performance of PC-ODT, here we consider the 3D RI reconstruction of diatom cells composed of silicon dioxide ($n_s \sim 1.45-1.46$) immersed in oil ($n_m \sim 1.518$, Olympus type-F) to deal with the weak object approximation. Specifically, we use the ORM in configuration 1. The ETL and the sCMOS camera have been synchronized allowing for automatic axial scanning of 50 refocused images. The measurement of the stack of intensity images ($400 \times 400 \times 50$ voxels) has been performed in 100 ms with an axial step of 250 nm.

The chosen diatom, shown in Fig. D.1, exhibits multiple tiny pores ($0.1-1\,\mu$m) allowing for the exchange of substances with the environment. The diversity of structural features of the diatoms is useful for testing different imaging methods and in particular for the C-ODT (see for example [57]) and PC-OCT techniques. In particular, Fig. D.1 (a1) shows a volumetric representation of a diatom, corresponding to its 3D RI contrast distribution $\Delta n(\mathbf{r}) = |n_s(\mathbf{r}) - n_{\mathrm{m}}|$, that has been reconstructed by using PC-OCT. A cross section of the diatom 3D RI contrast is also displayed in Fig. D.1 (a2) in which a cut-off plane is used to visualize the inner part of the sample. Several 2D RI slices in the *xy*-plane are also shown in Figs. D.1 (b1-b3) from which one is able to measure the diameter of the circular-like pores ($\sim 710\,$nm) as well as the cell wall RI value (in the range of $n_{\mathrm{s}} = 1.45-1.47$), which is in good agreement with those previously reported values elsewhere [115]. Note that the RI value is higher near the pores than on other parts of the cell wall because the immersion oil completely filled the holes.

As observed in Figs. D.1 (b1-b3), it is possible to distinguish different cell walls at the bottom ($z = 0\,\mu$m) and the top ($z = 4\,\mu$m) of the diatom. These walls of the diatom exhibit multiple perforations, unlike the intermediate slices (e.g., $z = 2\,\mu$m) in which the

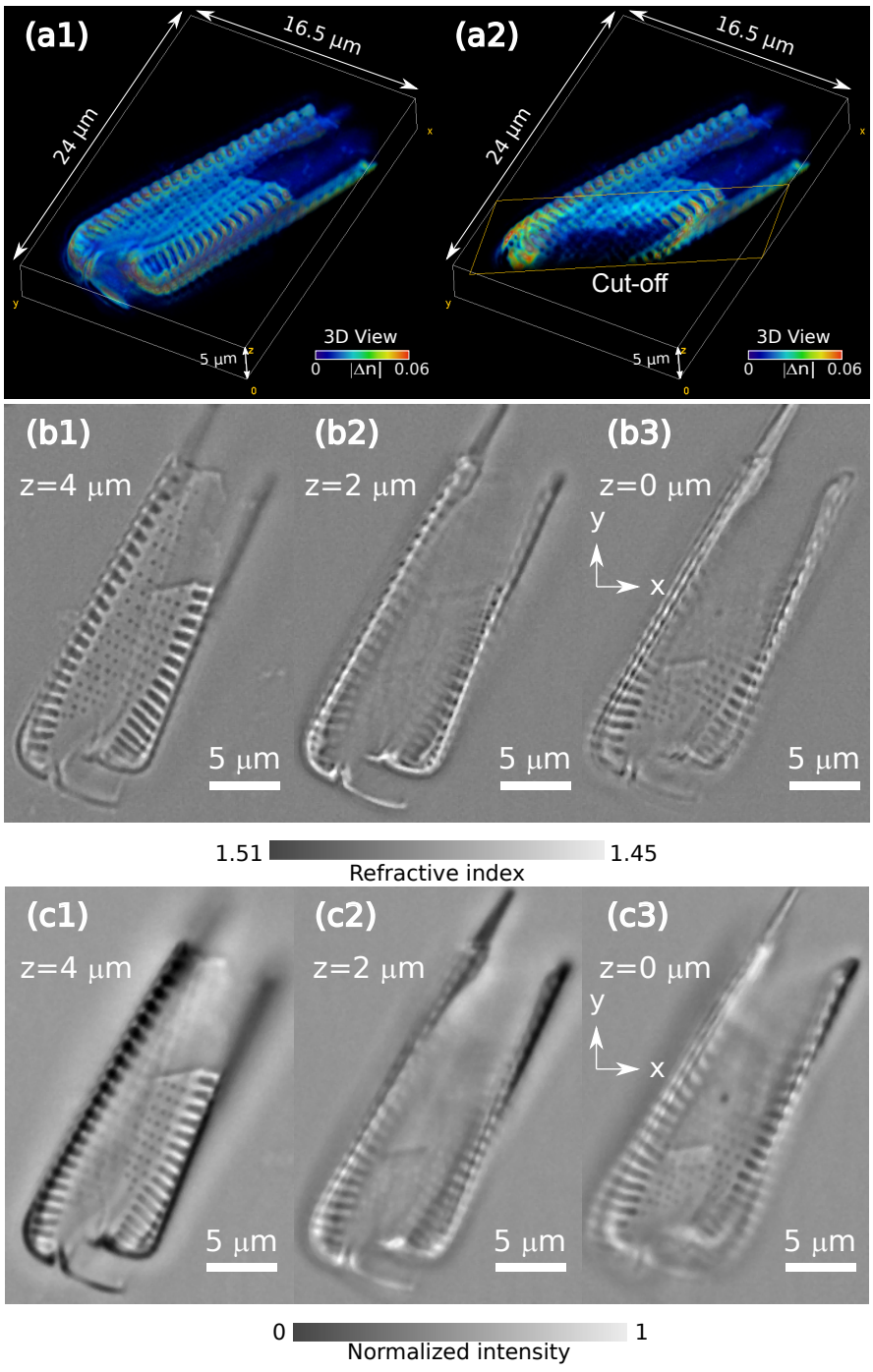

Figure D.1: (a1-a2) Volumetric representation of the reconstructed 3D RI constrast distribution of a diatom by using PC-ODT. The sample exhibits a clearly observable periodicity of the cell wall indents in the axial cross section. Note that part of the upper diatom wall has been broken. (b1-b3) 2D RI slices of in three different *xy*-planes. (c1-c3) The 2D intensity slices corresponding to the same RI planes displayed in the figures (b1-b3).

inner part of the diatom is mostly filled by the surrounding oil medium. The intensity slices corresponding to Figs. D.1 (b1-b3) are shown in Figs. D.1 (c1-c3) for comparison.

D.2 BFI and GI comparison using human cheek cell

Here, we use a buccal mucosa squamous cells sample attached to an epithelial layer and immersed in water in order to compare the results of the proposed GI illumination (with the ORM in configuration 1) with the conventional BFI in PC-ODT. Two intensity images of the sample at different depths are shown in Fig. D.2 (a). A stack ($400 \times 400 \times 50$ pixels) has been recorded and PC-ODT algorithm has been performed to reconstruct the RI contrast distribution of part of the sample (contained in the yellow box from Fig. D.2 (a)), as displayed in Fig. D.2 (b) for the epithelium and Fig. D.2 (c) for the cell itself. In Figs. D.2 (b, c) the 2D *xy*-slices of the RI reconstructions with both BFI and GI are displayed.

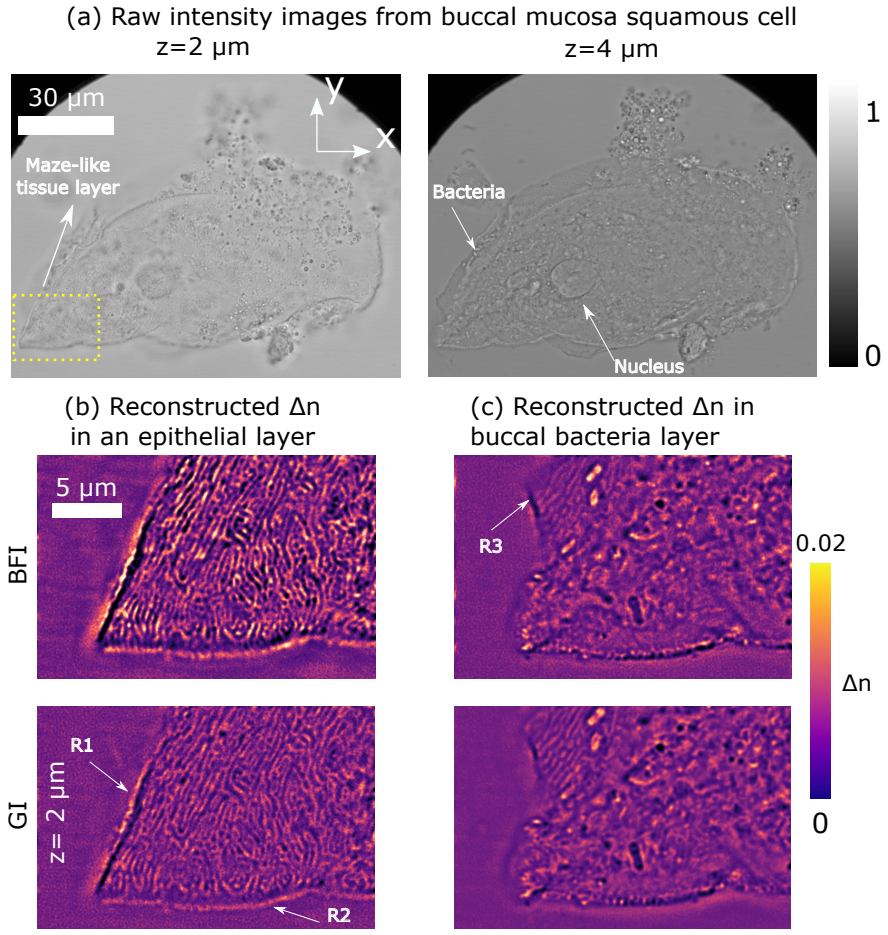

Figure D.2: (a) Intensity distributions (registered with GI) of a cheek cell image recoded at two different planes, showing the big nucleus and bacteria. (b-c) Reconstructed RI contrast (Δn) obtained with BFI and GI for a epithelial tissue layer (b), exhibiting a fine maze-like structure of fibers, and in buccal mucosa layers (c), where several bacteria are visible.

First of all, one notices that in the GI reconstruction the maze-like structure of the epithelial layer with approximately 300 nm diameter fibers is clearly resolved, which demonstrates high spatial resolution and appropriate balance between low and high frequency structures. Conversely, in BFI the maze structure is not completely resolved and suffers from more halo effects in the borders (see regions R1 and R2) and spatial resolution loss in some delicate structures (see R3). The average Δn of the epithelial maze-like fiber structure is 0.01, that is above the surrounding medium RI but below the averaged Δn value of bacteria (around 0.02).

D.3 Primary rat hepatocytes analysis

In Chapter 7 we have unraveled the interaction of metformin (ME) and diclofenac (DF) within the mitochondria of primary rat hepatocytes. Our goal has been to detect damage or morphological differences induced by different medications (mainly DF) through the analysis of the 3D RI tomogram recovered by using PC-ODT with ORM in configuration 2. The protective effect of ME against DF-induced apoptosis has been previously reported (see [190]) and the experimental results shown in Chapter 7 are in good agreement with this statement. The remaining tested drugs like ESI-05 (ES) and CE3FA (CE) are EPAC inhibitors applied in order to test whether the protective effect of metformin is abolished or not. However, they require further validation (respiration assays, immunofluorescence, etc.) before their use in pharmacology. The reconstruction of these samples comprising ES and CE is shown below, for the sake of completeness.

Relevant differences in mitochondria RI have been found when different cell treatments have been compared. Moreover, thanks to the feasibility of PC-ODT for 3D reconstruction one is able to detect and analyze the distribution of mitochondria 3D network. We remark that this study can not be addressed by conventional staining techniques as they are mainly appropiate for 2D imaging. The outcomes are summarized in Fig. D.3, where several representative 2D RI slices have been displayed, as well as in Fig. D.4 for the volumetric reconstructions of the same cells. Note that in these figures the absolute magnitude of the 3D RI contrast ($|\Delta n| = |n_s - n_m|$) is represented, as the surrounding medium RI ($n_m = 1.45$) is larger than that of the sample.

By inspection of 2D and 3D RI reconstructions one observes that the groups that do not include ME treatment exhibit granulated cytoplasm and isolated mitochondria. Conversely, when the ME is incorporated the mitochondria network is more likely to exist, which is observable in Fig. D.4 as organelles colored in orange. In Fig. D.4 there is also a noticeable depletion of the structure in those cells whose treatment involves DF so that they mainly flat. This fact further underlines the malfunctioning of the cell mitochondria.

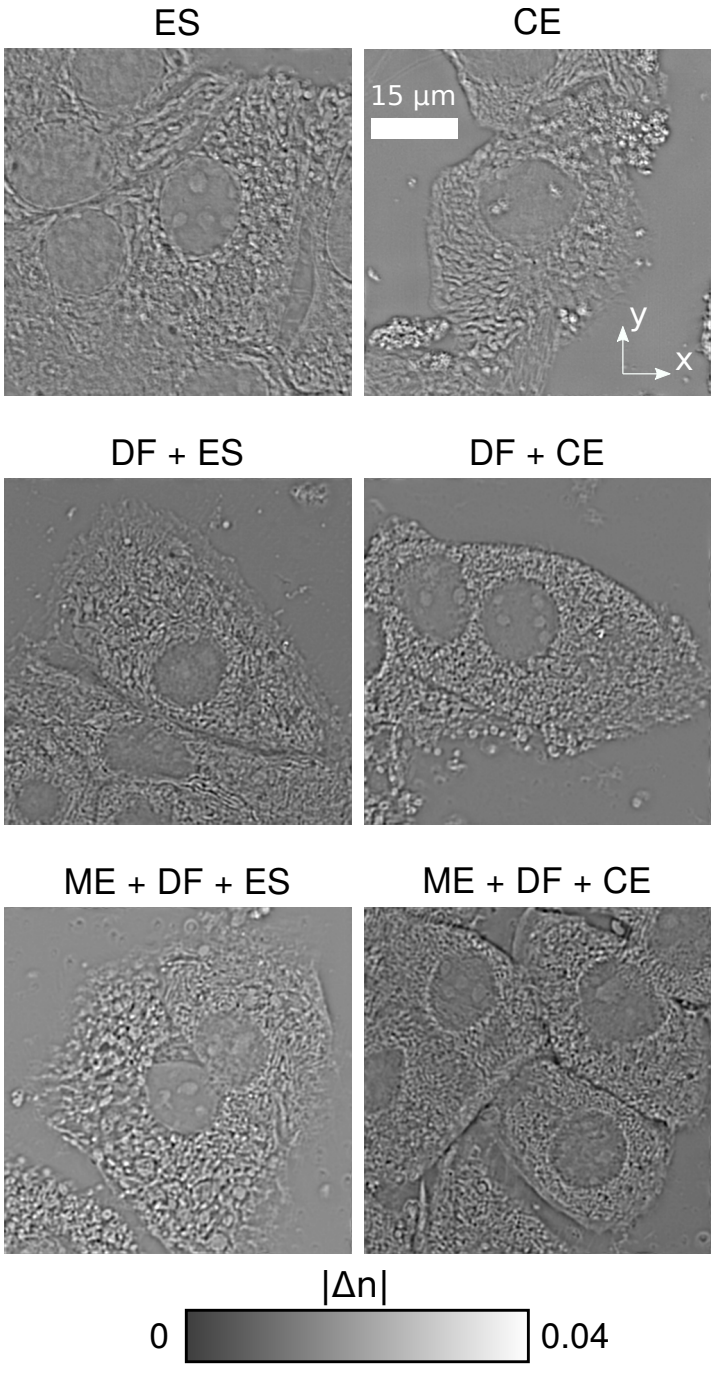

Figure D.3: 2D *xy*-slices of the RI for different primary rat hepatocyte groups, in which different drugs have been applied: ESI-05 (ES), metformin (ME), CE3FA (CE), diclofenac (DF) and combinations thereof.

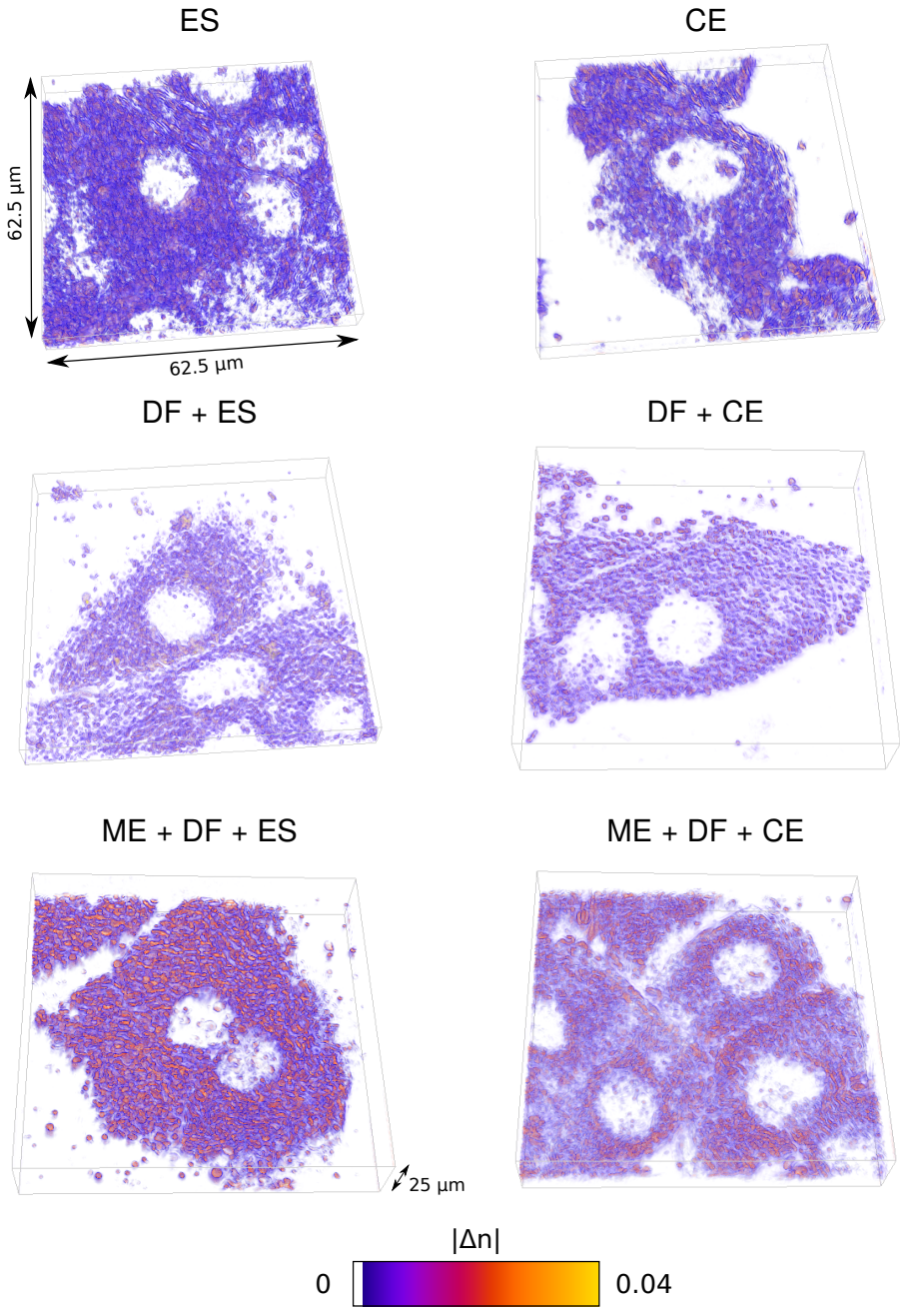

Figure D.4: 3D volumetric reconstructions of the RI for different primary rat hepatocyte groups, in which different drugs have been applied: ESI-05 (ES), metformin (ME), CE3FA (CE), diclofenac (DF) and combinations thereof.

Appendix E

Sample preparation protocols

In this Appendix all the methods used for sample preparation in the biological studies considered in this thesis are detailed.

E.1 Yeast preparation

To experimentally demonstrate the performance of fast 4D PC-ODT imaging in Chapter 6, we have considered living yeast cells (Schizosaccharomyces pombe bacteria dispersed in aqueous solution) that exhibit swimming motion and have fine cellular features. Specifically, 1 gr of the yeast sample is poured into a test tube containing 100 ml of sucrose solution (20 %) in distilled water. This sucrose dilution acts as a surrounding medium with $n_m = 1.37$ (see [209]). Then, the dilution is stirred and heated at 35º C for 10 minutes. Finally, it has been incubated 12 h at room temperature (25º C). S. pombe bacteria undergo aerobic fermentation in the presence of excess sugar, so 48 hours after the preparation the bacteria population has grown exponentially.

E.2 HeLa and COS-7 preparation protocol

The samples were prepared by the author of this thesis during his stay in the laboratory of Nanophotonics, in the Institut d'Optique (University of Bordeaux). The culture and preparation of HeLa and COS-7 cells were conducted as follows. First, the cells were cultured in Dulbecco's modified Eagle medium (DMEM) supplemented with 10% fetal bovine serum (FBS) and incubated at 37 ºC and 5 % CO_2 several days (a week for HeLa cells, 4 days for COS-7 samples). 12 h before fixation the cells were trypsinised and transferred to the cover slip as it takes some time for them to attach to the background. The trypsinization is useful for the manipulation and transfer of HeLa and COS-7 cells, mainly for detaching the samples from one culture plate to another, and comprises the following steps:

1. Prepare, under the hood, all the required material: pipettes, Dulbecco's Modified Eagle Medium (DMEM), trypsin and Phosphate-buffered saline (PBS). It is convenient to pre-warm DMEM and trypsin solutions.

2. Aspirate the DMEM.

3. Rinse the sample once with PBS to remove any rest of remaining DMEM, that would cancels trypsin effect.

4. Add 1.5-2 mL of trypsin solution, ensuring that the entire surface of the flask is covered.

5. Store the sample in the incubator (37ºC) during 5-8 min. Ocasionally it is possible to tap or shake the flask to help with the detachment.

6. Observe the sample with the microscope until the cells are detached and floating. At this point the cells should look rounded, which inform us that the trypsin must be canceled (an excessive time may damage the culture) by adding 10 mL DMEM.

7. Transfer the cells to a new flask or the final cover slip for observation.

E.3 Leishmania-infected DH82 cells

The samples were prepared by collaborators of veterinary microbial infectology research group, from the Faculty of Veterinary of the Complutense University of Madrid. With regard to sample preparation, DH82 (ATCC ©CRL-10389TM) is a macrophage cell line obtained from a dog with a neoplasm of histiocytic origin [210]. It was maintained in DMEM medium supplemented with 10 % Foetal Bovine Serum (FBS), 100 U/ml penicillin and 100 μg/ml streptomycin. Then, it was incubated at 37°C 5% CO_2 in six-well plates. *Leishmania infantum* BCN150 strain cells (classified as M/CAN/ES/96/BCN150 zymodeme MON-1), previously reported in [211], were cultivated in Schneider's Insect Medium (Biowest) supplemented with 20 % FBS, 100 U/ml penicillin and 100 mg/ml streptomycin at 26°C until the stationary phase and they were used to infect DH82 cells. DH82 macrophages were cultured in 24-well plates overnight at a concentration of $1 \cdot 10^6$ cells per well.

The infection protocol consists of adding promastigotes to the cells at a ratio 10 : 1 (parasites: cells) on the following day, according to the protocol previously described in [212]. Cells were incubated at 37°C and 5 % CO_2 for 4 hours and, subsequently, extracellular parasites were eliminated by washing twice with Dulbecco's Phosphate Buffered Saline (PBS) establishing the initial infection time point. Then fresh medium was added and cells were cultivated for 24 h and 72 h. The cells were fixed using methanol 70 % during 5 min at room temperature. Afterwards the samples are divided into two groups according to whether they undergo staining or not. For those ones that were stained, each slide had been immersed in 250 μl 5% Giemsa's stain improved R66 solution Gurr and stored for 15 min at ambient temperature. After that each sample was washed five times with distilled water and let it dry out. The stained samples are only used as a reference, while the unstained samples are the ones which have been applied for RI analysis by PC-ODT. Finally, four groups of samples have been considered: H24 and H72 (healthy samples cultivated during 24 h and 72 h, respectively, which have not been infected) and P24 and P72 (infected samples, 24 h and 72 h after the parasitization).

E.4 Rat hepatocytes for drug screening

The samples were prepared by collaborators from the Faculty of Medical Sciences of the University of Groningen. The preparation protocol for the rat hepatocytes has been conducted as follows. First, primary rat hepatocytes ($4.5 \cdot 10^5$cells) were seeded on glass coverslips in 12-well plates. 12 h after incubation and 4 h of attachment, the cells culture medium was removed and coverslips were washed three times with PBS (ThermoFisher scientific®). Then, cells were fixated using 4% paraformaldehyde (Merck®, Germany) solution (PFA) in PBS for 10 minutes at room temperature (RT), and washed three times with PBS at RT. Permeabilization was performed using 0.1% triton X-100 in PBS at RT for 10 min. 2% Bovine serum albumin (Sigma Aldrich®) in PBS was used to block non-specific binding of the antibodies for 30 min. Cells were incubated with diclofenac ($400\,\mu$M/L for 12 h) and without (control group), with ESI-05 ($15\,\mu$M/L for 12 h) or CE3FA ($10\,\mu$M/L for 2 h), prepared 30 min before metformin addition. Finally, the samples are mounted in Vectashield Antifade Mounting Medium with DAPI (Vector Laboratories®), characterized by a RI value of 1.45 ± 0.001 as measured by the manufacturer with a calibrated ATAGO PAL-RI refractometer at 25 ºC. Oxygen consumption rate is determined in XF base medium suplemented with 10 mM glucose and adjusted to pH 7.4 followed by the subsequent addition of oligomycin A (2.5 μM), dinitrophenol (50 μM) along with rotenone and antimycin A ($2-4\,\mu$M).

Appendix F

Statistical tests

In this Appendix we describe the statistical test applied for comparison between different sample groups, in order to verify whether the differences found by DMC or RI analysis are significant or not. In particular, in this thesis the independent samples Welch t-test and the multiple non-parametric Mann-Whitney-U test have been applied. Both tests have been performed in MATLAB by using built-in functions.

F.1 Independent Welch t-test

This test requires an input comprising two data populations (further referred to as a and b) of a certain variable corresponding to two sample groups (for instance, healthy and infected cells), as well as a significance level (typically 0.01 or 0.05). Moreover, this test can be applied without assuming equal population variances unlike the conventional t-test. In our case, the variables applied for comparison are the averaged DMC or the averaged RI. The goal of the t-test is to check whether the difference between the means of a and b is 0 (null hypothesis) or not. If the p-value is lower than the significance level, we can reject the null hypothesis that there is no difference between means of a and b. Otherwise, if the p-value is higher than said significance level, the null hypothesis can not be discarded and both populations may have the same mean value. In this way, the lower the p-value is, the more reliable are the differences between compared groups. For performing the Welch t-test, we use the MATLAB command *ttest2*, whose output is a binary value which indicates if the null hypothesis can be rejected or not, and the corresponding p-value of the comparison.

F.2 Multiple non-parametric Mann-Whitney-U test

The multiple non-parametric Mann-Whitney-U test (also known as Wilcoxon rank-sum test) has been used to study the averaged RI contrast among different (more than 2) sample groups. In this way, we test the null hypothesis that there is no difference between medians of sample groups, against the alternative that there is. Again, this test is performed in MATLAB and using the command *ranksum,* with the same inputs and outputs as Welch t-test.

Bibliography

[1] R. Murphy. The quest for quantitative microscopy. *Nat. Meth.*, 9:627–627, 2012.

[2] J. C. Waters. Accuracy and precision in quantitative fluorescence microscopy. *J. Cell Biol.*, 185(7):1135–1148, 2009.

[3] B. O. Leung and K. C. Chou. Review of super-resolution fluorescence microscopy for biology. *Appl. Spectrosc.*, 65(9):967–980, 2011.

[4] T. Wilson. Optical sectioning in fluorescence microscopy. *J. Microsc.*, 242(2):111–116, 2011.

[5] L. Möckl, D. C. Lamb, and C. Bräuchle. Super-resolved fluorescence microscopy: Nobel prize in chemistry 2014 for Eric Betzig, Stefan Hell, and William E. Moerner. *Angewandte Chemie International Edition*, 53(51):13972–13977, 2014.

[6] F. Zernike. Phase contrast, a new method for the microscopic observation of transparent objects part II. *Physica*, 9(10):974–986, 1942.

[7] R. D. Allen and G. B. David. The Zeiss-Nomarski differential interference equipment for transmitted-light microscopy. *Zeitschrift für wissenschaftliche Mikroskopie und mikroskopische Technik*, 69(4):193–221, 1969.

[8] M. R. Arnison, K. G. Larkin, C. J. R. Sheppard, N. I. Smith, and C. J. Cogswell. Linear phase imaging using differential interference contrast microscopy. *J. Microsc.*, 214(1):7–12, 2004.

[9] P. Marquet, B. Rappaz, P. J. Magistretti, E. Cuche, Y. Emery, T. Colomb, and C. Depeursinge. Digital holographic microscopy: a noninvasive contrast imaging technique allowing quantitative visualization of living cells with subwavelength axial accuracy. *Opt. Lett.*, 30(5):468–470, 2005.

[10] C. Hu and G. Popescu. *Quantitative Phase Imaging: Principles and Applications*. Springer, Cham, 2019.

[11] Y. Park, C. Depeursinge, and G. Popescu. Quantitative phase imaging in biomedicine. *Nat. Photonics*, 12(10):578, 2018.

[12] D. Gabor. A new microscopic principle. *Nature*, 161:777–778, 1948.

[13] P. Ferraro, A. Wax, and Z. Zalevsky. *Coherent Light Microscopy: Imaging and Quantitative Phase Analysis*. Springer Series in Surface Sciences. Springer, 2011.

[14] S. K. Debnath and Y. Park. Real-time quantitative phase imaging with a spatial phase-shifting algorithm. *Opt. Lett.*, 36(23):4677–4679, 2011.

[15] J. A. Picazo-Bueno, D. Cojoc, F. Iseppon, V. Torre, and V. Micó. Single-shot, dual-mode, water-immersion microscopy platform for biological applications. *Appl. Opt.*, 57(1):A242–A249, 2018.

[16] M. Trusiak, V. Micó, J. Garcia, and K. Patorski. Quantitative phase imaging by single-shot Hilbert–Huang phase microscopy. *Opt. Lett.*, 41(18):4344–4347, 2016.

[17] G. Popescu, T. Ikeda, R. R. Dasari, and M. S. Feld. Diffraction phase microscopy for quantifying cell structure and dynamics. *Opt. Lett.*, 31(6):775–777, 2006.

[18] Y. Park, C. A. Best, T. Auth, N. S. Gov, S. A. Safran, G. Popescu, S. Suresh, and M. S. Feld. Metabolic remodeling of the human red blood cell membrane. *Proceedings of the National Academy of Sciences*, 107(4):1289–1294, 2010.

[19] M. Mir, Z. Wang, Z. Shen, M. Bednarz, R. Bashir, I. Golding, S. G. Prasanth, and G. Popescu. Optical measurement of cycle-dependent cell growth. *Proc. of the National Academy of Sciences*, 108(32):13124–13129, 2011.

[20] B. Bhaduri, C. Edwards, H. Pham, R. Zhou, T. H. Nguyen, L. L. Goddard, and G. Popescu. Diffraction phase microscopy: principles and applications in materials and life sciences. *Adv. Opt. Photon.*, 6(1):57–119, 2014.

[21] C. Yang, A. Wax, R. R. Dasari, and M. S. Feld. Phase-dispersion optical tomography. *Opt. Lett.*, 26(10):686–688, 2001.

[22] A. Burvall, U. Lundström, P. A. C. Takman, D. H. Larsson, and H. M. Hertz. Phase retrieval in X-ray phase-contrast imaging suitable for tomography. *Opt. Express*, 19(11):10359–10376, 2011.

[23] M. Dierolf, A. Menzel, P. Thibault, P. Schneider, C. M. Kewish, R. Wepf, O. Bunk, and F. Pfeiffer. Ptychographic X-ray computed tomography at the nanoscale. *Nature*, 467(7314):436–439, 2010.

[24] M. Zdora, P. Thibault, W. Kuo, V. Fernandez, H. Deyhle, J. Vila-Comamala, M. P. Olbinado, A. Rack, P. M. Lackie, and O. L. Katsamenis. X-ray phase tomography with near-field speckles for three-dimensional virtual histology. *Optica*, 7(9):1221–1227, 2020.

[25] A. Roberts, E. Ampem-Lassen, A. Barty, K. A. Nugent, G. W. Baxter, N. M. Dragomir, and S. T. Huntington. Refractive-index profiling of optical fibers with axial symmetry by use of quantitative phase microscopy. *Opt. Lett.*, 27(23):2061–2063, 2002.

[26] T. C. Wedberg and W. C. Wedberg. Tomographic reconstruction of the cross-sectional refractive index distribution in semi-transparent, birefringent fibres. *J. Microsc.*, 177(1):53–67, 1995.

[27] F. Dubois, L. Joannes, and J. Legros. Improved three-dimensional imaging with a digital holography microscope with a source of partial spatial coherence. *Appl. Opt.*, 38(34):7085–7094, 1999.

[28] P. Langehanenberg, G. Bally, and B. Kemper. Application of partially coherent light in live cell imaging with digital holographic microscopy. *Journal of Modern Optics*, 57(9):709–717, 2010.

[29] B. Bhaduri, H. Pham, M. Mir, and G. Popescu. Diffraction phase microscopy with white light. *Opt. Lett.*, 37(6):1094–1096, 2012.

[30] P. Bon, G. Maucort, B. Wattellier, and S. Monneret. Quadriwave lateral shearing interferometry for quantitative phase microscopy of living cells. *Opt. Express*, 17(15):13080–13094, 2009.

[31] M. R. Teague. Deterministic phase retrieval: a green's function solution. *J. Opt. Soc. Am.*, 73(11):1434–1441, 1983.

[32] A. Barty, K. A. Nugent, D. Paganin, and A. Roberts. Quantitative optical phase microscopy. *Opt. Lett.*, 23(11):817–819, 1998.

[33] D. Paganin and K. A. Nugent. Noninterferometric phase imaging with partially coherent light. *Phys. Rev. Lett.*, 80:2586–2589, 1998.

[34] J. Frank, S. Altmeyer, and G. Wernicke. Non-interferometric, non-iterative phase retrieval by green's functions. *J. Opt. Soc. Am. A*, 27(10):2244–2251, 2010.

[35] S. S. Kou, L. Waller, G. Barbastathis, P. Marquet, C. Depeursinge, and C. J. R. Sheppard. Quantitative phase restoration by direct inversion using the optical transfer function. *Opt. Lett.*, 36(14):2671–3, 2011.

[36] L. Waller, L. Tian, and G. Barbastathis. Transport of intensity phase-amplitude imaging with higher order intensity derivatives. *Opt. Express*, 18(12):12552–12561, 2010.

[37] J. Rodenburg and A. Maiden. Ptychography. In P. W. Hawkes and J. C. H. Spence, editors, *Springer Handbook of microscopy*, pages 819–904. Springer Nature, 2019.

[38] J. Marrison, L. Räty, P. Marriott, and P. O'toole. Ptychography: a label free, high-contrast imaging technique for live cells using quantitative phase information. *Scientific reports*, 3:2369, 2013.

[39] P. C. Konda, L. Loetgering, K. C. Zhou, S. Xu, A. R. Harvey, and R. Horstmeyer. Fourier ptychography: current applications and future promises. *Opt. Express*, 28(7):9603–9630, 2020.

[40] G. Zheng, R. Horstmeyer, and C. Yang. Wide-field, high-resolution Fourier ptychographic microscopy. *Nat. Photonics*, 7(9):739–745, 2013.

[41] K. G. Phillips, S. L. Jacques, and O. J. T. McCarty. Measurement of single cell refractive index, dry mass, volume, and density using a transillumination microscope. *Phys. Rev. Lett*, 109(11):118105, 2012.

[42] R. Dandliker and K. Weiss. Reconstruction of the three-dimensional refractive index from scattered waves. *Opt. Commun.*, 1(7):323 – 328, 1970.

[43] E. Wolf. Three-dimensional structure determination of semi-transparent objects from holographic data. *Opt. Commun.*, 1(4):153–156, 1969.

[44] F. Charrière, A. Marian, F. Montfort, J. Kuehn, T. Colomb, E. Cuche, P. Marquet, and C. Depeursinge. Cell refractive index tomography by digital holographic microscopy. *Opt. Lett.*, 31(2):178–180, 2006.

[45] W. Choi, C. Fang-Yen, K. Badizadegan, S. Oh, N. Lue, R.R. Dasari, and M.S. Feld. Tomographic phase microscopy. *Nat. Methods*, 4(9):717–720, 2007.

[46] O. Haeberlé, K. Belkebir, H. Giovaninni, and A. Sentenac. Tomographic diffractive microscopy: basics, techniques and perspectives. *J. Mod. Opt.*, 57(9):686–699, 2010.

[47] Y. Cotte, F. M. Toy, C. Arfire, S. S. Kou, D. Boss, I. Bergoënd, and C. Depeursinge. Realistic 3D coherent transfer function inverse filtering of complex fields. *Biomed. Opt. Express*, 2(8):2216–30, 2011.

[48] Y. Kim, H. Shim, K. Kim, H. Park, J. H. Heo, J. Yoon, C. Choi, S. Jang, and Y. Park. Common-path diffraction optical tomography for investigation of three-dimensional structures and dynamics of biological cells. *Opt. Express*, 22(9):10398–10407, 2014.

[49] K. Kim, J. Yoon, and Y. Park. Simultaneous 3D visualization and position tracking of optically trapped particles using optical diffraction tomography. *Optica*, 2(4):343–346, 2015.

[50] K. Kim, H. Yoon, M. Diez-Silva, M. Dao, R. R. Dasari, and Y. Park. High-resolution three-dimensional imaging of red blood cells parasitized by Plasmodium falciparum and in situ hemozoin crystals using optical diffraction tomography. *J. Biomed. Opt*, 19(1):011005, 2013.

[51] J. Jung, K. Kim, J. Yoon, and Y. Park. Hyperspectral optical diffraction tomography. *Opt. Express*, 24(3):2006–2012, 2016.

[52] Y. Cotte, F. Toy, P. Jourdain, N. Pavillon, D. Boss, P. Magistretti, P. Marquet, and C. Depeursinge. Marker-free phase nanoscopy. *Nat. Photonics*, 7(2):113–117, 2013.

[53] Y. Sung, W. Choi, C. Fang-Yen, K. Badizadegan, R. R. Dasari, and M. S. Feld. Optical diffraction tomography for high resolution live cell imaging. *Opt. Express*, 17(1):266–277, 2009.

[54] Manuel Nieto-Vesperinas. *Scattering and Diffraction in Physical Optics*. World Scientific, 2nd edition, 2006.

[55] V. Lauer. New approach to optical diffraction tomography yielding a vector equation of diffraction tomography and a novel tomographic microscope. *J. Microsc.*, 205(2):165–176, 2002.

[56] K. Kim, K. S. Kim, H. J. Park, J. C. Ye, and Y. K. Park. Real-time visualization of 3-D dynamic microscopic objects using optical diffraction tomography. *Opt. Express*, 21(26):32269–32278, 2013.

[57] M. Debailleul, B. Simon, V. Georges, O. Haeberlé, and V. Lauer. Holographic microscopy and diffractive microtomography of transparent samples. *Meas. Sci. Technol*, 19(7):074009, 2008.

[58] T. Kim, R. Zhou, L. L. Goddard, and G. Popescu. Solving inverse scattering problems in biological samples by quantitative phase imaging. *Laser Photon. Rev.*, 10(1):13–39, 2016.

[59] J. A. Rodrigo and T. Alieva. Rapid quantitative phase imaging for partially coherent light microscopy. *Opt. Express*, 22(11):13472–83, 2014.

[60] N Streibl. Three-dimensional imaging by a microscope. *J. Opt. Soc. Am. A.*, 2(2):121–127, 1985.

[61] Tomocube website. http://www.tomocube.com/. Accessed: 2020-03-25.

[62] Nanolive website. http://nanolive.ch/. Accessed: 2020-03-25.

[63] M. Born and E. Wolf. *Principles of optics: electromagnetic theory of propagation, interference and diffraction of light*. Elsevier, 2013.

[64] M. H. Shoreh, A. Goy, J. Lim, U. Kamilov, M. Unser, and D. Psaltis. Optical tomography based on a nonlinear model that handles multiple scattering. In *2017 IEEE International Conference on Acoustics, Speech and Signal Processing (ICASSP)*, pages 6220–6224. IEEE, 2017.

[65] A. C. Kak, M. Slaney, and G. Wang. Principles of computerized tomographic imaging. *Medical Physics*, 29(1):107–107, 2002.

[66] M. H. Jenkins and T. K. Gaylord. Three-dimensional quantitative phase imaging via tomographic deconvolution phase microscopy. *Appl. Opt.*, 54(31):9213, 2015.

[67] J. Lim, K. Lee, K. H. Jin, S. Shin, S. Lee, Y. Park, and J. C. Ye. Comparative study of iterative reconstruction algorithms for missing cone problems in optical diffraction tomography. *Opt. Express*, 23(13):16933–16948, 2015.

[68] P. Müller, M. Schürmann, and J. Guck. The theory of diffraction tomography. *arXiv preprint arXiv:1507.00466*, 2015.

[69] D. L. Marks. A family of approximations spanning the Born and Rytov scattering series. *Opt. Express*, 14(19):8837–8848, 2006.

[70] S. Vertu, J. Delaunay, I. Yamada, and O. Haeberlé. Diffraction microtomography with sample rotation: influence of a missing apple core in the recorded frequency space. *Open Physics*, 7(1):22–31, 2009.

[71] B. Simon, M. Debailleul, M. Houkal, C. Ecoffet, J. Bailleul, J. Lambert, A. Spangenberg, H. Liu, O. Soppera, and O. Haeberlé. Tomographic diffractive microscopy with isotropic resolution. *Optica*, 4(4):460–463, 2017.

[72] Y. Bao and T. K. Gaylord. Quantitative phase imaging method based on an analytical nonparaxial partially coherent phase optical transfer function. *J. Opt. Soc. Am. A*, 33(11):2125, 2016.

[73] P. Bon, S. Aknoun, S. Monneret, and B. Wattellier. Enhanced 3D spatial resolution in quantitative phase microscopy using spatially incoherent illumination. *Opt. Express*, 22(7):817–819, 2014.

[74] B. Simon, M. Debailleul, V. Georges, O. Haeberlé, and V. Lauer. Three-dimensional coherent optical diffraction tomography of transparent living samples. *IFAC Proceedings Volumes*, 39(18):47–51, 2006.

[75] U. S. Kamilov, I. N. Papadopoulos, M. H. Shoreh, A. Goy, C. Vonesch, M. Unser, and D. Psaltis. Learning approach to optical tomography. *Optica*, 2(6):517, 2015.

[76] A. Berdeu, F. Momey, B. Laperrousaz, X. Bordy, T.and Gidrol, J. Dinten, N. Picollet-D'hahan, and C. Allier. Comparative study of fully three-dimensional reconstruction algorithms for lens-free microscopy. *Appl. Opt.*, 56(13):3939–3951, 2017.

[77] J. Kostencka, T. Kozacki, A. Kuś, and M. Kujawińska. Accurate approach to capillary-supported optical diffraction tomography. *Opt. Express*, 23(6):7908–7923, 2015.

[78] A. J. Devaney. A filtered backpropagation algorithm for diffraction tomography. *Ultrasonic imaging*, 4(4):336–350, 1982.

[79] V. Lauer. New approach to optical diffraction tomography yielding a vector equation of diffraction tomography and a novel tomographic microscope. *J. Microsc.*, 205(2):165–176, 2002.

[80] L. Granero, V. Micó, Z. Zalevsky, and J García. Synthetic aperture superresolved microscopy in digital lensless Fourier holography by time and angular multiplexing of the object information. *App. Opt.*, 49(5):845–857, 2010.

[81] V. Micó, Z. Zalevsky, C. Ferreira, and J. García. Superresolution digital holographic microscopy for three-dimensional samples. *Opt. Express*, 16(23):19260–19270, 2008.

[82] R. Dasgupta, S. K. Mohanty, and P. K. Gupta. Controlled rotation of biological microscopic objects using optical line tweezers. *Biotechnol. Lett.*, 25(19):1625–1628, 2003.

[83] S. Vertu, J. Flügge, J. Delaunay, and O. Haeberlé. Improved and isotropic resolution in tomographic diffractive microscopy combining sample and illumination rotation. *Open Phys.*, 9(4):969–974, 2011.

[84] Y. Sung and R. R. Dasari. Deterministic regularization of three-dimensional optical diffraction tomography. *J. Opt. Soc. Am. A.*, 28(8):1554–61, 2011.

[85] Q. Zhang, L. Zhong, P. Tang, Y. Yuan, S. Liu, J. Tian, and X. Lu. Quantitative refractive index distribution of single cell by combining phase-shifting interferometry and AFM imaging. *Sci. Rep.*, 7(1):1–10, 2017.

[86] M. Chen, L. Tian, and L. Waller. 3D differential phase contrast microscopy. *Biomed. Opt. Express*, 9718(10):971826, 2016.

[87] C. J. R. Sheppard. Defocused transfer function for a partially coherent microscope and application to phase retrieval. *J. Opt. Soc. Am. A*, 21(5):828, 2004.

[88] N. Streibl. Fundamental restrictions for 3-D light distributions. *Optik*, 66(4):341–354, 1984.

[89] J. M. Soto, J. A. Rodrigo, and T. Alieva. Label-free quantitative 3D tomographic imaging for partially coherent light microscopy. *Opt. Express*, 25(14):15699–15712, 2017.

[90] L. Turner, B. Dhal, J. Hayes, A. Mancuso, K. Nugent, D. Paterson, R. Scholten, C. Tran, and A. Peele. X-ray phase imaging: Demonstration of extended conditions for homogeneous objects. *Opt. Express*, 12(13):2960–2965, 2004.

[91] D. S. C. Biggs. 3D deconvolution microscopy. *Curr. Protoc. Cytom.*, (1):1–20, 2010.

[92] D. Sage, L. Donati, F. Soulez, D. Fortun, G. Schmit, A. Seitz, R. Guiet, C. Vonesch, and M. Unser. DeconvolutionLab2: An Open-Source Software for Deconvolution Microscopy. *Methods*, 115:28–41, 2017.

[93] C. N. H. Candia and B. Gutiérrez-Medina. Direct imaging of phase objects enables conventional deconvolution in bright field light microscopy. *PloS One*, 9(2):e89106, 2014.

[94] P. J. Tadrous. A method of PSF generation for 3D brightfield deconvolution. *J. Microsc.*, 237(2):192–199, 2010.

[95] A. Kuś, M. Dudek, B. Kemper, M. Kujawińska, and A. Vollmer. Tomographic phase microscopy of living three-dimensional cell cultures. *J. Biomed. Opt.*, 19(4):046009, 2014.

[96] S. Van Aert, D. Van Dyck, and J. Arnold. Resolution of coherent and incoherent imaging systems reconsidered-classical criteria and a statistical alternative. *Opt. Express*, 14(9):3830–3839, 2006.

[97] Microscopy U. Properties of microscope objectives. Available from: https://www.microscopyu.com/microscopy-basics/properties-of-microscope-objectives [last accesed April 2020].

[98] P. Giannios, K. G. Toutouzas, M. Matiatou, K. Stasinos, M. M. Konstadoulakis, G. C. Zografos, and K. Moutzouris. Visible to near-infrared refractive properties of freshly-excised human-liver tissues: marking hepatic malignancies. *Sci. Rep.*, 6:27910, 2016.

[99] L. V. Rodríguez de Marcos, J. I. Larruquert, J. A. Méndez, and J. A. Aznárez. Self-consistent optical constants of SiO_2 and Ta_2O_5 films. *Opt. Mater. Express*, 6(11):3622–3637, 2016.

[100] G. E. Healey and R. Kondepudy. Radiometric CCD camera calibration and noise estimation. *IEEE Transactions on Pattern Analysis and Machine Intelligence*, 16(3):267–276, 1994.

[101] H. J. Trussell and R. Zhang. The dominance of Poisson noise in color digital cameras. In *2012 19th IEEE International Conference on Image Processing*, pages 329–332. IEEE, 2012.

[102] L. Zhang, L. Zhang, X. Mou, and D. Zhang. FSIM: A feature similarity index for image quality assessment. *IEEE transactions on Image Processing*, 20(8):2378–2386, 2011.

[103] P. Kovesi. Image features from phase congruency. *J. Comput. Vis. Res.*, 1(3):1–26, 1999.

[104] M. Ziemczonok, A. Kuś, P. Wasylczyk, and M. Kujawińska. 3D-printed biological cell phantom for testing 3D quantitative phase imaging systems. *Sci. Rep.*, 9(1):1–9, 2019.

[105] Y. Bao and T. K. Gaylord. Iterative optimization in tomographic deconvolution phase microscopy. *J. Opt. Soc. Am. A.*, 35(4):652–660, 2018.

[106] K. Lee, K. Kim, G. Kim, S. Shin, and Y. Park. Time-multiplexed structured illumination using a DMD for optical diffraction tomography. *Opt. Lett.*, 42(5):999–1002, 2017.

[107] A.V. Belashov, A.A. Zhikhoreva, V.G. Bespalov, O.S. Vasyutinskii, N.T. Zhilinskaya, V.I. Novik, and I.V. Semenova. Determination of the refractive index of dehydrated cells by means of digital holographic microscopy. *Tech. Phys. Lett.*, 43(10):932–935, 2017.

[108] J. A. Rodrigo, J. M. Soto, and T. Alieva. Fast label-free microscopy technique for 3D dynamic quantitative imaging of living cells. *Biomed. Opt. Express*, 8(12):5507–5517, 2017.

[109] P. Evennett. Köhler illumination: a simple interpretation. In *Proc. R. Microsc. Soc.*, volume 28, pages 10–13, 1994.

[110] Optotune AG. Electric lens driver 4. lens driver manual. Available from: https://www.optotune.com/el-10-30-c-lens [last accesed April 2020].

[111] J. M. Jabbour, B. H. Malik, C. Olsovsky, R. Cuenca, S. Cheng, J. A. Jo, Y. L. Cheng, J. M. Wright, and K. C. Maitland. Optical axial scanning in confocal microscopy using an electrically tunable lens. *Biomed. Opt. Express*, 5(2):645–652, 2014.

[112] F. O. Fahrbach, F. F. Voigt, B. Schmid, F. Helmchen, and J. Huisken. Rapid 3D light-sheet microscopy with a tunable lens. *Opt. Express*, 21(18):21010–21026, 2013.

[113] J. A. Rodrigo and T. Alieva. Illumination coherence engineering and quantitative phase imaging. *Opt. Lett.*, 39(19):5634–7, 2014.

[114] Olympus. Data sheet of UPLSAPO 100XO. Available from: https://www.tengrant.com/upLoad/file/20160629/uplsapo_100xo_en.pdf [last accesed April 2020].

[115] S. Yamanaka, R. Yano, H. Usami, N. Hayashida, M. Ohguchi, H. Takeda, and K. Yoshino. Optical properties of diatom silica frustule with special reference to blue light. *J. Appl. Phys.*, 103(7):074701, 2008.

[116] S. A. Spaulding, D. J. Lubinski, and M. Potapova. Diatoms of the United States. Available from: http://westerndiatoms.colorado.edu/taxa/species/cocconeis_placentula [last accesed April 2020].

[117] C. J. R Sheppard, M. Gu, Y. Kawata, and S. Kawata. Three-dimensional transfer functions for high-aperture systems. *J. Opt. Soc. Am. A.*, 11(2), 1994.

[118] J. Yoon, K. Kim, H. Park, C. Choi, S. Jang, and Y. Park. Label-free characterization of white blood cells by measuring 3D refractive index maps. *Biomed. Opt. Express*, 6(10):3865–3875, 2015.

[119] M. Diez-Silva, M. Dao, J. Han, C. Lim, and S. Suresh. Shape and biomechanical characteristics of human red blood cells in health and disease. *MRS Bulletin*, 35(05):382–388, 2010.

[120] J. Li, Q. Chen, J. Sun, J. Zhang, J. Ding, and C. Zuo. Three-dimensional tomographic microscopy technique with multi-frequency combination with partially coherent illuminations. *Biomed. Opt. Express*, 9(6):2526–2542, 2018.

[121] A. S. Ostrovsky, G. Martínez-Niconoff, P. Martínez-Vara, and M. A. Olvera-Santamaría. The van cittert-zernike theorem for electromagnetic fields. *Opt. Express*, 17(3):1746–1752, 2009.

[122] J. Lim, A. Wahab, G. Park, K. Lee, Y. Park, and J. C. Ye. Beyond Born-Rytov limit for super-resolution optical diffraction tomography. *Opt. Express*, 25(24):30445–30458, 2017.

[123] J. A. Rodrigo, J. M. Soto, and T. Alieva. Fast label-free optical diffraction tomography compatible with conventional wide-field microscopes. In *Optical Methods for Inspection, Characterization, and Imaging of Biomaterials IV*, volume 11060, pages 139 – 148. International Society for Optics and Photonics, SPIE, 2019.

[124] J. M. Soto, J. A. Rodrigo, and T. Alieva. Partially coherent illumination engineering for enhanced refractive index tomography. *Opt. Lett.*, 43(19):4699–4702, 2018.

[125] S. Lee, K. Lee, S. Shin, and Y. Park. Generalized image deconvolution by exploiting the transmission matrix of an optical imaging system. *Sci. Rep.*, 7(1):8961, 2017.

[126] A. Limaye. Drishti: a volume exploration and presentation tool. In *Developments in X-Ray Tomography VIII*, volume 8506, page 85060X. International Society for Optics and Photonics, 2012.

[127] E. C. Samson and C. M. Blanca. Dynamic contrast enhancement in widefield microscopy using projector-generated illumination patterns. *New J. Phys.*, 9(10):363–363, 2007.

[128] C. S. Hoffman, V. Wood, and P. A. Fantes. An ancient yeast for young geneticists: A primer on the Schizosaccharomyces pombe model system. *Genetics*, 201(2):403–423, 2015.

[129] B. Rappaz, F. Charrière, C. Depeursinge, P. J. Magistretti, and P. Marquet. Simultaneous cell morphometry and refractive index measurement with dual-wavelength digital holographic microscopy and dye-enhanced dispersion of perfusion medium. *Opt. Lett.*, 33(7):744–746, 2008.

[130] J. Schindelin, I. Arganda-Carreras, E. Frise, V. Kaynig, M. Longair, T. Pietzsch, S. Preibisch, C. Rueden, S. Saalfeld, and B. Schmid. Fiji: an open-source platform for biological-image analysis. *Nat. Methods*, 9(7):676–682, 2012.

[131] S. L. Forsburg and N. Rhind. Basic methods for fission yeast. *Yeast*, 23(3):173–183, 2006.

[132] D. R. Rines, D. Thomann, J. F. Dorn, P. Goodwin, and P. K. Sorger. Live cell imaging of yeast. *Cold Spring Harbor Protocols*, 2011(9):pdb.top065482, 2011.

[133] S. Bianchi, F. Saglimbeni, and R. Di Leonardo. Holographic imaging reveals the mechanism of wall entrapment in swimming bacteria. *Phys. Rev. X*, 7(1), 2017.

[134] J. A. Rodrigo and T. Alieva. Freestyle 3D laser traps: tools for studying light-driven particle dynamics and beyond. *Optica*, 2(9):812–815, 2015.

[135] J. A. Rodrigo and T. Alieva. Polymorphic beams and Nature inspired circuits for optical current. *Sci. Rep.*, 6(1):1–8, 2016.

[136] J. A. Rodrigo and T. Alieva. Freestyle laser traps: Applications and future outlook. In *2016 IEEE 15th Workshop on Information Optics (WIO)*, pages 1–3, 2016.

[137] J. M. Soto, J. A. Rodrigo, and T. Alieva. Optical diffraction tomography with fully and partially coherent illumination in high numerical aperture label-free microscopy (invited). *Appl. Opt.*, 57(1):A205–A214, 2018.

[138] E. Streiblová, I. Málek, and K. Beran. Structural changes in the cell wall of Schizosaccharomyces pombe during cell division. *Journal of Bacteriology*, 91(1):428–435, 1966.

[139] J. Tinevez, N. Perry, J. Schindelin, G. M. Hoopes, G. D. Reynolds, E. Laplantine, S. Y. Bednarek, S. L. Shorte, and K. W. Eliceiri. Trackmate: An open and extensible platform for single-particle tracking. *Methods*, 115:80 – 90, 2017.

[140] S. Aknoun, J. Savatier, P. Bon, F. Galland, L. Abdeladim, B. F. Wattellier, and S. Monneret. Living cell dry mass measurement using quantitative phase imaging with quadriwave lateral shearing interferometry: an accuracy and sensitivity discussion. *J. Biomed. Opt*, 20(12):126009, 2015.

[141] PivLab website. https://www.mathworks.com/matlabcentral/fileexchange/27659-pivlab-particle-image-velocimetry-piv-tool. Accessed: 2020-03-25.

[142] J. G. Santiago, S. T. Wereley, C. D. Meinhart, D. Beebe, and R. J. Adrian. A particle image velocimetry system for microfluidics. *Exp. Fluids*, 25(4):316–319, 1998.

[143] Y. Sung, N. Lue, B. Hamza, J. Martel, D. Irimia, R. R. Dasari, W. Choi, Z. Yaqoob, and P. So. Three-dimensional holographic refractive-index measurement of continuously flowing cells in a microfluidic channel. *Phys. Rev. Applied*, 1:014002, 2014.

[144] N. C. Pegard, M. L. Toth, M. Driscoll, and J. W. Fleischer. Flow-scanning optical tomography. *Lab Chip*, 14:4447–4450, 2014.

[145] F. Merola, P. Memmolo, L. Miccio, R. Savoia, M. Mugnano, A. Fontana, G. D'Ippolito, A. Sardo, A. Iolascon, A. Gambale, and P. Ferraro. Tomographic flow cytometry by digital holography. *Light Sci. Appl.*, 6(4):e16241, 2016.

[146] M. Habaza, M. Kirschbaum, C. Guernth-Marschner, G. Dardikman, I. Barnea, R. Korenstein, C. Duschl, and N. T. Shaked. Rapid 3D Refractive-Index Imaging of Live Cells in Suspension without Labeling Using Dielectrophoretic Cell Rotation. *Adv. Sci.*, 4(2):1600205, 2017.

[147] A. E. Ekpenyong, S. M. Man, S. Achouri, C. E. Byant, J. Guck, and K. J. Chalut. Bacterial infection of macrophages induces decrease in refractive index. *J. Biophotonics*, 6(5):393–397, 2013.

[148] T. Kim, R. Zhou, M. Mir, S. D. Babacan, P. S. Carney, L. L. Goddard, and G. Popescu. White-light diffraction tomography of unlabelled live cells. *Nat. Photonics*, 8(3):256–263, 2014.

[149] T. A. Zangle and M. A. Teitell. Live-cell mass profiling: an emerging approach in quantitative biophysics. *Nat. Methods*, 11(12):1221–1228, 2014.

[150] H. Park, S. Hong, K. Kim, S. Cho, W. Lee, Y. Kim, S. Lee, and Y. Park. Characterizations of individual mouse red blood cells parasitized by Babesia microti using 3-D holographic microscopy. *Sci. Rep.*, 5:10827, 2015.

[151] S. Lee, H. Park, K. Kim, Y. Sohn, S. Jang, and Y. Park. Refractive index tomograms and dynamic membrane fluctuations of red blood cells from patients with diabetes mellitus. *Sci. Rep.*, 7(1):1039, 2017.

[152] W. Hsu, J. Su, C. Chang, and K. Sung. Investigating the backscattering characteristics of individual normal and cancerous cells based on experimentally determined three-dimensional refractive index distributions. In *Optics in Health Care and Biomedical Optics V*, volume 8553, page 85531O. International Society for Optics and Photonics, 2012.

[153] B. Simon, M. Debailleul, A. Beghin, Y. Tourneur, and O. Haeberlé. High-resolution tomographic diffractive microscopy of biological samples. *J. Biophotonics*, 3(7):462–467, 2010.

[154] V. L. Calin, M. Mihailescu, E. I. Scarlat, A. V. Baluta, D. Calin, E. Kovacs, T. Savopol, and M. G. Moisescu. Evaluation of the metastatic potential of malignant cells by image processing of digital holographic microscopy data. *FEBS Open Bio*, 7(10):1527–1538, 2017.

[155] P. Giannios, S. Koutsoumpos, K. G. Toutouzas, M. Matiatou, G. C. Zografos, and K. Moutzouris. Complex refractive index of normal and malignant human colorectal tissue in the visible and near-infrared. *J. Biophotonics*, 10(2):303–310, 2017.

[156] R. Chandramohanadas, Y. Park, L. Lui, A. Li, D. Quinn, K. Liew, M. Diez-Silva, Y. Sung, M. Dao, C. T. Lim, P. Rainer Preiser, and S. Suresh. Biophysics of malarial parasite exit from infected erythrocytes. *PloS One*, 6(6):e20869, 2011.

[157] Y. Park, M. Diez-Silva, G. Popescu, G. Lykotrafitis, W. Choi, M. S. Feld, and S. Suresh. Refractive index maps and membrane dynamics of human red blood cells parasitized by plasmodium falciparum. *Proc. Natl. Acad. Sci. U.S.A.*, 105(37):13730–13735, 2008.

[158] D. M. Mahlmann, J. Jahnke, and P. Loosen. Rapid determination of the dry weight of single, living cyanobacterial cells using the Mach-Zehnder double-beam interference microscope. *Eur. J. Phycol.*, 43(4):355–364, 2008.

[159] R. Barer. Determination of dry mass, thickness, solid and water concentration in living cells. *Nature*, 172(4389):1097–1098, 1953.

[160] A. Yakimovich, R. Witte, V. Andriasyan, F. Georgi, and U. F. Greber. Label-free digital holo-tomographic microscopy reveals virus-induced cytopathic effects in live cells. *mSphere*, 3(6):e00599–18, 2018.

[161] G. Li, T. Liu, A. Tarokh, J. Nie, L. Guo, A. Mara, S. Holley, and S. T. C. Wong. 3D cell nuclei segmentation based on gradient flow tracking. *BMC Cell Biol.*, 8(1):40, 2007.

[162] J. M. Soto, A. Mas, J. A. Rodrigo, T. Alieva, and G. Domínguez-Bernal. Label-free bioanalysis of Leishmania infantum using refractive index tomography with partially coherent illumination. *J. Biophotonics*, 12(9):e201900030, 2019.

[163] World Health Organization. Leishmaniasis. Key facts. Available from: http://www.who.int/news-room/fact-sheets/detail/leishmaniasis [last accessed October 2018].

[164] R. Kumar and C. Engwerda. Vaccines to prevent leishmaniasis. *Clin. Transl. Immunology*, 3(3):e13, 2014.

[165] J. F. Barbosa, S. M. de Figueiredo, F. M. Monteiro, F. Rocha-Silva, C. Gaciele-Melo, S. SC Coelho, S. Lyon, and R. B. Caligiorne. New approaches on leishmaniasis treatment and prevention: a review of recent patents. *Recent Pat. Endocr. Metab. Immune Drug Discov.*, 9(2):90–102, 2015.

[166] J. Dujardin, L. Campino, C. Cañavate, J. Dedet, L. Gradoni, K. Soteriadou, A. Mazeris, Y. Ozbel, and M. Boelaert. Spread of vector-borne diseases and neglect of leishmaniasis, europe. *Emerg. Infect. Dis.*, 14(7):1013, 2008.

[167] M. Podinovskaia and A. Descoteaux. Leishmania and the macrophage: a multifaceted interaction. *Future Microbiol.*, 10(1):111–129, 2015.

[168] K. Moutzouris, M. Papamichael, S. C. Betsis, I. Stavrakas, G. Hloupis, and D. Triantis. Refractive, dispersive and thermo-optic properties of twelve organic solvents in the visible and near-infrared. *Appl. Phys. B*, 116(3):617–622, 2014.

[169] I. Z. Kozma, P. Krok, and E. Riedle. Direct measurement of the group-velocity mismatch and derivation of the refractive-index dispersion for a variety of solvents in the ultraviolet. *J. Opt. Soc. Am. B.*, 22(7):1479–1485, 2005.

[170] F. Real, P. T. V. Florentino, L. C. Reis, E. M. Ramos-Sanchez, P. S. T. Veras, H. Goto, and R. A. Mortara. Cell-to-cell transfer of Leishmania amazonensis amastigotes is mediated by immunomodulatory LAMP-rich parasitophorous extrusions. *Cell. Microbiol.*, 16(10):1549–1564, 2014.

[171] J. M. Silverman, J. Clos, C. C. de Oliveira, O. Shirvani, Y. Fang, C. Wang, L. J. Foster, and N. E. Reiner. An exosome-based secretion pathway is responsible for protein export from leishmania and communication with macrophages. *J. Cell Sci.*, 123:842–852, 2010.

[172] G. D. Ruxton. The unequal variance T-test is an underused alternative to Student's T-test and the Mann-Whitney U-test. *Behav. Ecol.*, 17(4):688–690, 2006.

[173] F. Schmid. *Biological macromolecules: UV-visible spectrophotometry*. Wiley Online Library, 2001.

[174] H. Zhao, P. H. Brown, and P. Schuck. On the distribution of protein refractive index increments. *Biophys. J.*, 100(9):2309–2317, 2011.

[175] M. Friebel and M. Meinke. Model function to calculate the refractive index of native hemoglobin in the wavelength range of 250-1100 nm dependent on concentration. *Appl. Opt*, 45(12):2838–2842, 2006.

[176] V. T. Hoang, G. Stępniewski, K. H. Czarnecka, R. Kasztelanic, V. C. Long, K. D. Xuan, L. Shao, M. Śmietana, and R. Buczyński. Optical properties of buffers and cell culture media for optofluidic and sensing applications. *App. Sci.*, 9(6):1145, 2019.

[177] R. Barer and S. Tkaczyk. Refractive index of concentrated protein solutions. *Nature*, 173(4409):821–822, 1954.

[178] G. M. Hale and M. R. Querry. Optical constants of water in the 200-nm to 200-μm wavelength region. *App. Opt.*, 12(3):555–563, 1973.

[179] G. E. Perlmann and L.G. Longsworth. The specific refractive increment of some purified proteins. *J. Am. Chem. Soc.*, 70(8):2719–2724, 1948.

[180] D. Fu, W. Choi, Y. Sung, Z. Yaqoob, R. R. Dasari, and M. Feld. Quantitative dispersion microscopy. *Biomed. Opt. Express*, 1(2):347–353, 2010.

[181] Y. L. Jin, J. Y. Chen, L. Xu, and P. N. Wang. Refractive index measurement for biomaterial samples by total internal reflection. *Phys. Med. Biol.*, 51(20):N371, 2006.

[182] F. J. van der Meer, D. J. Faber, M. CG Aalders, A. A Poot, I. Vermes, and T. G van Leeuwen. Apoptosis-and necrosis-induced changes in light attenuation measured by optical coherence tomography. *Lasers Med. Sci.*, 25(2):259–267, 2010.

[183] B. Buendia, J-C. Courvalin, and P. Collas. Dynamics of the nuclear envelope at mitosis and during apoptosis. *Cell. Mol. Life Sci.*, 58(12-13):1781–1789, 2001.

[184] R. J Andrade, M. I. Lucena, M. C. Fernández, G. Pelaez, K. Pachkoria, E. García-Ruiz, B. García-Muñoz, R. González-Grande, A. Pizarro, and J. A. Durán. Drug-induced liver injury: an analysis of 461 incidences submitted to the spanish registry over a 10-year period. *Gastroenterology*, 129(2):512–521, 2005.

[185] D. Han, L. Dara, S. Win, T. A. Than, L. Yuan, S. Q. Abbasi, Z. Liu, and N. Kaplowitz. Regulation of drug-induced liver injury by signal transduction pathways: critical role of mitochondria. *Trends Pharmacol. Sci.*, 34(4):243–253, 2013.

[186] S. W. S Kang, G. Haydar, C. Taniane, G. Farrell, I. M. Arias, J. Lippincott-Schwartz, and D. Fu. AMPK activation prevents and reverses drug-induced mitochondrial and hepatocyte injury by promoting mitochondrial fusion and function. *PloS One*, 11(10), 2016.

[187] M. Karbowski and R. J. Youle. Dynamics of mitochondrial morphology in healthy cells and during apoptosis. *Cell Death Differ.*, 10(8):870–880, 2003.

[188] J. D. Wilson, W. J. Cottrell, and T. H. Foster. Index-of-refraction-dependent subcellular light scattering observed with organelle-specific dyes. *J. Biomed. Opt*, 12(1):1 – 10, 2007.

[189] G. F. Petrovick. Type 2 diabetes mellitus and metformin hydrochloride usage: A short. *J. Pharmacol.*, 2(2):5, 2018.

[190] L. C. de la Rosa, T. E. Vrenken, M. Buist-Homan, K. N. Faber, and H. Moshage. Metformin protects primary rat hepatocytes against oxidative stress-induced apoptosis. *Pharmacol. Res. Perspe.*, 3(2), 2015.

[191] K. Haseda, K. Kanematsu, K. Noguchi, H. Saito, N. Umeda, and Y. Ohta. Significant correlation between refractive index and activity of mitochondria: single mitochondrion study. *Biomed. Opt. Express*, 6(3):859–869, 2015.

[192] B. D. A. Levin, Y. Jiang, E. Padgett, S. Waldon, C. Quammen, C. Harris, U. Ayachit, M. Hanwell, P. Ercius, and D. A. Muller. Tutorial on the visualization of volumetric data using Tomviz. *Microscopy Today*, 26(1):12–17, 2018.

[193] B. Plitzko and S. Loesgen. Measurement of oxygen consumption rate (OCR) and extracellular acidification rate (ECAR) in culture cells for assessment of the energy metabolism. *Bio-protocol*, 8, 2018.

[194] B. Cao, L. Kelbauskas, S. Chan, R. M. Shetty, D. Smith, and D. R. Meldrum. Rotation of single live mammalian cells using dynamic holographic optical tweezers. *Opt. Laser. Eng.*, 92:70–75, 2017.

[195] H. Daniel Ou-Yang and M. Wei. Complex fluids: Probing mechanical properties of biological systems with optical tweezers. *Annu. Rev. Phys.*, 61(1):421–440, 2010.

[196] N. Rezaei, B. P. B. Downing, A. Wieczorek, C. K. Y. Chan, R. L. Welch, and N. R. Forde. Using optical tweezers to study mechanical properties of collagen. In *Photonics North 2011*, volume 8007, page 80070K. International Society for Optics and Photonics, 2011.

[197] C. Arbore, L. Perego, M. Sergides, and M. Capitanio. Probing force in living cells with optical tweezers: from single-molecule mechanics to cell mechanotransduction. *Biophys. Rev.*, pages 1–18, 2019.

[198] S. Chowdhury, M. Chen, R. Eckert, D. Ren, F. Wu, N. Repina, and L. Waller. High-resolution 3D refractive index microscopy of multiple-scattering samples from intensity images. *Optica*, 6(9):1211–1219, 2019.

[199] T. Pham, E. Soubies, A. Goy, J. Lim, F. Soulez, D. Psaltis, and M. Unser. Versatile reconstruction framework for diffraction tomography with intensity measurements and multiple scattering. *Opt. Express*, 26(3):2749–2763, 2018.

[200] Y. Sun, Z. Xia, and U. S. Kamilov. Efficient and accurate inversion of multiple scattering with deep learning. *Opt. Express*, 26(11):14678–14688, 2018.

[201] J. M. Soto, J. A. Rodrigo, and T. Alieva. Dual-wavelength cell's refractive index analysis with partially coherent optical diffraction tomography. In *Imaging and Applied Optics Congress*, page CF3C.3. Optical Society of America, 2020.

[202] J. M. Soto, J. A. Rodrigo, and T. Alieva. Achieving fast 3D label-free microscopy for optical tweezers experiments. In *Imaging and Applied Optics 2018 (DH)*, page DM2F.4. Optical Society of America, 2018.

[203] J. A. Rodrigo, J. M. Soto, and T. Alieva. Quantitative imaging with partially coherent illumination: problems and solutions. In *Digital Holography and Three-Dimensional Imaging*, page W4A.2. Optical Society of America, 2017.

[204] J. M. Soto, J. A. Rodrigo, and T. Alieva. Partially coherent optical diffraction tomography for label-free quantitative microscopy. In *2017 16th Workshop on Information Optics (WIO)*, pages 1–3, 2017.

[205] Edmund Optics. Introduction to modulation transfer function. Available from: https://www.edmundoptics.es/knowledge-center/application-notes/optics/introduction-to-modulation-transfer-function/ [last accesed April 2020].

[206] G. D. Boreman. *Modulation transfer function in optical and electro-optical systems*. SPIE press Bellingham, WA, 2001.

[207] G. Lubberts. The line spread-function and the modulation transfer function of X-ray fluorescent screen-film systems problems with double-coated films. *American Journal of Roentgenology*, 105(4):909–917, 1969.

[208] Hamamatsu official website. https://hamamatsu.magnet.fsu.edu/articles/digitalimagingdetectors.html. Accessed: 2020-03-25.

[209] W. M. b. M. Yunus and A. b. A. Rahman. Refractive index of solutions at high concentrations. *Appl. Opt.*, 27(16):3341–3343, 1988.

[210] M. L. Wellman, S. Krakowka, R. M. Jacobs, and G. J. Kociba. A macrophage-monocyte cell line from a dog with malignant histiocytosis. *In Vitro Cell. Dev. Biol.-Animal*, 24(3):223–229, 1988.

[211] J. Fernández-Cotrina, V. Iniesta, S. Belinchón-Lorenzo, R. Muñoz-Madrid, F. Serrano, J. C. Parejo, L. Gomez-Gordo, M. Soto, C. Alonso, and L. C. Gómez-Nieto. Experimental model for reproduction of canine visceral leishmaniosis by Leishmania infantum. *Vet. Parasitol.*, 192(1-3):118–128, 2013.

[212] G. Domínguez-Bernal, M. Jiménez, R. Molina, L. Ordóñez-Gutiérrez, A. Martínez-Rodrigo, A. Mas, M. T. Cutuli, and J. Carrión. Characterisation of the ex vivo virulence of Leishmania infantum isolates from Phlebotomus perniciosus from an outbreak of human leishmaniosis in Madrid, Spain. *Parasit. Vectors*, 7(1):499, 2014.